Relaxation of isolated self-gravitating systems in one and three dimensions

T. Worrakitpoonpon

THÈSE de DOCTORAT
de L'UNIVERSITÉ PIERRE ET MARIE CURIE

Spécialité :

Astronomie & Astrophysique
École Doctorale Astronomie & Astrophysique d'Île-de-France (ED127)
préparée au **Laboratoire de Physique Nucléaire et de Hautes Énergies**

Présentée par :

Tirawut WORRAKITPOONPON

Pour obtenir le grade de :

DOCTEUR DE L'UNIVERSITE PIERRE ET MARIE CURIE

Sujet de thèse :

Relaxation of isolated self-gravitating systems in one and three dimensions

Directeur de thèse :

Michael JOYCE

Thèse soutenue le 27 Juin 2011 devant le jury composé de :

M.	Pierre-Henri	CHAVANIS	Rapporteur
M.	Stéphane	COLOMBI	Examinateur
M.	Michael	JOYCE	Directeur de thèse
M.	Yan	LEVIN	Examinateur
M.	Stefano	RUFFO	Rapporteur
M.	Pascal	VIOT	Président du jury

Résumé

La gravité newtonienne joue un rôle essentiel dans l'évolution des objets célestes dans l'univers, mais la compréhension des systèmes gérés par celle-ci reste encore limitée. Dans cette thèse nous présentons une étude théorique de la dynamique des systèmes auto-gravitants à une dimension et à trois dimensions. La question centrale que nous abordons, en utilisant extensivement des simulations numériques, est si la mécanique statistique décrit bien leur comportement. À une dimension nous proposons d'étudier principalement deux questions: la relaxation vers équilibre thermique et la relaxation violente vers des état dit "quasi-stationnaire" (QSS). La première question considère la relaxation vers un état correspondant à l'équilibre thermique dans l'ensemble micro-canonique ou canonique, où la solution analytique est connue. Nous introduisons des paramètres d'ordre adaptés qui permettent de mettre en évidence cette relaxation. Plus spécifiquement nous observons que le temps caractéristique de cette relaxation est corrélé avec les fluctuations dans l'état quasi-stationnaire et est linéairement proportionnel au nombre de particules, indépendamment de la condition initiale. La deuxième question concerne la relaxation violente à partir de conditions initiales variées, et une comparaison avec la théorie de relaxation violente de Lynden-Bell. Cette théorie décrit avec une bonne approximation les propriétés de ces états quasi-stationnaires proche de la limite "dégénérée" ou, plus généralement, quand la relaxation est "calme". L'échec de la théorie est corrélé à l'emergence de structure "core-halo". Pour terminer nous étudions les mêmes questions sur les systèmes à trois dimensions. Dans le cas général la théorie de Lynden-bell donne, en absence d'une boîte de confinement, une solution de masse infinie. Nous remarquons que la solution est peu sensible à la taille de la boîte proche de la limite *dégénéré*. Elle peut être comparée aux résultats de simulations numériques pour le cas (plus physique) où le système est ouvert. Dans ce cas nous observons, comme en une dimension, un bon accord avec la prévision théorique dans le régime proche de la limite dégénérée ou autrement l'apparition de structure "core-halo".

Mot-clefs: Relaxation, Système auto-gravitant, Équilibre thermique, État quasi-stationnaire, Simulation à N-corps, Interaction à longue-portée

Abstract

Although Newtonian gravity plays an essential role in the evolution of celestial objects in the universe, the understanding of its dynamics is still limited. In this thesis we present a theoretical study of the dynamics of self-gravitating systems in one and three dimensions. The main question we study, using extensive numerical simulations, is whether existing statistical mechanical theories can describe their dynamical behavior. In one dimension we study principally two questions: the relaxation toward thermal equilibrium and the "violent relaxation" toward so-called "quasi-stationary states" (QSS). The first question considers the relaxation toward a state corresponding to the thermal equilibrium in the micro-canonical or canonical ensemble, where the analytical solution is known. We introduce the order parameters which can probe the relaxation. More specifically we establish that the characteristic time of this relaxation is correlated with fluctuations in the quasi-stationary state and scaled linearly with the particle number, independently of the initial condition. The second question considers the violent relaxation starting from different initial conditions, and the comparison with the violent relaxation theory of Lynden-Bell. This theory turns out to describe to a good approximation the properties of quasi-stationary states when the energy is close to the degenerate limit, or, more generally, when the initial conditions are such that the relaxation is "gentle". The breakdown of the theory on the other hand is correlated to the emergence of "core-halo" structure. Finally we study the same question for self-gravitating systems in three dimensions. For this case the theory of Lynden-Bell gives, in absence of a confining box, a solution of infinite mass. We show however that the solution is only weakly sensitive to the box size close to the *degenerate* limit. It can thus be compared with the (more physical) case of systems with open boundary conditions, which we simulate numerically. We observe as in one dimension a good agreement with the theory of Lynden-Bell in the regime close to the degenerate limit, and otherwise the emergence of core-halo structure when it breaks down.

Keywords: Relaxation, Self-gravitating system, Thermal equilibrium, Quasi-stationary state, N-body simulation, Long-range interaction

Contents

Introduction

In this thesis we present a theoretical study of basic aspects of the dynamics of classical Newtonian self-gravitating systems in one and three dimensions. The central question we address, using extensive numerical simulation, is to what extent well established statistical mechanical approaches can adequately explain their dynamical behavior.

The primary motivation for our study comes from astrophysics, as the idealized limit we consider in three dimensions should be relevant to understanding better the properties of real systems such as galaxies or dark matter "halos" in which gravity is the essential force at play. The simplified one dimensional (1D) model we consider is, however, equally relevant as a toy model of *any* long-range interaction, and our motivation for studying it comes also from the broader context of the statistical mechanics of long range interactions.

In this short introduction we recall first very briefly these two different contexts for our study and some of the principle relevant previous results. We then give a summary of the content of the thesis chapter by chapter.

Background

Self-gravitating systems in astrophysics

The gravitational force plays a crucial role in the evolution of celestial objects throughout the universe, on almost all scales ranging from planetary systems to galaxy clusters and even beyond. Although the inverse square law form of Newtonian gravity has been known since the 17th century, our understanding of the dynamics of self-gravitating systems is still far from complete despite the fact that it is widely treated in many research domains in astrophysics such as large scale structure formation, galaxy evolution and stellar evolution. In the second half of the 20th century important progress has, however, been made in applying statistical approaches, despite the apparent difficulties posed by the long-range (and unscreened) nature of the gravitational interaction. A pioneering development was the formulation of the "isothermal sphere distribution" (originally by Antonov in 1962 [1], see e.g. [2, 3] for review) as the mean-field state with maximized Boltzmann entropy. It is thus usually considered as the thermal equilibrium of 3D self-gravitating system. Observationally this isothermal sphere is in reasonable accordance with the characteristic flat rotation curve (corresponding to a density distribution decreasing as r^{-2}), outside the core of many spiral galaxies [4, 5] (see Fig. 1 for an example of a rotation curve for NGC 7217 extracted from [5]). The surface brightness of many elliptical galaxies, on the other hand, generally fits well with the so-called de Vaucouleurs' law [6, 7, 8].

The nature and time-scale for the relaxation of such systems to macroscopic dynamical equilibria was initially a puzzle. The estimation of the required relaxation time based on the rate of exchange of momentum (also known as "collisional relaxation" or "two-body relaxation")

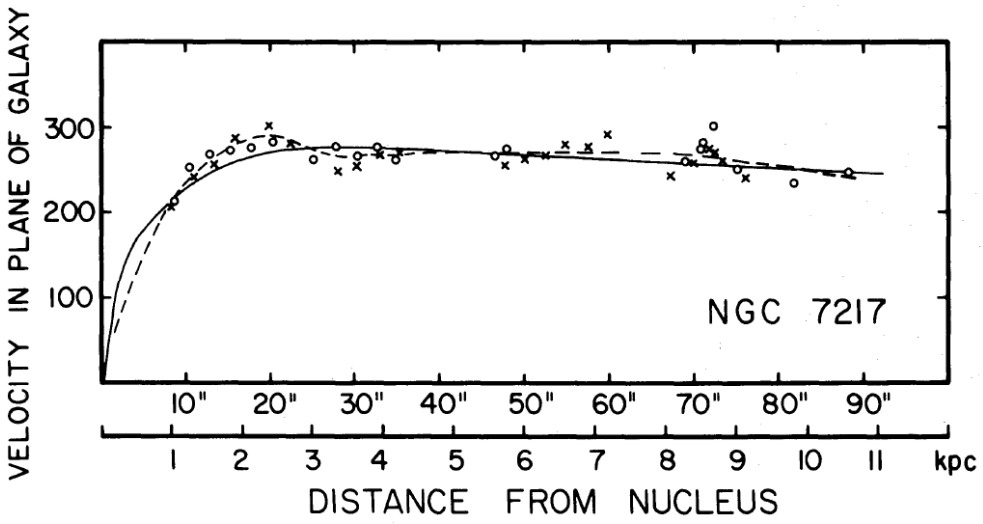

Figure 1: Circular velocities in the plane of NGC 7217. See [5] for more details about the observation and the determination of fitting lines.

indicated that it should diverge approximately linearly with particle number N [9, 10]. Thus celestial objects as massive as elliptical galaxies would require a time exceeding greatly the age of universe to relax. Globular clusters on the other hand (consisting of much fewer stars with more compact sizes) could be relaxed and indeed their distribution agree roughly with singular isothermal sphere distribution, i.e. $\rho \propto r^{-2}$, at inner radii [11]. A truncated isothermal sphere taking star evaporation in its outer parts into account was proposed by Michie [12] and King [13] which gave better agreement with many globular clusters (see [14, 15, 16] and references therein). Systems whose ages are much less than this two-body the relaxation time are referred as "collisionless system" [17, 18] and their "collisionless equilibria" are interpreted as stationary states of the "collisionless Boltzmann equation" (or Vlasov-Poisson equation).

In an attempt to answer these questions — and specifically to understand the observed light distribution of elliptical galaxies — Lynden-Bell introduced in 1967 [19] his theory of "violent relaxation". He not only explained qualitatively the physics of (much shorter time-scale for) the relaxation to collisionless equilibrium, but also postulated that the specific states resulting from it could be predicted based on a statistical mechanics of the collisionless dynamics. One of the striking features of this theory was that it could lead, in the so-called "non-degenerate" limit, to an isothermal sphere type solution. However, despite the fact that Lynden-Bell's explanation of mean-field relaxation became a cornerstone of the understanding of the dynamics of self-gravitating system, his statistical theory was rapidly abandoned in astrophysics: it did not appear to be adequate to explain the (non isothermal) property of stationary self-gravitating system as observed in astrophysical systems [20, 21]. Further the theory involves several difficulties which make its practical relevance in astrophysics questionable — notably the prediction of the theory are made in term of quantities which are, practically, not observable in this context. The fact that its prediction are extremely complicated to derive probably also led to its neglect.

In short as the size and sophistication of numerical studies of self-gravitating systems in astrophysics developed greatly the 1960s on, it became clear that neither the isothermal sphere nor Lynden-Bell's theory for collisionless relaxation could explain the "collisionless equilibria"

observed. Many simulations of isolated self-gravitating systems from simple classes of initial conditions give stationary states with density profiles well fitted by power-laws ranging from $r^{-3} - r^{-4}$ [22, 23, 24, 25, 26] (although some suggested the secondary infall could improve the density profile to $\sim r^{-2}$ [27, 28]) or by de Vaucouleur's law (or $R^{1/4}$ law) [29, 30, 31], depending on initial conditions. Further non-spherically symmetric (e.g. triaxial) stationary states are observed to result in certain cases starting even from spherically symmetric initial conditions [32, 33, 34], and anisotropy in velocity space is also a common feature of stationary states. In the context of cosmological simulation, on the other hand, the "universal" NFW mass profile [35, 36] fits strikingly well with simulations. Despite many attempts a full theoretical understanding of these results is still lacking. It is also very difficult numerically to simulate the evolution on sufficiently long time scales to probe the two-body relaxation. Studies in the literature (see e.g. [37, 32, 38, 39, 40]) provide some results but give still a very limited characterization and understanding of it.

Modeling and comparisons with observation are greatly complicated by the presence of dark matter, the existence of which was first postulated by Zwicky following his analysis of the nebulae and their "missing mass" [41, 42] (which later became known as "dark matter"). Observationally although dark matter may not be detected directly, gravitational lensing has proved to be a powerful method to probe its distribution. Dark matter is found to be present in low surface brightness (LSB) galaxies [43], spiral galaxies [44], elliptical galaxies [45] as well as in galaxy clusters [46]. In the context of current cosmological theories this mass is believed to be predominantly non-baryonic with extremely weak non-gravitational interaction. In the context of particle physics, there are many possible candidates for dark matter particles (see [47] for a review). A full dynamical treatment must then in principle take into account the fact that the baryonic matter has non-gravitational interactions (which are essential in stellar formation), and can result in the two components having different distributions. Although recent progress in numerical techniques allows one to simulate a system with both baryonic and dark matter, the theoretical understanding of this even more complex problem still remains very limited. The detailed understanding of galaxy evolution thus essentially rests on numerical simulations.

Statistical mechanics of long-range interactions

In the context of statistical mechanics, it is very natural to consider gravity as just one interaction of the broader class of *long-range* interactions, i.e. any interaction with two-body potential

$$V(r \to \infty) \sim \frac{1}{r^\alpha} \quad \text{and} \quad \alpha < d$$

where d is dimension of space. This classification is associated with the *non-extensive* nature of these interactions (i.e. their energy grows faster than linearly with the volume) which leads to fundamental differences (compared to short-range interactions) in both their equilibrium and out-of-equilibrium statistical mechanics. Apart from gravity, notable examples are unscreened Coulomb systems [48, 49], 2D vortices [50, 51] (with possible application to proto-planetary nebulae [52] or the great red spot of Jupiter [53, 54]) as well as systems like the free-electron laser [55, 56].

Research in the last decade or so in this field has made it clear that many of the behaviors of self-gravitating systems described above are generic to this class, and has given an improved understanding of these systems (for reviews see [57, 58, 59, 60]). Starting from kinetic equations derived from the BBGKY hierarchy [61], it can be shown that the evolution can (like for gravity)

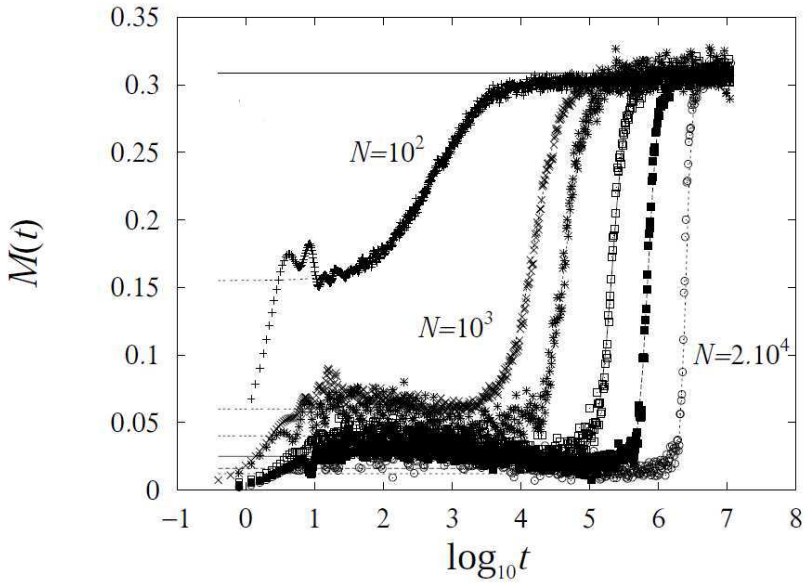

Figure 2: Ensemble-averaged time evolution of the magnetizations $M(t)$ with $N = 10^2, 10^3, 2 \times 10^3, 5 \times 10^3, 10^4$ and 2×10^4 from left to right. The shift toward the horizontal line with $M \sim 0.3$ of $M(t)$ indicates the relaxation to thermal equilibrium. For the determination of N-dependence, see [63].

be divided into two different regimes: the "collisionless" and "collisional". The former one corresponds to dynamics governed purely by the mean-field, where the kinetic equation reduces to the Vlasov equation [62]. Starting from a non-stationary initial condition the collisionless mean-field relaxation drives it at first to a stationary state (generally non-thermalized) subjected to the conservation of Casimir integrals. With lifetime diverging with N, the stationary state starts to evolve in the latter regime where the "collision term" comes into play. This collision term is a functional of the two-body correlation function. As a result of these collisional processes, these systems are expected to evolve toward the maximum entropy configuration, i.e. to thermal equilibrium when this is well defined. The non-thermalized intermediate states, i.e. the "collisionless equilibria", are usually referred as "quasi-stationary state (QSS)" in this context, and this is the nomenclature we will adopt here. The mechanics of this relaxation and the time scales characterizing it are currently open questions of research.

In the context of statistical mechanical investigations it is natural to study simplified toy models. One such model which has enjoyed a lot of attention in the last decade is the so-called Hamiltonian mean field (HMF) model [64]. It considers the dynamics of particles (sometimes called rotators) put on a ring and coupled with others by long-range force. For the attractive case the Hamiltonian may be written

$$H = \frac{1}{2}\sum_{i=1}^{N} p_i^2 + \frac{1}{2N}\sum_{i,j=1}^{N}\left[1 - \cos(\theta_i - \theta_j)\right]$$

for N identical rotators of unit mass and coupling constant. The dynamics is globally governed

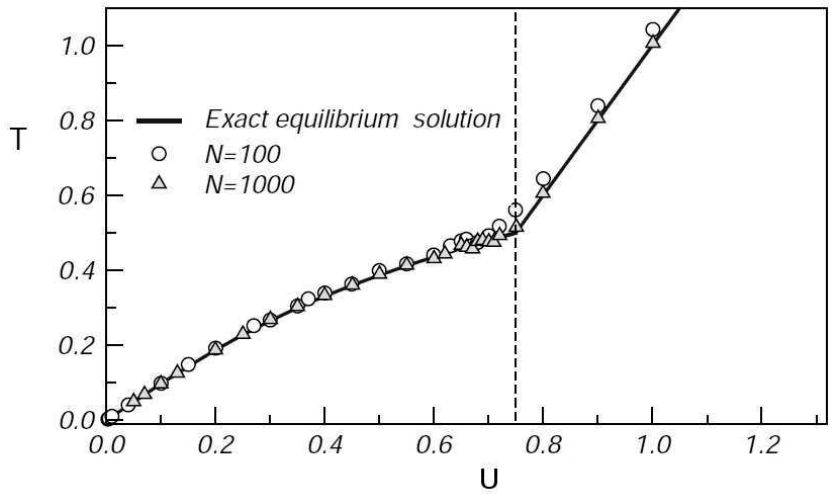

Figure 3: Caloric curve showing second order phase transition of the HMF model between the theoretical prediction (solid line) and the numerical simulations (point). This figure is taken from [68].

by the magnetization $\vec{M}$ defined as

$$\vec{M} = (m_x, m_y) = \frac{1}{N}\sum_{i=1}^{N}(\cos\theta_i, \sin\theta_i)$$

with $0 \leq |\vec{M}| \leq 1$. Hence the equation of motion of the rotator i reads

$$\ddot{\theta}_i = -m_x \sin\theta_i + m_y \cos\theta_i.$$

Given this (mean-field) property the calculation of the force for dynamical integration is very rapid which allows one to perform quite large N simulations over time scales sufficiently long to probe collisional relaxation. The model has a well-defined thermal equilibrium, showing a phase transition from an ordered phase with non-zero magnetization to a disordered phase with zero magnetization at higher temperature (see e.g. [65] and references therein). As the magnetization in thermal equilibrium is known, it can be used as a diagnostic for thermal relaxation (starting, for example, from a stationary state with zero magnetization at $U < 0.75$). The temporal evolution of magnetization for various N is shown in Fig. 2, from which the scaling with N of relaxation time yields $N^{1.7}$ as analyzed in [63, 66]. The analysis of the equilibrium phase transition can be found in [67]. The caloric curve is shown in Fig. 3 which shows a comparison between theory and numerical simulations. The curve manifests a second order phase transition at $U = 0.75$.

The HMF model also displays violent relaxation to QSS from classes of out of equilibrium initial conditions, and thus provides a simple context to test theories which might explain their properties. There has in this context been a revived interest in Lynden-Bell's theory of violent relaxation for self-gravitating systems: it turns out that in the HMF it can provide, at least in some of the space of initial conditions, excellent agreement with simulations [72]. More broadly, analysis has been published showing that, even if its detailed predictions are not accurate,

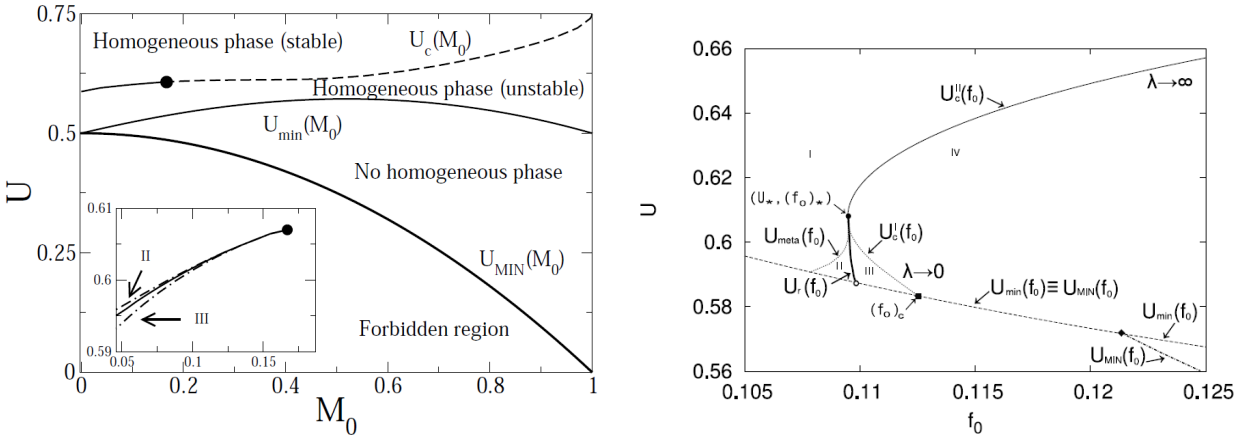

Figure 4: (Left panel) Phase diagram of the Lynden-Bell stationary state of the HMF model in the (M_0, U) plane (specific for the rectangular waterbag initial condition). See [69] for more detail about the calculation. (Right panel) Phase diagram of the same stationary state in the (f_0, U) plane (see [70, 71] for details).

LB prediction gives a very good qualitative understanding of the "out of equilibrium phase transitions" observed in the space of initial conditions leading to QSS. In this model, as shown in Fig. 4, Lynden-Bell theory predicts a non-trivial phase diagram for those states in the total energy/initial magnetization space (left) and in the total energy/initial phase space density (right), which is found to be quite well followed in numerical simulation (see [69, 70] for stability analysis and see [73, 74] for numerical investigation). The model has also been used to explore the possible relevance of so-called "Tsallis distribution functions" [75] in understanding the QSS, related to so-called polytropic distribution functions in the case of gravity which occur also in the HMF model [76, 77].

A theory analogous to that of Lynden-Bell was independently developed in the fluid mechanics context to describe the collisionless evolution of 2D vortices, the "Miller-Robert-Sommeria statistical theory" [78, 79]. The distribution of vortices is presented by the scalar vorticity field (equivalent to the distribution function in stellar systems) and their evolution is governed by the 2D Euler equations under mutual logarithmic interaction (analogous to the Vlasov-Poisson equations). The theory predicts the relaxation of vortices to stationary coherent structures. It was considered as successful in this context, most notably because of its agreement with laboratory experiment reproducing the system of vortices [80] or the persistence of the red spot of Jupiter. The analogies between 2D vortices and stellar systems are extensively discussed in [81, 82].

In our study we consider at length a different toy model in one dimension: the "sheet model", corresponding to particles interacting by attractive forces independent of their separation. This is the model in one dimension most directly analogous to 3D Newtonian gravity. It has been extensively studied both in the astrophysical literature (see e.g. [83, 84, 85, 86]) and in the statistical mechanics literature (see e.g. [87, 88, 89] and reference therein). It has the very nice feature that, because the forces change only when particles cross, it can be integrated numerically *up to machine precision* (and without any discretization of the equation of motion). It has been the subject of (mostly numerical) study in the literature for several decades following earlier

analytical studies [90, 91]. A fundamental question about this system is whether it relaxes to the statistical equilibrium calculated in the microcanonical or canonical ensemble. The latter were first calculated for this model, exactly and for any particle number N, in [92]. The literature on this model is marked by differing results (or, rather, interpretation of results) from different groups, and even some controversy. Works on relaxation to thermal equilibrium indicated that it was attained, and its scaling with N varied from one to another (see introduction of chapter 4 for more detail).

Recent results such as those on the HMF model have also led other authors to reconsider the theory of Lynden-Bell and re-evaluate it relevance. In a study of gravity in three dimensions, Levin et al. [37] have reported results showing Lynden-Bell theory to work well in certain parts of the relevant parameter space of initial conditions. These same authors have extended their analysis to 2D gravity [93] and also plasma systems [94] leading to the same conclusion. In the case of LB theory breakdown they proposed the distribution function based on the observed distribution function of core-halo which fitted very well in many cases. Yamaguchi [95] has revisited the 1D self-gravitating model, concluding agreement for a range of initial conditions and proposing also a phenomenological modification of distribution function fitting well with observed non Lynden-Bell QSS. These works in the statistical mechanics literatures have also provided motivation for the studies we report here.

Thesis plan

The report is divided into two main parts, each containing three chapters. The first part considers the underlying theories of the statistical mechanics, providing both a review of essential known results and our calculations of theoretical predictions from them. The second part then presents the results of our numerical simulations and comparison with theory.

Part I is organized as follows:

- Chapter 1 gives a brief basic introduction to Newtonian self-gravitating systems in one and three dimensions. We start with 3D self-gravity in the first part of the chapter. We derive first the kinetic equation from the BBGKY hierarchy to obtain the Vlasov equation, and then discuss some applications, including the Jeans equations, the virial theorem, polytrope solution and the Eddington formula. In the rest of the chapter we introduce the 1D self-gravitating system (or sheet model) and simplify (or generalize) the results presented in three dimensions to the 1D model.

- Chapter 2 reviews the central results obtained using equilibrium statistical mechanics applied to self-gravitating systems. First we discuss the isothermal sphere distributions corresponding to the local maxima of the micro-canonical entropy in the mean-field thermodynamic limit (i.e. the thermal equilibrium of 3D self-gravitating system), with a brief discussion about the negative specific heat and the gravothermal catastrophe. We then present the standard estimate of the rate of relaxation through momentum exchange rate due to close encounters. We also review the description of these effects as a diffusive Fokker-Planck process. The rest of the chapter then reviews in considerable detail the exact calculation of thermal equilibrium in one dimension. We consider the equilibrium in the canonical and micro-canonical ensembles, for finite N and then take the limit $N \to \infty$ with fixed mass and energy. We provide also a simple naive estimate for the rate of relaxation in one dimension. Finally we show a simple (but original) result: the thermal

equilibrium solution in one dimension is the *only* stationary solution to the Vlasov equation which is a separable function of spatial and velocity coordinates. This motivates the introduction of a family of "order parameters", which we will use in chapter 4 to probe the relaxation to thermal equilibrium.

- Chapter 3 discusses the violent relaxation theory of Lynden-Bell (LB). First of all we recall the estimation of the time scale of violent relaxation using the relative fluctuation rate of the gravitational mean-field. Then we review the derivation of the stationary state resulting from violent relaxation which maximizes the so-called Lynden-Bell entropy, and discuss a H-function theorem which shows that the Lynden-Bell entropy (or more generally coarse-grained entropy) increases with time. The rest of the chapter describes our calculations of the detailed prediction of the LB which we will use for our numerical simulations in chapters 5 and 6. We detail the application for 1D gravity with "waterbag" initial conditions in which the LB solution depends non-trivially only on a single parameter (the energy in suitable units). We explain the calculation to obtain the density profile, velocity distribution, energy distribution and order parameters for LB equilibria. Then we turn to the 3D system (again with "waterbag" initial conditions) in which the LB solution requires a cut-off radius, and thus depends on two parameters. We calculate the density profile, velocity distribution and energy distribution for 3D system. We examine in particular the dependence of results on the cut-off radius.

Part II is organized as follows:

- Chapter 4 reports our numerical investigation of the thermal relaxation of 1D systems. Compared to the previous literature, we perform simulations in a broader range of initial conditions and with greater statistics. We employ systems with relatively small N (of order a few hundred) and run them over the necessary very long time scales, smoothing out the finite N fluctuations by either time average or ensemble average. We use the order parameter defined in chapter 2, along with the equilibrium profiles derived previously in chapter 2, to study the relaxation. The main questions we focus on are: the attainment of thermal equilibrium and the dependence of the associated relaxation time both on N and the initial condition; and the correlation between the fluctuation of the QSS and the relaxation time. We give a determination of the scaling with N of the relaxation time. We also investigate the origin of various controversies in the previous literature. The text of this chapter is based essentially on an article published in J. Stat. Mech. [96].

- Chapter 5 considers violent relaxation in the 1D model, and specifically how well LB theory can account for the observed states. In this chapter we study principally three different classes of initial conditions, all of which are "waterbag". We simulate the system for relatively large N on the shorter time scale of violent relaxation. We measure the density profile, velocity distribution, energy distribution and the order parameters from simulations and compare with LB predictions derived in chapter 3. Compared to previous studies, we study a much broader range of initial conditions and the comparison with LB predictions is performed in much greater detail, allowing us to determine accurately the departures from theory and also assess the validity of modifications of LB theory recently proposed in the literature. The text of this chapter is taken from an article accepted for publication in Phys. Rev. E [97].

- Chapter 6 presents our numerical study of 3D self-gravitating systems, again focussing on the accuracy of LB theory. The study follows closely that in chapter 5, considering three classes of waterbag initial conditions. Our simulations are of systems with open boundary condition, which (following the discussion in chapter 3) limits the range of applicability of LB theory. As in one dimension we base our comparison with LB on the spatial, velocity and energy distributions. We also explore the effect of breaking spherical symmetry in the initial condition and the deviation from LB that it can lead to.

Each chapter in the second part contains a conclusion section synthesizing our results and conclusions.

Part I

Theoretical background

Chapter 1

Self-gravitating systems in one and three dimensions: definitions and basic results

In this chapter we recall first some well known results useful in the treatment of classical 3D systems of many particles interacting by Newtonian gravity (our treatment follows mostly [17]). We then define the analogous 1D systems — the so-called "sheet model" — and consider the extension of these same results to this case.

At the outset let us note that everywhere in this thesis we will consider self-gravitating systems of a finite (but large) number of *identical* point particles N.

1.1 3D Newtonian gravity

We consider a system of N identical particles of mass m with Hamiltonian

$$H = \sum_i \frac{|\vec{p_i}|^2}{2m} - \frac{Gm^2}{2} \sum_{i=1}^{N} \sum_{j=1, j\neq i}^{N} \frac{1}{|\vec{x}_i - \vec{x}_j|} \tag{1.1}$$

where $\vec{x}_i$ and $\vec{v}_i$ are the vectors of position and velocity of particle i and G is Newton's constant. The equation of motion of each particle reads

$$m\frac{d^2\vec{x}_i}{dt^2} = -Gm^2 \sum_{j=1, j\neq i}^{N} \frac{\vec{x}_i - \vec{x}_j}{|\vec{x}_i - \vec{x}_j|^3}. \tag{1.2}$$

1.1.1 Kinetic equation from the BBGKY hierarchy

In the study of systems of large N interacting by gravitational forces (or, more generally, by a long-range interaction), an important tool is the definition of an appropriate $N \to \infty$ limit in which the dynamics becomes "collisionless". In this limit the system's evolution can be determined by a closed set of equations for the one-particle phase space density $f(\vec{x}, \vec{v})$, the Vlasov-Poisson equations, known more generally in the case of gravity as the "collisionless Boltzmann equation". We reproduce here a standard derivation starting from the BBGKY hierarchy (see for example [61, 98, 99]) which allows a simple physical interpretation of this

limit. A rigorous mathematical derivation of it (for the general case) was given by Braun and Hepp [100].

Let $P_N(\vec{x}_1, \vec{v}_1, \ldots, \vec{x}_N, \vec{v}_N)$ be the N particle probability distribution. It is straightforward to show that it obeys the Liouville equation

$$\frac{\partial P_N(\vec{X}_1, \ldots, \vec{X}_N; t)}{\partial t} + \sum_{i=1}^{N} \left(\vec{v}_i \cdot \frac{\partial P_N(\vec{X}_1, \ldots, \vec{X}_N; t)}{\partial \vec{x}_i} - \sum_{j=1}^{N} \frac{\partial \Phi_{i,j}}{\partial \vec{x}_i} \cdot \frac{\partial P_N(\vec{X}_1, \ldots, \vec{X}_N; t)}{\partial \vec{v}_i} \right) = 0 \quad (1.3)$$

where $\vec{X}_i$ stands for $(\vec{x}_i, \vec{v}_i)$ and $\Phi_{i,j}$ is the gravitational potential experienced by particle i due to particle j. The normalization of P_N reads

$$\int P_N(\vec{X}_1, \ldots, \vec{X}_N) d^6X_1 \ldots d^6X_N = 1. \quad (1.4)$$

Defining the reduced j-particle probability distribution

$$P_j(\vec{X}_1, \ldots, \vec{X}_j) = \int P_N(\vec{X}_1, \ldots, \vec{X}_N) d^6X_{j+1} \ldots d^6X_N \quad (1.5)$$

and using (1.3) one can obtain the BBGKY hierarchy which connects the j-particle probability distribution to the $j+1$-particle probability distribution

$$\frac{\partial P_j}{\partial t} + \sum_{i=1}^{j} \vec{v}_i \cdot \frac{\partial P_j}{\partial \vec{x}_i} - \sum_{i=1}^{j} \sum_{k=1, k\neq i}^{j} \frac{\partial \Phi_{i,k}}{\partial \vec{x}_i} \cdot \frac{\partial P_j}{\partial \vec{v}_i} = (N-j) \sum_{i=1}^{j} \int d^6X_{j+1} \frac{\partial \Phi_{i,j+1}}{\partial \vec{x}_i} \cdot \frac{\partial P_{j+1}}{\partial \vec{v}_i}. \quad (1.6)$$

Specifically for the one-particle probability distribution $P_1(\vec{x}_1, \vec{v}_1; t)$, one obtains

$$\frac{\partial P_1}{\partial t} + \vec{v}_1 \cdot \frac{\partial P_1}{\partial \vec{x}_1} = (N-1) \frac{\partial}{\partial \vec{v}_1} \int \frac{\partial \Phi_{1,2}}{\partial \vec{x}_1} P_2 d^6X_2. \quad (1.7)$$

Decomposing the two-particle probability distribution P_2 into

$$P_2(\vec{X}_1, \vec{X}_2) = P_1(\vec{X}_1) P_1(\vec{X}_2) + P_2'(\vec{X}_1, \vec{X}_2) \quad (1.8)$$

where $P_2'(\vec{x}_1, \vec{x}_2)$ stands for the two-body correlation function, (1.7) can be written

$$\frac{\partial P_1}{\partial t} + \vec{v}_1 \cdot \frac{\partial P_1}{\partial \vec{x}_1} - (N-1) \frac{\partial P_1}{\partial \vec{v}_1} \cdot \int \frac{\partial \Phi_{1,2}}{\partial \vec{x}_1} P_1(\vec{X}_2) d^6X_2 = (N-1) \frac{\partial}{\partial \vec{v}_1} \int \frac{\partial \Phi_{1,2}}{\partial \vec{x}_1} P_2'(\vec{X}_1, \vec{X}_2) d^6X_2. \quad (1.9)$$

Writing the distribution function $f(\vec{x}, \vec{v}, t)$ (i.e. mass distribution in phase space) in term of $P_1(\vec{x}, \vec{v}, t)$ as

$$f(\vec{x}, \vec{v}, t) = NmP_1(\vec{x}, \vec{v}, t), \quad (1.10)$$

(1.7) becomes

$$\frac{\partial f}{\partial t} + \vec{v}_1 \cdot \frac{\partial f}{\partial \vec{x}_1} + \left[\frac{N-1}{N} \right] \vec{a}(\vec{x_1}) \cdot \frac{\partial f}{\partial \vec{v}_1} = C_N \quad (1.11)$$

where $\vec{a}(\vec{x}_1)$ is the mean acceleration given by

$$\vec{a}(\vec{x}_1) = -\int \frac{\partial \Phi_{1,2}}{\partial \vec{x}_1} P_1(\vec{x}_2, \vec{v}_2) d^3x_2 d^3v_2 \quad (1.12)$$

and C_N is the "collision term" which is a function of $P_2'(\vec{X}_1, \vec{X}_2)$. The Vlasov-Poisson limit is obtained taking $N \to \infty$ at constant total mass $M = Nm$, in which the collision term vanishes (for analysis of the N dependence of C_N, see for example [99, 101]), and (1.7) therefore reduces to

$$\frac{\partial f}{\partial t} + \vec{v} \cdot \frac{\partial f}{\partial \vec{x}} + \vec{a}(\vec{x}) \cdot \frac{\partial f}{\partial \vec{v}} = 0 \quad \text{and} \quad \vec{a}(\vec{x}) = -\vec{\nabla}\Phi(\vec{x}) \quad , \quad \nabla^2\Phi(\vec{x}) = 4\pi G \int f(\vec{x}, \vec{v}) d^3v. \tag{1.13}$$

Formally this limit corresponds therefore to neglecting the correlation between particles, and the particle dynamics is entirely governed by the mean-field. The Vlasov-Poisson evolution, in absence of the collision term, is therefore referred to as the "collisionless regime". The "collisional regime" is that, in contrast, which requires the inclusion of the physical effects described by the right-hand-side of 1.11. In the case of 3D gravity, as we will discuss in the next chapter, the leading process contributing to these terms is believed to be two-body collisionality, leading to deviation from the Vlasov-Poisson dynamics on a timescale $\sim N t_D$ where t_D is the characteristic dynamical time scale. Some analyses [102, 103] suggest that, except for the very special case of homogeneous states in one dimension, this result is generic. The long-lived QSS are thus interpreted, for gravity and more generally for long-range interaction, as corresponding to stationary solution of the Vlasov-Poisson equations. On the longer time scales on which the collisional processes come into play, relaxation to thermal equilibrium (if it is defined) is expected. Whether such relaxation does in fact take place, on what time scale and by what mechanism are open questions which we address some aspects of in this thesis.

Let us consider the energy and mass conservation during the collisionless evolution. Integrating (1.13) over phase space we obtain that the variation of total mass is given by

$$\frac{dM}{dt} + \int \vec{v} \cdot \frac{\partial f}{\partial \vec{x}} d^3x d^3v - \int \vec{\nabla}\Phi \cdot \frac{\partial f}{\partial \vec{v}} d^3x d^3v = 0.$$

with $M = \int f d^3x d^3v$. Supposing that the distribution function vanishes asymptotically in phase space (i.e. $f \to 0$ when $|\vec{x}|$ and $|\vec{v}| \to \infty$), we obtain the conservation of mass

$$\frac{dM}{dt} = 0. \tag{1.14}$$

Integrating (1.13) multiplied by $v^2/2$ over phase space, we obtain

$$\int \frac{v^2}{2} \cdot \frac{\partial f}{\partial t} d^3x d^3v + \int (\frac{v^2}{2}) \vec{v} \cdot \frac{\partial f}{\partial \vec{x}} d^3x d^3v - \int (\frac{v^2}{2}) \vec{\nabla}\Phi \cdot \frac{\partial f}{\partial \vec{v}} d^3x d^3v = 0.$$

The second term vanishes because $f(\vec{x}, \vec{v})$ vanishes asymptotically and we rearrange the third term using integration by parts to obtain

$$\frac{dK}{dt} = -\int f \vec{v} \cdot \vec{\nabla}\Phi d^3x d^3v \tag{1.15}$$

where $K \equiv \int \frac{v^2}{2} f d^3x d^3v$ is the total kinetic energy. Proceeding in the same way for the evolving gravitational field $\Phi(\vec{x}, t)$, we obtain

$$\int \frac{\Phi}{2} \cdot \frac{\partial f}{\partial t} d^3x d^3v + \int (\frac{\Phi}{2}) \vec{v} \cdot \frac{\partial f}{\partial \vec{x}} d^3x d^3v - \int (\frac{\Phi}{2}) \vec{\nabla}\Phi \cdot \frac{\partial f}{\partial \vec{v}} d^3x d^3v = 0$$

The third them vanishes because $f(\vec{x},\vec{v})$ vanishes asymptotically. Using integration by parts on the second term and decomposing the first term, we can express the time derivative of total potential energy $U \equiv \int \frac{\Phi}{2} f d^3x d^3v$ as

$$\begin{aligned} \int \frac{\partial}{\partial t}\big[\frac{f\Phi}{2}\big] d^3x d^3v - \int \frac{f}{2}\frac{\partial \Phi}{\partial t} d^3x d^3v - \frac{1}{2}\int f\vec{v}\cdot\vec{\nabla}\Phi d^3x d^3v &= 0 \\ \frac{dU}{dt} - \int \frac{f}{2}\frac{\partial}{\partial t}\Big[\int \rho(\vec{x}',t)\varphi(\vec{x},\vec{x}')d^3x'\Big] d^3x d^3v - \frac{1}{2}\int f\vec{v}\cdot\vec{\nabla}\Phi d^3x d^3v &= 0 \end{aligned} \tag{1.16}$$

where $\varphi(\vec{x},\vec{x}')$ and ρ denotes the pair potential and the density distribution respectively. Using the continuity equation of density flow

$$\frac{\partial \rho}{\partial t} = -\vec{\nabla}\cdot(\rho\vec{u}) = -\vec{v}\cdot\vec{\nabla}\Big[\int f(\vec{x},\vec{v})d^3v\Big] \quad \text{with} \quad \vec{u} = \frac{1}{\rho}\int \vec{v} f(\vec{x},\vec{v})d^3v,$$

(1.16) becomes

$$\frac{dU}{dt} = -\frac{1}{2}\int \Phi\vec{v}\cdot\vec{\nabla} f d^3x d^3v + \frac{1}{2}\int f\vec{v}\cdot\vec{\nabla}\Phi d^3x d^3v = \int f\vec{v}\cdot\vec{\nabla}\Phi d^3x d^3v. \tag{1.17}$$

Therefore the time derivative of total energy reads

$$\frac{d(K+U)}{dt} = \frac{dE}{dt} = 0. \tag{1.18}$$

This implies that during the collisionless evolution exchange between kinetic and potential energy is allowed while the total energy is conserved. These conservation laws can be in fact generalized to any "Casimir" integral I_h defined as

$$I_h = \int_\Omega h(f) d^3x d^3v \tag{1.19}$$

where $h(f)$ is any function of f. The time derivative of I_h reads

$$\begin{aligned} \frac{dI_h}{dt} &= \int \frac{\partial h(f)}{\partial t} d^3x d^3v = \int \frac{\partial h(f)}{\partial f}\Big[-\vec{v}\cdot\frac{\partial f}{\partial \vec{x}} - \vec{a}(\vec{x})\cdot\frac{\partial f}{\partial \vec{v}}\Big] d^3x d^3v \\ &= \int \Big[-\vec{v}\cdot\frac{\partial h(f)}{\partial \vec{x}} - \vec{a}(\vec{x})\cdot\frac{\partial h(f)}{\partial \vec{v}}\Big] d^3x d^3v = 0 \end{aligned} \tag{1.20}$$

if $f \to 0$ when $|\vec{x}|$ and $|\vec{v}| \to \infty$. A theory for determining the "collisionless equilibrium" will be discussed in chapter 3.

1.1.2 Jeans equations

Although the distribution function f gives full information about the system, in practice it is not possible to determine it with accuracy in astrophysical structures. Given the Vlasov equation one can obtain a useful relation between the spatial density and the moments of the velocity distribution known as the "Jeans equations".

Integrating the Vlasov equation (1.13) over velocity space, we obtain the continuity equation

$$\frac{\partial \rho}{\partial t} + \frac{\partial(\rho\bar{v}_i)}{\partial x_i} = 0 \tag{1.21}$$

expressing the conservation of mass, and where the bar over the velocity component denotes the averaged moment of velocity distribution given by

$$\overline{v_i^n}(\vec{x}) = \frac{1}{\rho(\vec{x})} \int v_i^n f(\vec{x}, \vec{v}, t) d^3v. \tag{1.22}$$

The first moment of $\vec{v}$ of (1.13) gives

$$\frac{\partial(\rho \bar{v}_j)}{\partial t} + \frac{\partial(\rho \overline{v_i v_j})}{\partial x_i} + \rho \frac{\partial \Phi}{\partial x_j} = 0. \tag{1.23}$$

This may be rearranged by eliminating the time derivative of ρ using (1.21) to obtain

$$\rho \frac{\partial \bar{v}_j}{\partial t} + \rho \bar{v}_i \frac{\partial \bar{v}_j}{\partial x_i} = -\rho \frac{\partial \Phi}{\partial x_j} - \frac{\partial(\rho \sigma_{ij}^2)}{\partial x_i} \tag{1.24}$$

where $\sigma_{ij}^2 = \overline{v_i v_j} - \bar{v}_i \bar{v}_j$ is the "velocity-dispersion tensor". This equation has the same form as Euler equation in fluid dynamics with the velocity field of the fluid being replaced by the average velocity of the particles, and the pressure by the stress tensor $\rho \sigma_{ij}^2$. Equations (1.21) together with (1.24) are the Jeans equations. They are widely employed in astrophysics to relate the observable streaming velocity $\bar{v}_i$ or velocity dispersion σ_{ij}^2 with the density distribution ρ. For a system which is spherically symmetric in coordinate space and in a stationary state the six component of stress tensor may be reduced to three and the Jeans equation (1.24) leads to

$$\frac{d(\rho \overline{v_r^2})}{dr} + 2\frac{\beta}{r} \rho \overline{v_r^2} = -\rho \frac{d\Phi}{dr} \tag{1.25}$$

where β is the "anisotropy parameter" defined as

$$\beta = 1 - \frac{\overline{v_\theta^2} + \overline{v_\phi^2}}{2\overline{v_r^2}} \tag{1.26}$$

with $\overline{v_r^2}$ being the radial component of mean square velocity and $\overline{v_\theta^2}$ and $\overline{v_\phi^2}$ for the tangential directions. If the velocity distribution is isotropic we obtain the equation of hydrostatic equilibrium:

$$\frac{dp}{dr} = -\rho \frac{d\Phi}{dr} \quad \text{with} \quad p = \rho \overline{v_r^2}. \tag{1.27}$$

1.1.3 Virial theorem

The virial theorem is a crucial tool in the analysis of self-gravitating system (and, more generally, long-range interacting systems). It provides a simple relation between the total potential and total kinetic energy for a system in a stationary state regardless of internal structure. It is straightforward to show the so-called Lagrange identity,

$$\frac{1}{2} \frac{d^2 I}{dt^2} = 2T + U, \tag{1.28}$$

where T and U are the total kinetic and potential energy, respectively, and I is the moment of inertia. The time average of expression (1.28) over a time window t_0 gives

$$\frac{1}{t_0} \left[\frac{1}{2} \frac{dI}{dt}(t_0) - \frac{1}{2} \frac{dI}{dt}(0) \right] = 2 < T > + < U > \tag{1.29}$$

where <> denotes the time average over that time window. The left-hand-side of (1.29) may vanish in various different cases. For example if the system's evolution is periodic in time and t_0 is the corresponding period, the left-hand-side is zero. Likewise it vanishes if t_0 is a very large time window, i.e.

$$\lim_{t_0\to\infty}\frac{1}{t_0}\left[\frac{1}{2}\frac{dI}{dt}(t_0)-\frac{1}{2}\frac{dI}{dt}(0)\right]=2<T>+<U>, \tag{1.30}$$

if all particles remain in a finite region. In either case we therefore obtain

$$0=2<T>+<U> \tag{1.31}$$

On the other hand a much more restrictive condition is satisfied in the case of a (macroscopic) stationary state. Since $\ddot{I}=0$, we have

$$0=2T+U. \tag{1.32}$$

Note that this will be valid exactly in the limit $N\to\infty$, and is true up to finite N fluctuations in a system of a finite number of particles. Note that it follows from (1.32) that, in a virialized state,

$$E=T+U=\frac{U}{2}=-T$$

and therefore that the *total energy of a virialized system is negative.* A generalized version of the virial theorem — the "tensor virial theorem" — can be obtained and reads

$$\frac{1}{2}\frac{d^2I_{jk}}{dt^2}=2T_{jk}+\Pi_{jk}+W_{jk} \tag{1.33}$$

where each element is defined as

$$\begin{aligned} I_{jk} &\equiv \int\rho(\vec{x})x_jx_kd^3x \quad , \quad T_{jk} \equiv \tfrac{1}{2}\int\rho\bar{v}_j\bar{v}_kd^3x \\ \Pi_{jk} &\equiv \int\rho(\overline{v_jv_k}-\bar{v}_j\bar{v}_k)d^3x \quad , \quad W_{jk} \equiv -\int\rho x_k\tfrac{\partial\Phi}{\partial x_j}d^3x. \end{aligned} \tag{1.34}$$

W_{jk} is the "potential-energy tensor". Both components T_{jk} and Π_{jk} form part of the kinetic-energy tensor with $K_{jk}=T_{jk}+\frac{1}{2}\Pi_{jk}$, where T_{jk} is associated to ordered motion and Π_{jk} to random motion. The trace of equation (1.33) gives (1.28), the "scalar virial theorem". To exploit the tensor virial theorem with astrophysical observations, the axes are chosen so that one axis is parallel to the line-of-sight direction and the structure is projected on the plane perpendicular to this axis. We consider, for example, an axisymmetric rotating galaxy with angular momentum in the z-direction and take the x-axis to be the line-of-sight direction, the virial theorem yields

$$\frac{<\bar{v}_{||}^2>}{<\bar{\sigma}_{||}^2>}=\frac{(1-\delta)W_{xx}/W_{zz}-1}{\alpha(1-\delta)W_{xx}/W_{zz}+1}$$

relating the averaged line-of-sight velocity square $<\bar{v}_{||}^2>$ and mean-square line-of-sight velocity dispersion $<\bar{\sigma}_{||}^2>$ to the global anisotropy parameter δ (see [17] or [104]). The two components of the tensor W can be determined using galaxy photometry, returning the ratio $\frac{W_{xx}}{W_{zz}}$ as a function solely of the ellipticity e. In the expression, α is a dimensionless constant depending on how the density $\rho(\vec{x})$ and streaming velocity $\bar{v}_i$ vary with position. There are also other versions of virial theorem such as for systems of charged particles [105], astrophysical magnetohydrodynamics [106] and rotating self-gravitating fluid [107].

1.1.4 Polytropes

Any time independent function in phase space which depends on the phase space coordinates through the energy $\varepsilon = \frac{v^2}{2} + \Phi(\vec{x})$ only is necessarily a solution of the Vlasov equation, since

$$\frac{\partial f}{\partial t} + \frac{\partial f}{\partial \varepsilon}\left[\vec{v}\cdot\frac{\partial \varepsilon}{\partial \vec{x}} - \vec{\nabla}\Phi(\vec{x})\cdot\frac{\partial \varepsilon}{\partial \vec{v}}\right] = 0 \quad \text{if} \quad \frac{\partial f}{\partial t} = 0. \tag{1.35}$$

An interesting class of such stationary solution are the so-called "polytropes". They are isotropic stationary solutions which have the simple property that

$$p = K\rho^{\gamma} \tag{1.36}$$

i.e. a "polytropic" equation of state. Using the (1.27) (valid since the system is isotropic) (1.36) implies that

$$\rho = \left(\frac{\gamma - 1}{K\gamma}\right)^{\frac{1}{\gamma-1}} (-\Phi)^{\frac{1}{\gamma-1}}. \tag{1.37}$$

It is straightforward to see that this behavior arises if $f = f(\varepsilon)$ is also a simple power-law function of ε:

$$f(\varepsilon) = \begin{cases} A(-\varepsilon)^{n-\frac{3}{2}} & , \quad \varepsilon < 0 \\ 0 & , \quad \varepsilon \geq 0 \end{cases} \tag{1.38}$$

where the cut-off at $\varepsilon = 0$ is required for boundedness. The spherical density distribution at $\Phi < 0$ is then

$$\rho = 4\pi \int_0^{\sqrt{-2\Phi}} v^2 f(\frac{1}{2}v^2 + \Phi)dv = c_n(-\Phi)^n \tag{1.39}$$

with

$$c_n = 2^{\frac{7}{2}}\pi A \int_0^1 x^2(1-x^2)^{n-\frac{3}{2}}dx = \frac{(2\pi)^{3/2}(n-\frac{3}{2})!A}{n!} \tag{1.40}$$

which is finite when $n > \frac{1}{2}$. Using (1.37) and (1.39) γ is thus related to n by

$$n = \frac{1}{\gamma - 1}. \tag{1.41}$$

Defining the dimensionless parameters

$$\xi \equiv \frac{r}{b} \quad , \quad \psi \equiv \frac{-\Phi}{|\Phi_0|} \quad \text{with} \quad b \equiv (4\pi G|\Phi_0|^{n-1}c_n)^{-\frac{1}{2}} \quad \text{where} \quad |\Phi_0| \equiv -\Phi(0), \tag{1.42}$$

we can write the Poisson equation as

$$\frac{1}{\xi^2}\frac{d}{d\xi}\left(\xi^2\frac{d\psi}{d\xi}\right) + \psi^n = 0 \tag{1.43}$$

for $\psi > 0$. This equation is the "Lane-Emden equation" [108, 109] widely known in stellar astrophysics. Defining ρ_c and p_c to be the density and pressure at $r = 0$, we have

$$\rho_c = c_n\Phi_0^n \quad \text{and} \quad K = \frac{p_c}{\rho_c^{1+\frac{1}{n}}} \tag{1.44}$$

so that

$$c_n = \left(\frac{\rho_c^{1+\frac{1}{n}}}{(n+1)p_c} \right)^n \tag{1.45}$$

and b may be expressed as

$$b \equiv \left(\frac{4\pi G \rho_c^2}{(n+1)p_c} \right)^{-\frac{1}{2}}. \tag{1.46}$$

Note that it is only for $n \leq 5$ that a physical (finite mass) solution exists (where the solution is considered from $\xi = 0$ to its cut-off radius ξ_c where $\Phi = 0$ for the first time, except for $n = 5$ where $\xi_c \to \infty$). For $n \geq 5$, solutions exist but the corresponding mass is infinite. Analytical solutions are known for the cases with $n = 0, 1$ and 5. They are summarized in Tab. 1.1 with their corresponding ξ_c. For numerical solution of (1.43) for other n, see [110]. More generally

Table 1.1: Analytical solutions of equation (1.43) for different n with cut-off radius ξ_c.

n	0	1	5
$\psi(\xi)$	$1 - \frac{\xi^2}{6}$	$\frac{\sin \xi}{\xi}$	$(1 + \frac{\xi^2}{3})^{-\frac{1}{2}}$
ξ_c	$\sqrt{6}$	π	∞

the polytropic equilibria in any number of spatial dimensions d (even $d > 3$) are given in [111], i.e. the solutions of the d-dimensional Lane-Emden equation. The article also analyzes their basic thermodynamic properties: thermodynamics statility and caloric curves, for example.

1.1.5 Eddington formula

The so-called "Eddington formula" [112] allows one, given an spherically symmetric mass profile $\rho(r)$ of a stationary structure, to infer a corresponding isotropic stationary solution of the Vlasov equation i.e. a corresponding QSS. To derive it consider again a phase space density $f(\varepsilon)$ with $f(\varepsilon) = 0$ for all $\varepsilon > 0$. The density distribution may be written as a function of Φ:

$$\rho(\Phi) = 4\pi \int v^2 f(\frac{1}{2}v^2 + \Phi) dv = 4\pi \int_\Phi^0 f(\varepsilon) \sqrt{2(\varepsilon - \Phi)} d\varepsilon. \tag{1.47}$$

Differentiating both sides with respect to Ψ, we obtain

$$\frac{1}{\sqrt{8}\pi} \frac{d\rho}{d\Phi} = \int_0^\Phi \frac{f(\varepsilon)}{\sqrt{\varepsilon - \Phi}} d\varepsilon. \tag{1.48}$$

Using the Abel integral equation, this relation can be inverted to give

$$f(\varepsilon) = \frac{1}{\sqrt{8}\pi^2} \frac{d}{d\varepsilon} \int_\varepsilon^0 \frac{d\rho}{d\Phi} \frac{d\Phi}{\sqrt{\Phi - \varepsilon}}. \tag{1.49}$$

The condition that $f(\varepsilon) \geq 0$ requires that

$$\int_0^\varepsilon \frac{d\rho}{d\Psi} \frac{d\Psi}{\sqrt{\mathcal{E} - \Psi}} \tag{1.50}$$

must be a strictly non-decreasing function of ε. Taking for example the polytropic density distribution (1.39), we recover

$$\begin{aligned} f(\varepsilon) &= \frac{nc_n}{\sqrt{8}\pi^2}\frac{d}{d\varepsilon}\left[\int_\varepsilon^0 (-\Phi)^{n-1}(\Phi-\varepsilon)^{-\frac{1}{2}}d\Phi\right] \\ &= -\frac{A(n-\frac{3}{2})!}{\sqrt{\pi}(n-1)!}\cdot\frac{d}{d\varepsilon}\left[(-\varepsilon)^{n-\frac{1}{2}}\int_0^1 z^{n-1}(1-z)^{-\frac{1}{2}}dz\right] \quad \text{with} \quad z\equiv\frac{\Phi}{\varepsilon} \\ &= A(-\varepsilon)^{n-\frac{3}{2}} \end{aligned}$$

as defined in (1.38), along with condition (1.50) satisfied. This formula can be used numerically to set up a finite N realization of such a QSS, for any $\rho(r)$ satisfying (1.50). Using the Poisson equation one can determine $\Phi(r)$ and thus $f(\varepsilon)$. Particles must then be distributed in space following the given $\rho(r)$, and with and r-dependent velocity PDF given by

$$P_r(v) = \frac{f(\varepsilon)}{\rho(r)}.$$

We note that these results can, in principle, be generalized to any long-range interactions.

1.2 1D Newtonian gravity, or the "sheet model"

We consider identical particles of mass m in one dimension which are mutually attracted by a force *independent of their separation*. The force on a particle at position x due to a particle at the origin at $x = 0$ is thus given by

$$F_{1d} = -gm^2\mathrm{sgn}(x) \tag{1.51}$$

where g is a coupling constant. This corresponds to the force derived from the pair potential

$$V(x) = gm|x|. \tag{1.52}$$

which is the solution of the Poisson equation in one dimension for a point source at the origin

$$\frac{d^2V(x)}{dx^2} = 2gm\delta(x) \tag{1.53}$$

(with the arbitrary integration constant chosen appropriately). Comparing to the 3D Poisson equation we see that this is equivalent to the interaction between infinitely thin planes of infinite extent with surface mass density $\Sigma = gm/2\pi G$, which explains why this model is widely called the "sheet model". For a particle at position x, the total force acting on it is thus

$$F(x) = gm^2[N_>(x) - N_<(x)] \tag{1.54}$$

where $N_>$ and $N_<(x)$ are the number of particles with coordinate greater than and less than x, respectively (or more simply: the total force on a given position is proportional to the difference between the number of particles on its right and on its left). For a system of N particles, the Hamiltonian reads

$$H = m\sum_{i=1}^N \frac{v_i^2}{2} + \frac{gm^2}{2}\sum_{i=1}^N\sum_{j=1}^N |x_i - x_j| \tag{1.55}$$

where x_i and v_i denote the position and velocity coordinate of particle i. The equation of motion of the particle i is thus

$$m\frac{d^2x_i}{dt^2} = -gm^2 \sum_{j=1,j\neq i}^{N} \frac{(x_i - x_j)}{|x_i - x_j|}. \tag{1.56}$$

Unlike the Newtonian gravity in three dimensions, the pair potential (1.52) is positive and divergent at large separation, so particles cannot escape to infinity. As we will discuss in chapters 2 and 3, this implies that it is not necessary, as in three dimensions, to enclose the system in a box to define thermal equilibrium (chapter 2) and collisionless equilibrium (chapter 3). We will always consider here the system with open boundary conditions. The smoothing of force is not required because of the absence of force divergence at small separation. As a result there is no equivalent of the so-called "gravothermal catastrophe" in three dimensions.

To specify fully the dynamics we must prescribe what happens when two particles arrive at the same point. Since the force is bounded as the separation goes to zero, the natural physical prescription for the 1D model is that the particles simply cross (i.e. pass through one another). In one dimension, however, this is equivalent, up to a change in particle labels, to a hard elastic collision, as such a collision (of equal mass particles) simply results in an exchange of their velocities. Thus, up to particle labels, the sheet model for equal masses is equivalent to one in which particles experience always the same spatially constant force equation (1.54) and simply exchange velocities when they "collide". As has been noted in some previous studies of models of this kind [113] it is convenient to exploit this equivalence in numerical simulation, described in appendix A.

1.2.1 Jeans equations (1D)

The Vlasov-Poisson equation simplifies in one dimension to

$$\frac{\partial f}{\partial t} + v\frac{\partial f}{\partial x} - \frac{\partial \Phi(x)}{\partial x} \cdot \frac{\partial f}{\partial v} = 0 \tag{1.57}$$

where $\Phi(x)$ is mean-field potential satisfying

$$\frac{d^2\Phi(x)}{dx^2} = g \int f(x,v)dv. \tag{1.58}$$

Direct integration of the Vlasov-Poisson equations in one dimension has been performed and showed the relaxation to QSS similar to those observed in N-body simulations (see e.g. [114, 115]). Integrating (1.57) over velocity gives

$$\frac{\partial \rho}{\partial t} + \frac{\partial(\rho\bar{v})}{\partial x} = 0. \tag{1.59}$$

which is the continuity equation, where ρ and $\bar{v}$ are the density distribution and the mean velocity. Multiplying (1.57) by velocity and integrating over velocity, we obtain

$$\frac{\partial(\rho\bar{v})}{\partial t} + \frac{\partial(\rho\overline{v^2})}{\partial x} + \rho \cdot \frac{\partial \Phi}{\partial x} = 0 \tag{1.60}$$

with $\overline{v^2}$ being mean velocity squared. Just as in three dimensions the Jeans equation then relates the density distribution to the first two velocity moments. The equation of hydrostatic equilibrium in one dimension is obtained for a stationary states with $\bar{v} = 0$, i.e.

$$\frac{dp}{dx} = -\rho\frac{d\Phi}{dx} \tag{1.61}$$

where $p = \rho\overline{v^2}$ is the pressure.

1.2.2 Virial theorem (1D)

We will generalize the usual 3D virial theorem to 1D gravity. Taking the first moment of x_i and using (1.56) we obtain

$$m\sum_i [\frac{d}{dt}(x_i v_i) - v_i^2] = -gm^2 \sum_i \sum_{j\neq i} x_i \frac{(x_i - x_j)}{|x_i - x_j|}. \tag{1.62}$$

Using the interchangeability of i and j, we obtain

$$\begin{aligned} m\sum_i \frac{d}{dt}(x_i v_i) - m\sum_i v_i^2 &= -\frac{gm^2}{2}\sum_i\sum_{j\neq i}\left[x_i\frac{(x_i - x_j)}{|x_i - x_j|} + x_j\frac{(x_j - x_i)}{|x_j - x_i|}\right] \\ m\sum_i \frac{d}{dt}(x_i v_i) &= m\sum_i v_i^2 - \frac{gm^2}{2}\sum_i\sum_{j\neq i}|x_i - x_j| = 2T - U. \end{aligned} \tag{1.63}$$

where T and U are the total kinetic and potential energy respectively. Performing the temporal average of equation (1.63), this gives

$$\begin{aligned} \frac{m}{t_0}\sum_i \int_\tau^{\tau+t_0} \frac{d(x_i v_i)}{dt} dt &= \frac{1}{t_0}\int_\tau^{\tau+t_0} 2T dt - \frac{1}{t_0}\int_\tau^{\tau_0+t_0} U dt \\ \sum_i \frac{m(x_i(\tau+t_0)v_i(\tau+t_0) - x_i(\tau)v_i(\tau))}{t_0} &= 2 < T > - < U > \end{aligned} \tag{1.64}$$

where $<>$ denotes a time average in a window of width t_0. Equation (1.64) implies that if all particles are always bound in a finite region, the term $x_i(\tau+t_0)v_i(\tau+t_0) - x_i(\tau)v_i(\tau)$ is always finite. Consider the temporal average in large time windows, i.e. $t_0 \to \infty$, the equation (1.64) reduces to

$$0 = 2 < T > - < U > . \tag{1.65}$$

Note that (1.63) can be rewritten in more strictly analogous manner to the 3D expression

$$\frac{1}{2}\frac{d}{dt}\cdot\frac{d}{dt}\sum_i (m x_i^2) = \frac{1}{2}\frac{d^2 I}{dt^2} = 2T - U \tag{1.66}$$

where I is the 1D moment of inertia. If the system is stationary, it thus obeys the relation

$$0 = 2T - U. \tag{1.67}$$

Following the same steps it is straightforward to show that, for a system with power law attractive force between particles $F_{ij} \propto -\frac{x_i - x_j}{|x_i - x_j|^{1-\alpha}}$, this result generalizes to

$$0 = 2T - (1+\alpha)U. \tag{1.68}$$

The virial theorem derived above is based on the particle dynamics. We can also recover it in the fluid limit (i.e. the system described by one-particle distribution function obeying the

Vlasov equation). Integrating the first moment with respect to x of the Jeans equation (1.60), we obtain

$$\int_{-\infty}^{\infty} x\frac{\partial(\rho\bar{v})}{\partial t}dx + \int_{-\infty}^{\infty} x\frac{\partial(\rho\overline{v^2})}{\partial x}dx + \int_{-\infty}^{\infty} x\rho\frac{\partial\Phi}{\partial x}dx = 0. \tag{1.69}$$

With some manipulation, the third term can be rearranged to give

$$\begin{aligned}\int x\rho\frac{\partial\Phi}{\partial x}dx &= \int x\rho\frac{\partial}{\partial x}\int g\rho(x')|x-x'|dx'dx = \int\int g\rho(x)\rho(x')\frac{x(x-x')}{|x-x'|}dx'dx \\ &= \frac{1}{2}\int\int g\rho(x)\rho(x')|x-x'|dx'dx = U.\end{aligned} \tag{1.70}$$

And similarly for the second term

$$\int x\frac{\partial(\rho\overline{v^2})}{\partial x}dx = -\int\rho\overline{v^2}dx = -2T. \tag{1.71}$$

We then rearrange the first term

$$\int x\frac{\partial(\rho\bar{v})}{\partial t}dx = \frac{d}{dt}\int x\rho\bar{v}dx = -\frac{1}{2}\frac{d}{dt}\int x^2\frac{\partial(\rho\bar{v})}{\partial x}dx$$

and, using the continuity equation (1.59), we obtain

$$-\frac{1}{2}\frac{d}{dt}\int x^2\frac{\partial(\rho\bar{v})}{\partial x}dx = \frac{1}{2}\frac{d}{dt}\int x^2\frac{\partial\rho}{\partial t}dx = \frac{1}{2}\frac{d^2}{dt^2}\int x^2\rho dx = \frac{1}{2}\frac{d^2I}{dt^2}. \tag{1.72}$$

Combining (1.70), (1.71) and (1.72) in (1.69), we thus recover

$$\frac{1}{2}\frac{d^2I}{dt^2} = 2T - U. \tag{1.73}$$

Note that since $E = T + U$, a virialized system has $E = 3T = \frac{3}{2}U$ (and $E \geq 0$ always by definition). The generalized virial theorem for d-dimensional gravity may be found in [116].

1.2.3 Polytropes (1D)

In this section we consider in 1D gravity the existence of polytropes analogous to those in three dimensions. We thus consider a distribution function which can be expressed in term of individual energy $\varepsilon = \frac{1}{2}v^2 + \Phi$ as

$$f(\varepsilon) = D\varepsilon^{-n-\frac{1}{2}}. \tag{1.74}$$

Note that no cut-off need to be imposed on ε as the system is necessarily bounded. The density distribution reads

$$\rho = \int_{-\infty}^{\infty} f(\frac{1}{2}v^2 + \Phi)dv = d_n\Phi^{-n} \tag{1.75}$$

where

$$d_n = 2^{\frac{3}{2}}D\int_0^{\infty}\frac{dx}{(x^2+1)^{n+\frac{1}{2}}} = 2^{\frac{3}{2}}D\int_0^{\pi/2}\cos^{2n-1}\theta d\theta = \frac{\sqrt{2\pi}D(n-1)!}{(n-\frac{1}{2})!}. \tag{1.76}$$

The condition that d_n be finite requires that $n > 0$ (which also is required so that $\rho \to 0$ as $\Phi \to \infty$). The condition of hydrostatic equilibrium (in one dimension) is

$$\frac{dp}{dx} = -\rho\frac{d\Phi}{dx}, \tag{1.77}$$

which, using (1.75), implies the power law equation of state

$$p = k\rho^{\gamma} \tag{1.78}$$

with

$$\gamma = 1 - \frac{1}{n} \quad \text{and} \quad k = \frac{d_n^{1/n}}{n-1}. \tag{1.79}$$

The condition $n > 0$ corresponds to $\gamma < 1$. Defining the dimensionless variables

$$\xi = (\frac{2gd_n}{\Phi_0^{n+1}})^{1/2} x \quad \text{and} \quad \psi = \frac{\Phi}{\Phi_0} \tag{1.80}$$

where $\Phi_0 \equiv \Phi(0)$, we can write the Poisson equation

$$\frac{\partial^2 \psi}{\partial \xi^2} - \psi^{-n} = 0 \tag{1.81}$$

analogous to Lane-Emden equation in three dimensions. Integrating (1.81) with boundary conditions $\frac{d\psi}{d\xi}(0) = 0$ and $\psi(0) = 1$ gives

$$\int_1^{\psi} \sqrt{\frac{1-n}{2(\psi'^{1-n} - 1)}}\, d\psi' = \xi \quad \text{for} \quad n \neq 1, \tag{1.82}$$

and

$$\int_1^{\psi} \frac{1}{\sqrt{2 \ln \psi'}}\, d\psi' = \xi \quad \text{for} \quad n = 1. \tag{1.83}$$

It is simple to derive the asymptotic large ξ behavior of ψ from (1.82). We have, for $n \neq 1$,

$$\begin{aligned} \xi &\sim \int_1^{\psi} \psi'^{-\frac{1-n}{2}} d\psi' = \psi^{\frac{n+1}{2}} - 1 \\ \psi &\sim \xi^{\frac{2}{n+1}}. \end{aligned} \tag{1.84}$$

Thus

$$\rho \sim \psi^{-n} \sim \xi^{-\frac{2n}{n+1}}. \tag{1.85}$$

To obtain a finite mass therefore requires

$$n > 1 \quad \text{or} \quad \gamma > 0.$$

Therefore the cases $n > 1$ correspond to finite mass polytropes. It is straightforward to obtain numerical solutions using (1.82) for any n. Analytical solutions may be given for some cases, notably:

- $n = 3$ ($\gamma = \frac{2}{3}$):
  Integration of (1.82) gives

  $$\xi = \sqrt{\psi^2 - 1} \quad \text{or} \quad \psi = \sqrt{\xi^2 + 1}. \tag{1.86}$$

  The corresponding density is then

  $$\rho(x) \propto \frac{d^2\psi}{d\xi^2} = (\xi^2 + 1)^{-3/2} \tag{1.87}$$

  with normalization condition

  $$\int_0^{\infty} \tilde{\rho}(\xi) d\xi = 1. \tag{1.88}$$

- $n \to \infty$ ($\gamma = 1$):
  The limit $n \to \infty$ corresponds to $\gamma = 1$ i.e. the equation of state becomes

$$p = K\rho. \tag{1.89}$$

  i.e. the ideal gas equation of state. Using the condition of hydrostatic equilibrium we then obtain

$$K\frac{d\rho}{dx} = -\rho\frac{d\Phi}{dx}$$

  from which the density distribution becomes

$$\rho = \rho_0 e^{-\frac{\Phi-\Phi_0}{K}} \tag{1.90}$$

  which is the Maxwell-Boltzmann density distribution. This is analogous to the 3D solution with $n \to \infty$ which gives the so-called isothermal sphere distribution. The 3D version has infinite mass but the 1D Maxwell-Boltzmann distribution function has finite mass. We will discuss these particular solutions at length in the next chapter.

1.2.4 Eddington formula (1D)

We consider the generalization of the Eddington formula to our 1D system. Given a stationary distribution function $f(\varepsilon)$, the density distribution as function of Φ in one dimension is given by

$$\rho(\Phi) = \int f(\varepsilon)dv = \sqrt{2}\int_\Phi^\infty \frac{f(\varepsilon)}{\sqrt{\varepsilon-\Phi}}d\varepsilon. \tag{1.91}$$

The Abel integral equation gives now the inversion

$$f(\varepsilon) = -\frac{1}{\sqrt{2}\pi}\frac{d}{d\varepsilon}\int_\varepsilon^\infty \frac{\rho(\Phi)}{\sqrt{\Phi-\varepsilon}}\,d\Phi \tag{1.92}$$

or, alternatively,

$$f(\varepsilon) = -\frac{1}{\sqrt{2}\pi}\int_\varepsilon^\infty \frac{d\rho}{d\Phi}\frac{d\Phi}{\sqrt{\Phi-\varepsilon}} \tag{1.93}$$

to be compared with (1.49) in three dimensions. To ensure that $f(\varepsilon) \geq 0$, one requires therefore that the integral

$$\int_\varepsilon^\infty \frac{\rho(\Phi)}{\sqrt{\Phi-\varepsilon}}\,d\Phi$$

is strictly non-increasing. Note that, as in three dimension, these results apply in principle for any Φ except in this case the condition about sufficiency of $\frac{d\rho}{dx} \leq 0$ which assures Φ to a strictly increasing function, which is a specific property of the 1D gravitational interaction. Thus one can always construct a QSS for any given monotonically decreasing mass density profile using this formula. It is straightforward to show that taking $\rho = d_n\Phi^{-n}$ in (1.93), we recover

$$\begin{aligned} f(\varepsilon) &= \frac{nd_n}{\sqrt{2}\pi}\int_\varepsilon^\infty \frac{\Phi^{-n-1}d\Phi}{\sqrt{\Phi-\varepsilon}} \\ &= \frac{Dn!}{\sqrt{\pi}(n-\frac{1}{2})!}\varepsilon^{-n-\frac{1}{2}}\int_0^1 y^{n-\frac{1}{2}}(1-y)^{-\frac{1}{2}}dy \quad \text{with} \quad y \equiv \frac{\varepsilon}{\Phi} \\ &= D\varepsilon^{-n-\frac{1}{2}}. \end{aligned}$$

The extension of the Eddington formula to a stationary solution in d dimensions is given in [117]. The author also discussed an application to chemotaxis in biological systems.

Chapter 2

Thermal equilibrium of 3D and 1D self-gravitating systems

In this chapter we review the central results obtained using equilibrium statistical mechanics applied to self-gravitating systems (for review see e.g. [2, 3]). We consider first, as in the previous chapter, the 3D case, in particular the isothermal sphere configurations which correspond to local maxima of the micro-canonical entropy in the mean-field thermodynamic limit, and briefly discuss also the appearance of negative specific heat and the "gravothermal catastrophe". We then review the standard estimations of the rate of relaxation due to two-body collisionality. We also review the description of those collisional effects using the diffusive Fokker-Planck equation. The rest of the chapter then considers the 1D case, which presents considerable simplification compared to the 3D case. Unlike in three dimensions, neither regularization at small distance (by removing the singularity in the potential) nor at large distance (by an enclosing box) is required to make the equilibrium statistical mechanics well defined. We review then the exact solution in the canonical ensemble and then in the micro-canonical ensemble, which were given (for any N) by Rybicki [92]. In this part we provide considerable detail, filling in some parts of Rybicki's calculation not included in the original paper. In the last part we discuss briefly the collisional relaxation mechanism in one dimension, and give a simple naive estimate for the associated rate. We then also show a simple property of the 1D equilibrium: it is the unique solution of the Vlasov equation which is separable in position and velocity space. This results leads us to define a set of "order parameters" which we will make extensive use of in our study of relaxation in this model in chapter 4.

2.1 Thermal equilibrium for 3D self-gravitating systems

In the section we first review briefly the maximization of the micro-canonical entropy in the mean-field limit, and describe the property of the resulting configuration. Our presentation here follows closely that of [118, 2].

2.1.1 Mean-field equilibrium

The micro-canonical entropy for a N identical particle system enclosed in a region of volume V, with energy E, is simply

$$S(E) = \ln g(E) \tag{2.1}$$

where $g(E)$ is the number of accessible states given by

$$g(E) = \frac{1}{N!}\int d^{3N}xd^{3N}p\delta(E-H). \tag{2.2}$$

For a purely self-gravitating system it is straightforward to show (see e.g. [2]) that this expression is badly defined: it diverges for

- $V \to \infty$, i.e. unless we confine the system in a box, and for
- $N > 2$, unless the singularity in the potential at $r = 0$ is regulated.

We will thus assume that the system is confined in a box and that an appropriate regularization of the potential is applied. It turns out that the results we derive here — in the mean-field limit — are independent of such a cut-off (because we will discard the contribution from the relevant part of phase space). The derived maxima are therefore only local maxima for unregulated system, but may be global maxima for sufficiently large values of the regularization [119]. Taking the Fourier transform of $\delta(E-H)$ and integrating over $\vec{p}$, we obtain

$$\begin{aligned} g(E) &= \frac{1}{N!}\int dk \int d^{3N}x\left[\int e^{2\pi ik(E-U-\sum_{i=1}^{3N}\frac{p_i^2}{2m})}d^{3N}p\right] = \frac{m^{\frac{3N}{2}}}{N!}\int d^{3N}x\int dk\frac{e^{2\pi ik(E-U)}}{(ik)^{\frac{3N}{2}}} \\ &= \frac{m^{\frac{3N}{2}}}{N!}\int d^{3N}x(2\pi ik(E-U))^{\frac{3N}{2}-1}\int_{-\infty}^{\infty}dk'\frac{e^{ik'}}{(ik')^{\frac{3N}{2}}} \end{aligned} \tag{2.3}$$

where $k' = 2\pi(E-U)k$. The integral in k-space can be done using the residue theorem and gives a constant. We also suppose that N is large so that $\frac{3N}{2}-1 \simeq \frac{3N}{2}$, so (2.3) becomes

$$g(E) = \frac{A}{N!}\int d^{3N}x(E-U)^{\frac{3N}{2}} \tag{2.4}$$

where all integration constants are absorbed into A. We divide the overall volume into M cells such that $M \ll N$ and suppose that each cell contains many particles. The interaction among particles in the same cell is assumed to be negligible. Therefore we can make the replacement

$$\frac{1}{N!}\int d^{3N}x \longrightarrow \frac{\delta(N-\sum_a n_a)}{n_1!n_2!\ldots n_M!}\sum_{l_1=1}^{M}\sum_{l_2=1}^{M}\cdots\sum_{l_N=1}^{M}(\frac{V}{M})^N$$

which, using Stirling's formula, (2.4) reduces to

$$g(E) = \sum_{l_1=1}^{M}\cdots\sum_{l_N=1}^{M}\delta(N-\sum_a n_a)e^{\frac{3N}{2}\ln(E-\frac{1}{2}\sum_a\sum_{b\neq a}n_aU_{ab}n_b)-\sum_a n_a\ln(\frac{Mn_a}{V})} \tag{2.5}$$

where U_{ab} is the pair potential between cells a and b. The mean-field entropy is thus

$$S(n_a) = \ln g(E) \approx \frac{3N}{2}\ln(E-\frac{1}{2}\sum_a\sum_{b\neq a}n_aU_{ab}n_b) - \sum_a n_a\ln(\frac{Mn_a}{V}). \tag{2.6}$$

Now we take the continuum limit for the density distribution, i.e. replacing $\frac{Mn_a}{V} \to \rho$ and $\sum_a \to \int d^3x$ in (2.6). This gives

$$S[\rho] \simeq \frac{3N}{2}\ln(E-\frac{1}{2}\int\rho(\vec{x})U(\vec{x},\vec{x}')\rho(\vec{x}')d^3xd^3x') - \int\rho\ln\rho d^3x. \tag{2.7}$$

We then calculate ρ that yields the maximum of S by considering the first variation with an additional Lagrange multiplier α imposing mass conservation. Then (2.7) gives

$$\delta S = \frac{-3N}{2K}\int\int \delta\rho(x)U(\vec{x},\vec{x}')\rho(x')d^3xd^3x' - \int[\delta\rho + \delta\rho\ln\rho]d^3x + \alpha\int\delta\rho d^3x = 0. \tag{2.8}$$

where $K = E - \frac{1}{2}\int\rho U\rho' d^3xd^3x'$ is the total kinetic energy. It follows that the corresponding equilibrium profile as

$$\rho(\vec{x}) \propto e^{-\beta\Phi(\vec{x})} \tag{2.9}$$

with

$$\beta = \frac{2K}{3N} \quad \text{and} \quad \Phi(\vec{x}) = \int U(\vec{x},\vec{x}')\rho(x')d^3x' \tag{2.10}$$

the inverse temperature and potential field respectively. The maximization of the entropy in the mean-field limit thus leads to a Maxwell-Boltzmann form for the density distribution, with Φ for the mean-field potential, obeying the self-consistent Poisson equation (i.e. Lane-Emden equation with polytropic index taking to infinity)

$$\nabla^2\Phi(\vec{x}) = 4\pi GAe^{-\beta\Phi(\vec{x})}$$

where A is a constant. Equivalently we can derive the equilibrium writing directly the Boltzmann entropy given by

$$S[f] = -\int f\ln f d^3xd^3v. \tag{2.11}$$

Performing the first variation subject to conservation of mass and (mean-field) energy

$$M = \int f(\vec{x},\vec{v})d^3xd^3v \quad \text{and} \quad E = \int(\frac{v^2}{2} + \int U(\vec{x},\vec{x}')f(\vec{x}',\vec{v}')d^3x'd^3v')f(\vec{x},\vec{v})d^3xd^3v, \tag{2.12}$$

we obtain

$$\delta S + \alpha\delta M + \beta\delta E = \int\big[\ln f + 1\big]\delta f d^3xd^3v + \alpha\int\delta f d^3xd^3v + \beta\int(\frac{v^2}{2} + \int Uf(\vec{x}',\vec{v}')d^3x'd^3v')\delta f d^3xd^3v = 0,$$

with α and β being the associated Lagrange multipliers, or

$$f(\vec{x},\vec{v}) = Ae^{-\beta(\frac{v^2}{2}+\Phi(\vec{x}))}. \tag{2.13}$$

For the canonical ensemble, we recall the Massieu function

$$J = -\frac{1}{T}F = S - \frac{1}{T}E \tag{2.14}$$

where F is the Helmholtz free energy. The equilibrium is determined by the first variation of J/k with the constraint of constant mass M associated to the Lagrange multiplier α

$$0 = \frac{\delta J}{k} + \alpha\delta M. \tag{2.15}$$

The solution is equivalent to (2.13) with

$$\beta = \frac{1}{kT}. \tag{2.16}$$

Inequivalence of those ensembles will be discussed briefly in section 2.1.3.

2.1.2 Isothermal sphere solution

Assuming that the enclosing box is a sphere, the mean-field equilibria are obtained by solving

$$\frac{1}{r^2}\frac{d}{dr}(r^2\frac{d\Phi}{dr}) = 4\pi G\rho_c e^{-\beta[\Phi(r)-\Phi(0)]} \tag{2.17}$$

subject to the boundary condition $\frac{d\Phi}{dr}(r=0)=0$ with ρ_c and $\Phi(0)$ for the density and potential, respectively, at $r=0$. The equation admits the solution $\rho \sim r^{-2}$ (and $\Phi \sim \ln r$) for $r \neq 0$ but this solution is not consistent with the boundary condition $\frac{d\Phi}{dr}(r=0)=0$. It is convenient to define the dimensionless variables

$$x \equiv \frac{r}{L_0} \quad , \quad n \equiv \frac{\rho}{\rho_c} \quad , \quad m \equiv \frac{M(r)}{M_0} \quad , \quad y \equiv \beta[\Phi - \Phi(0)] \tag{2.18}$$

where

$$L_0^{-1} = (4\pi G\rho_c\beta)^{1/2} \quad , \quad M_0 = 4\pi\rho_c L_0^3 \quad , \quad \Phi(0) = \beta^{-1} = \frac{GM_0}{L_0}. \tag{2.19}$$

We thus have

$$y' = \frac{m}{x^2} \quad , \quad m' = nx^2 \quad , \quad n' = -\frac{mn}{x^2} \tag{2.20}$$

where $'$ denotes the derivative with respect to x. Equation (2.17) is then

$$\frac{1}{x^2}\frac{d}{dx}(x^2\frac{dy}{dx}) = e^{-y} = n \tag{2.21}$$

with boundary conditions $y'(0) = y(0) = 0$. Note that this equation is invariant under the transformation $y \to y + a^2, x \to ax$. Let us define

$$v(x) \equiv \frac{m}{x} = xy' \quad , \quad u(x) \equiv \frac{nx^3}{m} = \frac{nx^2}{v(x)} = \frac{xn}{y'}. \tag{2.22}$$

We are therefore able to replace (2.21), of second order, by two coupled first order equations given by

$$\frac{x}{v}\frac{dv}{dx} = u - 1 \tag{2.23a}$$

$$\frac{x}{u}\frac{du}{dx} = 3 - v - u \tag{2.23b}$$

with boundary conditions $v(0) \equiv v_0 = 0$ and $u(0) \equiv u_0 = 3$ (see [120] for more detail). Dividing (2.23a) by (2.23b), we get

$$\frac{u}{v}\frac{dv}{du} = -\frac{u-1}{u+v-3}. \tag{2.24}$$

The problem hence becomes that of solving a simple first order differential equation where the solution in the (u, v) plane gives solution for $y(x)$ (and consequently $n(x)$ and $m(x)$). The differential equation (2.24) can be traced using numerical integration, but it is instructive to consider analytical approximations first. From (2.24) we deduce that the solution curve has the following characteristics:

(a) The tangent to the solution is horizontal at the intersection with the line

$$u = 1. \tag{2.25a}$$

(b) The tangent to the solution is vertical at the line

$$v + u = 3. \tag{2.25b}$$

(c) At $x \to \infty$, the asymptotic v and u (denoted v_s and u_s) are given by $v_s = 2u_s$ and $u_s = 3 - v_s$, i.e.

$$v_s = 2 \quad \text{and} \quad u_s = 1. \tag{2.25c}$$

This means that the point $(2, 1)$ is an attractor. We notice that the attractor point lies on the intersection between two loci (2.25a) and (2.25b). Note also that by sending $x \to \infty$ in $v(x)$ in equation (2.22), we recover the asymptotic solution $n \sim x^{-2}$.

(d) Consider the starting point at $(v_i, u_i) = (0, 3)$, we expand $y(x)$ near 0 in a power series of the form

$$y = ax^2 + bx^4 + cx^6 + \dots \quad .$$

Substituting this in (2.21) gives $a = \frac{1}{6}, b = -\frac{1}{120}$ and $c = \frac{1}{1890}$ which leads to

$$y' \simeq \frac{1}{3}x(1 - \frac{1}{10}x^2 + \dots) \quad , \quad n = e^{-y} \simeq 1 - \frac{1}{6}x^2 + \frac{1}{15}x^4 + \dots$$

and therefore

$$u \simeq 3(1 - \frac{1}{15}x^2 + \dots) \quad , \quad v \simeq \frac{1}{3}x^2(1 - \frac{1}{10}x^2 + \dots).$$

So the slope at (v_i, u_i) is then

$$\frac{dv}{du}\Big|_{(v_i,u_i)} = -\frac{5}{3}. \tag{2.25d}$$

The slope of isothermal curve is steeper than the locus (2.25b) and therefore the curve whirls in a counter-clockwise direction in approaching to attractor.

The numerically determined solution in the (v, u) plane is shown in Fig. 2.1, starting at $(v, u) = (0, 3)$ (corresponding to $x = 0$) and ending up at $(2, 1)$ (corresponding to $x \to \infty$). We see that outside the core the density decreases like $n \propto x^{-2}$. Taking $x \to \infty$ corresponds to an arbitrary large confining box. Given that $n \sim x^{-2}$, this violates the assumption of finite mass unless the solution is confined in a box of finite size. Let R be the radius of the box, the potential and kinetic energy is

$$U = -\int_0^R \frac{GM(r)}{r}\frac{dM}{dr}dr = -\frac{GM_0^2}{L_0}\int_0^{x_0} mnxdx \tag{2.26a}$$

$$K = \frac{3}{2}\frac{M}{\beta} = \frac{3}{2}\frac{GM_0^2}{L_0}\int_0^{x_0} nx^2 dx \tag{2.26b}$$

and the total energy is thus

$$E = K + U = \frac{GM_0^2}{2L_0}\int_0^{x_0}\frac{d}{dx}(2nx^3 - 3m)dx = \frac{GM_0^2 m_0}{L_0}(\frac{n_0 x_0^3}{m_0} - \frac{3}{2}) \tag{2.27}$$

where $x_0 \equiv \frac{R}{L_0}$ is the dimensionless cut-off radius. Let us define a dimensionless quantity

$$\lambda = \frac{RE}{GM^2}, \tag{2.28}$$

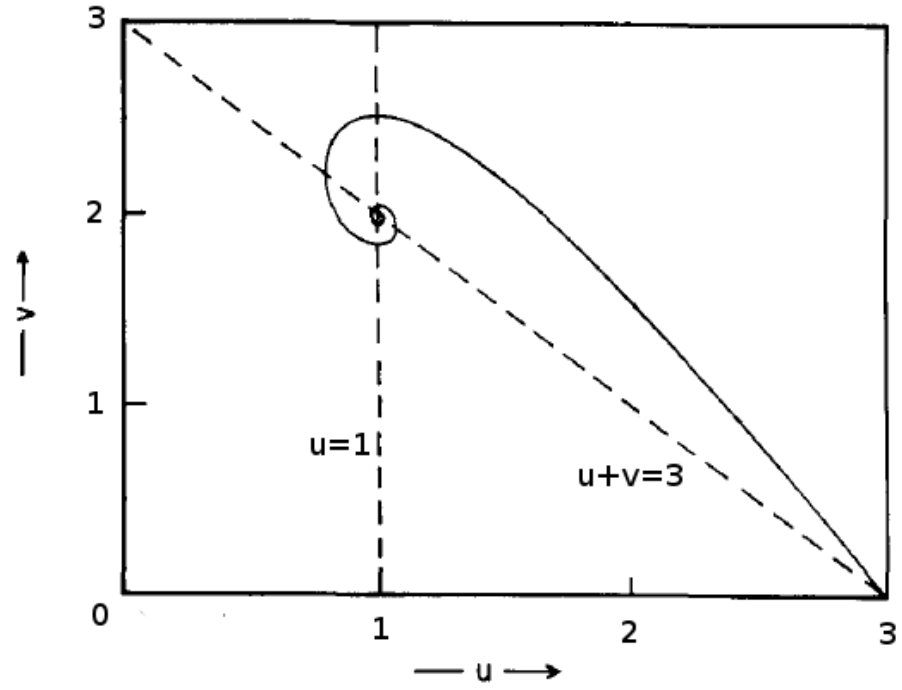

Figure 2.1: Isothermal sphere solution expressed in (u, v) plane. The solution starts from $(0, 3)$ and evolves along the solid line whirling in counter-clockwise to the attractor at $(2, 1)$ (see Padmanabhan 1990 [2] for more details).

we can write

$$\lambda = \frac{R}{GM^2}\frac{GM_0^2 m_0}{L_0}\left(\frac{n_0 x_0^3}{m_0} - \frac{3}{2}\right) = \frac{1}{v_0}(u_0 - \frac{3}{2}) \quad \text{or} \quad v_0 = \lambda^{-1}(u_0 - \frac{3}{2}). \tag{2.29}$$

The linear equation (2.29) acts as the delimitation of the isothermal profile (2.24) as the intersection between these two curves denote the cut-off radius of the isothermal sphere. We notice that if $\lambda > 0$, there is only one possible solution since the line (2.29) can cross (2.24) only once at most. For $\lambda < 0$ more than one solution can arise if the line passes through the "whirlpool". Further there exists a minimum $\lambda = \lambda_c$ below which there are no solutions. The value of λ_c is calculated to be -0.335 [2]. So the solution exists only when $E > -0.335GM^2/R$. A more schematic plot is shown in Fig. 2.2 in which the delimiting line (2.29) with different λ is plotted.

The isothermal sphere in the canonical ensemble is similar except that the delimiting line now relates to the fixed temperature of the heat bath. Taking (2.16) and (2.26b) it follows that

$$K = \frac{3}{2}MkT = \frac{3}{2}\frac{GM_0^2}{L_0}\int_0^{x_0} m' dx = \frac{3}{2}\frac{GM_0 M}{L_0}. \tag{2.30}$$

Converting (2.56) into dimensionless variables using (2.22), the canonical delimiting contour in (u, v) plane reads

$$v_0 = \eta \quad \text{with} \quad \eta = \frac{GM}{RkT}. \tag{2.31}$$

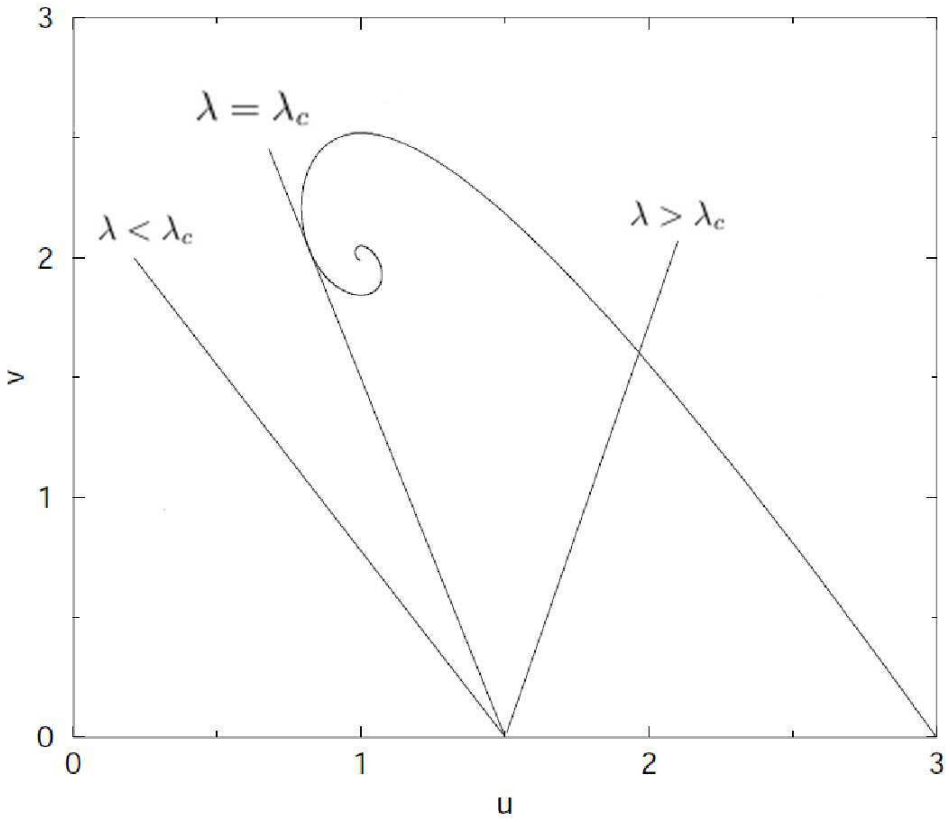

Figure 2.2: Solutions of cut-off isothermal sphere at different λ in (v, u) plane. λ_c stands for the critical solution below which there are no stable solutions. (figure from Chavanis 2002 [3])

The example of the determination of the isothermal sphere solution in the canonical ensemble subject to the normalized heat bath temperature η is shown in Fig. 2.3. The figure shows the solution to the critical (or maximum) value η_c, above which there is no solution. The calculation of [121] shows that $\eta_c = 2.52$. The generalization of the isothermal sphere to the grand-canonical ensemble and other hypothetical ensembles are given in [122] and to d dimensions in [116, 123].

2.1.3 Stability of isothermal sphere

Recall the equilibrium distribution function (2.13), which can be rearranged to

$$f(\vec{x}, \vec{v}) = \frac{1}{(2\pi T)^{3/2}} \rho(\vec{x}) e^{-\frac{v^2}{2T}}, \tag{2.32}$$

with $T = 2K/3M$, and thus we can rewrite the entropy as

$$\begin{aligned} S[\rho] &= \frac{3}{2} M \ln(2\pi T) - \int \rho \ln \rho d^3x + \frac{1}{T} \int \frac{v^2}{2} f(\vec{x}, \vec{v}) d^3x d^3v \\ &= \frac{3}{2} M \ln(2\pi T) - \int \rho \ln \rho d^3x + \frac{3}{2} M. \end{aligned} \tag{2.33}$$

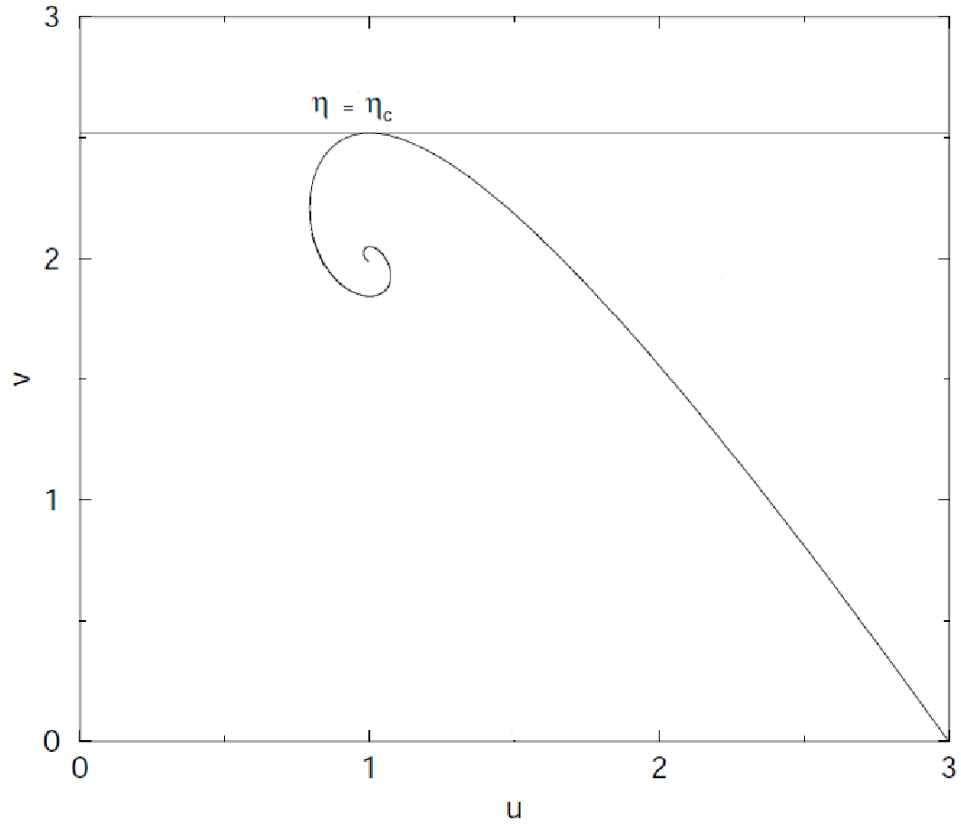

Figure 2.3: Solution of cut-off isothermal sphere at critical η (or η_c) in (v, u) plane (figure from Chavanis 2002 [3])

Consider a small perturbation on ρ, i.e. $\rho \to \rho + \delta\rho$, we suppose that the energy is unchanged, i.e.

$$\begin{aligned} \delta E &= E[\rho+\delta\rho] - E[\rho] = K[\rho+\delta\rho] - K[\rho] + \frac{1}{2}\int(\rho+\delta\rho)(\Phi+\delta\Phi)d^3x - \int\rho\Phi d^3x \\ &= \delta K + \int[\Phi\delta\rho + \frac{1}{2}\delta\rho\delta\Phi]d^3x = 0 \end{aligned} \tag{2.34}$$

in which the expression (2.34) is obtained using

$$\delta\Phi(\vec{x}) = \int U(\vec{x},\vec{x}')\delta\rho(\vec{x}')d^3x'. \tag{2.35}$$

The conservation of mass evidently yields

$$\delta M = \int \delta\rho d^3x = 0. \tag{2.36}$$

From $T = 2K/3M$, we thus obtain

$$\delta T = -\frac{2}{3M}\int(\Phi\delta\rho + \frac{1}{2}\delta\rho\delta\Phi)d^3x. \tag{2.37}$$

Consider the approximation of variation of entropy

$$S[\rho+\delta\rho]-S[\rho]=\frac{\delta S}{\delta\rho}\delta\rho+\frac{1}{2}\frac{\delta^2 S}{\delta\rho^2}(\delta\rho)^2+\ldots, \tag{2.38}$$

we then have, using (2.33) and keeping the first and second orders,

$$S[\rho+\delta\rho]-S[\rho]=-\int\delta\rho(1+\ln\rho+\frac{\Phi}{T})d^3x-\int\Big[\frac{\delta\rho\delta\Phi}{2T}+\frac{(\delta\rho)^2}{2\rho}\Big]d^3x-\frac{1}{3MT^2}\Big[\int\Phi\delta\rho d^3x\Big]^2 \tag{2.39}$$

from which we get

$$\delta^2 S=-\int\Big[\frac{\delta\rho\delta\Phi}{2T}+\frac{(\delta\rho)^2}{2\rho}\Big]d^3x-\frac{1}{3MT^2}\Big[\int\Phi\delta\rho d^3x\Big]^2. \tag{2.40}$$

Supposing spherical symmetry and defining

$$\delta\rho(r)=\frac{1}{4\pi r^2}\frac{dq}{dr} \tag{2.41}$$

with $q(r)$ being the "mass perturbation", equation (2.40) reads

$$\begin{aligned}\delta^2 S &= -\frac{1}{3MT^2}\bigg(\int_0^R\Phi\frac{dq}{dr}dr\bigg)^2-\int_0^R\bigg[\frac{1}{8\pi\rho r^2}(\frac{dq}{dr})^2+\frac{\delta\Phi}{2T}\frac{dq}{dr}\bigg]dr\\ &= -\frac{1}{3MT^2}\bigg(\int_0^R q\frac{d\Phi}{dr}dr\bigg)^2+\int_0^R q\frac{d}{dr}(\frac{1}{8\pi\rho r^2}\frac{dq}{dr})dr+\frac{1}{2T}\int_0^R\frac{d(\delta\Phi)}{dr}qdr.\end{aligned} \tag{2.42}$$

The derivative of $\delta\Phi$ is simply the fluctuation of gravitational field at r which can be written, using Gauss' law, as

$$\frac{d(\delta\Phi)}{dr}=\frac{G}{r^2}\int_0^r\delta\rho(r')4\pi r'^2dr'=\frac{Gq}{r^2}. \tag{2.43}$$

We thus rewrite (2.42) into

$$\begin{aligned}\delta^2 S &= -\int_0^R dr_1\int_0^R dr_2 q(r_2)\bigg\{-\frac{\Phi'(r_1)\Phi'(r_2)}{3MT^2}+\frac{1}{2}\delta(r_1-r_2)\Big[\frac{G}{Tr_1^2}+\frac{d}{dr_1}(\frac{1}{4\pi\rho r_1^2}\frac{d}{dr_1})\Big]\bigg\}q(r_1)\\ &= -\int_0^R dr_1\int_0^R dr_2 q(r_1)K(r_1,r_2)q(r_2)\end{aligned} \tag{2.44}$$

where

$$K(r_1,r_2)=-\frac{\Phi'(r_1)\Phi'(r_2)}{3MT^2}+\frac{1}{2}\delta(r_1-r_2)\big[\frac{G}{Tr_1^2}+\frac{d}{dr_1}(\frac{1}{4\pi\rho r_1^2}\cdot\frac{d}{dr_1})\big] \tag{2.45}$$

Consider the eigenvalue equation

$$\int_0^R dr_1 K(r,r_1)F_\xi(r_1)=\xi F_\xi(r), \tag{2.46}$$

the condition $\delta^2 S<0$ can be thus stated as the condition that the eigenvalues in the equation (2.46) are all negative. Let us first make the supposition that the isothermal sphere at small radius is stable since in this limit the kinetic energy overwhelms the binding potential and the particles behave like an ideal gas in thermal equilibrium. Therefore at small R we have $\xi>0$.

Then when the sphere grows larger, there exists a critical radius, r_c, when the sphere becomes unstable, implying that the eigenvalue vanishes at r_c. So the equation (2.46) reads

$$\frac{2\Phi'(r)}{3MT^2}V = \left[\frac{G}{Tr^2} + \frac{d}{dr}(\frac{1}{4\pi\rho r^2}\frac{d}{dr})\right]F(r) \tag{2.47}$$

where

$$V = \int_0^R dr_1 \Phi'(r_1)F(r_1) \tag{2.48}$$

being a constant depending on R. Rescaling the parameters using (2.18), we obtain

$$\left[\frac{1}{x^2} + \frac{d}{dx}(\frac{1}{nx^2}\frac{d}{dx})\right]f(x) = -\Lambda\frac{m}{x^2} \tag{2.49}$$

where

$$f = \frac{F}{M_0} \quad \text{and} \quad \Lambda = -\frac{2VL_0}{3GM_0^2 m(x_0)}. \tag{2.50}$$

Notice that

$$(\frac{d}{dx}(\frac{1}{nx^2}\frac{d}{dx}))nx^3 = \frac{m}{x^2} \qquad \text{and} \qquad (\frac{d}{dx}(\frac{1}{nx^2}\frac{d}{dx}))m = \frac{m}{x^2}$$

so we suppose that the eigenfunction f takes the form

$$f(x) = c_1(nx^3 - m) - \Lambda m. \tag{2.51}$$

To determine c_1 we consider the boundary condition $f(x_c) = 0$, therefore

$$c_1 = \frac{m(x_c)\Lambda}{nx_c^3 - m(x_c)} = \frac{\Lambda}{u_0 - 1}. \tag{2.52}$$

We substitute $f(x)$ in (2.48) and obtain

$$\begin{aligned}\frac{VL_0}{GM_0^2} &= c_1\int_0^{x_c} nxm dx - (\Lambda + c_1)\int_0^{x_c}\frac{m^2}{x^3}dx \\ &= \frac{\Lambda m_0}{u_0 - 1}(2u_0^2 + u_0v_0 - 7u_0 + 3).\end{aligned} \tag{2.53}$$

Then by substituting Λ from (2.50), we obtain

$$0 = \frac{4u_0^2 + 2u_0v_0 - 7u_0 + 3}{u_0 - 1} \tag{2.54}$$

which characterizes the critical radius of isothermal sphere. Consider the slope λ of the delimitation line (2.29), we calculate the extrema point as a function of x by

$$\frac{d\lambda}{dx} = \frac{d}{dx}\left[\frac{1}{v}(u - \frac{3}{2})\right] = -\frac{1}{2vx}(4u^2 + 2uv - 11u + 3) = 0 \tag{2.55}$$

which is identical to equation (2.54). It follows that that the critical radius corresponds to the first minimum of $\lambda(x)$, which is the first turning point in the (v, u) plane at λ_c. The corresponding numerical value of x_c is 34.2, or equivalently the density contrast $n^{-1}(x_c) = \frac{\rho_c}{\rho(R)} = 709$ [118]. We therefore conclude that

a) If $RE/GM^2 < -0.335$ there is no corresponding isothermal sphere solution (since the entropy has no extremum).

b) If $RE/GM^2 > -0.335$ and $\rho_c/\rho(R) > 709$ there is an isothermal sphere but it is only a metastable (and not an equilibrium) state since it corresponds to a local minimum.

c) If $RE/GM^2 > -0.335$ and $\rho_c/\rho(R) < 709$ there is an isothermal sphere equilibrium, corresponding to a local maximum of entropy.

Consider now the canonical ensemble, the Massieu function (2.14) can be expressed in terms of ρ and T as

$$J[\rho] = \frac{3M}{2}\ln(2\pi kT) - \int \rho \ln \rho d^3x + \frac{1}{2T}\int \rho\Phi d^3x. \tag{2.56}$$

Performing the same calculations as (2.39) for $J[\rho]$, we have

$$J[\rho+\delta\rho] - J[\rho] = -\int \big[\ln\rho + 1 + \frac{\Phi}{T}\big]\delta\rho d^3x + \int \big[\frac{(\delta\rho)^2}{2\rho} + \frac{\delta\rho\delta\Phi}{2T}\big]d^3x \tag{2.57}$$

where we omit the variations in higher orders. It thus follows that

$$\delta^2 J = \int \big[\frac{(\delta\rho)^2}{2\rho} + \frac{\delta\rho\delta\Phi}{2T}\big]d^3x. \tag{2.58}$$

Supposing the spherical symmetry and using the definitions (2.41) and (2.43), we rewrite (2.58) as

$$\begin{aligned}\delta^2 J &= \int_0^R dr_1 q(r_1)\frac{1}{2}\left[\frac{G}{Tr_1^2} + \frac{d}{dr_1}\left(\frac{1}{4\pi\rho r_1^2}\frac{d}{dr_1}\right)\right]q(r_1) \\ &= \int_0^R dr_1 q(r_1) L(r_1) q(r_1)\end{aligned} \tag{2.59}$$

where

$$L(r_1) = \frac{1}{2}\left[\frac{G}{Tr_1^2} + \frac{d}{dr_1}\left(\frac{1}{4\pi\rho r_1^2}\frac{d}{dr_1}\right)\right]. \tag{2.60}$$

This is equivalent to the analysis in the micro-canonical equilibrium for $V = 0$. According to [3] the turning point of the stability is at $\eta = \eta_c$, i.e. at the highest point of the whirlpool. It implies an inequivalence between the micro-canonical and canonical ensembles.

2.1.4 Negative specific heat and gravothermal catastrophe

Because the system considered must be enclosed in a box, the virial theorem in the form discussed in chapter 1 is modified by a surface term involving the pressure

$$2K + U = 3pV = 4\pi R^3 p(R) \tag{2.61}$$

with $U \to 0$ this is just the ideal gas law. Defining the kinetic temperature T as

$$K = \frac{3}{2}k_B T. \tag{2.62}$$

we have then

$$E = 4\pi R^3 p(R) - K = \frac{4\pi R^3 \rho(R)}{m}T - \frac{3Mk_bT}{2m} \tag{2.63}$$

where $p(R)$ is related to $\rho(R)$ and T by ideal gas law. One can plot the caloric curve, i.e. E as a function of T, and the result is that for

$$32.1 < \frac{\rho_c}{\rho(R)} < 709$$

the specific heat $C = \frac{dE}{dT}$ is negative. As the specific heat is positive, by definition, in the canonical ensemble, this implies non-equivalence of these ensembles. Indeed, more physically, a system with $C < 0$ placed in contact with a heat bath at this temperature would be unstable, as the heat transfer (either from or to the bath) is an unstable "run-away" process.

Lynden-Bell and Wood (1968) [121] emphasized also the dramatic consequence of the finding that no mean-field equilibria exist for $E < -0.335GM^2/R$. They carried out a thought experiment in which a self-gravitating system (in a box of non-conducting wall of size R) is initially in an thermal equilibrium with $E > -0.335GM^2/R$; as the size of the box increases the system crosses $E < -0.335GM^2/R$ and eventually undergoes a "catastrophic" evolution. It is separated into a core with negative specific heat and a halo with positive specific heat, both heating up indefinitely in a "run-away" process. This is the so-called "gravothermal catastrophe". It is perhaps the fundamental result for equilibrium statistical mechanics applied to self-gravitating systems: they are predicted — on sufficiently long time scales — to have a pathological behavior of this kind. The time scale of gravothermal catastrophe depends on the process of energy transfer. In stellar system it is related to the two-body collisionality (see section 2.1.5), which is confirmed by numerical simulation of stellar dynamics [124].

2.1.5 Two-body relaxation

Let us now consider (following again the classical treatment of this problem — see e.g. [17]) the time scale on which a 3D self-gravitating system might be expected to reach thermal equilibrium. To do so "collisional" physics is required (just as for short-range interacting systems) as the collisionless Vlasov dynamics has an infinite number of stationary solutions, and indeed has much more conserved quantities (as we will discuss in the next chapter) apart from the total energy of the system. We consider two-body collisions and estimate the rate at which the particle velocity are modified by the close encounter, cf. Fig. 2.4 which shows the relevant parameters.

We consider a "field star" which passes by a "subject star", and suppose that the former does not move during the encounter. The force perpendicular to the velocity of the subject star is thus

$$F_\perp = \frac{Gm^2}{b^2+x^2}\cos\theta = \frac{Gm^2 b}{(b^2+x^2)^{3/2}}.$$

We suppose weak deviation so that the trajectory may be approximated as rectilinear. Therefore

$$F_\perp = \frac{Gm^2}{b^2}\left[1+(\frac{vt}{b})^2\right]^{-\frac{3}{2}}. \tag{2.64}$$

This assumption breaks down when the deflection angle is not small. From Newton's law we can thus estimate the change of velocity as

$$\delta v = \frac{1}{m}\int_{-\infty}^{\infty} dt F_\perp = \frac{2Gm}{bv}. \tag{2.65}$$

Note that δv can be considered as the velocity change subject to an acceleration $\frac{Gm}{b^2}$ for a duration $\frac{2b}{v}$. Next suppose that the subject star crosses the self-gravitating system (galaxy or

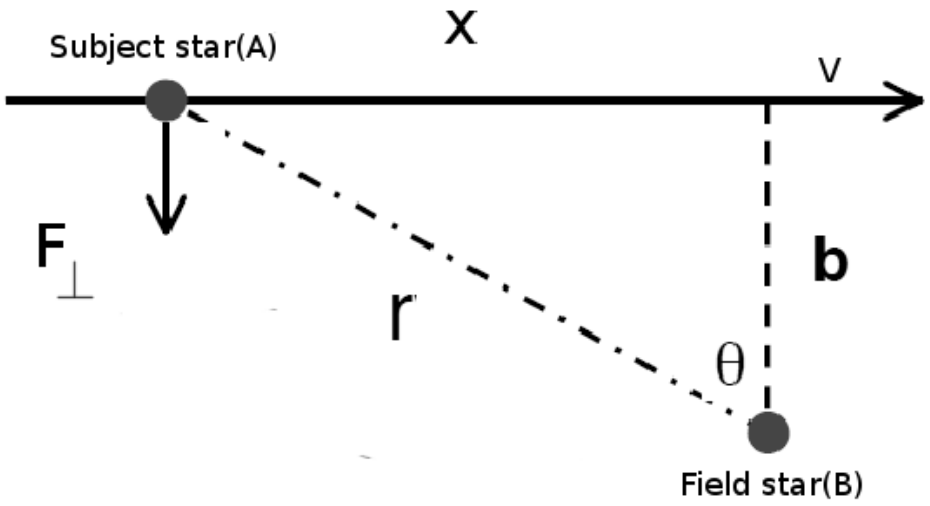

Figure 2.4: Close encounter (or collision) between "subject star" (A) and "field star" (B) with initial speed v and impact parameter b.

globular cluster for example) taken to be homogeneous and isotropic with radius R. As the surface density is $N/\pi R^2$, the number of field stars that the subject star passes at impact factor distance b is

$$\delta n = \frac{N}{\pi R^2} 2\pi b db = \frac{2N}{R^2} b db. \tag{2.66}$$

The quantity of interest to us is the total fluctuation of kinetic energy of the subject star, $(\delta v)^2$, which can be estimated as

$$\sum (\delta v)^2 \simeq (\delta v)^2 \delta n = (\frac{2Gm}{bv})^2 \frac{2N}{R^2} b db \tag{2.67}$$

and the total square velocity fluctuation is

$$\Delta v^2 = \int_{b_{min}}^{b_{max}} \sum (\delta v)^2 \simeq 8N (\frac{Gm}{Rv})^2 \ln \Lambda \tag{2.68}$$

where $\ln \Lambda = \ln(b_{max}/b_{min})$ is the "Coulomb logarithm", equal to the logarithm of the ratio between maximum and minimum impact factors. In general $b_{max} \gg b_{min}$. The order of magnitude of square velocity of star in a system composed of N particles is typically

$$v^2 \approx \frac{GNm}{R} \tag{2.69}$$

so the relative square velocity change per crossing is then

$$\frac{\Delta v^2}{v^2} \approx \frac{8 \ln \Lambda}{N}. \tag{2.70}$$

This implies that to obtain the total square velocity change of order of the average square velocity, i.e. $\Delta v^2 \simeq v^2$, the number of crossings required is

$$n_{relax} \simeq \frac{N}{8 \ln \Lambda}. \tag{2.71}$$

So the relaxation time is

$$t_{relax} = n_{relax} t_{cross} \tag{2.72}$$

where t_{cross} is the crossing time, i.e. the time in which a particle crosses the system once, which is approximately R/v. Taking b_{max} to be the size of system R and b_{min} to be the impact parameter at which the deflection angle is 90°, equal to $2Gm/v^2$, we obtain

$$\Lambda \approx \frac{Rv^2}{Gm} \approx N \tag{2.73}$$

from which we finally obtain the relaxation time

$$t_{relax} \simeq \frac{N}{8 \ln N} t_{cross} \tag{2.74}$$

originally proposed by Chandrasekhar [9].

2.1.6 Collisional relaxation in Fokker-Planck description

Soft collisions between particles can be considered alternatively as a diffusive process in momentum space described by a diffusion current $\vec{J}(\vec{p})$. Therefore we can model the effect of collisions by adding such a term to the Vlasov equation:

$$\frac{\partial f}{\partial t} + \vec{v} \cdot \frac{\partial f}{\partial \vec{x}} - \overrightarrow{\nabla} \Phi \cdot \frac{\partial f}{\partial \vec{v}} = -\overrightarrow{\nabla}_p \cdot \vec{J}(\vec{p}). \tag{2.75}$$

where the subscript p means the gradient is in p-space. We derive first $\vec{J}$ with simple arguments and show that it is equivalent to the Fokker-Planck diffusion equation [125]. We suppose that the momentum exchange between a pair of particles with momenta before collision $(\vec{p}, \vec{p}')$ to $(\vec{p} + \frac{\vec{q}}{2}, \vec{p}' - \frac{\vec{q}}{2})$ after collision, with $\vec{q}$ the momentum transfer. We define the transition rate $W(\vec{p} + \frac{\vec{q}}{2}, \vec{p}' - \frac{\vec{q}}{2}, \vec{q})$ by which

$$W(\vec{p} + \frac{\vec{q}}{2}, \vec{p}' - \frac{\vec{q}}{2}, \vec{q}) f(\vec{p}) f(\vec{p}') d\vec{p}' d\vec{q}$$

denotes the number of collisions per unit time for particles with momentum between $(\vec{p}, \vec{p} + d\vec{p})$ with particles having momentum between $(\vec{p}', \vec{p}' + d\vec{p}')$ such that the momentum change is in the range $(\vec{q}, \vec{q} + d\vec{q})$. Supposing the symmetry in $\vec{q}$, we have

$$W(\vec{p} + \frac{\vec{q}}{2}, \vec{p}' - \frac{\vec{q}}{2}, \vec{q}) = W(\vec{p} - \frac{\vec{q}}{2}, \vec{p}' + \frac{\vec{q}}{2}, -\vec{q}). \tag{2.76}$$

Consider a surface perpendicular to the p_x direction and located at $\vec{p}$, the flux of particles passing through this surface from left to right (i.e. particles which are accelerated) is

$$I_L = \int\limits_{q_x > 0} d^3q \int\limits_{p_x}^{p_x + q_x} dp_x \int d^3p' W(\vec{p} + \frac{1}{2}\vec{q}, \vec{p}' - \frac{1}{2}\vec{q}, \vec{q}) f(\vec{p}') f(\vec{p}) \tag{2.77}$$

and from right to left, i.e. particles which are decelerated,

$$I_R = \int\limits_{q_x > 0} d^3q \int\limits_{p_x}^{p_x - q_x} dp_x \int d^3p' W(\vec{p} - \frac{1}{2}\vec{q}, \vec{p}' + \frac{1}{2}\vec{q}, -\vec{q}) f(\vec{p}') f(\vec{p}). \tag{2.78}$$

Changing the integral limits from $\vec{p} \to \vec{p}+\vec{q}$ and $\vec{p}' \to \vec{p}'-\vec{q}$, the net flux can be obtained by merging (2.77) with (2.78) as

$$\begin{aligned} J_x &= I_L - I_R \\ &= \int d^3p' \int\limits_{q_x>0} d^3q \int\limits_{p_x}^{p_x+q_x} dp_x W(\vec{p}+\frac{1}{2}\vec{q},\vec{p}'-\frac{1}{2}\vec{q},\vec{q})[f(\vec{p})f(\vec{p}')-f(\vec{p}+\vec{q})f(\vec{p}'-\vec{q})] \end{aligned} \tag{2.79}$$

For soft collision criteria, we suppose that $|\vec{q}| \ll |\vec{p}|$ and thus $W(\vec{p}+\frac{1}{2}\vec{q},\vec{p}'-\frac{1}{2}\vec{q},\vec{q}) \simeq W(\vec{p},\vec{p}',\vec{q})$. Expanding $f(\vec{p}+\vec{q})$ and $f(\vec{p}'-\vec{q})$ using Taylor's expansion

$$f(\vec{p}+\vec{q}) \simeq f(\vec{p}) + \frac{\partial f}{\partial \vec{p}} \cdot \vec{q} \ , \quad f(\vec{p}'-\vec{q}) \simeq f(\vec{p}') - \frac{\partial f}{\partial \vec{p}'} \cdot \vec{q}$$

and substituting it into (2.79) by keeping only the linear term in $\vec{q}$, we obtain

$$J_x = \int d^3p' \int\limits_{q_x>0} d^3q \int\limits_{p_x}^{p_x+q_x} dp_x W(\vec{p},\vec{p}',\vec{q})\vec{q}\cdot[f(\vec{p})\frac{\partial f}{\partial \vec{p}'} - f(\vec{p}')\frac{\partial f}{\partial \vec{p}}]. \tag{2.80}$$

With infinitesimal $\vec{q}$ we assume that the integral over $\vec{p}$ is constant over the range of integration. Therefore the current vector is given by

$$\vec{J} = \frac{1}{2}\int d^3p' \int d^3q W(\vec{p},\vec{p}',\vec{q})\vec{q}\cdot[f(\vec{p})\frac{\partial f}{\partial \vec{p}'} - f(\vec{p}')\frac{\partial f}{\partial \vec{p}}]\vec{q} \tag{2.81}$$

where $1/2$ arises from the symmetry of $\vec{q}$. Thus (2.81) gives

$$\begin{aligned} J_i &= \frac{1}{2}\int d^3p' \int d^3q \ W(\vec{p},\vec{p}',\vec{q})q_i q_j \big[f(\vec{p})\frac{\partial f}{\partial p_j'} - f(\vec{p}')\frac{\partial f}{\partial p_j}\big] \\ &= \int d^3p' B_{ij}(\vec{p},\vec{p}')\big[f(\vec{p})\frac{\partial f}{\partial p_j'} - f(\vec{p}')\frac{\partial f}{\partial p_j}\big] \end{aligned} \tag{2.82}$$

where

$$B_{ij}(\vec{p},\vec{p}') = \frac{1}{2}\int q_i q_j W(\vec{p},\vec{p}',\vec{q})d^3q. \tag{2.83}$$

We change the coordinate from $\vec{p}$ to $\vec{k} = \vec{p}-\vec{p}'$ and suppose that in soft collisions the diffusion is transverse to $\vec{k}$, so $J_i k^i = 0$ (or equally $B_{ij}k^i = 0$). We can then construct B_{ij} as

$$B_{ij} = \frac{1}{2}B(\delta_{ij} - \frac{k_i k_j}{k^2}) \tag{2.84}$$

where $k = |\vec{k}|$ and

$$B = \frac{1}{2}\int q^2 W(\vec{p},\vec{p}',\vec{q})d^3q. \tag{2.85}$$

Recalling the number of collisions per passage as function of impact factor from (2.66) and dividing by time interval Δt, W is thus approximated as

$$W(\vec{p},\vec{p}',\vec{q}) \simeq \frac{\delta n}{\Delta t} \sim kbdb. \tag{2.86}$$

Using (2.65) for q, we obtain

$$q^2 \simeq (\frac{2Gm}{bk})^2. \tag{2.87}$$

We calculate B using (2.86) and (2.87) by

$$B \simeq \int (\frac{2Gm}{bk})^2 kbdb = \frac{B_0}{k} \tag{2.88}$$

where $B_0 = 4G^2m^2L$ and $L = \ln(b_{max}/b_{min})$ which is $\simeq N$. Therefore (2.82) can be rewritten as

$$J_i = \frac{1}{2}B_0 \int d^3p'(f(\vec{p})\frac{\partial f}{\partial p'_j} - f(\vec{p}')\frac{\partial f}{\partial p_j})(\frac{\delta_{ij}}{k} - \frac{k_i k_j}{k^3}). \tag{2.89}$$

Suppose that the velocity distribution takes the Maxwellian form, i.e. $f \propto e^{(-\sigma p^2)}$, the current becomes

$$J_i = \int d^3p' 2\sigma k f(\vec{p}) f(\vec{p}') k^j B_{ij} = 0 \tag{2.90}$$

which implies that the current $\vec{J}$ vanishes when the velocity distribution is Maxwellian. Thus (as required) the collisional relaxation ends once we are in thermal equilibrium. Notice that

$$\frac{\delta_{ij}}{k} - \frac{k_i k_j}{k^3} = \frac{\partial^2 k}{\partial k_i \partial k_j}, \tag{2.91}$$

we can rewrite (2.89) as

$$J_i = \frac{1}{2}B_0 f(\vec{p}) \int d^3p' \frac{\partial f}{\partial p'_j}\frac{\partial^2 k}{\partial k_i \partial k_j} - \frac{1}{2}B_0 \frac{\partial f}{\partial k_j}\int d^3p' f(\vec{p}')\frac{\partial^2 k}{\partial k_i \partial k_j}. \tag{2.92}$$

Changing $\vec{k}$ back to $(\vec{p} - \vec{p}')$, it follows that

$$\frac{\partial}{\partial k_i} = \frac{\partial}{\partial p_i} = -\frac{\partial}{\partial p'_i} \tag{2.93}$$

from which the second term of (2.92) can be rearranged as

$$\frac{1}{2}B_0 \frac{\partial f}{\partial k_j}\int d^3p' f(\vec{p}')\frac{\partial^2 k}{\partial k_i \partial k_j} = \frac{1}{2}B_0 \frac{\partial f}{\partial p_j}\frac{\partial^2 \psi}{\partial p_i \partial p_j} \tag{2.94}$$

where

$$\psi(\vec{p}) = \int d^3p' f(\vec{p}')|\vec{p} - \vec{p}'|. \tag{2.95}$$

With integration by parts, (2.94) reads

$$\begin{aligned} \frac{1}{2}B_0 \frac{\partial f}{\partial p_j}\frac{\partial^2 \psi}{\partial p_i \partial p_j} &= \frac{1}{2}B_0 \frac{\partial}{\partial p_j}\Big(f(\vec{p})\frac{\partial^2 \psi}{\partial p_i \partial p_j}\Big) - \frac{1}{2}B_0 f \frac{\partial}{\partial p_j}\frac{\partial^2 \psi}{\partial p_i \partial p_j} \\ &= \frac{1}{2}B_0 \frac{\partial}{\partial p_j}\Big(f(\vec{p})\frac{\partial^2 \psi}{\partial p_i \partial p_j}\Big) - \frac{1}{2}B_0 f(\vec{p})\frac{\partial \eta(\vec{p})}{\partial p_i} \end{aligned} \tag{2.96}$$

where

$$\eta(\vec{p}) = \nabla_p^2 \psi(\vec{p}) = \frac{\partial^2}{\partial p^i \partial p_i}\int d^3p' f(\vec{p}')|\vec{p} - \vec{p}'| = 2\int d^3p' \frac{f(\vec{p}')}{|\vec{p} - \vec{p}'|}. \tag{2.97}$$

Using the integration by parts, the first term of (2.92) becomes

$$\frac{1}{2}B_0 f(\vec{p})\int d^3p' \frac{\partial f}{\partial p'_j}\frac{\partial^2 k}{\partial k_i \partial k_j} = \frac{1}{2}B_0 f(\vec{p})\frac{\partial}{\partial p_i}\frac{\partial^2}{\partial p^j \partial p_j}\int d^3p' f(\vec{p}')|\vec{p}-\vec{p}'| = \frac{1}{2}B_0 f(\vec{p})\frac{\partial \eta(\vec{p})}{\partial p_i}. \quad (2.98)$$

Combining (2.96) and (2.98), we rewrite the diffusive current (2.92) as

$$J_i(\vec{p}) = B_0 f(\vec{p})\frac{\partial \eta(\vec{p})}{\partial p_i} - \frac{1}{2}B_0\frac{\partial}{\partial p_j}\Big(f(\vec{p})\frac{\partial^2 \psi}{\partial p_i \partial p_j}\Big) \equiv a_i(\vec{p})f(\vec{p}) - \frac{1}{2}\frac{\partial}{\partial p_j}(\sigma^2_{ij}(\vec{p})f(\vec{p})). \quad (2.99)$$

We notice that the form (2.99) is equivalent to the Fokker-Planck equation with $a_i(\vec{p})$ being the drift coefficient and σ^2_{ij} begin diffusion coefficient [2, 125]. We thus rewrite the diffusion equation (2.75)

$$\frac{\partial f}{\partial t} + \vec{v}\cdot\frac{\partial f}{\partial \vec{x}} - \overrightarrow{\nabla}\Phi\cdot\frac{\partial f}{\partial \vec{v}} == -\frac{\partial}{\partial p_i}\left[a_i(\vec{p})f(\vec{p}) - \frac{\partial}{\partial p_j}(\sigma^2_{ij}(\vec{p})f(\vec{p}))\right] \quad (2.100)$$

for the "collisional" Vlasov equation.

Note that the collision term conserves mass and energy. Integrating it in p-space, we have

$$-\int(\vec{\nabla}_p\cdot\vec{J})d^3p = -\oint \vec{J}\cdot d\vec{S}_p = 0 \quad (2.101)$$

assuming that the diffusion current vanishes at asymptotically large $\vec{p}$. The argument above implies the conservation of mass. Considering now the integration of second moment of momentum, we have

$$-\int p^2\vec{\nabla}_p\cdot\vec{J}d^3p = 2\int \vec{J}\cdot\vec{p}d^3p \quad (2.102)$$

plus a term involving the surface integral of $\vec{J}$ which again vanishes. As we have assumed the transverse weak collisions, equation (2.102) is always 0. For potential energy we consider

$$-\int \Phi(x)\vec{\nabla}_p\cdot\vec{J}d^3p \quad (2.103)$$

which vanishes as it is simply proportional to (2.101). Thus the collision term does not lead to the exchange between potential and kinetic energy and the fluctuation of potential and kinetic energy occurs only due to the mean-field. It also follows that the Boltzmann entropy is non-decreasing when the collision term is taken into account, and is constant when the system reaches the thermal equilibrium [2]. The more general kinetic equations taking into account the effect of spatial inhomogeneity is given in [102].

2.2 Thermal equilibrium in 1D self-gravitating model

We now turn to 1D gravity, i.e. the sheet model described in chapter 1. The equilibrium thermodynamics of this system was completely solved by Rybicki in 1971 [92]. In this section we reproduce these results, giving some additional detail in some parts. In contrast to the 3D calculation outlined above, the 1D model presents considerable simplification. Specifically:

- the fact that the potential is vanishing at small separation means that the micro-canonical entropy does not show the divergences which appears in three dimensions and which require a regularization of the gravitational potential.

- the fact that the potential diverges at large separation means that the entropy remains finite even in absence of a confining box.

Thus, in one dimension, the equilibrium thermodynamics of an open self-gravitating system is well defined. Further, as shown by Rybicki, the equilibrium thermodynamics, in both the micro-canonical and canonical ensemble, may be solved analytically for any N. The mean-field thermodynamics may then be used to obtain the corresponding results in this limit.

We first present the calculation of Rybicki in the canonical ensemble and then in the micro-canonical ensemble. In this model, both ensembles are equivalent — and indeed there is no region of negative specific heat. This is in line with what one would obtain from a simple analysis of the virial relation in one dimension, as shown in chapter 1, that the energy of system $E = 3K$ and therefore $C = \frac{\partial E}{\partial T} > 0$.

2.2.1 Definition

Let us consider a 1D system with N identical particles with individual mass m with Hamiltonian

$$H(\vec{p},\vec{x}) = K(\vec{p}) + U(\vec{x}) = \sum_{j=1}^{N} \frac{p_j^2}{2m} + \frac{gm^2}{2} \sum_{j=1}^{N} \sum_{k\neq j}^{N} |x_j - x_k| \tag{2.104}$$

with $\vec{p} \equiv \{p_1, p_2, \ldots, p_N\}$ and $\vec{x} \equiv \{x_1, x_2, \ldots, x_N\}$ denoting N dimensional vectors. It is more convenient to write the potential energy as sum of pair potential of all neighboring pairs, i.e.

$$U(\vec{x}) = \lambda \sum_{l=1}^{N-1} C_l (x_{l+1} - x_l) \tag{2.105}$$

where

$$C_l = l(N-l) \quad \text{and} \quad \lambda = gm^2 \tag{2.106}$$

and the particle's label is assigned such that

$$x_1 \leq x_2 \leq \ldots \leq x_N.$$

For simplicity we suppose that the center of mass of the system is stationary at the origin, i.e.

$$\bar{x}(\vec{x}) = \frac{1}{N} \sum_{j=1}^{N} x_j = 0 \tag{2.107}$$

$$\bar{p}(\vec{p}) = \sum_{j=1}^{N} p_j = 0. \tag{2.108}$$

The phase space distribution of N particle can be written as the exact (or Klimontovich) distribution function

$$\hat{f} = \frac{1}{N} \sum_{j=1}^{N} \delta(p - p_j)\delta(x - x_j). \tag{2.109}$$

2.2.2 Canonical ensemble equilibrium

Consider this system of N identical particles in contact with a heat reservoir with inverse temperature β. The canonical equilibrium distribution function is given by

$$f_c(p,x) = (zN!)^{-1} \int\int_r d\vec{p}d\vec{x}\delta(\bar{x})\delta(\bar{p})e^{-\beta H(\vec{p},\vec{x})} \cdot \frac{1}{N}\sum_{j=1}^{N}\delta(p-p_j)\delta(x-x_j). \tag{2.110}$$

The terms $\delta(\bar{x})$ and $\delta(\bar{p})$ are employed to constrain the center of mass to lie at the origin and z is the partition function, i.e.

$$z = (N!)^{-1} \int\int d\vec{p}d\vec{x}\delta(\bar{x})\delta(\bar{p})e^{-\beta H}. \tag{2.111}$$

where the factor $N!$ arises because the particles are assumed to be identical. From that assumption, the distribution function $(N)^{-1}\sum_{j=1}^{N}\delta(p-p_j)\delta(x-x_j)$ may be replaced by $\delta(p-p_N)\delta(x-x_N)$ and thus the equilibrium solution can be written as

$$f_c(p,x) = \rho_c(x)\theta_c(p)$$

which is separable. It thus follows that

$$\rho_c(x) = (QN!)^{-1} \int d\vec{x}\delta(\bar{x})e^{-\beta U(\vec{x})}\delta(x-x_N) \tag{2.112a}$$

$$\theta_c(p) = (R)^{-1} \int d\vec{p}\delta(\bar{p})e^{-\beta K(\vec{p})}\delta(p-p_N) \tag{2.112b}$$

where Q and R are partition functions:

$$Q = (N!)^{-1} \int d\vec{x}\delta(\bar{x})e^{-\beta U(\vec{x})} \tag{2.113a}$$

$$R = \int d\vec{p}\delta(\bar{p})e^{-\beta K(\vec{p})}. \tag{2.113b}$$

With the momentum distribution, we express $\delta(\bar{p})$ in Fourier space

$$\delta(\bar{p}) = (2\pi)^{-1} \int dk e^{ik\sum_j p_j} \tag{2.114}$$

and substitute in (2.112b) to obtain

$$\theta_c(p) = (2\pi R)^{-1} \int\int dk d\vec{p} e^{[ik\sum_j p_j - \beta\sum_j \frac{p_j^2}{2m}]}\delta(p-p_N).$$

p_N may be eliminated, giving

$$\begin{aligned}
\theta_c(p) &= (2\pi R)^{-1} e^{-\frac{\beta p^2}{2m}} \int dk e^{-\frac{m(N-1)}{2\beta}[k^2 - \frac{2i\beta kp}{m(N-1)}]} \int dp_1 \dots dp_{N-1} \prod_{j=1}^{N-1} e^{-\frac{\beta}{2m}[p_j^2 - \frac{ikm}{\beta}]^2} \\
&= (2\pi R)^{-1} e^{-\frac{N\beta p^2}{2m(N-1)}} (\frac{2\pi m}{\beta})^{\frac{N-1}{2}} \int dk e^{-\frac{m(N-1)}{2\beta}[k^2 - \frac{i\beta p}{m(N-1)}]^2} \\
&= R^{-1}(N-1)^{-1/2} (\frac{2\pi m}{\beta})^{\frac{N}{2}-1} e^{-\frac{N\beta p^2}{2m(N-1)}}.
\end{aligned} \tag{2.115}$$

We can integrate R in the same way:

$$\begin{aligned} R &= \frac{1}{2\pi}\int\int dkd\vec{p}e^{-\frac{\beta}{2m}\sum_{j=1}^{N}(p_j^2-\frac{2ikm}{\beta}p_j)} = \frac{1}{2\pi}\int dke^{-\frac{Nmk^2}{2\beta}}\int dpe^{-\frac{\beta}{2m}\sum_{j=1}^{N}(p_j-\frac{ikm}{\beta})^2} \\ &= N^{-1/2}(\frac{2\pi m}{\beta})^{\frac{N-1}{2}} \end{aligned} \tag{2.116}$$

from which both (2.115) and (2.116) give the momentum distribution

$$\theta_c(p) = \big[\frac{\beta N}{2\pi m(N-1)}\big]^{\frac{1}{2}}e^{-\frac{N\beta p^2}{2m(N-1)}} \tag{2.117}$$

that clearly gives the normalization $\int \theta_c(p)dp = 1$. For spatial distribution (2.112a), we take the N-point Klimontovich distribution function in space and transform it into Fourier space:

$$\begin{aligned} \bar{\rho_c}(k) &= \int dxe^{ikx}\rho_c(x) = (QN!)^{-1}\int\int dxd\vec{x}\delta(\bar{x})e^{-\beta U(\vec{x})}e^{ikx}N^{-1}\sum_{j=1}^{N}\delta(x-x_j) \\ &= \frac{1}{NQ}\sum_{j=1}^{N}F_j(k) \end{aligned} \tag{2.118}$$

where

$$F_j(k) = \int_{-\infty}^{\infty}dx_1\int_{x_1}^{\infty}dx_2\int_{x_2}^{\infty}dx_3\ldots\int_{x_{N-1}}^{\infty}dx_N\delta(\bar{x})e^{-\beta U(\vec{x})}e^{ikx_j}. \tag{2.119}$$

Noting that the total potential can be written in the form (2.105), we thus define a new set of parameters

$$\begin{aligned} u_l &= x_{l+1} - x_l \quad \text{with} \quad 1 \le l \le N-1 \\ u_N &= N^{-1}\sum_{j=1}^{N}x_j = \bar{x} \end{aligned} \tag{2.120}$$

from which we can invert to obtain x_j as a function of $\{u_l\}$:

$$x_j = u_N - N^{-1}\big[\sum_{l=1}^{N-1}D_{jl}u_l\big] \tag{2.121}$$

with

$$\begin{aligned} D_{jl} &= -l \quad , \quad i > l \\ &= N-l \quad , \quad i \le l. \end{aligned} \tag{2.122}$$

(2.119) then gives

$$F_j(k) = \int_0^{\infty}du_1\int_0^{\infty}du_2\ldots\int_{-\infty}^{\infty}du_N\delta(u_N)e^{-\beta\lambda\sum_{l=1}^{N-1}C_lu_l}\times e^{ik(u_N-N^{-1}\sum_{l=1}^{N-1}D_{jl}u_l)} \tag{2.123}$$

where u_N can be eliminated first to give

$$F_j(k) = \prod_{l=1}^{N-1}\int_0^{\infty}du_le^{-(\beta\lambda C_l+\frac{ik}{N}D_{jl})u_l} = \prod_{l=1}^{N-1}[\beta\lambda C_l + \frac{ik}{N}D_{jl}]^{-1}. \tag{2.124}$$

Substituting D_{jl} from (2.122), we obtain

$$\begin{aligned} F_j(k) &= \prod_{l=1}^{j-1}[\beta\lambda C_l - \frac{ik}{N}l]^{-1}\prod_{l=j}^{N-1}[\beta\lambda C_l + \frac{ik}{N}(N-l)]^{-1} \\ &= (\lambda\beta)^{-(N-1)}\prod_{l=1}^{j-1}[l(N-l-i\alpha)]^{-1}\prod_{l=j}^{N-1}[(N-l)(l+i\alpha)]^{-1} \end{aligned} \tag{2.125}$$

with $\alpha = k/N\beta\lambda$. Equation (2.125) can be expressed using the gamma function as

$$F_j(k) = (\lambda\beta)^{-(N-1)}\left[(j-1)!(N-j)!\frac{\Gamma(N-i\alpha)\Gamma(N+i\alpha)}{\Gamma(N-j-i\alpha+1)\Gamma(j+i\alpha)}\right]. \tag{2.126}$$

From (2.119), we notice that the spatial partition function Q is

$$Q = F_j(0) = \prod_{l=1}^{N-1}[\beta\lambda l(N-l)]^{-1} = \frac{1}{(\beta\lambda)^{(N-1)}[(N-1)!]^2} \tag{2.127}$$

from which it follows that

$$\bar{\rho_c}(k) = \frac{1}{N}\cdot\frac{[(N-1)!]^2}{\Gamma(N+i\alpha)\Gamma(N-i\alpha)}\sum_{j=1}^{N}\frac{\Gamma(N-j-i\alpha+1)\Gamma(j+i\alpha)}{(j-1)!(N-j)!}. \tag{2.128}$$

Using beta functions, the terms with gamma functions in summation can be manipulated so that

$$\begin{aligned} \bar{\rho_c}(k) &= \frac{1}{N}\cdot\frac{[(N-1)!]^2}{\Gamma(N+i\alpha)\Gamma(N-i\alpha)}\sum_{j=1}^{N}\frac{B(j+i\alpha,N-j-i\alpha+1)\Gamma(N+1)}{(j-1)!(N-j)!} \\ &= \frac{[(N-1)!]^2}{\Gamma(N+i\alpha)\Gamma(N-i\alpha)}\sum_{j=1}^{N}\int_0^1\frac{z^{i\alpha}(1-z)^{-i\alpha}[z^{j-1}(1-z)^{(N-1)-(j-1)}](N-1)!}{(j-1)!((N-1)-(j-1))!}dz. \end{aligned}$$

Using binomial coefficient notation, this becomes

$$\begin{aligned} \bar{\rho_c}(k) &= \frac{[(N-1)!]^2}{\Gamma(N+i\alpha)\Gamma(N-i\alpha)}\int_0^1 z^{i\alpha}(1-z)^{-i\alpha}\left[\sum_{j=1}^{N}\binom{N-1}{j-1}z^{j-1}(1-z)^{(N-1)-(j-1)}\right]dz \\ &= \frac{[(N-1)!]^2}{\Gamma(N+i\alpha)\Gamma(N-i\alpha)}\int_0^1 z^{i\alpha}(1-z)^{-i\alpha}[z+(1-z)]^{N-1}dz \\ &= \frac{[(N-1)!]^2}{\Gamma(N+i\alpha)\Gamma(N-i\alpha)}\int_0^1 z^{i\alpha}(1-z)^{-i\alpha}dz \end{aligned} \tag{2.129}$$

which is again the beta function. Hence we are able to convert again the integral to a gamma function and thus

$$\begin{aligned} \bar{\rho_c}(k) &= \frac{[(N-1)!]^2\Gamma(1+i\alpha)\Gamma(1-i\alpha)}{\Gamma(N+i\alpha)\Gamma(N-i\alpha)} = \prod_{l=1}^{N-1}\frac{l^2}{(l+i\alpha)(l-i\alpha)} \\ &= \prod_{l=1}^{N-1}\frac{(N\beta\lambda)^2l^2}{(k-iN\beta\lambda l)(k+iN\beta\lambda l)}. \end{aligned} \tag{2.130}$$

To obtain the density in direct space we perform the inverse Fourier transform on (2.130), which gives

$$\rho_c(x) = \frac{1}{2\pi}\int dk e^{-ikx}\bar{\rho}_c(k) = \frac{1}{2\pi}\int dk e^{-ikx}\prod_{l=1}^{N-1}\frac{(N\beta\lambda)^2 l^2}{(k - iN\beta\lambda l)(k + iN\beta\lambda l)}. \tag{2.131}$$

This can be evaluated using contour integration. For $x \geq 0$ we perform the integration with closed semi-circle contour enclosing the poles in negative imaginary zone. The integration contour is illustrated in Fig. 2.5 with all poles included. The contour we consider is in the clockwise direction along the lower half of the complex plane. From that contour, the residue theorem

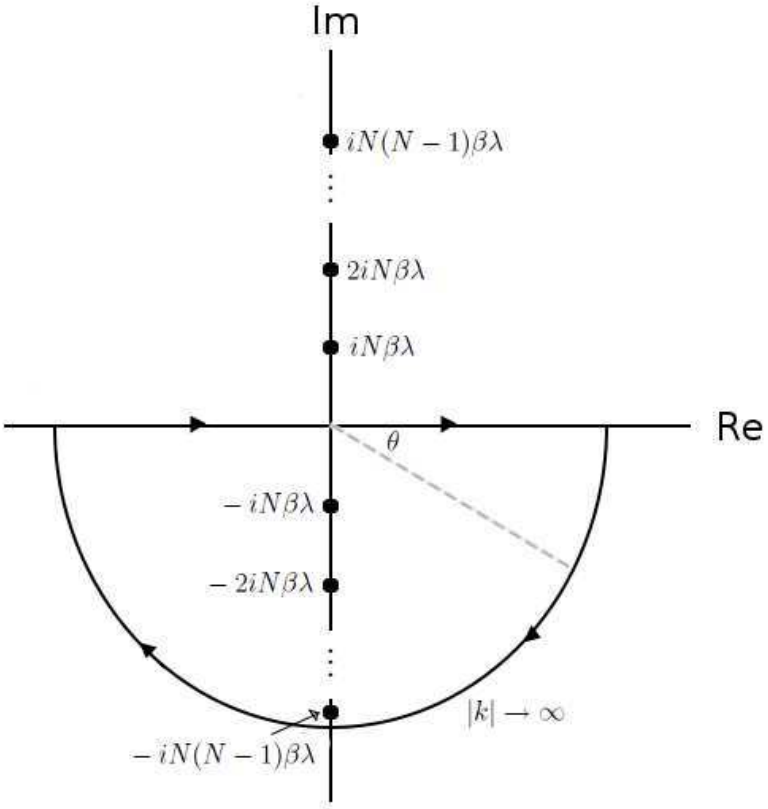

Figure 2.5: Integration contour with radius $|k|$ elongated to infinity. All poles are aligned in imaginary axis in which there are equally $(N-1)$ poles in upper and lower plane. The contour is in clockwise direction.

gives

$$\begin{aligned} -\oint e^{-ikx}\bar{\rho}_c(k)dk &= \int_{-\infty}^{\infty} e^{-ikx}\bar{\rho}_c(k)dk + \lim_{|k|\to\infty}\int_0^{-\pi} e^{-i|k|(\cos\theta + i\sin\theta)x}\bar{\rho}_c(k)dk \\ &= -2\pi i\sum_{j=1}^{N-1}\mathrm{Res}(e^{-ikx}\bar{\rho}_c(k), -iN\beta\lambda j) \end{aligned}$$

where the integral on semi-circle vanishes. Therefore we have

$$\begin{aligned}\int_{-\infty}^{\infty} e^{-ikx}\bar{\rho}_c(k)dk &= -2\pi i\sum_{j=1}^{N-1}\Bigg[e^{-N\beta\lambda jx}(N\beta\lambda)^{2N-2}\prod_{l=1}^{N-1}\frac{l^2}{(-iN\beta\lambda j - iN\beta\lambda l)} \\ &\quad\times\prod_{n=1}^{j-1}\frac{1}{(-iN\beta\lambda j + iN\beta\lambda n)}\prod_{q=j+1}^{N-1}\frac{1}{(-iN\beta\lambda j + iN\beta\lambda q)}\Bigg] \\ &= -2\pi N\beta\lambda\sum_{j=1}^{N-1}\Bigg[e^{-N\beta\lambda jx}(-1)^j\prod_{l=1}^{N-1}\frac{l^2}{(j+l)}\prod_{n=1}^{j-1}\frac{1}{(j-n)}\prod_{q=j+1}^{N-1}\frac{1}{(q-j)}\Bigg].\end{aligned}$$

We can convert the product notation using factorial to write them as

$$\begin{aligned}-\oint e^{-ikx}\bar{\rho}_c(k)dk &= -2\pi N\beta\lambda\sum_{j=1}^{N-1}\left[e^{-N\beta\lambda jx}(-1)^j\cdot\frac{[(N-1)!]^2 j!}{(N-1+j)!(N-1-j)!(j-1)!}\right] \\ &= 2\pi N\beta\lambda\sum_{j=1}^{N-1}\left[e^{-N\beta\lambda jx}(-1)^{j+1}\cdot\frac{[(N-1)!]^2 j}{(N-1+j)!(N-1-j)!}\right]. \qquad (2.132)\end{aligned}$$

h The density distribution is thus given as

$$\rho_c(x) = N\beta\lambda\sum_{j=1}^{N-1}A_j^N e^{-N\beta\lambda jx} \qquad (2.133)$$

where

$$A_j^N = \frac{j(-1)^{j+1}[(N-1)!]^2}{(N-1-j)!(N-1+j)!}. \qquad (2.134)$$

Note that the integral (2.131) for $x<0$ can be done by flipping the contour in Fig. 2.5 upward to cover the positive imaginary axis. As the poles are symmetric about the real axis, we can deduce that the density distribution can be written by

$$\rho_c(x) = N\beta\lambda\sum_{j=1}^{N-1}A_j^N e^{-N\beta\lambda j|x|} \qquad (2.135)$$

for all x with A_j^N defined in (2.134). The normalization of $\rho_c(x)$ can be calculated

$$\begin{aligned}\int_{-\infty}^{\infty}\rho_c(x)dx &= 2N\beta\lambda\sum_{j=1}^{N-1}A_j^N\int_0^{\infty}e^{-N\beta\lambda}dx = 2\sum_{j=1}^{N-1}\frac{A_j^N}{j} \\ &= 2\sum_{j=1}^{N-1}\frac{(-1)^{j+1}[(N-1)!]^2}{(N-1-j)!(N-1+j)!}. \qquad (2.136)\end{aligned}$$

We will return to (2.136) later and now we will do a simple arithmetic on the integral formula. From the known integration formulae

$$\int_{-\pi/2}^{\pi/2} \cos^n t \; dt = \frac{n-1}{n} \int_{-\pi/2}^{\pi/2} \cos^{n-2} t \; dt \tag{2.137a}$$

$$\int_{-\pi/2}^{\pi/2} \cos ct \cos^n t \; dt = \frac{n(n-1)}{n^2-c^2} \int_{-\pi/2}^{\pi/2} \cos ct \cos^{n-2} t \; dt \tag{2.137b}$$

and if we suppose that both n and c are positive even integer, i.e. we replace by $2(N-1)$ and $2c$, the formulae above become

$$\begin{aligned} \int_{-\pi/2}^{\pi/2} \cos^{2(N-1)} t \; dt &= \left[\frac{2N-3}{2N-2} \cdot \frac{2N-5}{2N-4} \cdot \frac{2N-7}{2N-6} \cdots \frac{1}{2}\right] \int_{-\pi/2}^{\pi/2} dt \\ &= \frac{\pi(2N-2)!}{2^{2(N-1)}[(N-1)!]^2} \end{aligned} \tag{2.138a}$$

and

$$\begin{aligned} \int_{-\pi/2}^{\pi/2} \cos 2ct \cos^{2(N-1)} t \; dt &= \frac{(2N-2)(2N-3)(2N-4)\ldots 1}{[(2N-2)^2-4c^2][(2N-4)^2-4c^2]\ldots[2^2-4c^2]} \int_{-\pi/2}^{\pi/2} \cos 2ct \; dt \\ &= \frac{(2N-2)!}{2^{2(N-1)}} \cdot \frac{\sin c\pi}{c} \cdot \frac{1}{[(N-1-c)(N-2-c)\ldots(1-c)]} \\ &\quad \times \frac{1}{[(N-1+c)(N-2+c)\ldots(1+c)]}. \end{aligned} \tag{2.138b}$$

Note that when $c = N$, the expression is defined as

$$\lim_{c \to N} \frac{\sin c\pi}{N-c} = \pi(-1)^{c+1}.$$

Notice that the denominator in (2.138b) has $c-1$ negative terms, therefore we rearrange it to

$$\begin{aligned} \int_{-\pi/2}^{\pi/2} \cos 2ct \cos^{2(N-1)} t \; dt &= \frac{\pi(2N-2)!c!(-1)^{c+1}}{2^{2(N-1)}(N-1+c)!(N-1-c)!(c-1)!(-1)^{c-1}} \\ &= \frac{\pi(2N-2)!}{2^{2(N-1)}(N-1+c)!(N-1-c)!}. \end{aligned} \tag{2.138c}$$

From (2.138a) and (2.138c) we can deduce that

$$\frac{\int_{-\pi/2}^{\pi/2} \cos 2ct \cos^{2(N-1)} t \; dt}{\int_{-\pi/2}^{\pi/2} \cos^{2(N-1)} t \; dt} = \frac{\int_{-\pi/2}^{\pi/2} e^{-2cit} \cos^{2(N-1)} t \; dt}{\int_{-\pi/2}^{\pi/2} \cos^{2(N-1)} t \; dt} = \frac{[(N-1)!]^2}{(N-1+c)!(N-1-c)!} \tag{2.139}$$

where we write $\cos 2ct$ in the complex polar form since $\sin 2ct$, being an odd function, vanishes on integration. Returning to the density normalization (2.136) and (2.139), we have

$$\int \rho_c(x)dx = \frac{-2\int\limits_{-\pi/2}^{\pi/2}\sum\limits_{j=1}^{N-1}(-e^{-2it})^j\cos^{2(N-1)}t\ dt}{\int\limits_{-\pi/2}^{\pi/2}\cos^{2(N-1)}t\ dt}. \tag{2.140}$$

To eliminate the summation in the integral in (2.140), we use the summation formula

$$\begin{aligned}\sum_{j=1}^{N-1}(-e^{-2it})^j &= \frac{1-(-e^{-2it})^N}{1-(-e^{-2it})} - 1 = \frac{-e^{-it}-(-1)^N e^{-it(2N-1)}}{e^{it}+e^{-it}} \\ &= -\frac{e^{-it}}{2\cos t} - \frac{(-1)^N e^{-it(2N-1)}}{2\cos t}\end{aligned} \tag{2.141}$$

from which we substitute (2.141) in (2.140) and convert the complex exponential to trigonometric function:

$$\begin{aligned}\int \rho_c(x)dx &= \frac{\int\limits_{-\pi/2}^{\pi/2} e^{-it}\cos^{2N-3}t\ dt}{\int\limits_{-\pi/2}^{\pi/2}\cos^{2(N-1)}t\ dt} + \frac{(-1)^N\int\limits_{-\pi/2}^{\pi/2} e^{-(2N-1)ti}\cos^{2N-3}t\ dt}{\int\limits_{-\pi/2}^{\pi/2}\cos^{2(N-1)}t\ dt} \\ &= 1 + \frac{(-1)^N\int\limits_{-\pi/2}^{\pi/2}\cos(2N-1)t\ \cos^{2N-3}t\ dt}{\int\limits_{-\pi/2}^{\pi/2}\cos^{2(N-1)}t\ dt}.\end{aligned} \tag{2.142}$$

From (2.137b) we can write (2.142) as

$$\begin{aligned}\int \rho_c(x)dx &= 1 + \left[\frac{(-1)^N(2N-3)!}{\prod\limits_{s=1}^{N-2}\left[(2N-2s-1)^2-(2N-1)^2\right]}\right]\left[\frac{\int\limits_{-\pi/2}^{\pi/2}\cos(2N-1)t\ \cos t\ dt}{\int\limits_{-\pi/2}^{\pi/2}\cos^{2(N-1)}t\ dt}\right] \\ &= 1 + \frac{B_N}{2}\left[\frac{\int\limits_{-\pi/2}^{\pi/2}[\cos(2N-2)t+\cos 2Nt]\ dt}{\int\limits_{-\pi/2}^{\pi/2}\cos^{2(N-1)}t\ dt}\right] = 1 + \frac{B_N}{2}\left[\frac{\frac{\sin(N-1)\pi}{N-1}+\frac{\sin N\pi}{N}}{\int\limits_{-\pi/2}^{\pi/2}\cos^{2(N-1)}t}\right]\end{aligned}$$

with

$$B_N = \left[\frac{(-1)^N(2N-3)!}{\prod\limits_{s=1}^{N-2}\left[(2N-2s-1)^2-(2N-1)^2\right]}\right].$$

Since B_N is non-zero, and N is an integer, we finally deduce that $\int \rho_c(x)dx = 1$, and we obtain moreover the useful summation rule involving A_j^N as follows:

$$\sum_{j=1}^{N-1} \frac{A_j^N}{j} = \frac{1}{2}. \tag{2.143}$$

By combining (2.117) and (2.135) the canonical equilibrium distribution function reads finally

$$f_c(p,x) = \frac{(N\beta)^{3/2}\lambda}{[2\pi m(N-1)]^{1/2}} \sum_{j=1}^{N-1} A_j^N e^{\left[-\frac{\beta N}{2m(N-1)}p^2 - N\beta\lambda j|x|\right]}. \tag{2.144}$$

The partition function is

$$z = QR = \frac{(2\pi m)^{\frac{N-1}{2}}}{[(N-1)!]^2 N^{\frac{1}{2}}\lambda^{N-1}} \cdot \frac{1}{\beta^{\frac{3}{2}(N-1)}} \tag{2.145}$$

with Q and R as given in (2.116) and (2.127). The average total energy is therefore

$$< E >= -\frac{\partial}{\partial\beta}\log z = \frac{3(N-1)}{2\beta}. \tag{2.146}$$

2.2.3 Micro-canonical ensemble

Let us consider now this system in the micro-canonical ensemble, the micro-canonical equilibrium profile is given by

$$f_{mc}(p,x) = (\Omega N!)^{-1} \int\int d\vec{p}d\vec{x}\delta(\bar{x})\delta(\bar{p})\delta(E - H(\vec{p},\vec{x})) \cdot \frac{1}{N}\sum_{j=1}^{N} \delta(p-p_j)\delta(x-x_j) \tag{2.147}$$

where $\delta(E - H(\vec{p},\vec{x}))$ imposes the equiprobable weight, and where

$$\Omega = \frac{1}{N!}\int\int d\vec{p}d\vec{x}\delta(\bar{x})\delta(\bar{p})\delta(E - H(\vec{p},\vec{x})) \tag{2.148}$$

is the partition function. To evaluate this expression we use the fact that the canonical equilibrium and micro-canonical equilibrium are related through Laplace transform as

$$zf_c = \int_0^\infty e^{-\beta E}(\Omega f_{mc})dE \quad \text{and} \quad z = \int_0^\infty e^{-\beta E}\Omega dE.$$

Thus the micro-canonical equilibrium is obtained by doing the inverse Laplace transform

$$\Omega f_{mc} = \frac{1}{2\pi i}\int_C e^{\beta E}(zf_c)d\beta \tag{2.149a}$$

with

$$\Omega = \frac{1}{2\pi i}\int_C e^{\beta E} z d\beta \tag{2.149b}$$

where the integration contour C extends from $-i\infty$ to $i\infty$ on the right of all singularities in the complex plane. We determine first the micro-canonical partition function Ω

$$\Omega = \frac{(2\pi m)^{\frac{N-1}{2}}}{[(N-1)!]^2 N^{\frac{1}{2}}\lambda^{N-1}} \cdot \frac{1}{2\pi i}\int_C e^{\beta E}\beta^{-\frac{3}{2}(N-1)}. \tag{2.150}$$

Given the inverse Laplace transform formula

$$\frac{(t)_+^{q-1}}{\Gamma(q+1)} = \frac{1}{2\pi i}\int_C \frac{e^{st}}{s^{q+1}}ds \tag{2.151}$$

where $(t)_+ \equiv t\Theta(t)$ with $\Theta(t)$ the Heaviside step function, (2.150) becomes

$$\Omega = \frac{(2\pi m)^{\frac{N-1}{2}} E^{\frac{3N}{2}-\frac{5}{2}}}{\Gamma(\frac{3N}{2}-\frac{3}{2})[(N-1)!]^2 N^{\frac{1}{2}}\lambda^{N-1}}. \tag{2.152}$$

Using these expressions, we have

$$f_{mc}(p,x) = \frac{1}{\Omega}\cdot\frac{(2\pi m)^{\frac{N}{2}-1}N}{[(N-1)!]^2 N^{\frac{1}{2}}\lambda^{N-2}}\cdot\frac{1}{2\pi i}\sum_{j=1}^{N-1}A_j^N\int_C \frac{e^{\beta(E-\frac{Np^2}{2m(N-1)}-N\lambda j|x|)}}{\beta^{\frac{3N}{2}-3}}d\beta$$

and thus

$$f_{mc}(p,x) = \frac{\lambda N^{\frac{3}{2}}}{(2\pi m(N-1))^{\frac{1}{2}}E^{\frac{3}{2}}}\cdot\frac{\Gamma(\frac{3N}{2}-\frac{3}{2})}{\Gamma(\frac{3N}{2}-3)}\sum_{j=1}^{N-1}A_j^N(1-\frac{Np^2}{2m(N-1)E}-\frac{N\lambda j|x|}{E})_+^{\frac{3N}{2}-4}. \tag{2.153}$$

Note that, differently to the result in the canonical ensemble, the phase space density is neither separable nor characterized by a Maxwellian velocity distribution. We will see below that in the limit $N\to\infty$ both aspects are recovered and the two results coincide. Consider now the density profile

$$\rho_{mc}(x) = \frac{\lambda N^{\frac{3}{2}}}{(2\pi m(N-1))^{\frac{1}{2}}E^{\frac{3}{2}}}\cdot\frac{\Gamma(\frac{3N}{2}-\frac{3}{2})}{\Gamma(\frac{3N}{2}-3)}\sum_{j=1}^{N-1}2A_j^N\int_0^{\tilde{p}_0}(1-\frac{Np^2}{2m(N-1)E(1-\frac{N\lambda j|x|}{E})})_+^{\frac{3N}{2}-4}dp. \tag{2.154}$$

Changing the integral variable with

$$p' = \frac{p^2}{\tilde{p}_0^2} \quad \text{where} \quad \tilde{p}_0 = \left[\frac{2m(N-1)E}{N}\Big(1-\frac{N\lambda j|x|}{E}\Big)\right]^{\frac{1}{2}},$$

we can rewrite the integral in (2.154) in term of a beta function as

$$\begin{aligned}\rho_{mc}(x) &= \frac{\lambda N}{E\sqrt{\pi}}\cdot\frac{\Gamma(\frac{3N}{2}-\frac{3}{2})}{\Gamma(\frac{3N}{2}-3)}\sum_{j=1}^{N-1}A_j^N(1-\frac{N\lambda j|x|}{E})_+^{\frac{3N}{2}-\frac{7}{2}}\int_0^1(1-p')^{\frac{3N}{2}-4}p'^{-\frac{1}{2}}dp' \\ &= \frac{\lambda N}{E}(\frac{3N}{2}-\frac{5}{2})\sum_{j=1}^{N-1}A_j^N\left(1-\frac{N\lambda j|x|}{E}\right)_+^{\frac{3N}{2}-\frac{7}{2}}.\end{aligned} \tag{2.155}$$

Note that the normalization condition on (2.155) is indeed satisfied:

$$\int\rho_{mc}(x)dx = \frac{\lambda N}{E}(\frac{3N}{2}-\frac{5}{2})\sum_{j=1}^{N-1}2A_j^N\int_0^{E/N\lambda j}(1-\frac{N\lambda jx}{E})_+^{\frac{3N}{2}-\frac{7}{2}}dx = 2\sum_{j=1}^{N-1}\frac{A_j^N}{j} = 1$$

where we have used the relation (2.143). Next we consider the velocity distribution

$$\begin{aligned}\theta_{mc}(p) &= \frac{\lambda N^{\frac{3}{2}}}{(2\pi m(N-1))^{\frac{1}{2}}E^{\frac{3}{2}}}\cdot\frac{\Gamma(\frac{3N}{2}-\frac{3}{2})}{\Gamma(\frac{3N}{2}-3)}\sum_{j=1}^{N-1}2A_j^N\Big(\frac{N\lambda j}{E}\Big)^{\frac{3N}{2}-4}\int_0^{\tilde{x}_0}(\tilde{x}_0-x)_+^{\frac{3N}{2}-4}dx \\ &= \left(\frac{N}{2\pi m(N-1)E}\right)^{\frac{1}{2}}\cdot\frac{\Gamma(\frac{3N}{2}-\frac{3}{2})}{\Gamma(\frac{3N}{2}-2)}\cdot\left(1-\frac{Np^2}{2m(N-1)E}\right)_+^{\frac{3N}{2}-3} \qquad (2.156)\end{aligned}$$

in which we define $\tilde{x}_0 = \frac{E}{N\lambda j} - \frac{p^2}{2m(N-1)\lambda j}$ to be the cut-off distance. The normalization condition of (2.156) gives

$$\int\theta_{mc}(p)dp = \left(\frac{N}{2\pi m(N-1)E}\right)^{\frac{1}{2}}\cdot\frac{\Gamma(\frac{3N}{2}-\frac{3}{2})}{\Gamma(\frac{3N}{2}-2)}\int_{-p_0}^{p_0}\left(1-\frac{p^2}{p_0^2}\right)_+^{\frac{3N}{2}-3}dp \qquad (2.157)$$

where $p_0 = \sqrt{\frac{2m(N-1)E}{N}}$. Integrating (2.157) in the same manner as for (2.155), this yields

$$\int\theta_{mc}(p)dp = \frac{1}{\sqrt{\pi}}\cdot\frac{\Gamma(\frac{3N}{2}-\frac{3}{2})}{\Gamma(\frac{3N}{2}-2)}\int_0^1(1-p')^{\frac{3N}{2}-3}p'^{-\frac{1}{2}}dp' = 1. \qquad (2.158)$$

Despite the fact that these equilibria in both canonical and micro-canonical ensembles can be determined analytically, the expressions are not in simple forms.

2.2.4 Mean-field thermodynamic limit

We consider the mean-field limit where $N\to\infty$ at fixed mass M and energy E. Denoting the limit by an asterisk, we have

$$\begin{aligned}f_{mc}^*(p,x) &= \lim_{N\to\infty}\frac{\lambda N}{(2\pi m)^{\frac{1}{2}}E^{\frac{3}{2}}}\cdot\frac{\Gamma(\frac{3N}{2}-\frac{3}{2})}{\Gamma(\frac{3N}{2}-3)}\sum_{j=1}^{N-1}A_j^N(1-\frac{3Mp^2}{4m^2E}\cdot\frac{2}{3N}+\frac{3gM^2j|x|}{2E}\cdot\frac{2}{3N})_+^{\frac{3N}{2}-4} \\ &= \lim_{N\to\infty}\frac{\lambda N}{(2\pi m)^{\frac{1}{2}}E^{\frac{3}{2}}}\cdot\frac{\Gamma(\frac{3N}{2}-\frac{3}{2})}{\Gamma(\frac{3N}{2}-3)}\sum_{j=1}^{N-1}A_j^N e^{-(\frac{p}{\sigma})^2}e^{-2|\frac{x}{\Lambda}|} \qquad (2.159)\end{aligned}$$

with characteristic momentum scale σ and length scale Λ given by

$$\sigma^2 = \frac{4m^2E}{3M} \quad \text{and} \quad \Lambda = \frac{4E}{3gM^2}. \qquad (2.160)$$

Consider the large N behavior of the ratio of gamma functions, we have

$$\lim_{N\to\infty}\frac{\Gamma(\frac{3N}{2}-\frac{3}{2})}{\Gamma(\frac{3N}{2}-3)}\to(\frac{3N}{2})^{\frac{3}{2}}.$$

Given the relation of average energy and inverse temperature in (2.146), the large N micro-canonical ensemble is equivalent to canonical ensemble, i.e. $f_c^*\to f_{mc}^*$. Therefore the ensemble

equivalence is obtained in the thermodynamic limit. Let us derive further

$$\begin{aligned} f^*_{mc}(p,x) &= \lim_{N\to\infty} \frac{\lambda N}{(2\pi m)^{\frac{1}{2}}}(\frac{3N}{2E})^{\frac{3}{2}} e^{-(\frac{p}{\sigma})^2} \sum_{j=1}^{N-1} \frac{[(N-1)!]^2(-1)^{j+1} j e^{-2j|\frac{x}{\Lambda}|}}{(N-1+j)!(N-1-j)!} \\ &= \lim_{N\to\infty} \frac{\lambda N}{(2\pi m)^{\frac{1}{2}}}(\frac{3N}{2E})^{\frac{3}{2}} e^{-(\frac{p}{\sigma})^2} \cdot \frac{-\int_{-\pi/2}^{\pi/2} \sum_{j=1}^{N-1} j(-e^{(-2it-2|\frac{x}{\Lambda}|)})^j \cos^{2(N-1)} t \; dt}{\int_{-\pi/2}^{\pi/2} \cos^{2(N-1)} t \; dt} \end{aligned}$$

where the summation uses the formula

$$\lim_{N\to\infty} \sum_{i=0}^{N} i x^i = \frac{x}{(1-x)^2}$$

and gives

$$\begin{aligned} f^*_{mc}(p,x) &= \frac{\lambda N}{(2\pi m)^{\frac{1}{2}}}(\frac{3N}{2E})^{\frac{3}{2}} e^{-(\frac{p}{\sigma})^2} \cdot \frac{\int_{-\pi/2}^{\pi/2} \left[\frac{1}{e^{2it+2|\frac{x}{\Lambda}|}+e^{-2it-2|\frac{x}{\Lambda}|}+2}\right] \cos^{2(N-1)} t \; dt}{\int_{-\pi/2}^{\pi/2} \cos^{2(N-1)} t \; dt} \\ &= \frac{1}{2\sqrt{\pi}} \cdot \frac{1}{\sigma\Lambda} e^{-(\frac{p}{\sigma})^2} \cdot \frac{\int_{-\pi/2}^{\pi/2} \mathrm{sech}^2(|\frac{x}{\Lambda}| + it) \cos^{2(N-1)} t \; dt}{\int_{-\pi/2}^{\pi/2} \cos^{2(N-1)} t \; dt} \end{aligned} \tag{2.161}$$

where the constants in front of the integral are those defined in (2.160). When $N \to \infty$ the function $\cos t$ is equal to 1 at $t = 0$ and 0 elsewhere as $\cos t < 1$, (2.161) converges to

$$f^*_{mc}(p,x) = \frac{1}{2\sqrt{\pi}} \cdot \frac{1}{\sigma\Lambda} \mathrm{sech}^2(\frac{x}{\Lambda}) e^{-(\frac{p}{\sigma})^2} \tag{2.162}$$

from which we can derive that

$$\rho^*_{mc}(x) = \frac{1}{2\Lambda}\mathrm{sech}^2\xi \quad \text{rm} \quad \theta^*_{mc}(\eta) = \frac{1}{\sigma\sqrt{\pi}} e^{-(\frac{p}{\sigma})^2} \tag{2.163}$$

where each one satisfies the appropriate required normalization condition:

$$\int\int f^*_V(p,x)dxdp = \int \rho^*_V(x)dx = \int \theta^*_V(p)dp = 1.$$

It is convenient to write this distribution function (and underlying coordinates) in dimensionless form by

$$\tilde{f}^*(\eta,\xi) \equiv \sigma\Lambda f^*(p,x) \tag{2.164}$$

with dimensionless momentum and position given as following

$$\eta = \frac{p}{\sigma} \quad \text{and} \quad \xi = \frac{x}{\Lambda} \tag{2.165}$$

from which the dimensionless momentum and spatial distributions are

$$\tilde{\theta}^*(\eta) \equiv \sigma\theta^*(x) \quad \text{and} \quad \tilde{\rho}^*(\xi) \equiv \Lambda\rho^*(x) \tag{2.166}$$

such that

$$\int\int \tilde{f}^*(\eta,\xi)d\xi d\eta = \int \tilde{\rho}^*(\xi)d\xi = \int \tilde{\theta}^*(\eta)d\eta = 1$$

and where

$$\tilde{\theta}(\eta) = \frac{e^{-\eta^2}}{\sqrt{\pi}} \quad \text{and} \quad \tilde{\rho}(\xi) = \frac{\text{sech}^2(\xi)}{2}. \tag{2.167}$$

This same density profile (2.167) was also derived earlier by Spitzer [126], who considered such a model to describe the dynamics of the interstellar medium around the equatorial plane of galaxy. The equilibrium is thus a state of finite mass clustered in a finite region of space (in contrast to the thermodynamic equilibrium of ideal gas) with $\tilde{\rho}(\xi)$ decaying exponentially at large distance, and a Maxwellian velocity distribution.

It is straightforward to show that this result for equilibrium in the mean-field thermodynamic limit, is just that one obtained by a direct mean-field calculation analogous to that previously used earlier in the chapter for three dimensions. Indeed maximizing the Boltzmann entropy given by

$$S[f] = \int f \ln f dx dv$$

at fixed mass and energy yields

$$f(x,v) = Ae^{-\beta(\frac{v^2}{2}+\Phi(x))} \equiv \rho(x)\theta(v) \tag{2.168}$$

where $\Phi(x)$ is the solution of Lane-Emden equation

$$\frac{d^2\Phi}{dx^2} = 2g\rho_c e^{-\beta[\Phi(x)-\Phi(0)]}. \tag{2.169}$$

It is straightforward to show that $\rho = \rho_c e^{-\beta[\Phi(x)-\Phi(0)]}$ is indeed equivalent to the density profile (2.167), using Poisson equation with boundary condition $\Phi'(x)|_{x=0} = 0$ and $\Phi(x)|_{x=0} = \Phi(0)$.

To see how much the momentum and density distribution vary with N, we show in Fig. 2.6 the dimensionless momentum and density distributions defined in (2.166) in micro-canonical ensemble, i.e.

$$\tilde{\theta}_{mc}(\eta) = \frac{B(\frac{3N}{2}-\frac{3}{2})}{\pi}(\frac{3N}{2}-2)\Big(\frac{2}{3(N-1)})\Big)^{\frac{1}{2}}\Big(1-\frac{2\eta^2}{3(N-1)}\Big)^{\frac{3N}{2}-3}$$

and

$$\tilde{\rho}_{mc}(\xi) = \frac{4}{3N}\Big(\frac{3N}{2}-\frac{5}{2}\Big)B(N,N)\sum_{j=1}^{N-1}\frac{j(-1)^{j+1}}{B(N-j,N+j)}(1-\frac{4j|\xi|}{3N})^{\frac{3N}{2}-\frac{7}{2}},$$

for various N. The equilibrium in the thermodynamic limit is also shown. The effect of finite N is visible at small N but, at $N = 50$ for example, the equilibrium is already most indistinguishable from the continuum limit. In our numerical studies, we use at least 100 particles in each simulation therefore it will be reasonable to consider the mean-field equilibrium only*.

*Note that at $N = 2$ the solution is not well defined as $\tilde{\rho}_{mc}(\xi)$ is increasing and $\tilde{\theta}_{mc}(\eta)$ is uniform.

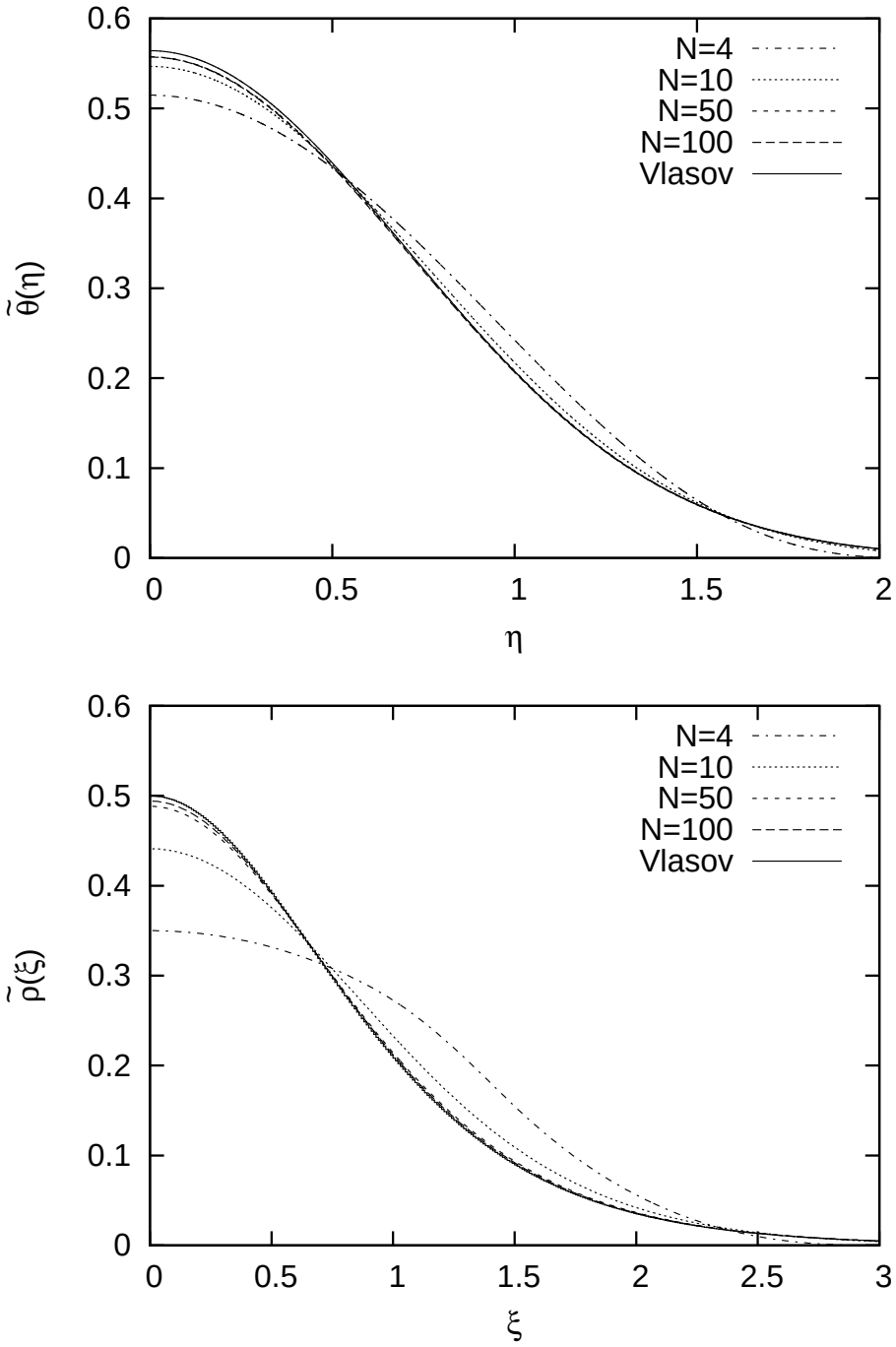

Figure 2.6: $\tilde{\theta}(\eta)$ (top) and $\tilde{\rho}(\xi)$ (bottom) of micro-canonical equilibrium for different N. The solid curves in both panel indicate the equilibrium in Vlasov limit.

2.2.5 Collisionality and relaxation rate in one dimension

A simple "derivation" of this scaling, along the lines of those applied originally by Chandrasekhar (see [9] or [17]) to obtain such an estimate for 3D self-gravitating systems, may be given as

follows. Relaxation is in principle due to the discretization, in N particles, of a continuous mass distribution. Let us suppose that this latter field density varies spatially on a scale, L. The typical change in the force F of a test particle due to its interaction with one (localized) particle, rather than the continuous mass distribution, can be estimated as

$$\Delta F \sim gm^2 \tag{2.170}$$

and the change in velocity is

$$\delta v = \frac{\Delta F \cdot \Delta t}{m} \simeq gm(\frac{L}{v}) \tag{2.171}$$

or

$$(\delta v)^2 \simeq (\frac{gmL}{v})^2. \tag{2.172}$$

As it crosses the system (in a time $\sim t_{dyn}$) such a particle will interact with all N particles. Assuming the contribution from each particle adds incoherently, one estimates

$$(\Delta v)^2 \simeq N(\frac{gmL}{v})^2. \tag{2.173}$$

Scaling with N at fixed mass and energy (and fixed L) requires

$$m \sim \frac{1}{N} \tag{2.174}$$

and therefore

$$\frac{(\Delta v)^2}{v^2} \sim \frac{1}{N} \quad \text{or} \quad n_{coll} \sim N \tag{2.175}$$

where n_{coll} is the number of crossings required. The relaxation time can then be estimated by

$$t_{relax} \sim N t_{cross} \tag{2.176}$$

leading to the relaxation time scales linear with N in units of the t_{dyn}. A slightly different argument leading to the same result may be found in [87], and a more developed analysis in [127]. In the framework of approaches based on kinetic theory, a linear scaling is obtained as collisional terms arise as the leading corrections in a formal expansion in $1/N$ which gives the collisionless (Vlasov) limit at leading order (see, e.g. [61, 98]).

This scaling linear in N is to be contrasted with the case of the scaling observed for the lifetime in QSS in the HMF, proportional to $N^{1.7}$. While the exponent found is not understood, the fact that it is larger than unity is consistent with these considerations as this result applies for spatially homogeneous QSS (which are possible in the HMF because of its periodicity) for which it has been shown that the leading collisional term vanishes (see, e.g., contributions of P.H. Chavanis, and of F. Bouchet and J. Barré in [57]). A discussion of the role of "resonances" which arise in the case of spatially inhomogeneous QSS and can lead to shorter relaxation times, and specifically linear in N, is described in [102].

2.2.6 Separability of thermal equilibrium

We note an evident property of the distribution function (2.162) is that it is separable function in its spatial and velocity coordinates. It is straightforward to show that it is, in fact, the *only* stationary solution of the Vlasov equation which is separable. Recall the Vlasov equation

$$\frac{\partial f}{\partial t} + v \cdot \frac{\partial f}{\partial x} + a(x) \cdot \frac{\partial f}{\partial v} = 0, \tag{2.177}$$

where $a(x)$ is the mean-field acceleration given by

$$a(x) = \int \frac{x' - x}{|x' - x|} \rho(x) dx' \tag{2.178}$$

satisfying the Poisson equation

$$\frac{da(x)}{dx} = -\frac{d^2\Phi(x)}{dx^2} = -2g\rho(x). \tag{2.179}$$

Seeking the "stationary separable" solution, i.e., solution of the form

$$f(x, v) = \rho(x)\theta(v), \tag{2.180}$$

we substitute in (2.177) and obtain

$$-\frac{1}{v} \cdot \frac{\partial(\ln \theta(v))}{\partial v} = \frac{1}{a(x)} \cdot \frac{\partial(\ln \rho(x))}{\partial x}. \tag{2.181}$$

It follows that only solution is that both sides are equal to a constant, C, therefore the left-hand-side reads

$$\theta(v) = \theta_0 e^{-C\frac{v^2}{2}} \tag{2.182}$$

and the right-hand-side is then

$$\rho(x) = \rho_0 e^{-C\Phi(x)} \tag{2.183}$$

with appropriate boundary condition. This corresponds indeed to (2.162).

2.2.7 Order parameters for thermal relaxation

This last result suggests that "order parameter" characterizing the degree of "entanglement" of the phase space density may be useful in probing the relaxation toward thermal equilibrium of QSS. Specifically we thus define

$$\phi_{\alpha\beta} = \frac{< |x|^\alpha |v|^\beta >}{< |x|^\alpha >< |v|^\beta >} - 1 \tag{2.184}$$

for any non-zero α and β where

$$< u(x, v) >= \frac{\int u(x, v) f(x, v) dx dv}{\int f(x, v) dx dv} \tag{2.185}$$

estimated in an N-particle realization by

$$< u(x, v) > \equiv \frac{1}{N} \sum_{i=1}^{N} u_i \tag{2.186}$$

where $u_i = u(x_i, v_i)$. This order parameter vanishes in thermal equilibrium for all α and β. While it is possible that $\phi_{\alpha\beta}$ vanishes for specific values of α and β in a (non-separable) stationary states, we expect them to be typically non-zero in such states. In our investigation of relaxation in chapter 4, we will use, specifically, ϕ_{11} and ϕ_{22}. We will see that they are indeed very efficient diagnostic of the thermal relaxation. We will also make use of them in our discussion of violent relaxation in chapter 5.

Chapter 3

Lynden-Bell's theory of violent relaxation

Early observations resolving astrophysical systems governed by gravitational forces, such as galaxies and globular clusters, made it clear that many of them appear to be in dynamical equilibrium. However the observed profiles (inferred, in practice, from light distributions) was not compatible with their interpretation as thermodynamics equilibria, i.e. as isothermal spheres. Furthermore the estimates of two-body relaxation times (recalled in chapter 2) gave time scales many of orders of magnitude larger than the age of universe for these systems. The fundamental question thus arose as to the nature of these stationary states, and of the explanation for how they could be established on such "short" time scales.

In an attempt to answer these questions — and specifically to understand the observed light distribution of elliptical galaxies — Lynden-Bell introduced in 1967 [19] his theory of "violent relaxation". He not only explained qualitatively the physics of the relaxation — driven by fluctuations of mean-field — but he also postulated that the states resulting from it could be predicted based on a statistical mechanics of the collisionless dynamics of the Vlasov-Poisson equations: introducing a coarse-graining in phase space, he postulated that the equilibria would be the states maximizing the entropy calculated by counting all the possible "microscopic" (i.e. fine-grained) distribution compatible with the conservation laws of the Vlasov-Poisson system. One of the striking features of this theory was that it could lead, in the so-called "non-degenerate" limit, to an isothermal sphere type solution — with, however, equipartition of kinetic energy *per unit mass* (because it is a mean field theory in which the distribution of mass is independent of particle mass), i.e. it could account for isothermal type equilibria without segregation of stars according to their masses.

However, despite the fact that Lynden-Bell's explanation of mean-field relaxation became a cornerstone of the understanding of the dynamics of self-gravitating systems, his statistical theory was rapidly abandoned in astrophysics: it did not appear to be adequate to explain the (non isothermal) properties of stationary self-gravitating system either as observed in astrophysical systems or in numerical simulations (whose size and sophistication increased through the 70s and 80s). Further the theory, as we will discuss, involves several difficulties which make its practical relevance in astrophysics questionable — notably the prediction of the theory are made in terms of quantities which are, practically, not observable in this context. The fact that its prediction are extremely complicated to derive probably also led to its neglect (once it was clear that it was not a strictly "correct" theory).

The motivations for reconsidering in detail this theory have been briefly outlined in our introduction. In the context of the statistical mechanics of long-range interaction system, interest in Lynden-Bell theory has been revived notably by studies showing it to explain quite well the properties of stationary states resulting from violent relaxation in a toy 1D model [72]. More recently studies of both 3D and 2D self-gravitating systems, by Levin et al. [37, 93], have reported results showing Lynden-Bell theory to work well in certain parts of the relevant parameter space of initial conditions. Likewise a study of 1D gravity [95] has come to similar conclusions. In both cases modifications of Lynden-Bell's theory have been proposed to account for the QSS observed in a broader space of initial condition studied. Thus, in this context, Lynden-Bell theory appears as an important reference for understanding the states resulting from violent relaxation, even if it is clearly not a fully adequate theory to account for them. Our work greatly extends the 1D and 3D studies of Levin et al. [37] and Yamaguchi [95], and will be presented in detail in chapter 5 and 6.

In this chapter we review first the original theory of Lynden-Bell (for 3D self-gravitating systems), and give in addition some simple considerations about the evolution of coarse-grained entropy. We then detail in the rest of chapter how we actually calculate the prediction of this theory for the quantities we measure in our simulations (of which the results are reported in chapters 5 and 6). We first consider, in section 3.4, the 1D case as it is considerably simpler than three dimensions (just as we have seen to be the case for the thermodynamics in the previous chapter). Specifically the fact that the 1D potential diverges at large distances means that the theory is well defined without a confining box. In section 3.5 we consider the 3D case, and study in particular the dependence on the confining box required in this case. Our analyses in both these sections extend significantly those presented in previous studies in one dimension [95, 128, 129] and three dimensions [37].

3.1 Estimation of time scale for violent relaxation

In this section we describe the simple estimation of the time scale for violent relaxation given originally by Lynden-Bell [19]. Starting from an out-of-equilibrium initial condition, violent relaxation induces rapid exchange of the individual energy of particles in the fluctuating mean-field. The rate of change of the individual energy ε of each particle is given by

$$\frac{d\varepsilon}{dt} = \vec{\nabla}\varepsilon \cdot \vec{v} + \vec{\nabla}_v\varepsilon \cdot \vec{a} + \frac{\partial \varepsilon}{\partial t} = \frac{\partial \Phi}{\partial t} \tag{3.1}$$

with $\epsilon = \frac{v^2}{2} + \Phi(\vec{x}, t)$. We now define the relaxation time as the time scale at which the fluctuation of energy is of order the total energy:

$$t_{relax} = \left[\frac{(\frac{d\varepsilon}{dt})^2}{\varepsilon^2} \right]^{-\frac{1}{2}}. \tag{3.2}$$

During violent relaxation we estimate the order of magnitudes of the kinetic and potential energy using the virial theorem by

$$2T \sim -U \quad \text{or} \quad U \sim 2E \tag{3.3}$$

which then gives

$$\frac{1}{2}mv^2 \sim -\frac{1}{4}m\Phi \quad \text{and} \quad \varepsilon \sim \frac{3}{4}\Phi. \tag{3.4}$$

The relaxation time then reduces to

$$t_{relax} = \frac{3}{4}\left[\frac{\dot{\Phi}^2}{\Phi^2}\right]^{-\frac{1}{2}}. \tag{3.5}$$

Consider now the 3D non-equilibrium form of virial theorem (1.28). Using it with the approximation (3.3), we have

$$\frac{1}{2}\frac{d^2I}{dt^2} = 2T + U \approx 2E - U$$

where I is the moment of inertia. Let us define R as an effective radius by taking

$$U = -\frac{GM^2}{R}, \tag{3.6}$$

and write the moment of inertia

$$I = \lambda^2 M R^2. \tag{3.7}$$

If the shape of the structure is only slightly deformed during the evolution, λ is approximately constant. Taking the second derivative of I, the virial theorem becomes then

$$\lambda^2(R\ddot{R} + (\dot{R})^2) = \frac{2E}{M} + \frac{GM}{R} \tag{3.8}$$

which is a differential equation for the temporal evolution of R. Considering the perturbative evolution of R about its equilibrium value, i.e. $R = \bar{R}_0 + \delta R(t)$, equation (3.8) becomes

$$\lambda^2 \bar{R}_0 \frac{d^2(\delta R)}{dt^2} = \frac{2E}{M} + \frac{GM}{\bar{R}_0} - \frac{GM}{\bar{R}_0^2}\delta R + \mathcal{O}((\delta R)^2). \tag{3.9}$$

Substituting $\bar{R}_0 = -GM^2/2E$ and omitting the higher order in δR, equation (3.9) then becomes simply

$$\frac{d^2(\delta R)}{dt^2} = -\frac{GM}{2\lambda^2 \bar{R}_0^3}\delta R \tag{3.10}$$

from which we can obtain the angular frequency and the oscillation period

$$\omega^2 = \frac{GM}{2\lambda^2 \bar{R}_0^3} = \frac{2\pi}{3\lambda^2} G\bar{\rho} \tag{3.11}$$

with $\bar{\rho} = M/(\frac{4}{3}\pi R_0^3)$ for the mean density. Recalling the expansion for potential energy given in (3.6), we can estimate that

$$\Phi \simeq -\frac{GM}{NR} \quad \text{and} \quad \dot{\Phi} \simeq -\frac{GM\dot{R}}{NR^2}$$

and the relaxation time is given by

$$t_{relax} = \frac{3}{4}\left[\frac{\dot{R}^2}{R^2}\right]^{-\frac{1}{2}} = \frac{3}{4\omega} = \frac{3}{\lambda}\sqrt{\frac{3}{32\pi G\bar{\rho}}}. \tag{3.12}$$

We notice that the term $\sqrt{3/32\pi G\bar{\rho}}$ is the free-fall time (i.e. the time for a cold uniform mass density to collapse). Since λ is of order unity, the relaxation time is thus of order a few free-fall times and is independent of the particle number N. A more precise estimation of time scale is not feasible but according to many simulations (including ours in chapter 6) the time scales of virialization to QSS are indeed of order a few free-fall times. An investigation of virial oscillations is given in [130]. The free-fall time of a globular cluster is of order $100,000$ years, while it is around 10^8 years for elliptical galaxies. Both are considerably shorter than the age of universe ($\sim 10^{10}$ years).

3.2 Equilibrium of collisionless self-gravitating systems

Consider the distribution function of a system in 6-dimensional one particle phase space divided into a very large number of identical "microcells" of equal volume. The microcells are so fine that the phase space density may be taken uniform inside them and the coordinate of microcells can be treated as continuous. We define the "fine-grained distribution function", $f(\vec{x}, \vec{v})$, to be the phase space density of a microcell centered at (x, v). Its evolution is assumed to be given by (see section 1.1.1)

$$\frac{\partial f}{\partial t} + \vec{v} \cdot \frac{\partial f}{\partial \vec{x}} - \vec{\nabla}\Phi \cdot \frac{\partial f}{\partial \vec{v}} = 0 \tag{3.13}$$

with mean-field potential Φ determined self-consistently by f through the Poisson equation. The conservation of phase space density encoded in the Liouville flow form of this equation implies that the number of microcells with any given values of f is conserved. In terms of conservation laws this property implies, as discussed in section 1.1.1, that energy and mass are conserved, and also the conservation of the Casimir integrals given by

$$I_h = \int_\Omega h(f) d^3x d^3v \tag{3.14}$$

for any continuous function $h(f)$ [131]. The number of Casimir integrals is, in general, infinite.

We suppose now that a number of microcells is grouped together to form a "macrocell", and define the "coarse-grained distribution function", $\bar{f}(\vec{x}, \vec{v})$, to be the phase space density averaged inside the macrocell centered at $(\vec{x}, \vec{v})$ over the corresponding microcells. The size of macrocells is assumed to be small enough so that we can treat the coordinates of them as continuous. In the Lynden-Bell theory we take the observable stationary distribution function to be the coarse-grained one. While equilibrium can never be attained at the fine-grained level because of the reversibility of the Vlasov-Poisson equation, such a coarse-grained distribution function can reach equilibrium. Likewise the conservation of Casimirs does not apply at coarse-grained level (hence they are sometimes referred as the "hidden constraints"). An illustration of the fine-grained and coarse-grained distributions is shown in Fig. 3.1 (for 2-dimensional phase space), in which the small square cells enclosed by thin lines represent the microcells and the groups of 9 microcells enclosed by thick lines are for the macrocells. The filled microcells mean they are "occupied" while the white blank cells are the "unoccupied" cells. The occupied cells with different contrast mean the phase space densities are different in each.

3.2.1 Distribution function at equilibrium

We will determine the distribution function at equilibrium of the coarse-grained distribution function. For simplicity we deal with a system that has a single value of the fine-grained phase space density, f_0. This single level system has the advantage that all Casimirs depend only on f_0 and their conservation is thus encoded in the constraint that the number of "occupied" microcells is constant. We suppose that all micro-cells have the same size equal to ω and all macrocells are equally composed of n microcells. We define n_i to be number of occupied microcells (with $n_i \leq n$) in the macrocell i, so the number of states of arranging n_i in the macrocell i is

$$\frac{n!}{(n - n_i)!} \tag{3.15}$$

in which we suppose that all cells are distinguishable. The mass of the occupied microcell is thus ωf_0. The total number of states of distributing N particles (where $N = \sum_i n_i$) into a number

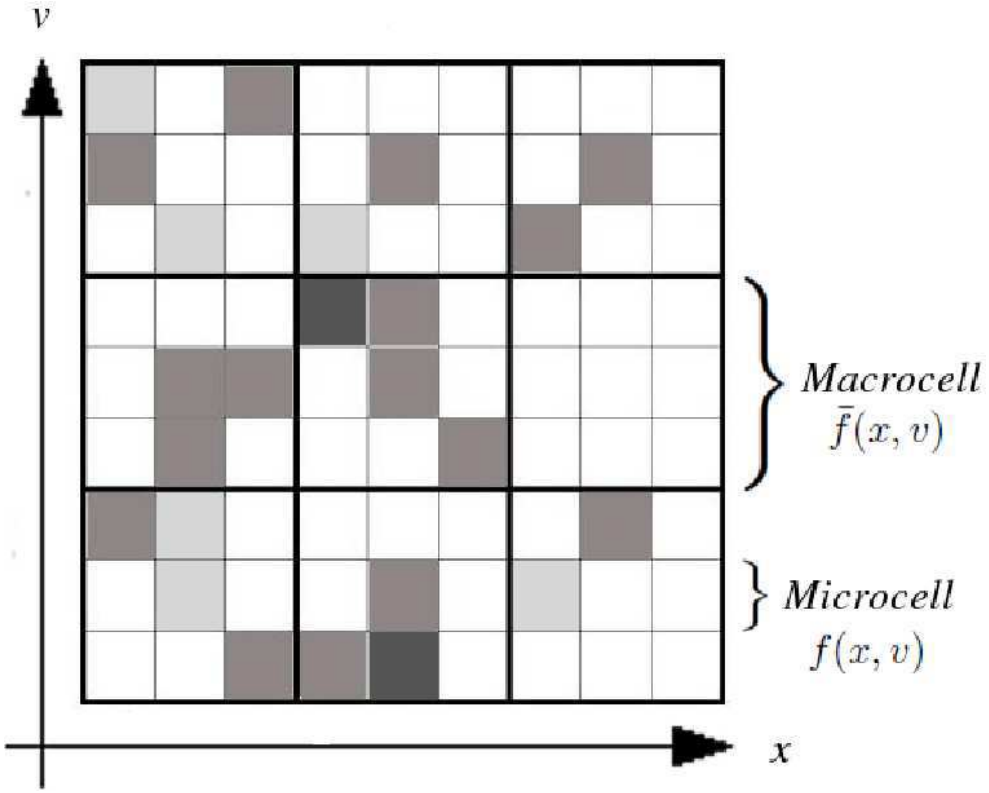

Figure 3.1: An example of distribution function in 2-dimensional phase space (x, v). The cells enclosed by thin lines are the microcells associated to the fine-grained distribution function, $f(x, v)$. The groups of adjacent microcells enclosed by thick lines are the macrocells associated to the coarse-grained distribution function $\bar{f}(x, v)$. The different grey tones indicates the different phase space densities.

of macrocells is

$$W = \frac{N!}{\prod_i n_i!} \times \prod_i \frac{n!}{(n-n_i)!}. \tag{3.16}$$

The total mass of system is then equal to $M = N\omega f_0$. In the large N limit, we put N, n_i and $n \gg 1$ so that we can apply Stirling's approximation. The coarse-grained entropy is then given by

$$\ln W \simeq N(\ln N - 1) - \sum_i \Big[n_i(\ln n_i - 1) + (n - n_i)\{\ln(n - n_i) - 1\} - n(\ln n - 1) \Big] \tag{3.17}$$

We define the continuous coarse-grained distribution function

$$\bar{f}(\vec{x}, \vec{v}) \equiv \frac{n_i f_0}{n} \tag{3.18}$$

and change $\sum_i \to \int \frac{d^3x d^3v}{n\omega}$, so the coarse-grained entropy becomes

$$\begin{aligned} \ln W \quad &\simeq \quad N(\ln N - 1) \\ &- \int \Big[\bar{f}(\ln(\frac{n\bar{f}}{f_0}) - 1) + (f_0 - \bar{f})\{\ln(n - \frac{n\bar{f}}{f_0}) - 1\} + f_0(\ln n - 1) \Big] \frac{d^3x d^3v}{f_0 \omega} \end{aligned} \tag{3.19}$$

which is evidently different from the Boltzmann entropy. The coarse-grained distribution function at equilibrium can be obtained by maximizing (3.19) with the two additional constraints

$$M = \int \bar{f}(\vec{x},\vec{v})d^3xd^3v \tag{3.20a}$$

$$E = \int \frac{v^2}{2}\bar{f}(\vec{x},\vec{v})d^3xd^3v - \frac{G}{2}\int \frac{\bar{f}(\vec{x},\vec{v})\bar{f}(\vec{x}',\vec{v}')}{|\vec{x}-\vec{x}'|}d^3xd^3vd^3x'd^3v'. \tag{3.20b}$$

We define two Lagrange multipliers μ and β (or for simplicity, we prefer to use $-\mu\beta/f_0\omega$ and $\beta/f_0\omega$). First variation yields

$$\delta S - \frac{\mu\beta}{f_0\omega}\delta M + \frac{\beta}{f_0\omega}\delta E = -\int \frac{d^3xd^3v}{f_0\omega}\delta\bar{f}\left[\ln\left[\frac{\bar{f}}{f_0-\bar{f}}\right] - \mu\beta + \beta\varepsilon(\vec{x},\vec{v})\right] \tag{3.21}$$

with

$$\varepsilon(\vec{x},\vec{v}) \equiv \frac{v^2}{2} + \Phi(\vec{x}) = \frac{v^2}{2} - G\int \frac{\bar{f}(\vec{x}',\vec{v}')}{|\vec{x}-\vec{x}'|}d^3x'd^3v' \tag{3.22}$$

denoting the energy density of phase space element located at $(\vec{x},\vec{v})$. Equating the left-hand-side of (3.21) to 0, the distribution function of equilibrium is given by

$$\bar{f}(\vec{x},\vec{v}) = \frac{f_0}{1+e^{\beta(\varepsilon(\vec{x},\vec{v})-\mu)}}. \tag{3.23}$$

The fact that the equilibrium configuration (3.23) takes the form of Fermi-Dirac distribution arises from the exclusion principle we impose in the microcell arrangement. The conservation of phase space volume thus excludes the possibility of a singularity in phase space. Analyses of the thermodynamic properties of the LB distribution function (3.23) have been reported in [132, 133, 134]. They were also extended to the cases in d dimensions in [135] and with rotation in [136]. The more general case with continuous fine-grained density value, the memory function is employed (see [137, 21] for example). The predictions of LB theory for 3D gravity have been discussed at length by Chavanis. Notably an analysis in [132] determined the diagram of stability of LB equilibria as function of E and R_c. The extension including the rotational motion is given in [136] and to any number of spatial dimension d in [135]. Phase transition is also discussed in [134].

Non-degenerate limit

The non-degenerate (or dilute) limit is obtained by taking $e^{-\beta\mu} \to \infty$ and $\beta \to 0$ (i.e. "temperature" goes to infinity) so that the distribution function (3.23) reduces to

$$\bar{f}_{nd} \simeq f_0 e^{-\beta(\varepsilon-\mu)} \ll f_0. \tag{3.24}$$

In this limit we recover the isothermal sphere distribution (see section 2.1) but β is an inverse "temperature" which is independent of mass. In the astrophysical literature this dilute limit has often been used in considering LB theory (see for example [138, 139]).

Degenerate limit

The degenerate limit of (3.23) is the case where $\beta \to \infty$ and the distribution function becomes

$$\bar{f}_d(\vec{x},\vec{v}) = \begin{cases} f_0 & , \quad \varepsilon(\vec{x},\vec{v}) \le \mu \\ 0 & , \quad \varepsilon(\vec{x},\vec{v}) > \mu \end{cases} \tag{3.25}$$

with μ equivalent to the Fermi energy for a fermionic gas. Using (3.25) with the Poisson equation in three dimensions gives

$$\frac{1}{r^2}\frac{\partial}{\partial r}(r^2\frac{\partial\Phi}{\partial r}) = (4\pi)^2 f_0 G\int_0^{\sqrt{2(\mu-\Phi)}} v^2 dv = \frac{(4\pi)^2 2^{\frac{3}{2}}}{3} f_0 G(\mu-\Phi)^{\frac{3}{2}}. \tag{3.26}$$

Defining dimensionless variables

$$\psi \equiv \frac{\mu-\Phi}{G^2 f_0^{\frac{2}{3}} M^{\frac{4}{3}}} \quad \text{and} \quad \xi \equiv \frac{4\cdot 2^{\frac{3}{4}}\pi}{3^{\frac{1}{2}}} G f_0^{\frac{3}{2}} M^{\frac{1}{3}} r, \tag{3.27}$$

(3.27) simplifies to

$$\frac{1}{\xi^2}\frac{\partial}{\partial\xi}(\xi^2\frac{\partial\psi}{\partial\xi}) + \psi^{\frac{3}{2}} = 0 \tag{3.28}$$

which takes the form of the Lane-Emden equation with polytropic index equal to $\frac{3}{2}$ (see section 1.1.4). There is no analytical solution for this case so we trace it using numerical integration. $\psi(\xi)$ is plotted in Fig. 3.2 (left), where we have imposed the boundary condition $\psi(0) = 1$ and $\psi'(0) = 0$. We truncate the solution when the curve cuts the x-axis (at which $\psi = \mu$) and the cut-off radius is calculated to be $\xi_c = 3.65$ (for larger ξ, the solution is unphysical because the density is negative). As $n < 5$, the solution thus has finite mass. We also plot

$$\tilde{\rho}_d(\xi) = -\frac{1}{\xi^2}\frac{\partial}{\partial\xi}(\xi^2\frac{\partial\psi}{\partial\xi})$$

for the dimensionless density distribution as well as

$$\tilde{M}_d(\xi) = \xi^2\tilde{\rho}_d(\xi)$$

for the dimensionless mass distribution together in Fig. 3.2 (right). The full derivation of the degenerate solution (also the generalization to d dimensions) is considered in [135, 111]. Further the extension of the King model implementing the effect of degeneracy from the LB theory was also proposed in [140].

Stationary state with non-zero angular momentum

For system with total angular momentum given by

$$\vec{J} = \int \bar{f}\vec{x}\times\vec{v}d^3xd^3v, \tag{3.29}$$

there is an additional constraint to which one associates the vectorial Lagrange multiplier $-\beta\vec{\Omega}/f_0\omega$. The first variation equation becomes

$$0 = \delta S - \frac{\mu\beta}{f_0\omega}\delta M + \frac{\beta}{f_0\omega}\delta E - \frac{\beta\vec{\Omega}}{f_0\omega}\cdot\delta\vec{J} = -\int\frac{d^3xd^3v}{f_0\omega}\delta\bar{f}\left[\ln\left[\frac{\bar{f}}{f_0-\bar{f}}\right] - \mu\beta + \beta\varepsilon(\vec{x},\vec{v}) - \beta\vec{\Omega}\cdot(\vec{x}\times\vec{v})\right] \tag{3.30}$$

leading to the the solution

$$\bar{f}(\vec{x},\vec{v}) = \frac{f_0}{1+e^{\beta(\varepsilon(\vec{x},\vec{v})-\mu-(\vec{\Omega}\times\vec{x})\cdot\vec{v})}}. \tag{3.31}$$

We will consider here only the initial condition without angular momentum for simplicity.

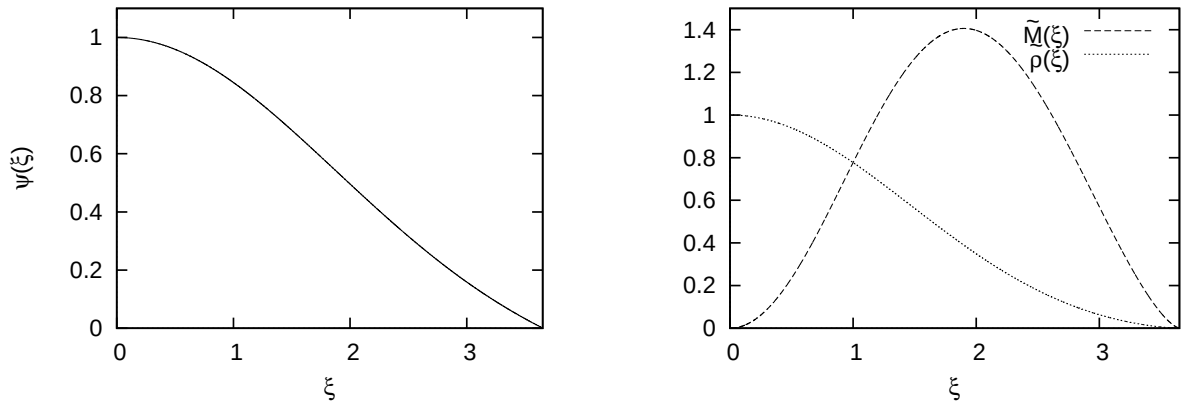

Figure 3.2: $\psi(\xi)$ (left panel), $\tilde{\rho}_d(\xi)$ and $\tilde{M}_d(\xi)$ (right panel) for the Lynden-Bell degenerate limit of 3D gravity. The boundary conditions are $\psi(0) = 1$ and $\psi'(0) = 0$. The cut-off radius, ξ_c, is equal to 3.65.

System with non-single valued phase space densities

We consider now the more general case where the system with many fine-grained phase space density values. Each phase space density value is denoted by f_0^j. Denoting by n_i^j the number of occupied cells with phase space density f_0^j inside the macrocell i, the number of ways of arranging n_i^j for all j in the macrocell i (supposed non-overlapping) is

$$\frac{n!}{(n - \sum_j n_i^j)!}$$

with $\sum_j n_i^j \leq n$. Defining N_j to be the total occupied cells of phase space density f_0^j, the total number of states from all j reads

$$W = \prod_j \frac{N^j!}{\prod_i n_i^j!} \times \prod_i \frac{n!}{(n - \sum_j n_i^j)!}. \tag{3.32}$$

Hence the total mass from all cells with f_0^j is $M^j = N^j f_0^j \omega$. Using Stirling's formula the entropy becomes

$$\begin{aligned} \ln W \simeq & \sum_j N^j (\ln N^j - 1) - \sum_j \sum_i n_i^j (\ln n_i^j - 1) \\ & + \sum_i [n(\ln n - 1) - (n - \sum_j n_i^j)(\ln(n - \sum_j n_i^j) - 1)]. \end{aligned} \tag{3.33}$$

Defining the coarse-grained phase space density in macro-cell i located at $(\vec{x}, \vec{v})$ measured only from the cells with f_0^j as

$$\bar{f}^j(\vec{x}, \vec{v}) = \frac{n_i^j f_0^j}{n} \tag{3.34}$$

and the combined coarse-grained phase space density for all j as

$$\bar{f}(\vec{x},\vec{v}) = \sum_j \bar{f}^j(\vec{x},\vec{v}) = \sum_j \frac{n_i^j f_0^j}{n} \tag{3.35}$$

The constraints requiring the total energy and M^j to be individually conserved are

$$M^j = \int \bar{f}^j(\vec{x},\vec{v}) d^3x d^3v \qquad \text{for all } j \tag{3.36a}$$

$$E = \int \frac{v^2}{2} \bar{f}(\vec{x},\vec{v}) d^3x d^3v - \frac{G}{2} \int \frac{\bar{f}(\vec{x},\vec{v})\bar{f}(\vec{x}',\vec{v}')}{|\vec{x}-\vec{x}'|} d^3x d^3v d^3x' d^3v'. \tag{3.36b}$$

Maximizing (3.33) subject to (3.36a) and (3.36b) with corresponding Lagrange's multiplier μ^j and β gives

$$\bar{f}^j(\vec{x},\vec{v}) = \frac{f_0^j e^{-\beta^j(\varepsilon-\mu^j)}}{1+\sum_j [e^{-\beta^j(\varepsilon-\mu^j)}]} \tag{3.37}$$

for the equilibrium distribution function of an individual component with

$$\beta^j = \frac{f_0^j}{\bar{f}_0}\beta \quad \text{and} \quad \bar{f}_0 = \frac{\sum_j f_0^j M^j}{\sum_j M^j} \tag{3.38}$$

and thus

$$\bar{f}(\vec{x},\vec{v}) = \frac{\sum_j [f_0^j e^{-\beta^j(\varepsilon-\mu^j)}]}{1+\sum_j e^{-\beta^j(\varepsilon-\mu^j)}}. \tag{3.39}$$

In the non-degenerate limit, the distribution function of the component j reduces to

$$\bar{f}_{nd}^j \simeq f_0^j e^{\beta^j \mu^j} e^{-\beta^j \varepsilon} \tag{3.40}$$

and the equilibrium therefore becomes

$$\bar{f}_{nd} \simeq \sum_j A^j e^{-\beta^j \varepsilon} \tag{3.41}$$

with constant

$$A^j = f_0^j e^{\beta^j \mu^j}$$

related to M^j via μ^j. The equilibrium profile in this limit is thus simply the superposition of Maxwellians with their corresponding β^j inversely proportional to the phase space density f_0^j, implying a different distribution for different components. Each Maxwellian is also weighted by A^j related to the total mass of the component j. This feature was criticized by Shu [141, 142], who proposed a "particulate" description instead of continuum description, and later by Nakamura [143], using an approach based on information theory. Their alternative versions led to equilibrium stationary states resulting from collisionless evolution in which the velocity distribution is a simple Maxwellian.

3.3 H-functions and increase of entropy

The Lynden-Bell equilibrium distribution function is derived on a coarse-grained scale. In this section we discuss (following [144]) the derivation of how the associated coarse-grained entropy increases. Given the fine-grained distribution function $f(\vec{x}, \vec{v}, t)$, the coarse-grained distribution function is defined by

$$F(\vec{x}, \vec{v}, t) = \frac{1}{(\Delta x \Delta v)^3} \int\limits_{\Delta\vec{x}, \Delta\vec{v}} d^3x' d^3v' f(\vec{x'}, \vec{v'}, t) \tag{3.42}$$

representing the averaged fine-grained distribution function in a microcell of volume $(\Delta x \Delta v)^3$ centered at $(\vec{x}, \vec{v})$. We consider the H-function given by

$$H[F] = -\int C(F) d^3x d^3v \tag{3.43}$$

where $C(F)$ is arbitrary convex function of F and $C(0) = 0$. The entropy of LB is a specific case of such a H-function.

Such a H-function for any fine-grained distribution function thus corresponds to the Casimir integrals defined in (1.19) and it follows (as shown in chapter 1) that

$$\frac{dH[f]}{dt} = \int \frac{dC(f)}{dt} d^3x d^3v = 0.$$

Any fine-grained entropy defined in this way is thus always constant in time and, indeed at the fine-grained level, the system can never reach an equilibrium. Now we consider the evolution of the coarse-grained H-function

$$H(t_2) - H(t_1) = \int d^3x d^3v [C(F(\vec{x}, \vec{v}, t_1)) - C(F(\vec{x}, \vec{v}, t_2))] \tag{3.44}$$

with $t_2 > t_1$. If we suppose that at time t_1 the distribution function starts with fine-grained structure, equation (3.44) becomes

$$\Delta H = \int d^3x d^3v [C(f(\vec{x}, \vec{v}, t_1)) - C(F(\vec{x}, \vec{v}, t_2))]. \tag{3.45}$$

Considering ΔH in a single macrocell, labeled by j, composed of K microcells, labeled by i from 1 to K, with equal size, the change of H-function in this macrocell is

$$\Delta H^j = \frac{(\Delta x \Delta v)^3}{K} \sum_i^K \left[C(f_i) - C(\sum_i^K \frac{f_i}{K}) \right] = (\Delta x \Delta v)^3 \left[\frac{1}{K} \sum_i^K C(f_i) - C(\sum_i^K \frac{f_i}{K}) \right]. \tag{3.46}$$

Using the property of convex functions that

$$C(\frac{\sum_i^N f_i}{N}) \leq \sum_i^N C(f_i)$$

we then deduce from equation (3.46) that $\Delta H^j \geq 0$. The sum of ΔH_j over all j is thus always greater or equal to 0. In conclusion, the coarse-grained entropy can increase, and when the

maximum of coarse-grained entropy is attained the system is at equilibrium. Let us consider the equilibrium obtained from the maximization of *any* $H[F]$ subject to the conservation of the coarse-grained mass and energy

$$M = \int F(\vec{x},\vec{v})d^3xd^3v \quad \text{and} \quad E = \int F(\vec{x},\vec{v})\varepsilon d^3xd^3v$$

where $\varepsilon = \frac{v^2}{2} + \frac{\Phi(\vec{x})}{2}$ is the energy density of phase space element at $(\vec{x},\vec{v})$. The first variation of $H(F)$ yields

$$\delta H = \int \delta F\Big[\frac{dC(F)}{dF} + \alpha + \beta\varepsilon\Big]d^3xd^3v \tag{3.47}$$

from which the equilibrium solution is determined with $\delta H = 0$ as

$$\frac{dC(F)}{dF} + \alpha + \beta\varepsilon = 0. \tag{3.48}$$

Taking the derivative with respect to F on (3.48), we have

$$\frac{d^2C(F)}{dF^2} = -\beta\frac{d\varepsilon}{dF}. \tag{3.49}$$

As $\frac{d^2C(F)}{dF^2} \geq 0$ for a convex function, and we suppose that β is a positive constant, the term $\beta\frac{d\varepsilon}{dF}$ must be less than or equal to 0. This implies that given any convex function $C(F)$, there exists a corresponding stationary state $F(\varepsilon)$ which is a decreasing function of ε. Or in other words, for any stationary state with coarse-grained distribution function $F(\varepsilon)$ non-increasing with ε, there exists an associated convex function $C(F)$ that maximizes the H-function. The Lynden-Bell entropy (3.19) is of course only one particular H-function.

3.4 Predictions of LB theory for measurable quantities in 1D gravity

This section explains how to calculate the prediction of LB theory in the 1D sheet model. We restrict ourselves to initial conditions with uniform initial phase space density equal to f_0 (known as "waterbag" initial conditions). The predictions in this section will be compared with numerical simulations in chapter 5.

3.4.1 Determination of μ and β

In one dimension the LB distribution function derived above reduces to

$$\bar{f}(x,v) = \frac{f_0}{1 + e^{\beta(\varepsilon(x,v)-\mu)}} \tag{3.50}$$

with

$$\varepsilon(x,v) = \frac{v^2}{2} + \Phi(x) \tag{3.51}$$

and $\Phi(x)$ is the mean-field potential at x given by

$$\Phi(x) = g\int \bar{f}(x',v')|x-x'|dv'dx'. \tag{3.52}$$

The two Lagrange multipliers μ and β are determined according to the constraints of the mass and energy conservation

$$M = f_0 \int_{-\infty}^{\infty}\int_{-\infty}^{\infty} \frac{dxdv}{1+e^{\beta(\frac{v^2}{2}+\Phi(x)-\mu)}} \tag{3.53a}$$

$$E = f_0 \int_{-\infty}^{\infty}\int_{-\infty}^{\infty} \frac{(\frac{v^2}{2}+\Phi(x))dxdv}{1+e^{\beta(\frac{v^2}{2}+\Phi(x)-\mu)}}. \tag{3.53b}$$

For simplicity, we use the virial theorem which implies $E = 3T$ (which, as we have seen in section 1.2.2, is valid for any stationary state). Supposing also inversion symmetry in both x and v, the constraints (3.53a) and (3.53b) become

$$M = 4f_0 \int_{0}^{\infty}\int_{0}^{\infty} \frac{dxdv}{1+e^{\beta(\frac{v^2}{2}+\Phi(x)-\mu)}} \tag{3.54a}$$

$$E = 6f_0 \int_{0}^{\infty}\int_{0}^{\infty} \frac{v^2dxdv}{1+e^{\beta(\frac{v^2}{2}+\Phi(x)-\mu)}}. \tag{3.54b}$$

Defining

$$a(\Phi) = \frac{d\Phi}{dx} \tag{3.55}$$

we rewrite the Poisson equation as

$$\frac{da(\Phi)}{dx} = \frac{d(\frac{1}{2}a^2(\Phi))}{d\Phi} = 2g\rho(\Phi) \quad \text{or} \quad a(\Phi) = \sqrt{4g\int_0^{\Phi}\rho(\Phi')d\Phi'} \tag{3.56}$$

with $\rho(\Phi)$ obtained from

$$\rho(\Phi) = 2f_0 \int_{0}^{\infty} \frac{dv}{1+e^{\beta(\frac{v^2}{2}+\Phi-\mu)}} \tag{3.57}$$

with boundary conditions $\Phi(0) = 0$ and $\Phi'(0) = 0$. Changing the coordinate from x to Φ, the equations (3.54a) and (3.54b) are

$$M = 4f_0 \int_{0}^{\infty}\int_{0}^{\infty} \frac{1}{a(\Phi)}\cdot\frac{dvd\Phi}{1+e^{\beta(\frac{v^2}{2}+\Phi-\mu)}} \tag{3.58a}$$

$$E = 6f_0 \int_{0}^{\infty}\int_{0}^{\infty} \frac{1}{a(\Phi)}\cdot\frac{v^2dvd\Phi}{1+e^{\beta(\frac{v^2}{2}+\Phi-\mu)}}. \tag{3.58b}$$

The aim of this section is to determine μ and β corresponding to given M and E. To do this, we consider M and E as functions of μ and β and define M_0 and E_0 to be the correct mass and energy. We define two functions

$$F(\mu,\beta) \equiv M_0 - M(\mu,\beta) = M_0 - 4f_0 \int_0^{\infty}\int_0^{\infty} \frac{dvd\Phi}{a(\Phi)[1+e^{\beta(\frac{v^2}{2}+\Phi-\mu)}]} \tag{3.59a}$$

$$G(\mu,\beta) \equiv E_0 - E(\mu,\beta) = E_0 - 6f_0 \int_0^{\infty}\int_0^{\infty} \frac{v^2dvd\Phi}{a(\Phi)[1+e^{\beta(\frac{v^2}{2}+\Phi-\mu)}]}. \tag{3.59b}$$

so that at the correct values of μ and β, we have

$$F(\beta,\mu)=0 \quad \text{and} \quad G(\beta,\mu)=0.$$

Given a pair of guessed μ and β, we make the iteration to the right value by employing the Newton-Raphson method which yields the matrix equation

$$\begin{pmatrix} dF(\beta,\mu) \\ \\ dG(\beta,\mu) \end{pmatrix} = \begin{pmatrix} \frac{\partial F}{\partial \beta} & \frac{\partial F}{\partial \mu} \\ \\ \frac{\partial G}{\partial \beta} & \frac{\partial G}{\partial \mu} \end{pmatrix} \begin{pmatrix} d\beta \\ \\ d\mu \end{pmatrix} \tag{3.60}$$

where dF and dG denote the infinitesimal changes of F and G when (β,μ) change to $(\beta+d\beta,\mu+d\mu)$. To determine the new $\mu\to\mu+\Delta\mu$ and $\beta\to\beta+\Delta\beta$, we use the relation

$$\begin{pmatrix} \Delta\beta \\ \\ \Delta\mu \end{pmatrix} = \begin{pmatrix} \frac{\partial F}{\partial \beta} & \frac{\partial F}{\partial \mu} \\ \\ \frac{\partial G}{\partial \beta} & \frac{\partial G}{\partial \mu} \end{pmatrix}^{-1} \begin{pmatrix} \Delta F(\mu,\beta) \\ \\ \Delta G(\mu,\beta) \end{pmatrix} \tag{3.61}$$

in which $\Delta F(\mu,\beta)$ and $\Delta G(\mu,\beta)$ are simply $-F(\mu,\beta)$ and $-G(\mu,\beta)$ respectively. The elements of the Jacobian matrix in (3.61) are given by

$$\frac{\partial G}{\partial \beta}=-\frac{\partial E}{\partial \beta} = 6f_0\int_0^\infty\int_0^\infty \frac{v^2(\frac{v^2}{2}+\Phi-\mu)e^{\beta(\frac{v^2}{2}+\Phi-\mu)}}{a(\Phi)[1+e^{\beta(\frac{v^2}{2}+\Phi-\mu)}]^2}dvd\Phi \tag{3.62a}$$

$$\frac{\partial G}{\partial \mu}=-\frac{\partial E}{\partial \mu} = -6f_0\beta\int_0^\infty\int_0^\infty \frac{v^2e^{\beta(\frac{v^2}{2}+\Phi-\mu)}}{a(\Phi)[1+e^{\beta(\frac{v^2}{2}+\Phi-\mu)}]^2}dvd\Phi \tag{3.62b}$$

$$\frac{\partial F}{\partial \beta}=-\frac{\partial M}{\partial \beta} = 4f_0\int_0^\infty\int_0^\infty \frac{(\frac{v^2}{2}+\Phi-\mu)e^{\beta(\frac{v^2}{2}+\Phi-\mu)}}{a(\Phi)[1+e^{\beta(\frac{v^2}{2}+\Phi-\mu)}]^2}dvd\Phi \tag{3.62c}$$

$$\frac{\partial F}{\partial \mu}=-\frac{\partial M}{\partial \mu} = -4f_0\beta\int_0^\infty\int_0^\infty \frac{e^{\beta(\frac{v^2}{2}+\Phi-\mu)}}{a(\Phi)[1+e^{\beta(\frac{v^2}{2}+\Phi-\mu)}]^2}dvd\Phi \tag{3.62d}$$

which are all calculated numerically. Iteration is stopped once precision conditions

$$\left|\frac{M(\mu,\beta)-M_0}{M_0}\right|\le\delta \quad \text{and} \quad \left|\frac{E(\mu,\beta)-E_0}{E_0}\right|\le\delta \tag{3.63}$$

are satisfied. For the results reported here, we take $\delta=10^{-3}$. At each iteration, we have to integrate for M, E and 4 elements in Jacobian matrix which consumes most of computation time. If we choose initial β and μ not too far from the right values, they can converge within a few iterations. An example of the determination of β and μ (in arbitrary unit) is shown in Fig. 3.3, in which the number of the iteration is marked beside the corresponding point in (μ,β) plane. The unnumbered point corresponds to the guessed initial values and the calculation is terminated within 4 iterations (for $\delta=10^{-3}$).

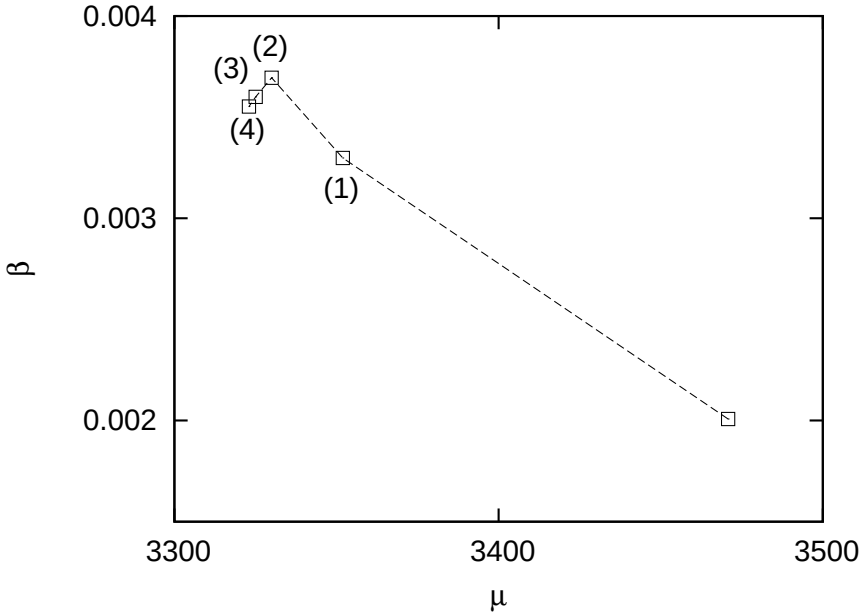

Figure 3.3: (μ, β) plane showing the convergence to the solution (i.e. $M(\mu,\beta) \to M_0$ and $E(\mu,\beta) \to E_0$) by Newton-Raphson method with Jacobian matrix elements given in (3.62a)-(3.62d). The calculation finishes with 4 iterations where the condition (3.63) is fulfilled with $\delta = 10^{-3}$.

3.4.2 Non-degenerate limit

As noted in section 3.2.1, this limit corresponds to $e^{-\beta\mu} \to \infty$ and $\beta \to 0$ so that

$$\bar{f} \approx f_0 e^{-\beta\varepsilon} e^{\beta\mu} \ll f_0 \quad \text{where} \quad \varepsilon = \frac{1}{2}v^2 + \Phi(x). \tag{3.64}$$

The density distribution as a function of Φ is then given by

$$\rho(\Phi) = f_0^{\beta\mu} e^{-\beta\Phi} \int_{-\infty}^{\infty} e^{-\beta\frac{v^2}{2}} dv = f_0 \sqrt{\frac{2\pi}{\beta}} e^{\beta\mu} e^{-\beta\Phi} \tag{3.65}$$

and $a(\Phi)$ by

$$a(\Phi) = \left[4g f_0 \sqrt{\frac{2\pi}{\beta}} e^{\beta\mu} \int_0^{\Phi} e^{-\beta\Phi'} d\Phi'\right]^{\frac{1}{2}} = \left[4g f_0 \sqrt{\frac{2\pi}{\beta^3}} e^{\beta\mu} (1 - e^{-\beta\Phi})\right]^{\frac{1}{2}}. \tag{3.66}$$

Hence the total mass is equal to

$$M = e^{\frac{\beta\mu}{2}} \left(\frac{2\pi}{\beta}\right)^{\frac{1}{4}} \sqrt{\frac{\beta f_0}{g}} \int_0^{\infty} \frac{e^{-\beta\Psi} d\Phi}{(1 - e^{-\beta\Phi})^{\frac{1}{2}}} = \left(\frac{32\pi f_0^2}{\beta^3 g^2}\right)^{\frac{1}{4}} e^{\frac{\beta\mu}{2}}. \tag{3.67}$$

Using the virial theorem, the total energy is

$$\begin{aligned} E &= 6f_0 e^{\beta\mu}\int_0^\infty v^2 e^{-\beta\frac{v^2}{2}}dv\int_0^\infty \frac{e^{-\beta\Phi}d\Phi}{a(\Phi)} = \frac{3}{2}\Big(\frac{2\pi}{\beta}\Big)^{\frac{1}{4}}\sqrt{\frac{f_0}{g\beta}}e^{\frac{\beta\mu}{2}}\int_0^\infty \frac{e^{-\beta\Phi}d\Phi}{(1-e^{-\beta\Phi})^{\frac{1}{2}}} \\ &= \frac{3}{\beta}\sqrt{\frac{f_0}{g}}\Big(\frac{2\pi}{\beta^3}\Big)^{\frac{1}{4}}e^{\frac{\beta\mu}{2}}. \end{aligned} \tag{3.68}$$

From (3.67) and (3.68), β can be determined by

$$\frac{E}{M} = \frac{3}{2\beta}. \tag{3.69}$$

The expression (3.69) is identical to (2.146). The non-degenerate limit of the collisionless equilibrium predicted by Lynden-Bell theory thus corresponds exactly to the thermal equilibrium (in this case).

3.4.3 Degenerate limit

As noted above the degenerate limit corresponds to $\beta \to \infty$ in which the distribution reduces to

$$\bar{f}(x,v) = \begin{cases} f_0 & , \quad \varepsilon \le \mu \\ 0 & , \quad \varepsilon > \mu \end{cases} \tag{3.70}$$

with μ analogous to the Fermi energy in a fermionic gas. The density distribution as a function of Φ is then given by

$$\rho(\Phi) = 2f_0\int_0^{\sqrt{2(\mu-\Phi)}} dv = 2\sqrt{2}f_0(\mu-\Phi)^{\frac{1}{2}} \tag{3.71}$$

and $a(\Phi)$ by

$$a(\Phi) = \Big[8\sqrt{2}gf_0\int_0^\Phi(\mu-\Phi')^{\frac{1}{2}}d\Phi'\Big]^{\frac{1}{2}} = 2^{\frac{9}{4}}(\frac{gf_0}{3})^{\frac{1}{2}}\big[\mu^{\frac{3}{2}}-(\mu-\Phi)^{\frac{3}{2}}\big]^{\frac{1}{2}}. \tag{3.72}$$

The total mass is

$$\begin{aligned} M &= 2^{\frac{1}{4}}(\frac{3f_0}{g})^{\frac{1}{2}}\int_0^\mu \frac{(\mu-\Phi)^{\frac{1}{2}}d\Phi}{\big[\mu^{\frac{3}{2}}-(\mu-\Phi)^{\frac{3}{2}}\big]^{\frac{1}{2}}} = 2^{\frac{5}{4}}(\frac{f_0}{3g})^{\frac{1}{2}}\int_{\Phi=0}^{\Phi=\mu}\frac{d\big[\mu^{\frac{3}{2}}-(\mu-\Phi)^{\frac{3}{2}}\big]}{\big[\mu^{\frac{3}{2}}-(\mu-\Phi)^{\frac{3}{2}}\big]^{\frac{1}{2}}} \\ &= 2^{\frac{9}{4}}(\frac{f_0}{3g})^{\frac{1}{2}}\mu^{\frac{3}{4}} \end{aligned} \tag{3.73}$$

and the total energy

$$\begin{aligned} E &= 6f_0\int_0^\mu\int_0^{\sqrt{2(\mu-\Phi)}}\frac{v^2dvd\Phi}{a(\Phi)} = 2^{\frac{1}{4}}f_0\Big(\frac{3}{gf_0}\Big)^{\frac{1}{2}}\int_0^\mu\frac{(\mu-\Phi)^{\frac{3}{2}}d\Phi}{[\mu^{\frac{3}{2}}-(\mu-\Phi)^{\frac{3}{2}}]^{\frac{1}{2}}} \\ &= 2^{\frac{9}{4}}\Big(\frac{f_0}{3g}\Big)^{\frac{1}{2}}\int_0^\mu(\mu^{\frac{3}{2}}-(\mu-\Phi)^{\frac{3}{2}})^{\frac{1}{2}}d\Phi = \frac{2^{\frac{13}{4}}}{3}\Big(\frac{f_0}{3g}\Big)^{\frac{1}{2}}\mu^{\frac{7}{4}}\int_0^1(1-\Psi)^{\frac{1}{2}}\Psi^{-\frac{1}{3}}d\Psi \end{aligned}$$

with $\Psi = (1 - \frac{\Phi}{\mu})^{\frac{3}{2}}$. The integral term above can be rewritten by

$$E = E_D \equiv \frac{2^{\frac{13}{4}}}{3}\Big(\frac{f_0}{3g}\Big)^{\frac{1}{2}} B(\frac{3}{2}, \frac{2}{3})\mu^{\frac{7}{4}} \tag{3.74}$$

where $B(\frac{3}{2}, \frac{2}{3})$ is the corresponding beta function. Using (3.73) we can then determine the energy E_D as a function of M and f_0 only. To determine the density distribution as function of distance, numerical integration is required. Recalling $\partial E/\partial\beta$ from (3.62a), we can rearrange it (using integration by parts) to obtain

$$\frac{\partial E}{\partial \beta} = -\frac{3}{2\beta}\Big[\frac{7E}{3} - \mu M\Big]. \tag{3.75}$$

In the degenerate limit the energy per unit mass is obtained by (3.73) and (3.74) and gives

$$\frac{E}{M} = \frac{2}{3}B(\frac{3}{2}, \frac{2}{3})\mu = 0.74\mu. \tag{3.76}$$

Thus it follows that

$$\lim_{\beta\to\infty} \frac{\partial E}{\partial \beta} \to 0^- \quad \text{and} \quad \lim_{\beta\to\infty} \frac{\partial^2 E}{\partial \beta^2} \to 0^+$$

therefore the degenerate limit corresponds to state with minimum energy at given M and f_0.

It is useful to define the dimensionless quantity

$$\xi_D \equiv \frac{E - E_D}{E_D} \tag{3.77}$$

which we will refer to as the "degeneracy ratio" to measure how far the system is from the degenerate limit. While the LB equilibrium state depends formally, as we have discussed, on the three parameters M, E and f_0, choice of units allows us to fix two of them. The LB equilibrium (for waterbag initial condition) depends therefore on a sole parameter, which we will choose to be ξ_D.

3.4.4 1D Density profile

Recalling equation (3.57), the Poisson equation for the Lynden-Bell distribution function is written

$$\frac{\partial^2 \Phi}{\partial x^2} = 4g f_0 \int_0^\infty \frac{dv}{1 + e^{\beta(\frac{v^2}{2} + \Phi - \mu)}}. \tag{3.78}$$

We solve for $\Phi(x)$ using the 4^{th} order Runge-Kutta method with boundary conditions $\Phi(0) = 0$ and $\Phi'(0) = 0$. Then the density profile is obtained using

$$\rho(x) = \frac{1}{2g}\frac{\partial^2 \Phi(x)}{\partial x^2} \tag{3.79}$$

with the normalization condition

$$\int_{-\infty}^{\infty} \rho(x)dx = M. \tag{3.80}$$

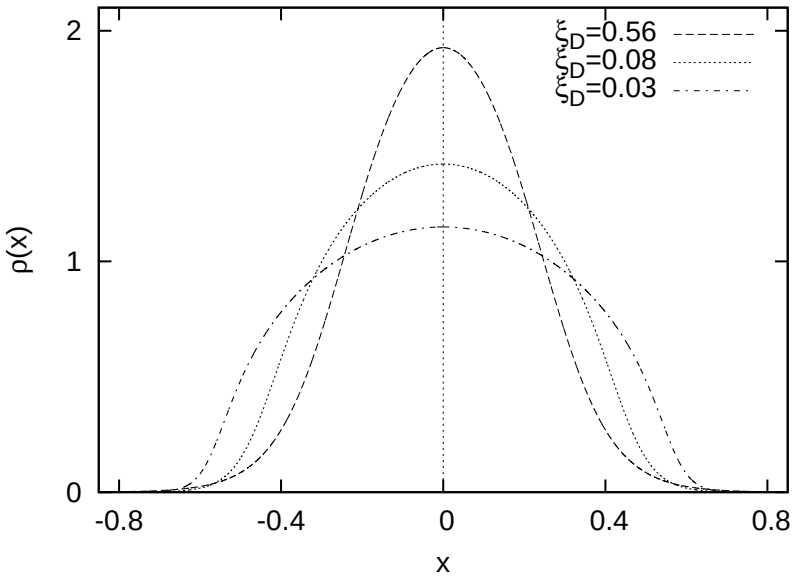

Figure 3.4: $\rho(x)$ predicted from LB theory for different ξ_D.

In general, if we assume the two body potential (1.52), $\Phi(0)$ will take some non-zero value. Note that the choice $\Phi(0) = 0$ has no effect on the density profile.

The examples of $\rho(x)$ are plotted in Fig. 3.4 for a few values of ξ_D (with $M = 1$). We see that at higher ξ_D the predicted density profile is more concentrated and the density drops rapidly with x. For the cases $\xi_D = 0.08$ and 0.03, close to the degenerate limit, the density profiles are less condensed.

3.4.5 1D Velocity distribution

The velocity distribution derived from the Lynden-Bell distribution function is given by

$$\theta(v) = 2f_0 \int_0^\infty \frac{dx}{1 + e^{\beta(\frac{v^2}{2} + \Phi(x) - \mu)}} = 2f_0 \int_0^\infty \frac{d\Phi}{a(\Phi)[1 + e^{\beta(\frac{v^2}{2} + \Phi - \mu)}]} \tag{3.81}$$

where we change the variable in the integration from x to Φ with $a(\Phi)$ as defined in (3.56). In fact the integration over x could be done directly as $\Phi(x)$ can be calculated using the Poisson equation (3.78), but we choose to integrate with Φ (because $a(\Phi)$ is easier to handle because it does not diverge). The normalization condition is

$$\int_{-\infty}^{\infty} \theta(v) dv = M. \tag{3.82}$$

The calculated $\theta(v)$ for the same values of ξ_D as in Fig. 3.4 are shown in Fig. 3.5. The shape of $\theta(v)$ shows the same tendency as $\rho(x)$ above: when ξ_D is lowered, the distribution is less markedly peaked.

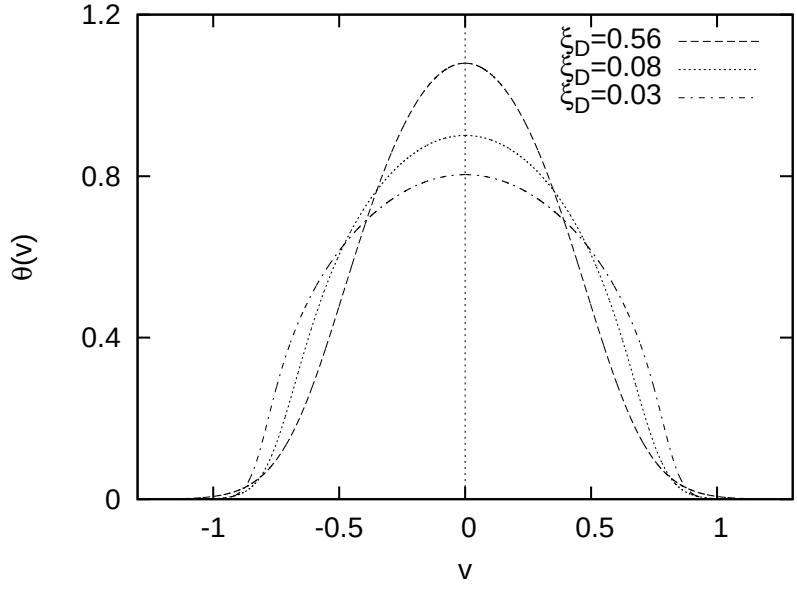

Figure 3.5: $\theta(v)$ predicted from LB theory for the same values of ξ_D as in Fig. 3.4.

3.4.6 1D Energy distribution

The energy distribution is defined as

$$F(\varepsilon) = \int_{-\infty}^{\infty}\int_{-\infty}^{\infty} \delta(\varepsilon - [\frac{v^2}{2} - \Phi(x)])\bar{f}(\varepsilon)dxdv \tag{3.83}$$

with normalization condition

$$M = \int F(\varepsilon)d\varepsilon. \tag{3.84}$$

It can be rearranged to give

$$F(\varepsilon) = 4\bar{f}(\varepsilon)\int_{0}^{\infty}\int_{0}^{\infty}\left[\frac{\delta(v - \sqrt{2(\varepsilon-\Phi)})}{\sqrt{2(\varepsilon-\Phi)}} + \frac{\delta(v + \sqrt{2(\varepsilon-\Phi)})}{\sqrt{2(\varepsilon-\Phi)}}\right]dvdx = D(\varepsilon)\bar{f}(\varepsilon) \tag{3.85}$$

where

$$D(\varepsilon) = \int_0^{\varepsilon} \frac{2\sqrt{2}}{a(\Phi)\sqrt{\varepsilon-\Phi}}d\Phi \tag{3.86}$$

is the density of states at energy ε.

While the results for $\rho(x)$ and $\theta(v)$ do not depend on the choice of the zero point of the potential, the energy distribution does. It is straightforward numerically, to use, rather than $\varphi|_{x=0} = 0$,

$$\Phi_0 \equiv \Phi|_{x=0} = g\int_{-\infty}^{\infty} |x|\rho(x)dx, \tag{3.87}$$

i.e., that corresponding to a pair potential strictly proportional to the separation between particles. Given that $a(x)$ defined in (3.55) is necessarily positive for all $x \neq 0$, this is the minimum

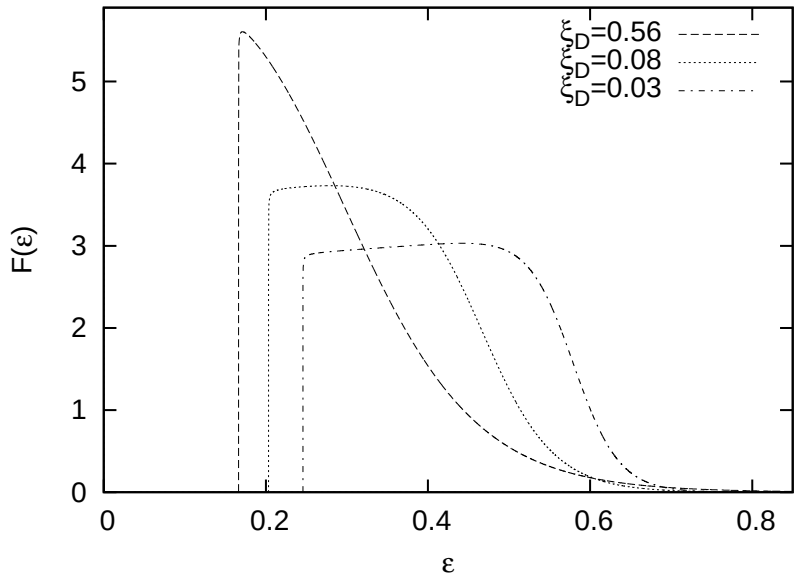

Figure 3.6: $F(\varepsilon)$ of LB theory for the cases with ξ_D equal to the plots above.

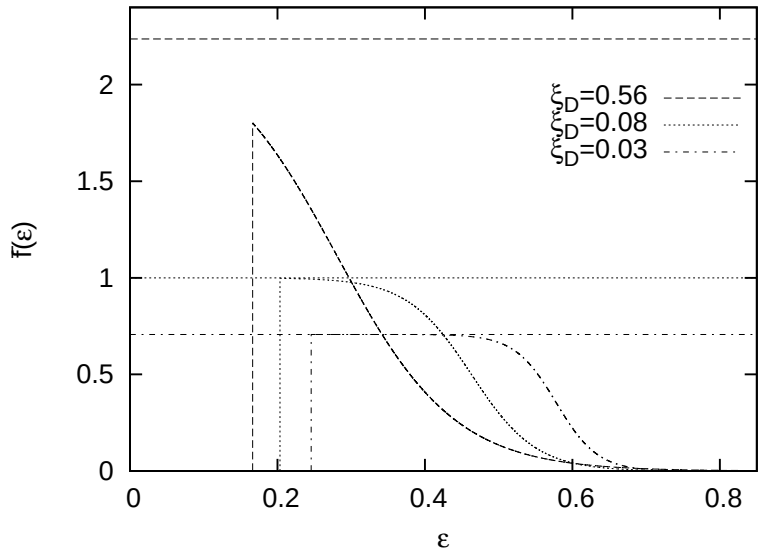

Figure 3.7: $\bar{f}(\varepsilon)$ of the curves in Fig. 3.6. The horizontal lines are equal to f_0 of each ξ_D that indicate the degenerate phase space density.

value of the potential (and of the energy particle energy). Adapting this definition the energy distribution is still given by (3.85), but with $D(\epsilon) = 0$ for $\epsilon < \Phi_0$ and

$$D(\epsilon) = \int_{\Phi_0}^{\epsilon} \frac{1}{a(\Phi)} \cdot \frac{2\sqrt{2}}{\sqrt{\epsilon - \Phi}} d\Phi. \tag{3.88}$$

from which the normalization condition reads

$$M = \int_{\Phi_0}^{\epsilon} F(\varepsilon) d\varepsilon. \tag{3.89}$$

The calculated $F(\varepsilon)$ for the same ξ_D as in the plots above are shown in Fig. 3.6. We see that higher ξ_D produces a more peaked $F(\varepsilon)$ while the cases with lower ξ_D have a flattened distribution. The lower value of Φ_0 at higher ξ_D corresponds to the higher central density (or mass less spread out).

It is instructive to compare these with the plots of the full phase space distribution function $\bar{v}(x, v)$ which are shown in Fig. 3.7, for the same cases as plotted in Fig. 3.6. The horizontal lines indicate the phase space density f_0 of the corresponding cases with the same line type. For the highest ξ_D, the entire curve lies well below f_0, indicating that it indeed far from degenerate. For the two lower ξ_D, the curves partly overlap with the f_0 lines, in a broader range for the lower ξ_D (closer to degenerate limit).

3.4.7 Order parameter in QSS

In order to characterize and compare the macroscopic properties of QSS it is convenient to use the order parameters defined in chapter 2.2.4

$$\phi_{\alpha\beta} = \frac{< |x|^\alpha |v|^\beta >}{< |x|^\alpha >< |v|^\beta >} - 1$$

for non-zero α and β, where

$$\langle u \rangle \equiv \frac{\int\int u f(x, v) dx dv}{\int\int f(x, v) dx dv}.$$

In thermal equilibrium the distribution function is separable, and so $\phi_{\alpha\beta} = 0$. Thus generically we expect these moments to be non-zero in a QSS (although any finite number of them can in principle vanish without implying separability).

Here we will use specifically the two moments ϕ_{11} and ϕ_{22} to characterize and compare the QSS we obtain in our numerical simulations. Given the LB solutions determined above (for waterbag initial conditions) it is straightforward to calculate numerically the values of ϕ_{11} and ϕ_{22} predicted by LB for this case. These are shown in Fig. 3.8 as a function of the parameter ξ_D (which, as discussed above, can be taken as the single parameter on which the LB result depends). We note that both parameters are always negative but increase toward zero as we go to the non-degenerate limit. Indeed in this limit the LB prediction tends to the (separable) thermal equilibrium solution.

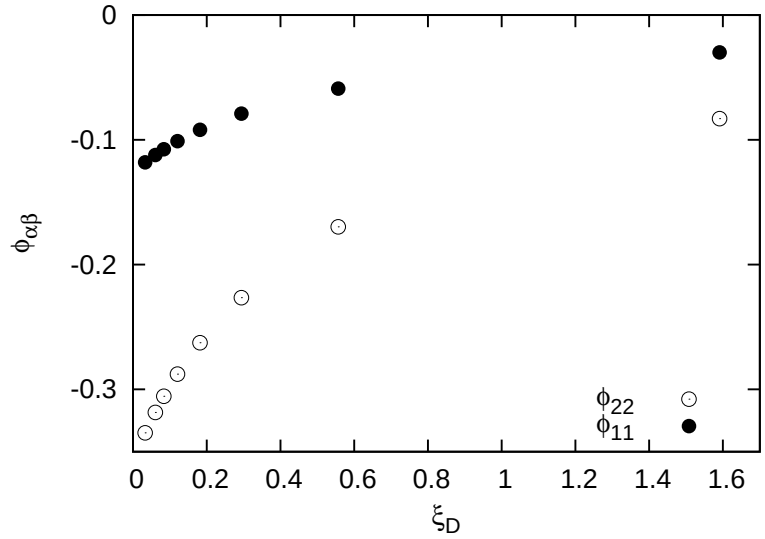

Figure 3.8: The "order parameters" ϕ_{11} and ϕ_{22} of the QSS predicted by LB theory for waterbag initial conditions, plotted as a function of ξ_D.

3.5 Predictions of Lynden-Bell theory for 3D gravity

We now turn to the prediction of Lynden-Bell theory in three dimensions. Just as in the case of the thermal equilibrium considered in chapter 2, the 3D case for Lynden-Bell theory has the feature that it is only well defined in the presence of a confining box. The reason for this difference between one and three dimensions comes from the different large distance behavior of the interactions. We have seen that

$$\bar{f} \to 0 \quad \text{as} \quad x \to \infty$$

in one dimension but

$$\bar{f} \to \text{cste} \neq 0 \quad \text{as} \quad |\vec{x}| \to \infty$$

in three dimensions. In other words the possible configurations in three dimensions include those in which mass is distributed throughout space, and such configuration in fact dominates the entropy. The Lynden-Bell solution in a confining box is sometimes referred as "cut-off Lynden-Bell" solution. The predictions made in this section will be in use with numerical simulations in chapter 6.

3.5.1 Calculation of β and μ for system with single value phase space density

For simplicity we consider again only the case of a single valued phase space density, denoted as f_0. We also suppose the spherical symmetry of the stationary state, confined in a *spherical* box of radius R_c. The Lagrange multipliers β and μ are now related to the total mass and energy

by

$$M = (4\pi)^2 f_0 \int_0^{R_c}\int_0^{\infty} \frac{r^2 v^2}{1+e^{\beta(\frac{v^2}{2}+\Phi(r)-\mu)}} dvdr \tag{3.90a}$$

$$E = (4\pi)^2 f_0 \int_0^{R_c}\int_0^{\infty} \frac{(\frac{v^2}{2}+\Phi(r))}{1+e^{\beta(\frac{v^2}{2}+\Phi(r)-\mu)}} v^2 r^2 dvdr. \tag{3.90b}$$

To integrate these equations, we start from the Poisson equation

$$\begin{aligned} \nabla^2\Phi(r) &= 4\pi G\rho(r) \\ \frac{\partial^2\Phi}{\partial r^2} &= (4\pi)^2 G f_0 \int_0^{\infty} \frac{v^2 dv}{1+e^{\beta(\frac{v^2}{2}+\Phi(r)-\mu)}} - \frac{2}{r}\frac{\partial\Phi}{\partial r} \end{aligned} \tag{3.91}$$

from which we can solve numerically for $\Phi(r)$ with boundary condition $\Phi'(0) = 0$ and $\Phi(0) = 0$. Like in one dimension, the choice of $\Phi(0)$ has no effect on the density profile, and so we will work with this choice of boundary condition except when we consider the energy distribution (see below). A considerable simplification of the problem is given by using, just as we have done in one dimension, the virial relation $E = -T$, so that

$$E = -8\pi^2 f_0 \int_0^{R_c}\int_0^{\infty} \frac{v^4 r^2}{1+e^{\beta(\frac{v^2}{2}+\Phi(r))}} dvdr. \tag{3.92}$$

However, this is now an approximation because, given the presence of a confining box, we may have an additional term involving the pressure force on the confining wall ($= 3pV$). As we will in fact be interested only in the cases where the predictions are weakly dependent on the box size, the approximation should be a good one. We will check a posteriori whether this is the case below.

We will now use the same method as in the 1D calculation by defining two functions denoting the deviations of $M(\beta,\mu)$ and $E(\beta,\mu)$ from the correct values M_0 and E_0, respectively, as

$$F(\beta,\mu) \equiv M_0 - M(\mu,\beta) = M_0 - (4\pi)^2 f_0 \int_0^{R_c}\int_0^{\infty} \frac{r^2 v^2}{1+e^{\beta(\frac{v^2}{2}+\Phi(r)-\mu)}} dvdr \tag{3.93a}$$

$$G(\beta,\mu) \equiv E_0 - E(\mu,\beta) = E_0 + 8\pi^2 f_0 \int_0^{R_c}\int_0^{\infty} \frac{r^2 v^4}{1+e^{\beta(\frac{v^2}{2}+\Phi(r)-\mu)}} dvdr. \tag{3.93b}$$

They are thus two coupled functions of μ and β, of which will determine the μ and β such that

$$F(\beta,\mu) = 0 \quad \text{and} \quad G(\beta,\mu) = 0.$$

Given a pair of guessed β and μ, the determination of the next values, i.e. $\beta \to \beta + \Delta\beta$ and $\mu \to \mu + \Delta\mu$, is done with the Newton-Raphson method as following

$$\begin{pmatrix} \Delta\beta \\ \\ \Delta\mu \end{pmatrix} = \begin{pmatrix} \frac{\partial F}{\partial\beta} & \frac{\partial F}{\partial\mu} \\ \\ \frac{\partial G}{\partial\beta} & \frac{\partial G}{\partial\mu} \end{pmatrix}^{-1} \begin{pmatrix} \Delta F(\mu,\beta) \\ \\ \Delta G(\mu,\beta) \end{pmatrix} \tag{3.94}$$

with $\Delta F = -F(\mu,\beta)$ and $\Delta G = -G(\mu,\beta)$. Each element of Jacobian matrix can be rearranged with some manipulations and reduce to

$$\frac{\partial G}{\partial \beta} = -\frac{\partial E}{\partial \beta} = -\frac{1}{2\beta}[7E - 3\mu M] \tag{3.95a}$$

$$\frac{\partial G}{\partial \mu} = -\frac{\partial E}{\partial \mu} = \frac{3}{2}M \tag{3.95b}$$

$$\frac{\partial F}{\partial \beta} = -\frac{\partial M}{\partial \beta} = \frac{1}{\beta}\left[\frac{3}{2}M + f_0(4\pi)^2 \int_0^{R_c}\int_0^{\infty} \frac{(\Phi(r)-\mu)r^2 dv dr}{1+e^{\beta(\frac{v^2}{2}+\Phi(r)-\mu)}}\right] \tag{3.95c}$$

$$\frac{\partial F}{\partial \mu} = -\frac{\partial M}{\partial \mu} = -f_0(4\pi)^2 \int_0^{R_c}\int_0^{\infty} \frac{r^2 dv dr}{1+e^{\beta(\frac{v^2}{2}+\Phi(r)-\mu)}}. \tag{3.95d}$$

We repeat the iterations until we satisfy the precision conditions

$$\left|\frac{E(\mu,\beta)-E_0}{E_0}\right| \leq \delta \quad \text{and} \quad \left|\frac{M(\mu,\beta)-M_0}{M_0}\right| \leq \delta \tag{3.96}$$

where, just as in the 1D case, we use in practice $\delta = 10^{-3}$.

While the 1D solution depends only on a single parameter, which we have chosen to be ξ_D, the 3D problem, because of the presence of the box, depends on two parameters. Unlike in one dimension we cannot find an analytical expression for the energy in degenerate limit E_D and therefore we normalize instead with the characteristic energy given by*

$$\tilde{E}_0 = -\frac{3}{10}(\frac{4}{3}\pi)^{\frac{4}{3}} G^2 M^{\frac{7}{3}} f_0^{\frac{2}{3}}, \tag{3.97}$$

which should differ from the degenerate energy by a constant of order unity, and the characteristic length

$$\tilde{L}_0 = \frac{1}{GM^{\frac{1}{3}} f_0^{\frac{2}{3}}}. \tag{3.98}$$

The Lynden-Bell solution may then be characterized by two parameters

$$\tilde{\xi} \equiv \frac{E-\tilde{E}_0}{|\tilde{E}_0|} \quad \text{and} \quad \tilde{R}_c \equiv \frac{R_c}{\tilde{L}_0}. \tag{3.99}$$

Since $\tilde{E}_0$ is not exactly the degenerate energy, $\tilde{\xi} = 0$ does not correspond to the degenerate limit. Likewise the characteristic length $\tilde{L}_0$ is of order (but not equal to) the radius of the degenerate system, so the normalized cut-off radius $\tilde{R}_c$ gives approximately how far the cut-off radius is from the size of the corresponding degenerate system (with the same M and f_0). The fact that the LB predictions depend on two parameters has been noted in [132, 136, 135, 134].

*The reason for this particular choice of reference energy will become clear in chapter 6: it is the lowest energy of the initial condition we consider, equal to that of a uniform spherical configuration with initial virial ratio equal to unity.

3.5.2 3D Spatial distributions and dependence on box size

The density profile can be most easily obtained directly from the Poisson equation

$$\rho(r) = \frac{1}{4\pi G}\left[\frac{\partial^2\Phi}{\partial r^2} + \frac{2}{r}\frac{\partial\Phi}{\partial r}\right] \tag{3.100}$$

where $\Phi(r)$ is determined, at given β and μ, as described above. It is also interesting to consider

$$M_\rho(r) = 4\pi r^2\rho(r), \tag{3.101}$$

i.e. the mass per unit radius, with

$$M = \int_0^{R_c} M_\rho(r)dr = \int_0^{R_c} 4\pi r^2\rho(r)dr. \tag{3.102}$$

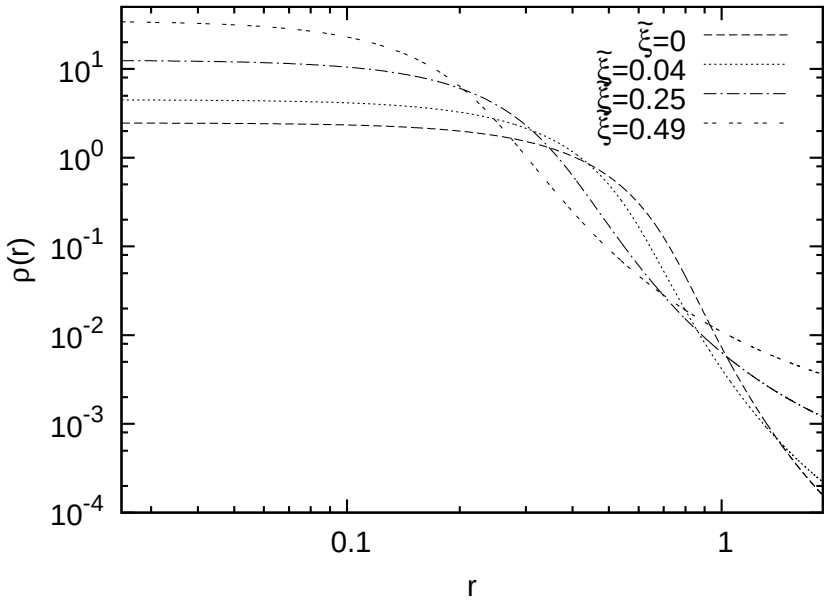

Figure 3.9: $\rho(r)$ predicted by LB theory with different $\tilde{\xi}$. All of them have the same total mass. The cut-off radius $\tilde{R}_c$ are equal to $0.44, 0.56, 0.89$ and 1.48 for $\tilde{\xi} = 0, 0.04, 0.25$ and 0.49, respectively. The end of r-axis corresponds to the cut-off radius. See text for explanation of units.

The resulting Lynden-Bell prediction of $\rho(r)$ for different values of $\tilde{\xi}$ are shown in Fig. 3.9[†]. In a very similar manner to one dimension we see that the profiles become more condensed as ξ_D increases. The same tendency is also observed in the plots of $M_\rho(r)$, for the same cases, shown in Fig. 3.10. We also notice the non-decreasing tail, more visible when $\tilde{\xi}$ increases, in $M_\rho(r)$ plots for sufficiently high $\tilde{\xi}$.

[†]In this figure, and in those that follow in this chapter, the units are those in which $G = 1, M = 1$ and R_c is constant. The explanation for the choice of the given value of R_c will be explained in chapter 6.

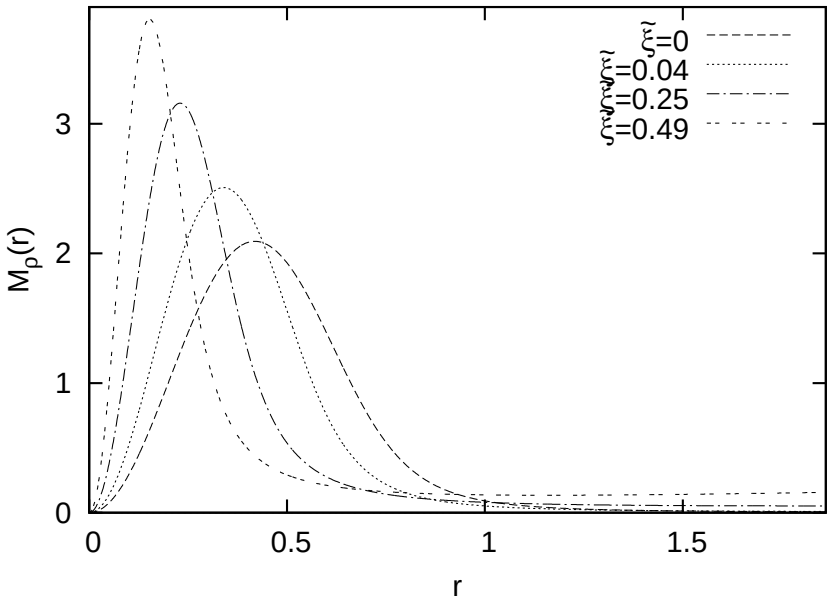

Figure 3.10: $M_\rho(r)$ predicted by LB theory with the same cases as shown in Fig. 3.9 (see more details about $\tilde{R}_c$ therein). The end of r-axis corresponds to the cut-off radius. The units are as in Fig. 3.9.

As noted above our calculation involved one approximation: the use of the virial relation $E = -T$ valid exactly only for an open system. To check the validity of this approximation, i.e. the correction of the virial relation due to the box, we have calculated the virial ratio $R = -2T/U$. The results are shown in Tab. 3.1. We see that the result deviates only slightly from the assumption $R = 1$, even at the highest $\tilde{\xi}$. As we will discuss below the range in which we use our results is that in which the deviation is small.

Table 3.1: The virial ratio, R, of the LB distribution function calculated for different $\tilde{\xi}$.

$\tilde{\xi}$	0	0.01	0.04	0.09	0.16	0.25	0.36	0.49
$\tilde{R}_c$	0.44	0.49	0.56	0.64	0.74	0.86	1.11	1.48
R	1.002	1.002	1.002	1.004	1.009	1.018	1.036	1.068

Dependence on box size

An important issue in Lynden-Bell theory for 3D gravity is the dependence on the box size R_c. Indeed the predictions of this theory are only potentially relevant to open systems (which is what we are physically interested in and will consider in chapter 6) insofar as they are not strongly dependent on this scale. This point has been emphasized by Levin et al. [37] in their study of Lynden-Bell theory applied in three dimensions, but has apparently received little attention in discussion of earlier studies (e.g. [21]). As discussed above the necessity for a cut-off arises from

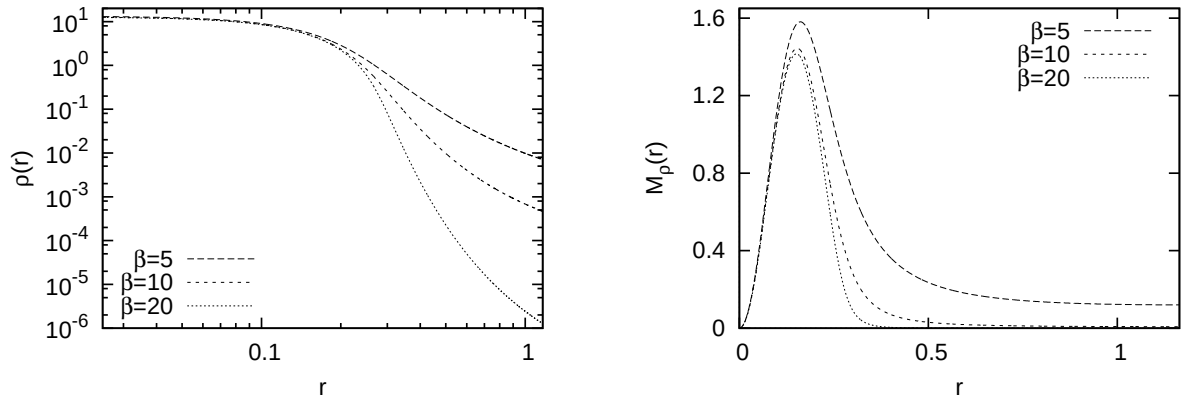

Figure 3.11: $\rho(r)$ (left) and $M_\rho(r)$ (right) with different β and fixed μ, f_0 and R_c (see text for the choice of unit and cut-off radius). The end of r-axis corresponds to the cut-off radius.

the fact that

$$\bar{f}(\vec{x},\vec{v}) = \frac{f_0}{1+e^{\beta(\frac{v^2}{2}+\Phi(\vec{x})-\mu)}} \to \text{cste} \neq 0 \quad \text{as} \quad |\vec{x}| \to \infty$$

for any finite β. Thus if β, μ and $\Phi(\vec{x})$ are independent of the box size, the mass cannot be finite, i.e. for a finite mass β, μ and $\Phi(\vec{x})$ must depend on R_c. In other words, in absence of a box, maximization of Lynden-Bell entropy would lead to mass spread throughout space (just as for the Boltzmann entropy). The only case in which this is not true is the degenerate limit $\beta \to \infty$, in which case the system determines its own size. As a result as β becomes large (i.e. as the system approaches the degenerate limit) one might expect that the dependence on R_c becomes increasingly weak. To see that this is the case, consider that

$$\frac{\partial M}{\partial R_c} = 4\pi R_c^2 \rho(R_c) = (4\pi)^2 R_c^2 f_0 \int_0^\infty \frac{v^2}{1+e^{\beta(\frac{v^2}{2}+\Phi(R_c)-\mu)}} dv. \tag{3.103}$$

Now for fixed negative μ, and R_c sufficiently large so that $\Phi(R_c) - \mu > 0$, and sufficiently large β, we have

$$\frac{v^2}{1+e^{\beta(\frac{v^2}{2}+\Phi(R_c)-\mu)}} \ll 1$$

and therefore

$$\frac{\partial M}{\partial R_c} \ll 1.$$

Similarly for the energy

$$\frac{\partial E}{\partial R_c} = (4\pi)^2 R_c^2 f_0 \int_0^\infty \frac{v^2(\frac{v^2}{2}+\Phi(R_c))}{1+e^{\beta(\frac{v^2}{2}+\Phi(R_c)-\mu)}} dv. \tag{3.104}$$

so that

$$\frac{\partial E}{\partial R_c} \ll 1$$

on the same conditions.

Shown in Fig. 3.11 are plots of $\rho(r)$ (left panel) and $M_\rho(r)$ (right panel) determined at fixed values of μ and f_0, and fixed radius R_c, as β is varied. Units are such that $G = 1, \mu = 1$ and $f_0 = 1$ and $R_c = 1.19$ which corresponds to the length of the x-axis in the plots. It is clear that as β increases the mass becomes more clearly concentrated well inside the box, and that as a result the mass (and energy) will change very little at larger β as a function of box size. To illustrate this further we shown in Tab. 3.2 the mass and energy obtained at fixed μ, f_0 (with corresponding $\tilde{E}_0$ and $\tilde{\xi}$) for various values of β corresponding to Fig. 3.11, and for two different values of the box size. As anticipated we see that at large β (or low $\tilde{\xi}$) the changes in M and E are extremely small (and we infer that, conversely, the changes in β and μ would be similarly small if we consider Lynden-Bell solutions at fixed E and M, varying R_c around these values).

Table 3.2: Total mass and energy increments calculated from doubling the box size for the system represented in Fig. 3.11. See text for the choice of unit.

β	R_c	M	% of M increment	E	% of E change	$\tilde{E}_0$	$\tilde{\xi}$
5	1.19	0.490	-	-1.680e-1	-	-3.83e-1	0.56
5	2.38	0.592	20.8%	-1.709e-1	1.73%	-5.95e-1	0.71
10	1.19	0.2806	-	-9.3268e-2	-	-1.04e-1	0.10
10	2.38	0.2871	2.31%	-9.3407e-2	0.15%	-1.10e-1	0.15
20	1.19	0.234683	-	-7.59586e-2	-	-6.88e-2	-0.10
20	2.38	0.234703	0.0085%	-7.59600e-2	0.0018%	-6.88e-2	-0.10

3.5.3 3D Velocity distribution

The velocity distribution of Lynden-Bell is given by

$$\theta(v) = 4\pi f_0 \int_0^{R_c} \frac{r^2 dr}{1 + e^{\beta(\frac{v^2}{2} + \Phi(r) - \mu)}}. \tag{3.105}$$

which can be calculated numerically using $\Phi(r)$ determined by solution of (3.91). By definition $\theta(v)$ stands for the mass inside the spherical shell in v-space of thickness dv between v and $v+dv$ divided by shell volume. In the same way as for the spatial distribution, we define the mass distribution in v-space

$$N_\theta(v) = 4\pi v^2 \theta(v) \tag{3.106}$$

with normalization condition

$$M = \int_0^\infty N_\theta(v) dv = \int_0^\infty 4\pi v^2 \theta(v) dv. \tag{3.107}$$

Unlike the density distribution, the velocity space does not require the cut-off velocity since the distribution function goes rapidly to zero as $v \to \infty$. The plots of $\theta(v)$ and $N_\theta(v)$ for the same cases as shown previously for spatial distribution are shown in Fig. 3.12 and in Fig. 3.13 respectively.

We see that at higher $\tilde{\xi}$, $\theta(v)$ is more concentrated at low v, and decays at large v more rapidly at lower $\tilde{\xi}$. $N_\theta(v)$, likewise, is more peaked at high $\tilde{\xi}$ than at lower $\tilde{\xi}$. The position of the peak is shifted toward lower v when $\tilde{\xi}$ increases. The qualitative features are quite similar

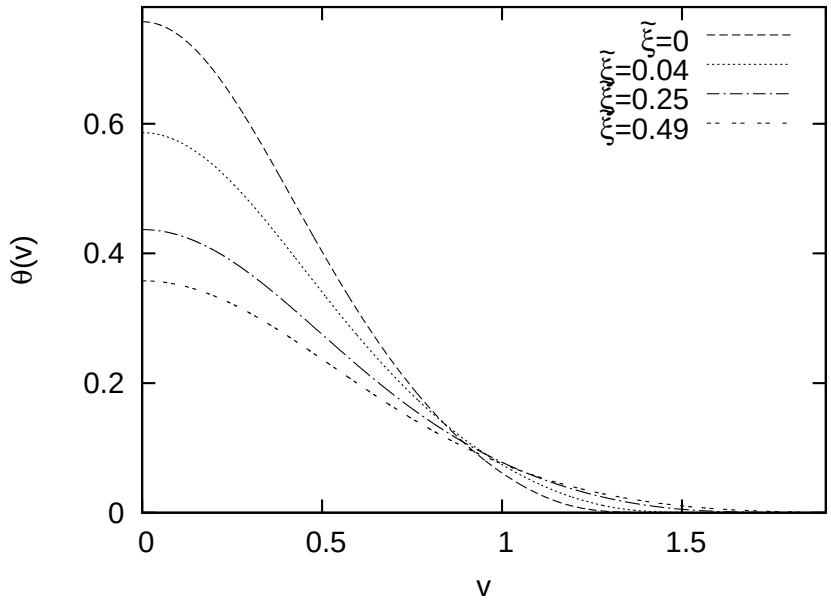

Figure 3.12: $\theta(v)$ predicted by Lynden-Bell theory for the same cases as shown in Fig. 3.9 and the same values of R_c (see caption of Fig. 3.9 for details.)

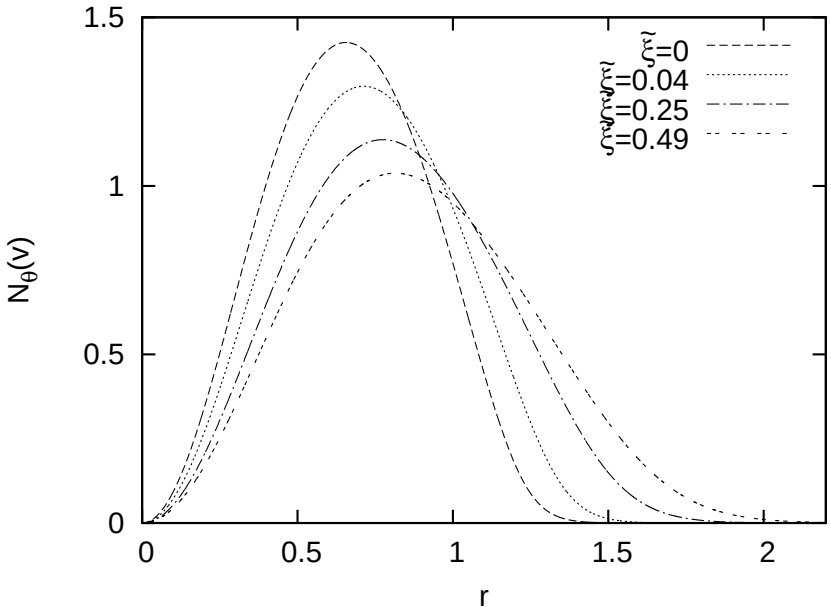

Figure 3.13: $N_\theta(v)$ predicted by Lynden-Bell theory for the same cases as shown in Fig. 3.9 (see caption of Fig. 3.9 for details.)

to the plots of spatial distribution but the deviation between different $\tilde{\xi}$ is less pronounced. The tail of $N_\theta(v)$ is also absent.

We investigate also the influence of varying β on the velocity distribution. Shown in Fig. 3.14 are the plots for $\theta(v)$ and $N_\theta(v)$ of the same cases as presented in Fig. 3.11. The effect of the variation of β is simply to spread out the distribution.

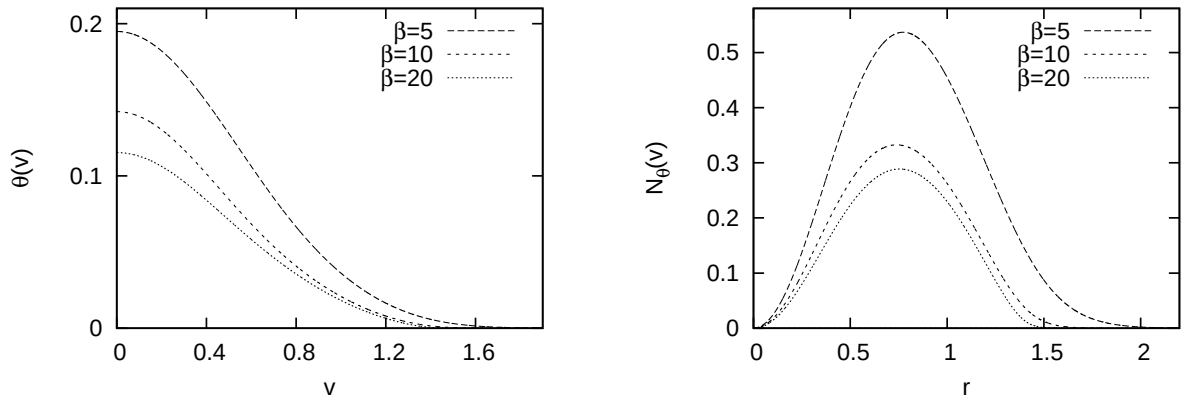

Figure 3.14: $\theta(v)$ (left) and $N_\theta(v)$ (right) with various β but fixed μ, f_0 and R_c for the same cases as shown in Fig. 3.11.

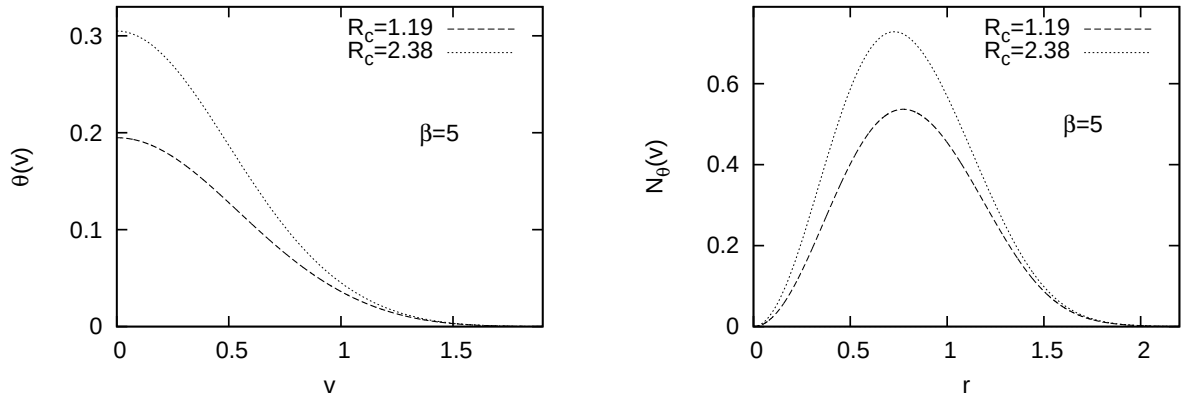

Figure 3.15: $\theta(v)$ (left) and $N_\theta(v)$ (right) for $\beta = 5$. The cut-off radius, R_c, are 1.19 (extracted from Fig. 3.14) and 2.38.

To study the dependence on the box size, we pick the cases with $\beta = 5$ and 10 and double the cut-off radius R_c (from 1.19 to 2.38). The results are shown in Fig. 3.15 (for $\beta = 5$) and Fig. 3.16 (for $\beta = 10$). In line with our discussions in the previous subsection, we see that the change in $\theta(v)$ and $N_\theta(v)$ is reduced as β increases. While the differences are very large at $\beta = 5$, at $\beta = 10$ they are quite small, but still visible, particularly at low v in the plot of $\theta(v)$. These results are very well in line with Tab. 3.2. At $\beta = 20$ (not shown) the curves for the two R_c are perfectly superimposed.

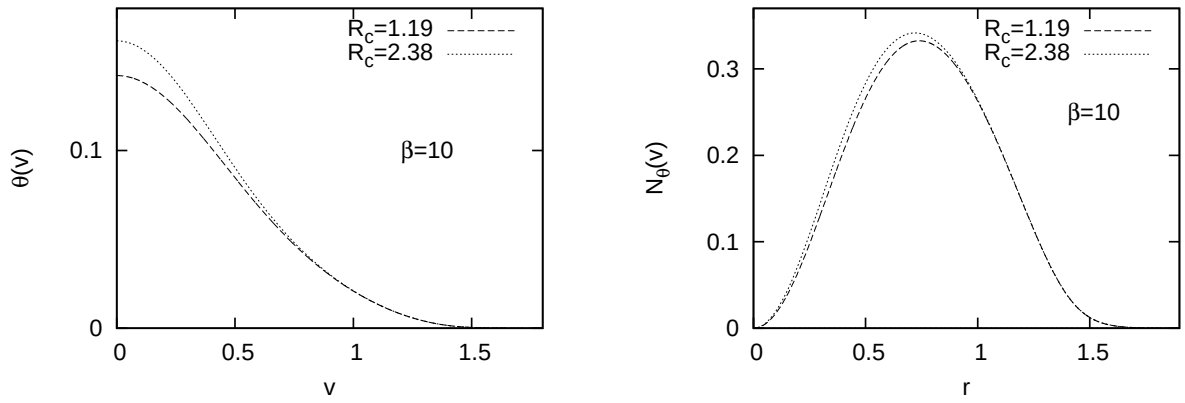

Figure 3.16: $\theta(v)$ (left) and $N_\theta(v)$ (right) for $\beta = 10$. The cut-off radius, R_c, are 1.19 (extracted from Fig. 3.14) and 2.38.

3.5.4 3D Energy distribution

Analogous to one dimension, we define

$$F(\varepsilon) = \int_0^{R_c} \int_0^{\infty} \delta(\varepsilon - (\frac{v^2}{2} + \Phi(r))) \bar{f}(\varepsilon) 4\pi r^2 4\pi v^2 dv dr \tag{3.108}$$

to be the energy distribution with the normalization

$$M = \int_0^{\infty} F(\varepsilon) d\varepsilon. \tag{3.109}$$

With some simple manipulations of the delta function, we have

$$\begin{aligned} F(\varepsilon) &= \bar{f}(\varepsilon)(4\pi)^2 \int_0^{R_c} \int_0^{\infty} \left[\frac{\delta(v - \sqrt{2(\varepsilon - \Phi(r))})}{\sqrt{2(\varepsilon - \Phi(r))}} + \frac{\delta(v + \sqrt{2(\varepsilon - \Phi(r))})}{\sqrt{2(\varepsilon + \Phi(r))}} \right] v^2 dv r^2 dr \\ &= \bar{f}(\varepsilon)\sqrt{2}(4\pi)^2 \int_0^{R_c} r^2 \sqrt{(\varepsilon - \Phi(r))} dr \end{aligned} \tag{3.110}$$

or

$$F(\varepsilon) = g(\varepsilon)\bar{f}(\varepsilon) \tag{3.111}$$

with

$$g(\varepsilon) = \sqrt{2}(4\pi)^2 \int_0^{R_c} r^2 \sqrt{\varepsilon - \Phi(r)} dr. \tag{3.112}$$

Note that these expressions are derived using the boundary condition $\Phi(0) = 0$. To have the result consistent to a pair potential $\Phi(r \to \infty) = 0$, we shift the energy by the potential at the center

$$\Phi_0 = -4\pi G \int_0^{R_c} r\rho(r) dr \tag{3.113}$$

which can be determined numerically (and is strictly negative). Thus the normalization condition changes to

$$M = \int_{\Phi_0}^{\infty} F(\varepsilon) d\varepsilon. \tag{3.114}$$

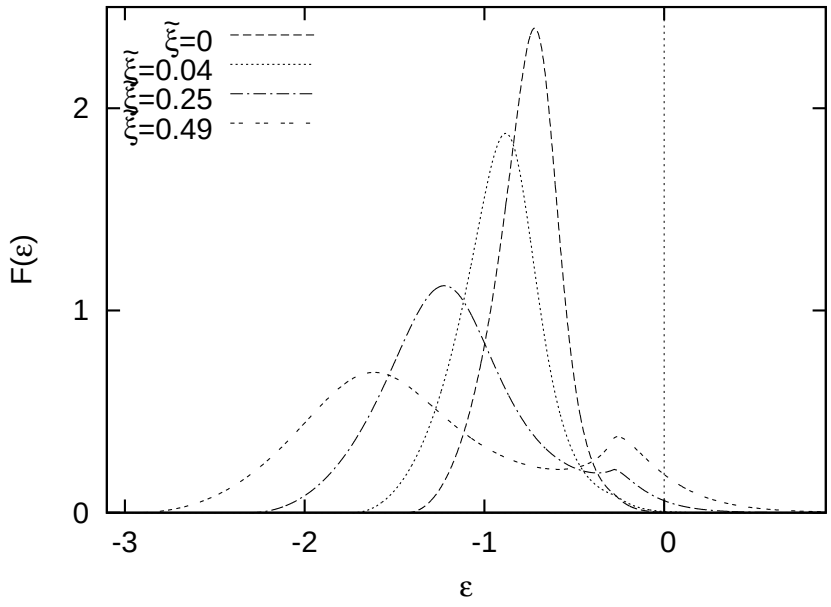

Figure 3.17: $F(\varepsilon)$ predicted by LB theory for the same cases as shown in Fig. 3.9 (see more details about $\tilde{R}_c$ therein). The dotted vertical line indicates $\varepsilon = 0$.

Table 3.3: (Left table) Values of M^-/M and M^+/M for different $\tilde{\xi}$ (with their corresponding $\tilde{R}_c$ beside). (Right table) The same quantities as on the left but for systems with different β while $\mu = 1, f_0 = 1$ and $R_c = 1.19$.

$\tilde{\xi}$	$\tilde{R}_c$	M^-/M	M^+/M
0.49	1.48	0.9534	0.0466
0.36	1.11	0.9779	0.0221
0.25	0.89	0.9903	0.0097
0.16	0.74	0.9961	0.0039
0.09	0.64	0.99853	0.00147
0.04	0.56	0.99947	0.00053
0.01	0.49	0.99978	0.00022
0	0.44	0.99986	0.00014

β	M^-/M	M^+/M
5	0.9714	0.0286
10	0.99744	0.00256
20	0.999999084	9.16e-07

with $F(\varepsilon)$ now vanishes where $\varepsilon < \Phi_0$.

Plots of $F(\varepsilon)$ for various $\tilde{\xi}$ are shown in Fig. 3.17. At high $\tilde{\xi}$, the energy distribution is more spread out in ε space and yields a more negative Φ_0, corresponding to a more condensed central density. Note further that at the larger value of $\tilde{\xi}$, $F(\varepsilon)$ is visibly non-zero for $\varepsilon > 0$. This corresponds to unbound mass (which would escape to infinity in the absence of the box). To quantify this more precisely we define the bound and unbound mass:

$$M^- = \int_{\Phi_0}^{0} F(\varepsilon) d\varepsilon \quad \text{and} \quad M^+ = \int_{0}^{\infty} F(\varepsilon) d\varepsilon \tag{3.115}$$

(with $M = M^- + M^+$). Summarized in Tab. 3.3 (left panel) are M^-/M and M^+/M for various $\tilde{\xi}$ (including the cases plotted in Fig. 3.17). At higher $\tilde{\xi}$, M^+/M clearly increases. However even at $\tilde{\xi} = 0$, M^+/M is non-zero. It is indeed only in the degenerate limit that $M^+ = 0$[‡].

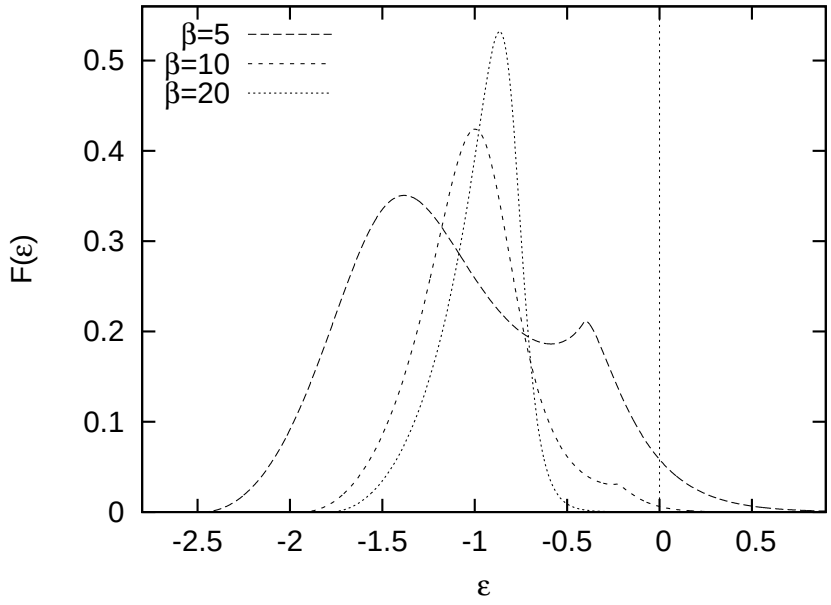

Figure 3.18: $F(\varepsilon)$ predicted by LB theory with different value of β but fixed μ, f_0 and R_c.

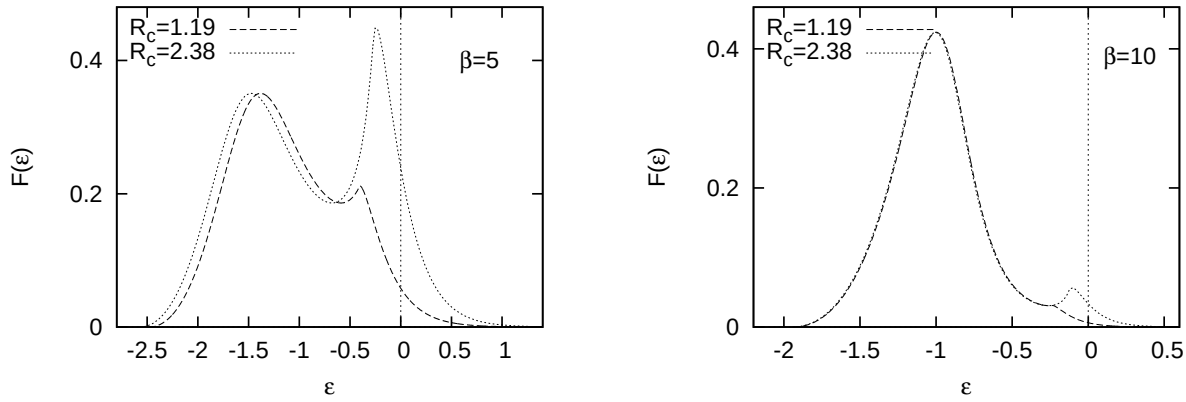

Figure 3.19: $F(\varepsilon)$ predicted by LB theory with different R_c for $\beta = 5$ (left) and 10 (right). The system parameters μ and f_0 are the same in all case.

We finally investigate again the influence of β on $F(\varepsilon)$ and M^+/M. Plotted in Fig. 3.18 are $F(\varepsilon)$ of the same cases shown in Fig. 3.11 (see text above for the choice of unit) and shown in

[‡] M^+ could, in fact, alternatively be eliminated using the escape velocity as the integration limit. This is complicated because the escape velocity is also a function of r. The implementation of such a cut-off in escape velocity was originally implemented by Michie [12, 145, 146] and King [13, 147] for the isothermal sphere distribution.

Tab. 3.3 (right) are M^-/M and M^+/M for the same cases. At smaller β, $F(\varepsilon)$ is more spread out in ε-space (similarly to the cases with high $\tilde{\xi}$ above) and M^+/M is greater. The curve at low β extends to more negative ε, implying that the core is more strongly bound. The higher β case is similar to the case with low $\tilde{\xi}$, with a distribution which is steep and peaked, with almost all the area under the curve lies at $\varepsilon < 0$.

Plotted in Fig. 3.19 are $F(\varepsilon)$ for $\beta = 5$ (left panel) and 10 (right panel) with $R_c = 1.19$ and 2.38. In line again with what was observed above, we see that the features reflecting a sensitivity to the box size become visible for smaller value of β, most evidently in the increase of the peak on the right consisting of loosely bound and unbound mass when R_c increases. The peak on the left, consisting of more tightly bound mass, is much less changed. This is because the increment of mass from the expanded box (i.e. between $r = 1.19 - 2.38$) is situated far from the center, thus much more weakly bound.

Part II

Numerical simulations

Chapter 4

Relaxation to thermal equilibrium of 1D self-gravitating systems

The so-called "sheet model" is an interesting toy model for the study of self-gravitating systems, or more generally of systems with long-range interactions. It is simply the one dimensional (1D) generalization of Newtonian gravity, consisting of particles interacting by attractive forces independent of their separation (or, equivalently, infinite parallel planes embedded in three dimensions interacting via Newtonian gravity). Because the particle trajectories are exactly integrable between crossings, it has the nice feature that its numerical integration can be performed with an accuracy limited only by machine precision. It has been the subject of (mostly numerical) study in the literature for several decades (see, e.g., [89] for a review of the literature on the model) following earlier analytical studies [90, 91]. A fundamental question about this system — and more generally for any system with long-range interactions — is whether they relax to the statistical equilibrium calculated in the microcanonical or canonical ensemble first calculated in [92] and which we have discussed at length in chapter 2. The literature on this model — which we will discuss in greater detail in our conclusions section below — is marked by differing results (or, rather, interpretation of results) from different groups, and even some controversy. Work by two groups in the eighties (see, e.g. [88] for a summary) led to the conclusion that relaxation could not be observed, except perhaps in some special cases. Studies by two other groups over a decade ago [87, 148] found results indicating relaxation, and [87] gave a determination of the N dependence of the characteristic time. However doubts about the interpretation of these latter results as establishing relaxation to equilibrium were raised by further analysis [149, 150]. In more recent work [89, 151] clear evidence for relaxation in a version of the model in which there are different particle masses has been found, but the dependence on N has not been determined*. The mechanism of relaxation (if it indeed takes place) in these models remains, as in other long-range interacting systems, very poorly understood, and a basic subject of research in the statistical mechanics of long-range interacting systems (for recent reviews see e.g. [58, 153]). In this chapter we report an essentially numerical study of relaxation in the single mass sheet model. To characterize the long-time evolution and relaxation of the system we make extensive use of the order parameters introduced in section 2.2.7. This tool allows us to resolve some outstanding issues about the relaxation in this system, and, in particular, to establish more definitively both that relaxation does indeed occur and the scaling with particle number of the time characterizing it. We consider a broader range of initial conditions, which

*Other variants of the model have also been studied in [83, 85, 152].

allows us to establish also dependences of relaxation on these. We also study the fluctuations — both in time and over realizations of the initial conditions — about the average macroscopic evolution of the system, showing phenomenologically the correlation of their amplitude with the lifetimes of the intermediate "quasi-stationary" states.

The "sheet model" is probably the oldest toy model of long range interactions — it was first explored in astrophysics as a toy model for self-gravitating systems in three dimensions — and is also, arguably, closer to reality than the HMF which is constrained on a circle. It has, further, as mentioned above the nice feature that it numerical integration can be performed up to machine precision. Despite this, the results concerning its dynamics and relaxation are less clearly determined than for the HMF, and the literature on the subject has, as we have discussed above, been marked by some controversy and results showing that the model has, apparently, some very peculiar behaviors — rapid relaxation to equilibrium for some classes of initial states [154, 155], persistent phase space structures impeding relaxation to QSS [156, 157], macroscopically chaotic behavior in the long time evolution [158] — which indicate that it might not be a very useful toy model (in that its behaviors are perhaps non-generic). In this article our main conclusion is that, 1) by using appropriate diagnostics of the macroscopic evolution and 2) by extending simulations to sufficiently large N and/or averaging over sufficiently large numbers of realization, one finds behavior in this toy model very similar in crucial respects to that in the HMF: to a very good first approximation a generic initial configuration relaxes to a long-lived QSS, and then relaxes to its statistical equilibrium at sufficiently long time. This latter phase can be characterized apparently by a single time-scale, with the evolution of the order parameter during relaxation well fit by a simple function (in our case a better fit is obtained using a simple stretched exponential, rather than a hyperbolic tangent in the HMF as in [63]). On the other hand the N dependence of this time scale, linearly proportional to the number of particles N, is different to that found in [63] for the HMF. This latter result, however, applies to spatially homogeneous states which, in the HMF, can occur due to the periodicity of the system. Relaxation which is slower than linear in N is expected in this case, as shown using analysis of kinetic equations (see, e.g. contributions of P.H. Chavanis, and of F. Bouchet and J. Barré in [57]).

The chapter is organized as follows. In the section 4.1 we first describe our numerical simulations and the initial conditions we study, and then give our results in section 4.2. In presenting them we give first results for single realizations, and then use temporal averages and finally ensemble averages to derive the scaling with N of the relaxation time. This is followed by further study of the fluctuations about the average behaviors of the order parameters. Considering both temporal fluctuations and those in the ensemble, which we show to be very consistent with one another, we observe the correlation between their amplitude in the QSS and the observed relaxation time. The section 4.3 will present a brief study about the miscellaneous factors (mostly unphysical) that can also add effect to the relaxation, for example the machine precision, machine capacity or data format. In the conclusion sections we return to a more detailed discussion of the previous literature, presenting further results which allow one to understand the reasons for the divergence in conclusions in certain cases.

4.1 Numerical simulations

4.1.1 Order parameters

Recall the order parameters defined in (2.184):

$$\phi_{\alpha\beta} = \frac{< |x|^\alpha |v|^\beta >}{< |x|^\alpha >< |v|^\beta >} - 1$$

which is used to probe the "entanglement" (or correlation) between spatial and velocity coordinates of the distribution function. Because such entanglement is absent in thermal equilibrium (see expression 2.162), the stationary state with zero order parameters thus indicates the thermal equilibrium. We principally use ϕ_{11} and ϕ_{22} entirely in this chapter to probe the relaxation (as the magnetization serves the HMF model in the same purpose).

4.1.2 Algorithm

As remarked above in section 1.2, it is convenient for the numerical integration of the model to exchange particles' labels when they cross, which is equivalent to treating them as if they undergo an elastic collision in which they exchange their velocities when they meet. The force on each particle is then constant in space and time [and given by equation (1.54)], and the numerical algorithm must simply determine, at any time, the next crossing which occurs, and then exchange the velocities of the "colliding" particles. The optimal way to treat this kind of problem is, as has been pointed out and discussed in detail in appendix A (or [159]), by using a so-called "heap-based" algorithm, which uses an object called a "heap" to store in an ordered way the next crossing times of the pairs. This algorithm requires a number of operations of order $\log(N)$ to determine the next crossing (rather than of order N for the evident direct algorithm in which one calculates and compares directly at each step the next crossing of each of the $N-1$ pairs). Given that the number of crossings per particle per unit time grows in proportion to N, the simulation time thus grows in proportion to $N^2 log(N)$.

Because the particle trajectories are integrated exactly, the only limit on the accuracy of the numerical integration is thus the numerical precision. As is common practice we will use the total energy (which is conserved in the continuum model) as a control parameter. For the longest simulations we report the error in total energy of the order of $10^{-8}\%$.

4.1.3 Initial condition

We will consider principally a simple class of spatially uniform initial conditions (IC), generated by randomly distributing the N particles on a finite interval. As initial velocity distribution we will consider both the case that initial velocities are zero ("cold IC") and the case that this distribution is also uniform in a finite interval. The latter are thus random samplings of a particular class of "waterbag" initial conditions in phase space (i.e. in which the phase space density in equal in the region in which it is non-zero), while the cold case can be considered as the limit in which the width of the velocity distribution goes to zero. In Fig. 4.1 the phase space distribution for a typical IC is shown.

The IC may thus be characterized solely by the particle number N and a single parameter characterizing the waterbag. Rather than the width of the velocity distribution or phase space density, it is convenient to choose this parameter to be the dimensionless *initial virial ratio*:

$$R_0 \equiv \frac{2T_0}{U_0} \tag{4.1}$$

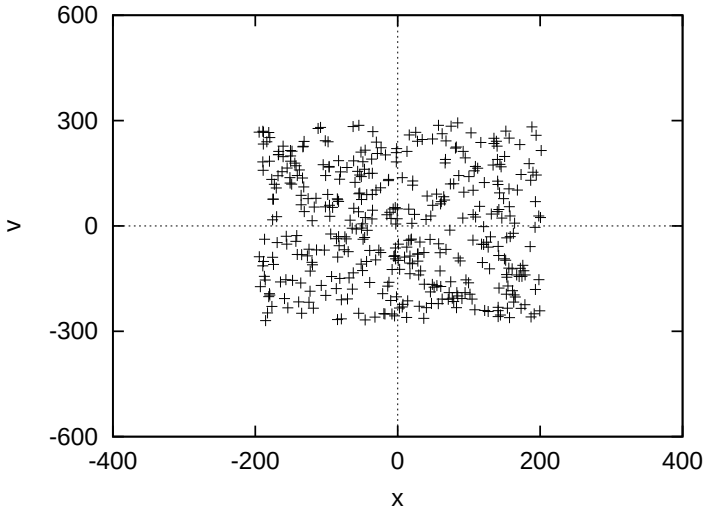

Figure 4.1: A rectangular waterbag initial condition in phase space, for $N = 400$ and $R_0 = 1.0$. See text for definition of units.

where T_0 is the initial total kinetic energy and U_0 is the initial total potential energy.

We remark on a particularity of the cold IC which we will return to below. In the limit $N \to \infty$, the evolution from this IC becomes singular at a finite time: an element of mass initially at coordinate position x_0 feels a force $-2g\rho_0 x_0$, where ρ_0 is the initial mass density; all particles are in free-fall under a force proportional to their distance, and therefore arrive at the origin at the same time, producing a density singularity. This is completely analogous to the singularity in three dimensions which results from a cold spherical initial condition (see [160] for a discussion).

It is simple to show, given that the particle positions and velocities are both randomly sampled from a PDF which is uniform in a finite interval, that the relative fluctuation in U_0 and T_0 scale as $1/\sqrt{N}$ for large N. An exact calculation (see appendix B) shows, for example, that at $N = 100$, the normalized variance of U_0, which corresponds to that in the energy for the case $R_0 = 0$, is ≈ 0.05. This means that the typical amplitude of the fluctuation in the energy for cold initial condition at $N = 100$ is of order the difference between the mean energy of cold initial condition and initial condition with $R_0 = 0.1$.

4.1.4 Units and coordinates

For convenience we choose our coordinate system such that the center of the mass of the system lies at $x = 0$ and is at rest (i.e. after distributing the particles as described we add a spatial translation and constant velocity to all particles so that these conditions are satisfied).

We make the following choice of units: we set the particle mass m and the coupling g to unity, and take $L = N$. This corresponds to a mass (and particle) density of unity, and a time unit equal to the *dynamical time*:

$$t_{\rm dyn} = \sqrt{\frac{L}{Mg}} \tag{4.2}$$

which is the characteristic time for the system's evolution under the mean field forces (the mean

field forces, of order Ngm^2, moves a system particle of mass m over the system size L on this time-scale). $t_{\rm dyn}$ also coincides with the time of the singularity noted above in the smooth limit of the cold IC.

4.2 Results

The difficulty in this study of relaxation, as in such a study for any long-range system, is that one is interested in studying large N systems — so that finite N deviations from the mean-field behavior are small — on a time scale which grows rapidly with N (typically, one expects, in proportion to some power of N). Because of numerical limitations, particularly strong because of the computational cost of integrating a long-range interaction, it is in practice often difficult to arrive at definitive conclusions. In the case of gravity in three dimensions, notably, numerical studies exist (see e.g. [32, 38, 39, 40, 37]) but they give only a very incomplete characterization and understanding of relaxation. As we have discussed in the introduction one of the attractive features of the HMF model is that, because of its mean field nature, the numerical cost of the force calculation is of order N, allowing much larger particle numbers — $N \sim 10^4 - 10^5$ [63] — to be simulated on the relevant long time scales than is feasible in other cases. The principal reason why the early literature on the sheet model was marked by controversy on the question of relaxation is simply, as we will discuss further below, that such relaxation could not be observed on the required time scales for systems sufficiently large so that the finite N fluctuations were sufficiently small to allow the clear identification of the average behaviors. The study of [87], taking advantage of the greater numerical resources available already in the nineties, detected relaxation for $N \sim 10^2$ from specific waterbag configurations and found a scaling of the relaxation time, over a small range in N, linear in N. This result was obtained, however, by doing a time average of their chosen diagnostic over a very broad time window (of order 10^5, only an order of magnitude less than the typical relaxation time for the cases explored), and its solidity has been placed in question in subsequent work [149, 161]. Exploiting the increase in numerical power since then, and aided greatly by the diagnostics we have defined in the previous section, we report here[†] results showing relaxation for systems with $N \sim 10^3$. Further we obtain our results for the scaling of the relaxation time by doing ensemble averages (over realizations of the initial conditions) without time averages.

4.2.1 Temporal evolution of order parameters

Shown in Fig. 4.2 is the evolution of the virial ratio R, and the order parameters ϕ_{11} and ϕ_{22} in a *single realization* of a system with $N = 100$, and $R_0 = 0$. Note that the time axis (as it will be invariably here) is logarithmic. In Fig. 4.3 are plotted the same quantities for $N = 400$. While the fluctuations are very large, particularly in the first case, one can make out that there are, as expected, two stages in the macroscopic evolution probed by these parameters: a first stage ($t < 100$) of "violent relaxation" during which all quantities (and notably the virial ratio) fluctuates strongly before settling down to behaviors which appear to fluctuate about a well defined average, and specifically about unity for the virial ratio. The averages of the parameters

[†]Evolution of $N = 10^2$ particles to $t = 10^6$ requires about 20 minutes on a single processor; thus, given the scaling with $N^2 \log N$ of the computational cost per unit physical time, and a linear growth (see below) in the relaxation time itself, simulation times of order several weeks are required for the most rapidly relaxing case with $N = 10^3$. Our largest N results are ensemble averages over systems with $N = 800$, obtained by running simultaneously on a large number of work stations.

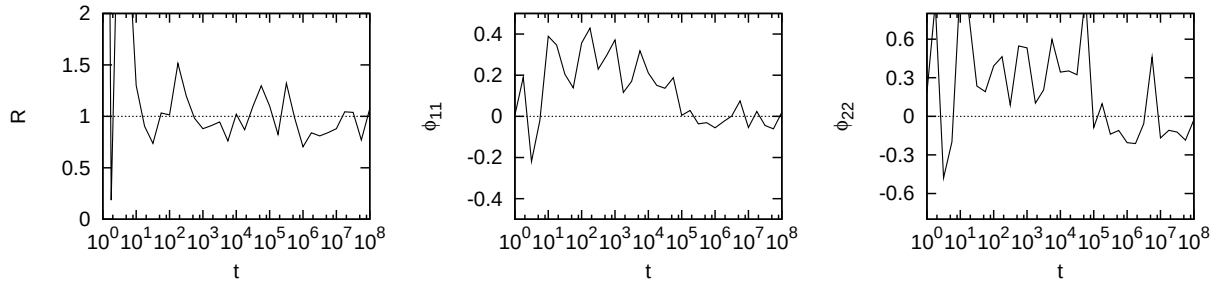

Figure 4.2: Temporal evolution of the virial ratio (left), ϕ_{11} (middle) and ϕ_{22} (right), for $N = 100$ and $R_0 = 0$.

ϕ_{11} and ϕ_{22} are clearly non-zero on a much longer time scale than that characterizing the virialization. These non-zero averages, which appear to be approximately the same in each case for the two different N, appear to remain roughly stable until at least about $10^4 - 10^5$, after which both ϕ_{11} and ϕ_{22} start to evolve toward zero. The time scale at which the evolution sets in is clearly significantly shorter for $N = 100$. This behavior should indicate, as we have discussed above, the relaxation to statistical equilibrium.

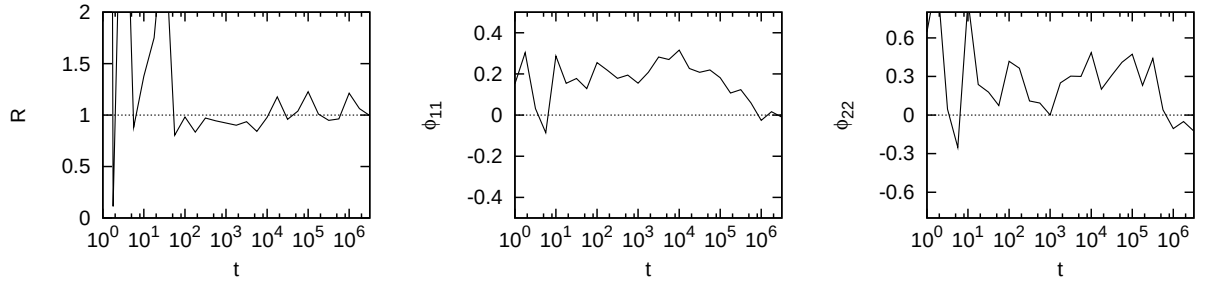

Figure 4.3: Temporal evolution of the same parameters as in Fig. 4.2, except that now $N = 400$ (and $R_0 = 0$).

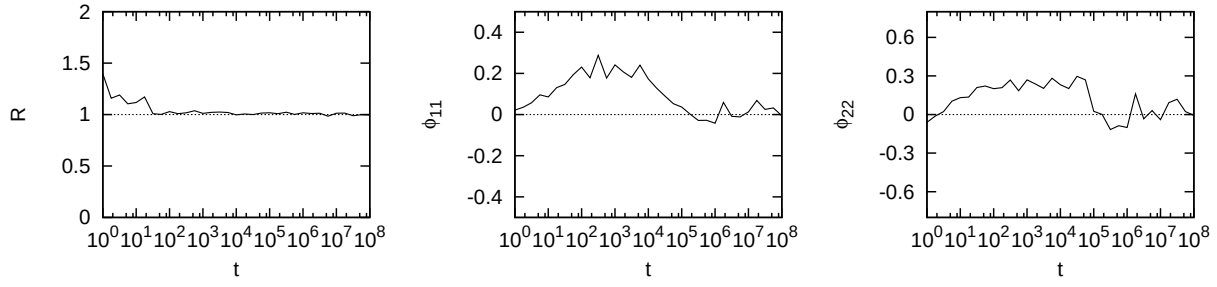

Figure 4.4: Temporal evolutions for the same case as in Fig. 4.2, but now averaged in a time window of width $\Delta t = 10$ as described in text.

These behaviors can be seen more clearly by averaging in a temporal window, of width small

compared to the characteristic times scales of this apparent evolution. Shown in Fig. 4.4 and 4.5 are the same quantities for the same simulations, but now each point represents the average over one hundred time slices, equally spaced in a window of width $\Delta t = 10$ centered on the given time.

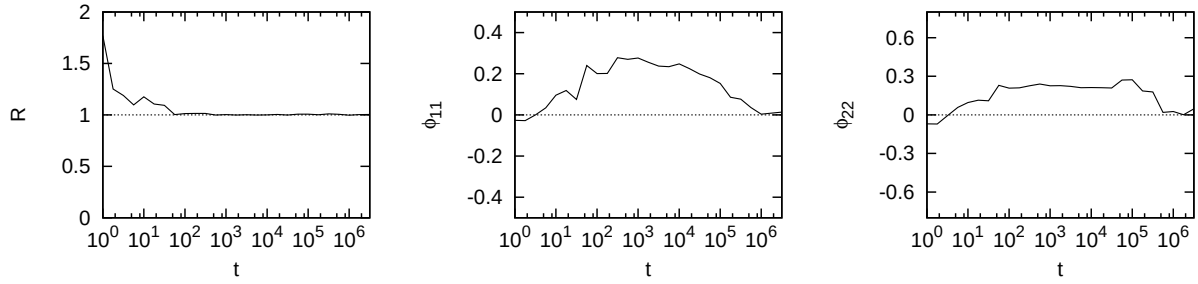

Figure 4.5: Temporal evolutions for the same case as in Fig. 4.3, but now averaged in a time window of width $\Delta t = 10$.

These behaviors are thus clearly indicative of the evolution expected, which is that believed to be typical of long-range interacting systems: violent relaxation brings one on a short time scale to a QSS, as a result of a mean field dynamics described by the coupled Vlasov-Poisson equations (and this independent of N). On longer, $N-$*dependent* times scales, one relaxes to the mean-field equilibrium, given in this case by Eq. (2.162). That the decay to zero of ϕ_{11} and ϕ_{22} does indeed correspond to relaxation to the statistical equilibrium of Eq. (2.162) can be tested in further detail. Fig. 4.6 shows the velocity and space distributions for $R_0 = 0$ and $N = 400$ particles, averaged again over a time window of width $\Delta t = 10$, at $t = 10^3$ and $t = 10^6$. The continuous lines correspond to Eq. (2.162), clearly in very good agreement at the later time, and very different in the QSS phase. We have also checked (but do not show here) the agreement of the distribution of particle energies. These results indicate that ϕ_{11} and ϕ_{22} are very good diagnostics of the evolution toward equilibrium: indeed below we will see that they are typically more discriminating of relaxation than the full density and velocity distributions.

4.2.2 Dependence on initial virial ratio R_0

Shown in Fig. 4.7 are the evolution of ϕ_{11} for $N = 100$ and $N = 400$ starting now from four different values of R_0, as indicated $(0, 0.1, 0.5, 1)$. The results are averaged again in a time window of width $\Delta t = 10$. Note that results for $N = 100$, which extend up to $t = 10^8$, indicate that the evolution toward the statistical equilibrium is really a relaxation to a definitive equilibrium behavior, i.e., which is stable and persists. This is further confirmed by Fig. 4.8 which shows the spatial and velocity distributions for the case $R_0 = 0$ and $N = 100$ at $t = 10^8$ (with the same time averaging window as used above in Fig. 4.6). Fig. 4.7 shows that there are, nevertheless, very significant fluctuations in ϕ_{11} and ϕ_{22}. These could indicate significant macroscopic, but stochastic, deviations from the equilibrium persisting over very significant times (see [158]). We will present evidence below that they are, as one would expect, finite N effects, with an amplitude which decreases as N increases.

We observe in Fig. 4.7 that, as expected, the QSS resulting from violent relaxation is clearly different depending on the initial condition, with very different values of ϕ_{11}. Further the relaxation toward equilibrium is evident in most cases, but at a time which depends not only

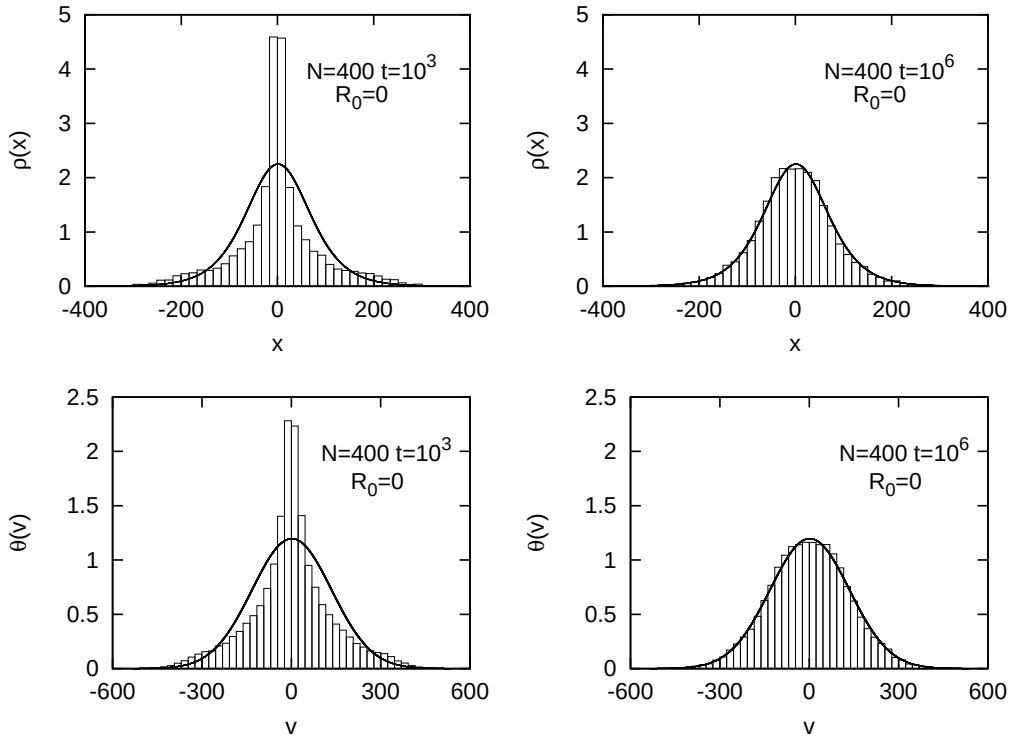

Figure 4.6: Density (top, left and right panels) and velocity (bottom, left and right panels) distributions at $t = 10^3$ (left) and $t = 10^6$ (right), for $N = 400$ and $R_0 = 0$. The same time average as in the previous two figures has been used.

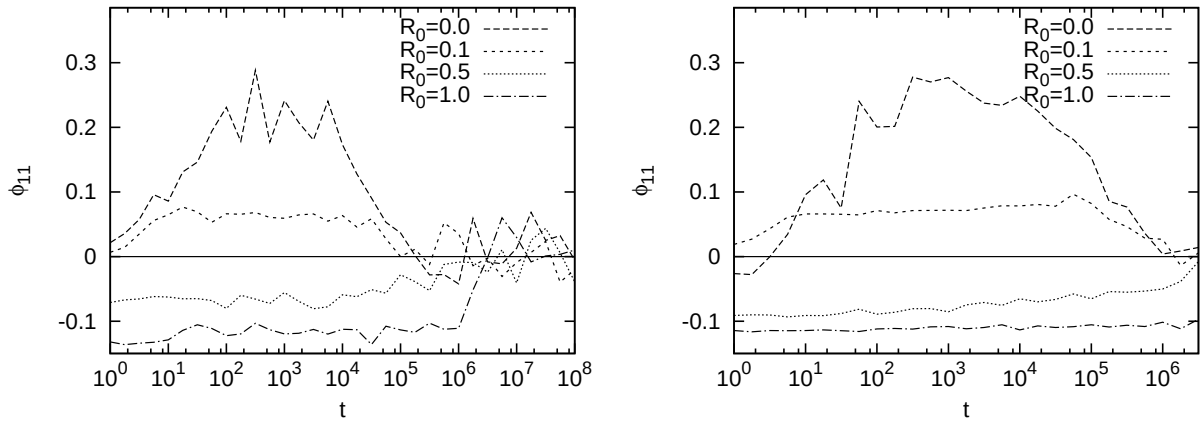

Figure 4.7: Evolution of ϕ_{11} for different R_0, averaged in time window of width $\Delta = 10$, for $N = 100$ (left) and $N = 400$ (right).

on N, but also on R_0 (or the intermediate QSS state). More specifically, the smaller is R_0 the shorter is the lifetime. Indeed for $R_0 = 1$ we just see the onset of the relaxation for the case $N = 100$, but do not see it at all for $N = 400$. For $N = 100$ there is a difference of a factor

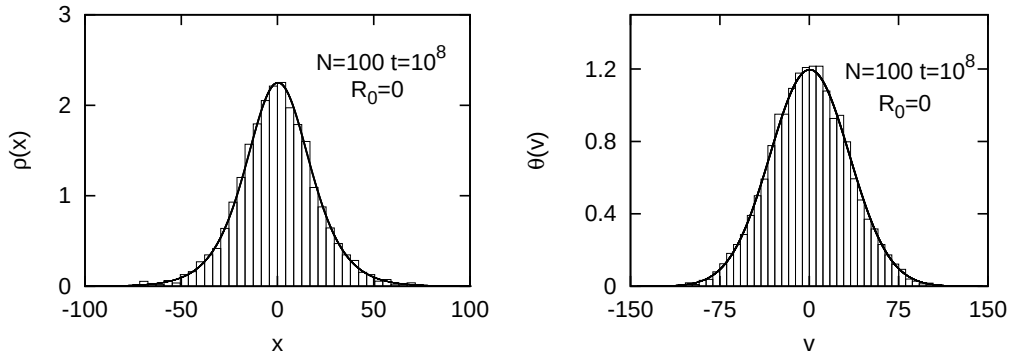

Figure 4.8: Density (left) and velocity (right) distributions at $t = 10^8$, averaged in a time window of width $\Delta = 10$, for $N = 100$ and $R_0 = 0$.

of about one hundred in the time at which relaxation appears to becomes clearly visible in the cases $R_0 = 1$ and $R_0 = 0$. In the respect we remark that earlier studies have not considered this kind of cold initial condition, in which relaxation occurs more rapidly.

4.2.3 Estimation of N dependence using ensemble average

Let us focus now on the N dependence of the relaxation. We wish to determine the scaling with N of the characteristic time for relaxation, at a fixed value of the initial virial ratio. Given the very significant noise in the order parameters at the particle numbers we can simulate numerically up to times on which relaxation occurs to do so we must average out these fluctuations. This can be done using either a time average on a single realization (as above) or an average over realizations (or possibly some combination of both).

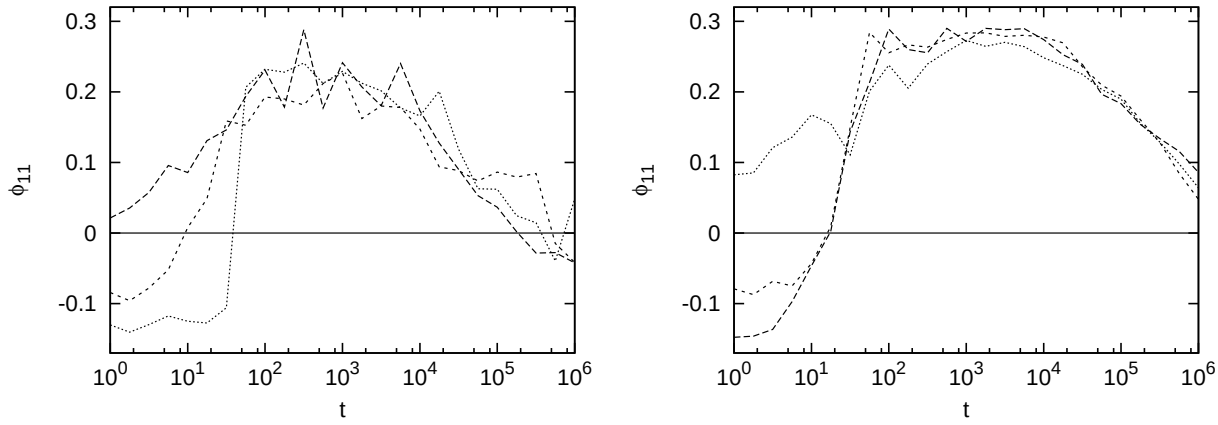

Figure 4.9: Evolution of ϕ_{11} for $N = 100$ (left) and $N = 800$ (right) for $R_0 = 0$ in different realizations, with time average in window of width $\Delta t = 10$.

Shown in Fig. 4.9 is a plot of the evolution of ϕ_{11} in three different realizations for $N = 100$ and $N = 800$ and $R_0 = 0$, up to 10^6. The quantities are again averaged in the same window

as above. The variance, albeit clearly decreasing with N, is in fact still so significant as to make an accurate determination of the scaling difficult. Averaging over larger time windows the curves become smoother, but such differences persist if we use a time window which is small compared to the time scale of the relaxation itself. In short the intrinsic finite N fluctuations from realization to realization in the (N dependent) relaxation time are still so large for N of this order as to limit significantly the determination of the average behavior from a single realization.

We thus consider a simple ensemble average, over realizations of the initial conditions. While we could combine time averaging and such an ensemble average, we choose not to do so as this may complicate the interpretation of our result. More precisely, if we perform a time average, we would need to check carefully for any possible dependence of our results on the chosen averaging window. We will explore below in some detail the relation between time averages and ensemble averages over initial conditions.

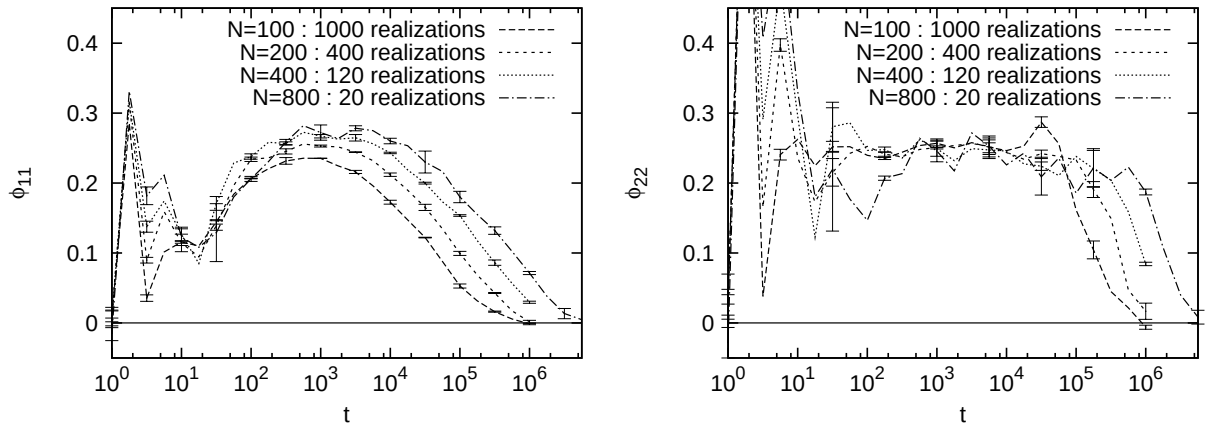

Figure 4.10: Evolution of ϕ_{11} (left) and ϕ_{22} (right) for $R_0 = 0$ in different N with ensemble average. The number of realizations averaged over is indicated in the panel. The error-bar is derived (see text) by determining the values in two sub-ensembles.

Shown in Fig. 4.10 are plots of ϕ_{11} and ϕ_{22} averaged over the indicated number of realizations (and without any time average) for each of the indicated particle numbers, for $R_0 = 0$. The error bars in this plot have been estimated by dividing randomly the realizations into two subsamples and recomputing the average in each of them (i.e. the error bar corresponds to the difference in the two averages).

Using these results we now determine the scaling with N. Shown in Fig. 4.11 is a plot of t_{relax}, the characteristic time scale for relaxation, as a function of N estimated from each of the curves for ϕ_{11} and ϕ_{22}. We have determined the value of t_{relax} in each case as that at which the order parameter reaches half its "plateau" value (i.e. in the QSS), i.e., we estimate the value of the parameter which corresponds to the approximate plateau and then determine the time at which half this value is attained. The error bars correspond to those estimated from those given in the previous figure. Shown also are linear behaviors, which in both cases provide a good fit to the results.

Shown in Fig. 4.12 are the ensemble averaged evolution of ϕ_{11} for the three other initial conditions, for the same four values of N. The determinations of the relaxation times, for each

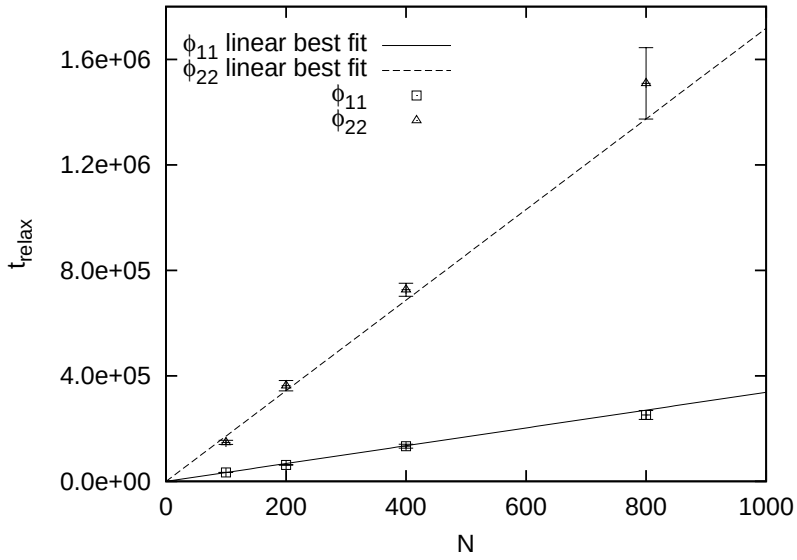

Figure 4.11: Plot of estimated relaxation time as a function of N, estimated using ϕ_{11} and ϕ_{22} as described in the text. Linear best fit lines are also shown. The error-bar indicated is derived from those in the preceding figure.

Table 4.1: Estimated relaxation time t_{relax} for different initial conditions. "-"indicates that our data does not allow us a determination of this time using our chosen criterion.

N	$R_0 = 0$	$R_0 = 0.1$	$R_0 = 0.5$	$R_0 = 1$
100	3.4e+04	8.4e+04	2.7e+05	-
200	6.5e+04	1.7e+05	5.3e+05	-
400	1.3e+05	6.8e+05	-	-
800	2.5 e+05	-	-	-

case where this is possible by the same method as used above, are shown in Table 4.1. As there are so few points we have not performed the same fitting procedure (with estimated error bars) as above, but it is clear that the given values are consistent with a scaling of the relaxation time linear in N. In the case $R = 1$, however, we cannot deduce any reliable estimate of the scaling with N, as we can just see the onset of the relaxation for $N = 100$ but not in the other cases.

This last curve and the data in Table 4.1 allow us to see more quantitatively the dependence of the relaxation time on the initial value of R_0 also. At fixed N we see that, between $R_0 = 0$ and $R_0 = 0.5$ the estimated relaxation time increases by a factor of about eight. These considerable differences translate into a very different appearance to the curves: in the case of $R_0 = 0$ the "QSS plateau" is much less visible as there is only a very small separation between the time scales for the establishment of the QSS ($\sim 10^2$) and the onset of relaxation.

The exact definition taken here for the relaxation time is somewhat arbitrary — we could equally consider the time at which ϕ_{11} deviates by 10% from its plateau value, or, say, reaches 10% of this value. Because the relaxation is very slow — to show the evolution of ϕ_{11} we

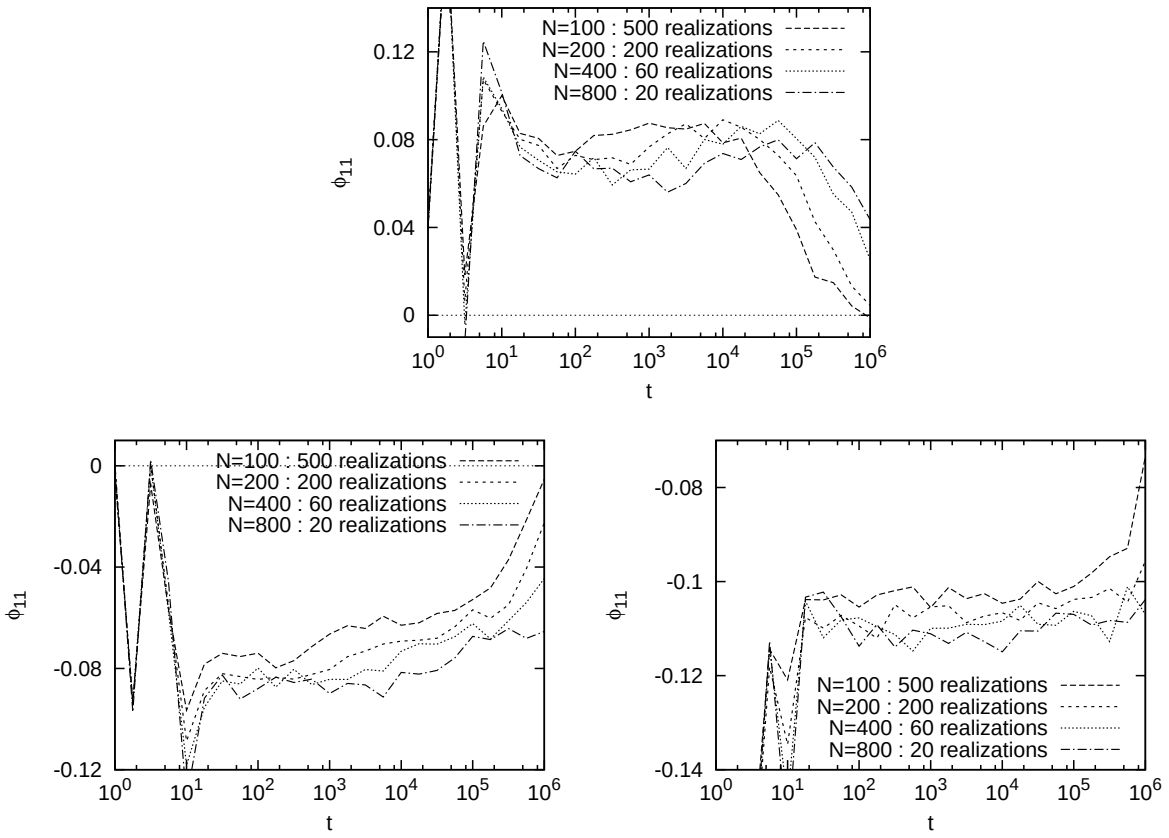

Figure 4.12: Ensemble averaged ϕ_{11} evolution for $R_0 = 0.1$ (top), 0.5 (bottom-left) and 1 (bottom-right) for different N.

must plot it as a function of the logarithm of time — such definitions would give enormously different results for the estimated time (differing by two to three orders of magnitude). Equally we see from Fig. 4.11 that if we use ϕ_{22} rather than ϕ_{11}, employing the same criterion we obtain times differing by an order of magnitude. That this factor indeed changes only the overall normalization of the times, and not their scaling with N, is evident from the fact that, as can be seen by eye, the curves in the decay phase can be superimposed on one another well by a translation parallel to the time axis.

It is interesting to see if a simple functional behavior can be fit to the decay of the order parameters. Shown in Fig. 4.13 are best fits to two simple functions for the case of initial conditions R_0 and $N = 100$, for which we have the best statistics. We have restricted to the range $t > 10^3$ to cut out the initial (violent) relaxation phase. One employs a hyperbolic tangent given by

$$\frac{\phi_{QSS}}{2}\left\{1 - \tanh[\alpha_h(\log t - \log t_{relax})]\right\} \tag{4.3}$$

in which, therefore, t_{relax} corresponds to the time estimated above. The best fit values of the parameters are $\phi_{QSS} = 0.24$, $t_{relax} = 10^{4.5}$ and $\alpha_h = 1.4$. The other is a stretched exponential

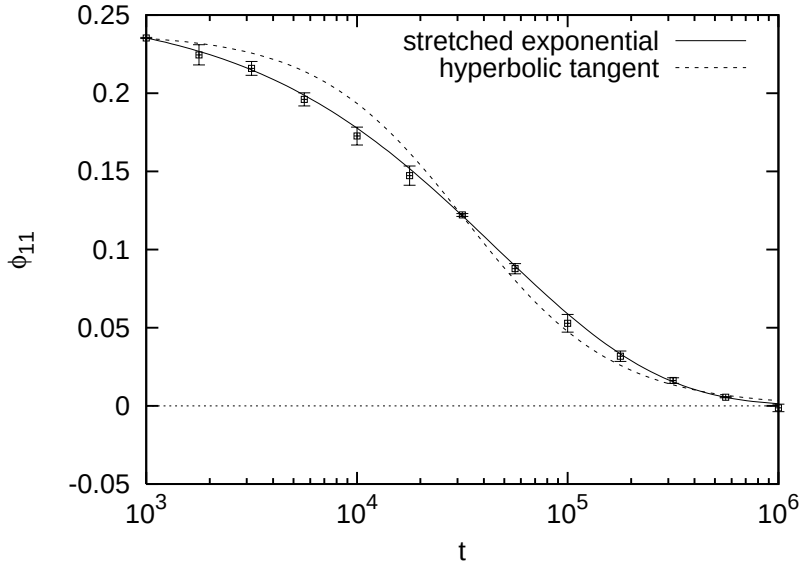

Figure 4.13: ϕ_{11} as a function of time ($t > 10^3$), for $N = 100$ and $R_0 = 0$. A best-fit to a hyperbolic tangent [see Eq. (4.3)] is shown as a dashed line, while the solid line is that for a stretched exponential form [see Eq. (4.4)].

form:

$$\phi_{QSS} \exp\Big\{ -[\frac{t}{t'_{relax}}]^{\alpha_s} \Big\} \tag{4.4}$$

and gives the best-fit values $\phi_{QSS} = 0.26$ $t'_{relax} = 10^{4.7}$ and $\alpha_s = 0.56$. The second function is clearly a significantly better fit. We note that the former function has been shown in [63] to give a good fit to the temporal evolution of the magnetization during relaxation in the HMF model. Stretched exponential relaxation, on the other hand, is observed in a range of physical systems, and notably in the relaxation of structural and spin glasses (see, e.g., [162]).

Another interesting quantity is the variance as the function of x, i.e. $\bar{v}^2(x)$, given by

$$\bar{v}^2(x) = \frac{1}{\rho(x)} \int_{-\infty}^{\infty} v^2 f(x,v) dv$$

which becomes constant for thermal equilibrium. Plots of $\bar{v}^2(x)$ are shown in Fig. 4.14 for $N = 100$ and $R_0 = 0$ at the indicated times, averaged over 1000 realizations. To calculate the variance from the data, we first divide the particles into 10 contiguous subgroups, of $N/10$ particles. The variance is determined in each subgroup and averaged over realizations and the position x is the ensemble-averaged center of mass of the corresponding subgroup. We clearly observe the relaxation of $\bar{v}^2(x)$ toward a constant value as time passes.

We draw attention to one important feature of these results which introduces a systematic uncertainty into them, which could only be reduced by doing significantly larger simulations: in principle the intermediate QSS is independent of the number of particles N, i.e., we are estimating the N dependence of the relaxation time of a state which is, up to fluctuations, N-independent; in practice it is clear in our data that there is some residual N dependence in the QSS at the N we are simulating — the "plateau" in the curves of the time evolution of our

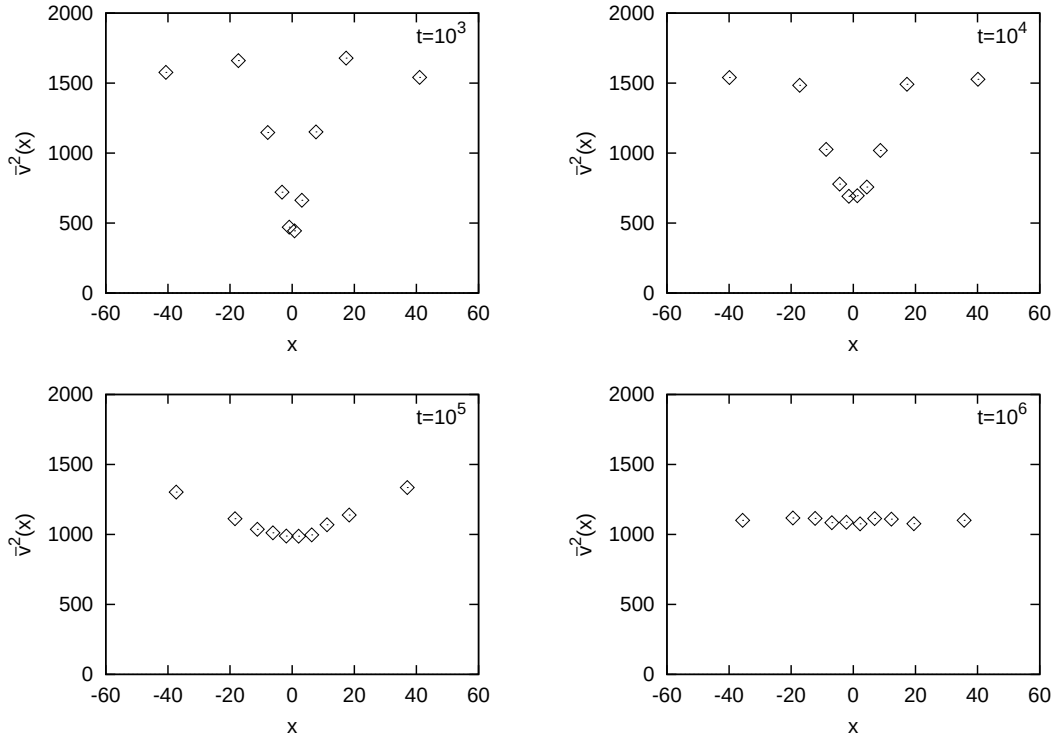

Figure 4.14: The variance of velocity as a function of x, $\bar{v}^2(x)$, for $N = 100$ and $R_0 = 0$ averaged over 1000 realizations at times indicated in each panel. The calculation of $\bar{v}^2(x)$ is described in the text.

order parameters do not exactly coincide. As we have seen that there is clearly a significant dependence of the lifetime on R_0, which we interpret to be one on the intermediate QSS rather than the initial condition itself, it is possible that the N dependence we measure at fixed R_0 is due to, or partially due to, this residual N dependence of the QSS. We believe, however, that such an effect, if present, is probably negligible: the differences in the QSS "plateau" at given R_0 for different N are very small compared to the differences between the QSS over the range of R_0, and further, for the larger N, the QSS do appear to converge. This is even the case for $R_0 = 0$, where the N dependence in the "plateau" is most evident. In this case, as we mentioned above when we discussed our initial conditions, an intrinsic N dependence of the QSS might be anticipated: as $N \to \infty$ the evolution becomes singular at $t = 1$, and the evolution at finite N is regulated by the fluctuations about a uniform distribution which are N dependent[‡]. That such intrinsic N dependence is weak, if present at all, is also indicated by the absence of visible N dependence of ϕ_{22} in Fig. 4.10.

4.2.4 Relaxation and fluctuation in the QSS

Analytically the relaxation toward equilibrium of systems with long range interactions may be described by kinetic equations, derived for example from the BBGKY hierarchy. In practice these

[‡]For the analogous 3D problem — evolution from cold uniform initial conditions — the precise N dependence of the virialized QSS state has been determined numerically in [160].

equations are intractable, and despite many attempts to develop appropriate approximation schemes which might make them tractable, there are really no solid results which allow us rigorously to model analytically the detailed phenomenology of relaxation observed in numerical simulations, and determine for example the observed N dependence of the relaxation time.

Inspection of our results for the temporal evolution of the parameters ϕ_{11} and ϕ_{22} lead to one simple observation: the relaxation time appears to be correlated with the amplitude of the fluctuations about the relevant QSS, i.e., the smaller the fluctuations in the QSS, the longer is its lifetime. While this is somewhat trivial when we consider a given initial condition (i.e. R_0) at fixed N — in postulating that there is a QSS we mean that the fluctuations about it are N dependent (and decaying with N) — it is not evident that this should be so for the different R_0 at fixed N. Theoretically such a correlation might not be surprising — in kinetic theory approaches the leading corrections to the collisionless (Vlasov) limit are, in perturbative approaches, sourced by fluctuations about the QSS (see, e.g., contributions of P.H. Chavanis, and of F. Bouchet and J. Barré in [57].).

Such a trend can be seen a little in Fig. 4.7, although in this case it is greatly obscured by the time averaging (i.e. it is much clearer if one plots a single realization in each case, which we have not done here). It is shown clearly to be present by the results in Figs. 4.15 and 4.16. The first shows the standard deviation, $\sigma_{\phi_{11}}$, of ϕ_{11} as a function of time, estimated in the indicated number of realizations of initial conditions $R_0 = 0$, for each of the different values of N indicated. The error bars in the plot correspond to the spread in $\sigma_{\phi_{11}}$ when it is estimated in two sub-ensembles defined by randomly dividing the realizations into two. As remarked above the fact that $\sigma_{\phi_{11}}$ decreases with N — and thus, given that the lifetimes of the states have been observed to increase with N, that there is a correlation of the lifetime with their amplitude — is not surprising: it simply means that the fluctuations about the QSS are, predominantly, due to finite N effects which will vanish as $N \to \infty$. We note that the amplitude of $\sigma_{\phi_{11}}$ in the approximate "plateau" region — corresponding to the QSS – scales as $1/\sqrt{N}$, i.e., as they would if the fluctuations of ϕ_{11} is the sum of N uncorrelated contributions from the N particles.

Shown in Fig. 4.16 is the same quantity but now for the different values of R_0, at two different fixed N ($N = 100$ and $N = 800$). In both cases we see clearly (except perhaps for the lowest curve in the lower panel, which is noisier due to the much smaller number of realizations) that the amplitude of fluctuations decreases as R_0 increases, i.e., that the amplitude is (inversely) correlated with the lifetimes we have observed for these states.

We note that these figures giving the behavior of the variance of our macroscopic parameters also contain a lot of other useful information beyond the correlation we have just observed. Indeed these curves themselves show very clearly the different time-scales in the dynamics: the first period of "violent relaxation" is clearly identifiable by a very large variance, which decays on a time scale of order several tens of dynamical times; this is followed by an approximately stable value depending on the QSS (Fig. 4.16), which then evolves on a much longer time scale, dependent on and increasing with N, toward a value which is independent of the initial state (i.e. thermal equilibrium).

These results also allow us to conclude more about the meaning of our quantitative results for the scaling of the relaxation time, which have been calculated using the ensemble average: the systematic decrease with N of the variance of ϕ_{11} (and, we have verified, of ϕ_{22}) implies that such an ensemble average, for sufficiently large N, can indeed be interpreted consistently to give the macroscopic behavior of a single realization in the ensemble. Thus, as we have been implicitly assuming, we can indeed take our determined relaxation times to represent those of single realizations, at sufficiently large N.

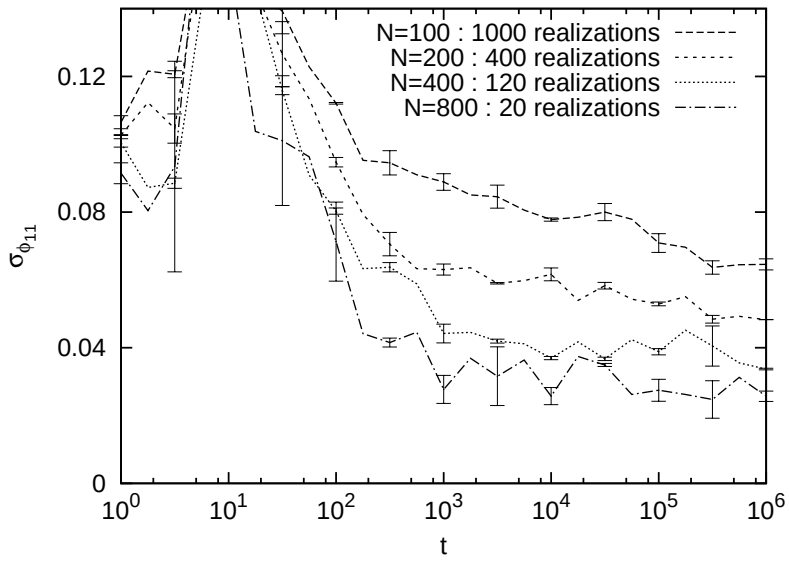

Figure 4.15: Temporal evolution of the standard deviation of ϕ_{11}, estimated for each N over the indicated number of realizations of the initial condition with $R_0 = 0$. The error-bars are derived as described in the text.

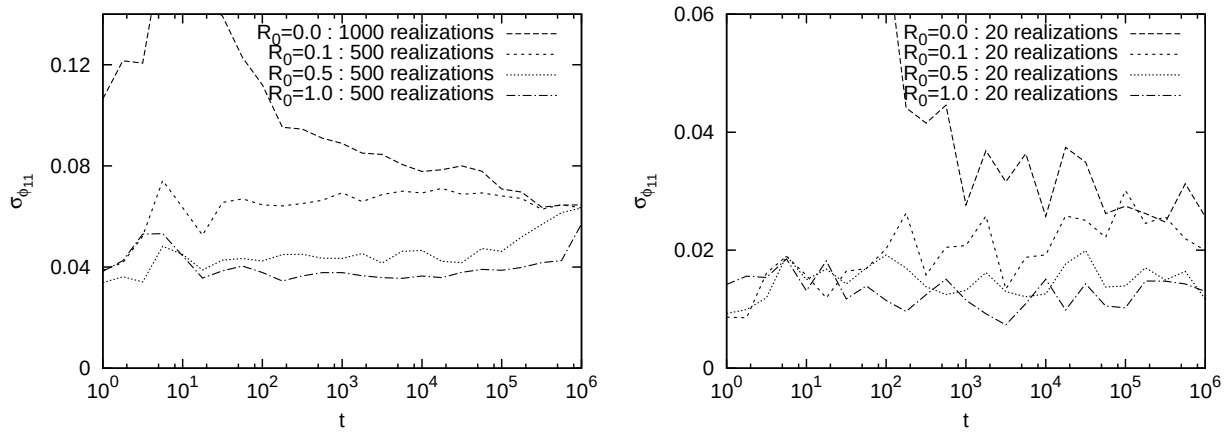

Figure 4.16: Temporal evolution of the standard deviation of ϕ_{11}, estimated over the indicated number of realizations of each of the initial conditions with the indicated R_0. The left panel is for $N = 100$, the right panel $N = 800$.

It is interesting to go a little further and consider what the relation is, at finite (but large) N, between the fluctuations in the ensemble average and the temporal fluctuations in a single realization. Indeed *if*, as we have postulated above, there is a real correlation between the amplitude of the fluctuations measured in the ensemble average and the lifetime of the corresponding QSS, it must be that these fluctuations measured in the ensemble bear some close relation to the temporal fluctuations in the same parameters in a single realization. That this is the case, to a good first approximation, can be seen from Figs. 4.17 and 4.18, which show exactly the

same quantities as in the previous two figures, but that the standard deviations are calculated in one hundred time slices equally spread over a time window of width $\Delta t = 10$ centered on the indicated point. We see the same quantitative behaviors as in the previous plots, and even, in particular for $N = 800$, quite good qualitative agreement.

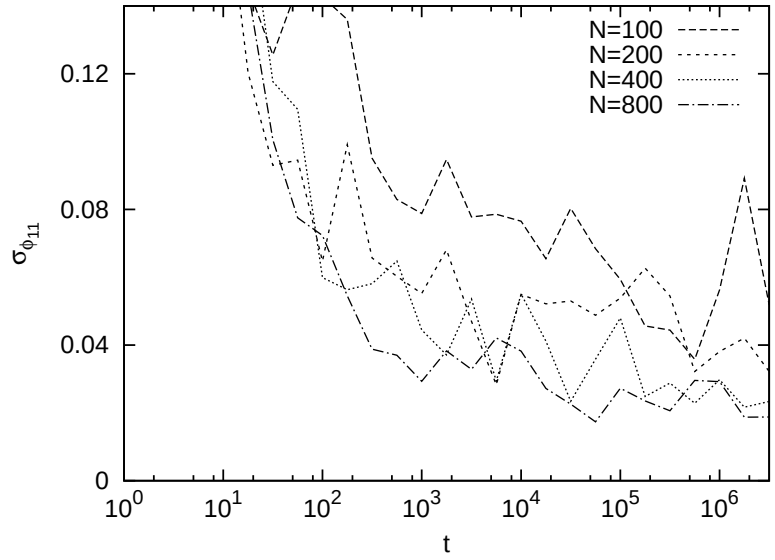

Figure 4.17: Temporal evolution of the estimated variance of ϕ_{11} in the same case as Fig. 4.15, but with a time average now over a window of width $\Delta t = 10$.

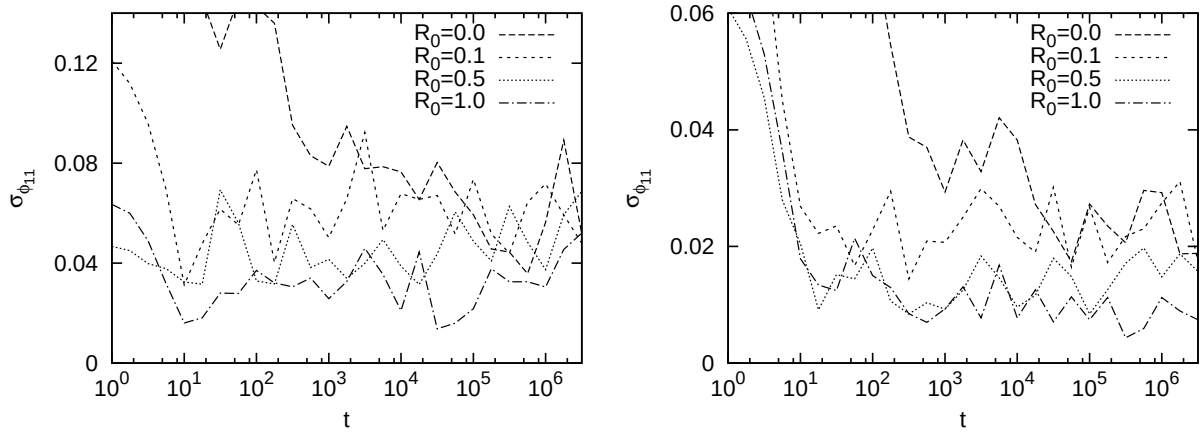

Figure 4.18: Temporal evolution of the estimated variance of ϕ_{11} in the same case as Fig. 4.16, but with a time average now over a window of width $\Delta t = 10$.

To allow further detailed comparison, in Fig. 4.19 and Fig. 4.20 are shown, for $R_0 = 0$ (left panels) and $R_0 = 1$ (right panels), and $N = 200$ in both cases, the histogram of the values of ϕ_{11}, at the indicated time measured, in Fig. 4.19, in one hundred simulations from realizations of the same initial conditions, and, in Fig. 4.20, in one hundred snapshots in a window of width

$\Delta t = 10$ in a single realization from one realization of the same initial conditions. Comparing the four panels in the two figures one by one, we see that, although the fluctuations in each case are clearly not sampled from an identical distribution, the agreement is strikingly good: not only, as expected from what we have already seen above, do the averages and variances agree well in each case, but the general shape of the histograms, which is quite different in each QSS, resemble one another strongly. The results are also clearly in line with the conclusion drawn above for what concerns the relaxation to thermal equilibrium: at $t = 10^6$ we see that the cold initial conditions have relaxed to a distribution centered on the value in thermal equilibrium, while for the case $R_0 = 1$ the system is still in a QSS but has evolved very slightly toward equilibrium.

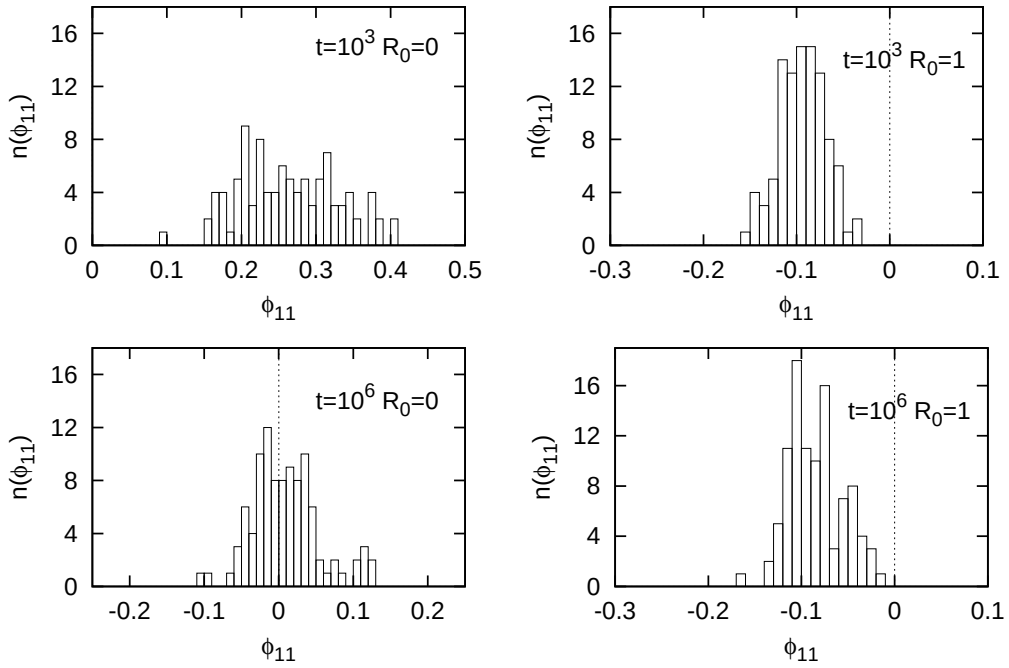

Figure 4.19: Histogram of the values of ϕ_{11} measured at the indicated time in one hundred simulations started from independent realizations of initial conditions with the indicated values of R_0, for $N = 200$ particles. The dashed line indicates $\phi_{11} = 0$, the value at thermal equilibrium. For $R_0 = 0$ the relaxation of the system from the QSS to thermal equilibrium is clearly visible, with both the central value and shape of the distribution evolving. For $R_0 = 1$ we observe, in line with the results above, that the system is still in a QSS but that the distribution has started to shift slightly toward the equilibrium one.

It would be interesting to develop this study with greater statistics, varying the width of the time window to see how good agreement can be obtained, but we will not do so here. Such a study is related to the fundamental (and so far unanswered) question as to whether the properties of QSS may be determined by averaging over an appropriate (non-equilibrium) ensemble, determined by the initial conditions. The theory of violent relaxation formulated by Lynden-Bell, for example, postulates an answer to this question [19]: the appropriate ensemble is that of all configurations corresponding to a phase space distribution function permitted by the (collisionless) Vlasov dynamics. If this theory were correct (which is not the case for this

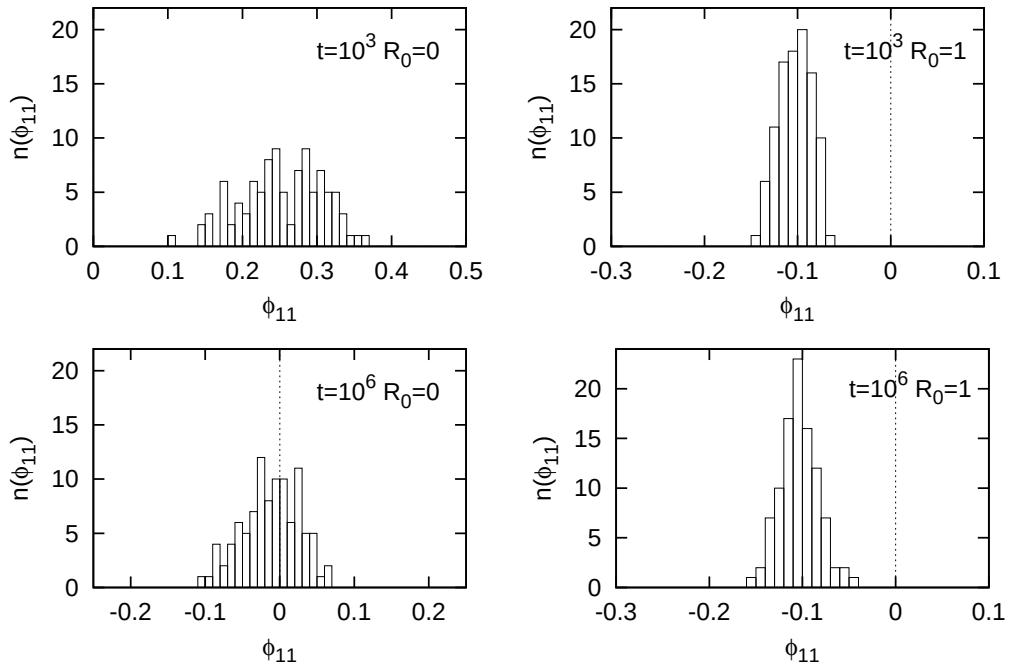

Figure 4.20: Histogram of the values of ϕ_{11} measured at one hundred equally spaced times in a temporal window of width $\Delta t = 10$ centered on the time indicated in each panel. The simulations are from the same cases as in Fig. 4.19. We observe a qualitative agreement between the amplitudes and shapes of those in Fig. 4.19.

system [95]) we should perform our ensemble average over such configurations rather than the more restricted one we have considered.

4.3 Some numerical tests

Although the method of numerical simulation is, as we have emphasized, very precise, it is still possible that the numerical error associated to the finite machine precision may be a relevant limitation (and could even invalidate our conclusions). We report here some tests we have performed in this respect.

4.3.1 Time reversibility

The dynamics of the continuum system is time reversible, but (as the system is chaotic) such reversibility would be expected to be reproduced in the simulations only for a finite time. To explore how precise our simulations are in this respect, we test reversibility directly: starting from a chosen initial condition at $t = 0$ we integrate up to a time $t = t_{rev}$; we then reverse the particle velocity and see whether the system has returned to its initial state at $t = 2t_{rev}$. Shown in Fig. 4.21 are the final configuration (in phase space) obtained in that way, for $t_{rev} = 1, 10, 100$ starting from an initial condition with $R_0 = 0$ (i.e. cold initial condition), $N = 10^2$. For $t_{rev} = 1$ almost perfect reversibility is found (the v-axis has been amplified by three orders of magnitude), at $t_{rev} = 10$ the agreement is still extremely good, with just a few particles off axis, while at

$t_{rev} = 100$ the reversibility has clearly been lost.

Thus on the time scale we have studied our simulations are clearly not reversible, and thus we cannot be completely certain that the finite machine precision does not invalidate our results.

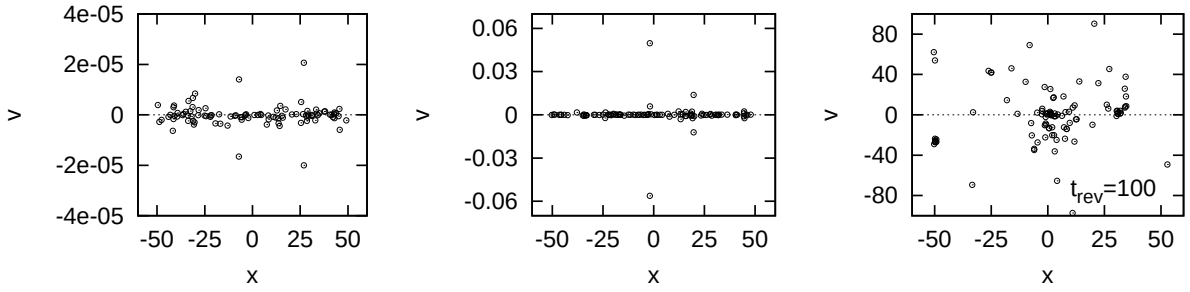

Figure 4.21: Configuration in phase space of reversibility test with $t_{rev} = 1$ (left), 10 (middle) and 100 (right) for $N = 100$ and $R_0 = 0$.

4.3.2 Effects from data-format precision and machine of integration

One further check on the role of precision we can do is to compare the results of calculations done using double precision format for the date (employed in all the simulations reported above) with those obtained using single precision format. Shown in Fig. 4.22 are the temporal evolution of ϕ_{22} (averaged in time window of width $\Delta t = 10$) for two different initial conditions. In the first case ($R_0 = 0, N = 100$) we see that the two differ somewhat, although the same overall trend of relaxation is observed on a similar time scale. The differences between the two are in fact about the same as those we observe between two different realizations of the initial condition evolved at double precision. Given the irreversibility of the numerical simulations, this is what we would expect. The result we have obtained, averaged over realizations (or time), should therefore be unchanged at single precision or double precision. In the second case ($R_0 = 1, N = 100$) we see, on the other hand, good agreement up to $t \sim 10^5$ and a very different behavior afterward, with the single precision simulation apparently relaxing. We interpret this to indicate that the relaxation is in this case actually caused by the additional fluctuation introduced by the numerical rounding error. Indeed, as we have seen, for the case $R_0 = 1$ the fluctuation about the QSS are very suppressed compared to that for $R_0 = 0$. In this case therefore we believe that the use of single precision would produce spurious results.

Finally in Fig. 4.23 we show the result of another test of precision: the evolution of ϕ_{22} obtained, from a chosen initial condition, run on two different machines (but with similar characteristics). The excellent agreement presumably reflects the fact that the numerical rounding error is actually performed in the same way (rather than introducing a random error). We expect that this would not be the case if we run the simulations on two very different machines.

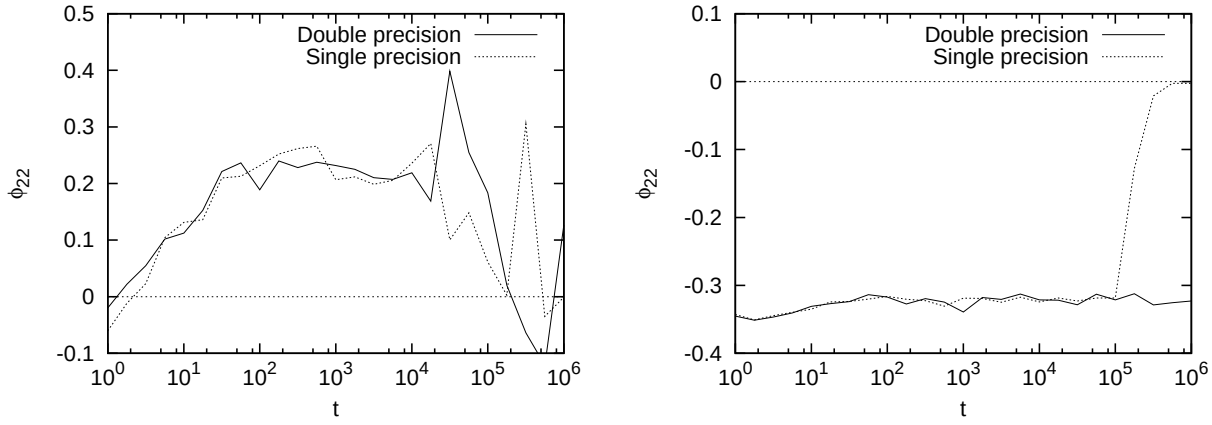

Figure 4.22: Temporal evolution of ϕ_{22} for $N = 100$ with $R_0 = 0$ (left) and $R_0 = 1$ (right) using the single and double precisions, starting from the same initial configurations for each R_0.

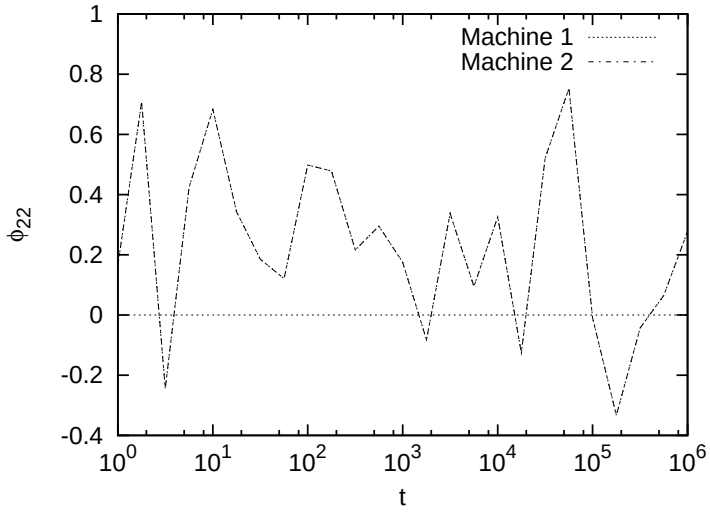

Figure 4.23: Temporal evolution of ϕ_{22} of $N = 100$ and $R_0 = 0$ of the same initial condition run in two different machines of almost the same capacity.

4.4 Conclusions and discussions

4.4.1 Summary

Our primary aim in this chapter has been to establish and characterize more fully than in the previous literature the relaxation to thermodynamic equilibrium of one of the simplest toy models for long-range interacting systems: equal mass self-gravitating particles in one dimension (or infinite sheets in three dimensions). Compared to the much studied HMF model, notably, the basic properties of this model have remained somewhat unclear, and indeed marked by some controversy in the literature. The novelty of our work compared to previous studies is not just that we do more and larger simulations from a broader range of initial conditions,

but that we have identified a tool which is very useful to characterize the evolution of the system: the measurement of appropriately normalized moments of the distribution function which characterize the "entanglement" of the one particle distribution function in configuration and velocity space. This is particularly appropriate as a measure simply because the thermal equilibrium has the property that such entanglement is absent while, we have shown, in *any other* stationary solution of the Vlasov-Poisson equations such entanglement is present. We note that this result, which we showed to be valid for any interaction in one dimension (but, as noted, excluding periodic systems like the HMF), can be generalized easily to three dimensions if we restrict to stationary solutions which have radial symmetry in space and velocity. This suggests that these "order parameters" may also be useful indicators of relaxation in much more general, and perhaps, as we discuss below, even useful tools for understanding the mechanisms of such relaxation.

With the aid of these macroscopic measures, we have shown in our numerical study, of a range of simple "waterbag" and cold initial conditions, that the system manifests the behavior thought to be generic in long-range systems: there are essentially two phases in the evolution with two completely different time-scales. An initially non-stationary state evolves first, on timescales characterized by the "dynamical time" $t_{\rm dyn}$ (roughly the crossing time of a particle in the mean-field due to the others), to a QSS, an out of equilibrium state, which then evolves on a much longer time scale, dependent on the number of particles, to thermal equilibrium. In other words it is reasonable to suppose that the system is ergodic (and mixing) on these very long time scales, but not so on the shorter time scales. Further we can identify clearly that the QSS resulting from different initial conditions (i.e. different values of R_0) are very different macroscopically, characterized by very different phase space entanglement.

Focussing on the the N dependence of the relaxation, averaging over a very large number of realizations to average out the fluctuations, we have concluded that the characteristic time scale for relaxation behaves, to a very good approximation, as

$$t_{\rm relax} \sim f_{QSS}\, N\, t_{\rm dyn} \tag{4.5}$$

where f_{QSS} is a numerical factor which depends on the initial condition, which we have denoted in this way as we expect that this dependence is not strictly on the initial condition but on the QSS which results from it. We have seen that this prefactor increases as R_0 does, by about a factor of ten between $R_0 = 0$ and $R_0 = 0.5$, and approximately a further factor of ten for $R_0 = 1$. We have noted that the overall normalization of f_{QSS} is rather arbitrary, as it depends greatly on the exact criterion used to define the relaxation time-scale. Given that the evolution toward zero of ϕ_{11}, which is what we have used to determine this time scale, is in fact well fit by the simple functional behavior as a function of the time on a logarithmic scale, the normalization of f_{QSS} can differ by two orders of magnitude by a trivial change in its definition. More specifically we have seen, that in the case where we have accumulated the greatest statistics allowing us to constrain the temporal evolution, a very good fit to our order parameter ϕ_{11} is obtained to a stretched exponential form.

Although the relaxation of this system, and in general long-range interacting systems, is not well understood, we can say that this finding of a linear scaling — besides the fact that it is, as we will discuss below, in line with less complete previous analyses — is not a surprising result: such a scaling can be anticipated both on the basis of simple naive estimates of the effects of collisionality, as well from general considerations based on kinetic theory.

We note that our study suggests also that the "order parameters" we have defined and studied may be relevant quantities for understanding relaxation in this and other long-range systems.

Indeed in all cases we have observed that, at sufficiently large N, these parameters start from a non-zero value in the initial QSS and evolve monotonically toward zero, i.e., the relaxation of the QSS can apparently be described as a process of progressive "disentanglement" of the one particle phase space density. In this respect the very different, much less efficient, relaxation observed in the HMF might be interpreted as a result of the absence of such entanglement in spatially uniform QSS. Further, in the case where we have enough statistics to provide a precise fit to the evolution of the parameter ϕ_{11}, we found that it is well fit by a simple stretched exponential form. It would be interesting to see in further study whether this fit is more than an approximate numerical fit for the case we have studied, and, if so, whether the exponent characterizing it is the same or not. As we have remarked such a functional form has been observed in other slowly relaxing (e.g. glassy) systems and theoretical tools derived in this context to understand relaxation may be relevant. In [162], for example, this behavior is linked to the existence of a fractal structure in a bounded accessible region of phase space. Indeed we note that in [89] it has been speculated (albeit for quite different reasons) that such a structure may be present in this model.

4.4.2 Comparison with previous literature

Let us now turn finally to compare our findings in greater detail with those in the previous literature.

An early numerical study by Hohl and Broaddus [163] which concluded a relaxation time proportional to $N^2 t_{dyn}$ was found to be incorrect by two groups, who studied the problem in greater detail (and with greater numbers of particles). However, these two groups found conflicting results: one found no evidence for relaxation at all to thermal equilibrium in their simulations [164], while the other [154] found relaxation on a time scales even shorter than $N t_{dyn}$. Further study (see [88, 155], which also contain a detailed synthesis of the previous literature) by the former group concluded that the discrepancy was related to the very specific initial condition studied by the other group. Studying this case in detail they found that it indeed appears to thermalize very rapidly, but some further, but not completely conclusive analysis of the evolution at longer times, suggested that this thermalization was not complete.

To determine whether these cases are consistent with our findings — and see whether our analysis using the parameters ϕ_{11} and ϕ_{22} can throw light on these previous findings — we have resimulated the relevant initial conditions. These are "counterstreamed" waterbag initial conditions, an example of which is shown in Fig. 4.24. We have simulated a range of such initial conditions, in particular the cases (one of which is that shown in the figure) considered by [154] and [88]. Shown in Fig. 4.25 are the density profile and velocity distribution at $t = 10^2$ obtained starting from a realization of initial conditions like those shown in Fig. 4.24, but with $N = 100$. We see that the profiles indeed agree very well with the equilibrium ones. In Fig. 4.26 is shown the evolution of ϕ_{11} as a function of time for the indicated values of N averaged in each case over the number of realizations indicated. We observe that, although small and fluctuating, its value is clearly on average non-zero, indicating that the state, despite the good agreement of the density and velocity profiles, is not in fact an equilibrium. Just as in the cases we studied we see clearly the relaxation toward equilibrium at longer times, and indeed that the characteristic time increases on N. Although we have not done the more extensive study required to determine precisely this N dependence, the results are quite consistent with Eq. (4.5) with a value of f_{QSS} of order that found for the case $R_0 = 0$.

This case illustrates the usefulness of the parameters ϕ_{11} and ϕ_{22} as discriminants of re-

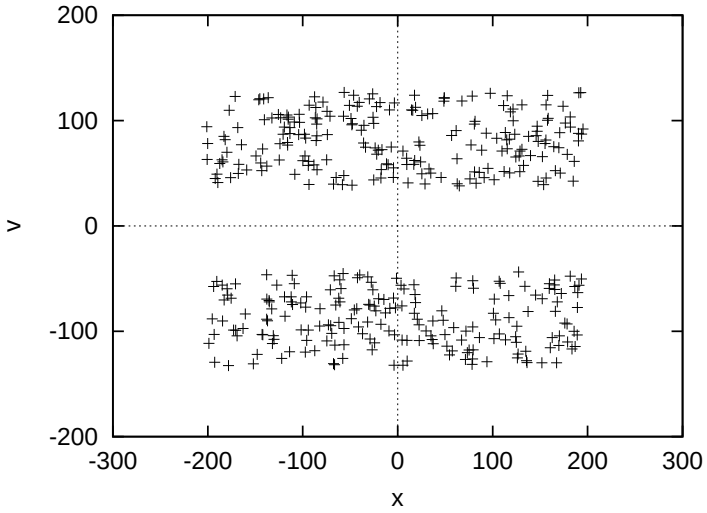

Figure 4.24: A "counterstreamed" waterbag initial condition in phase space, for $N = 400$ and $R_0 = 0.3$.

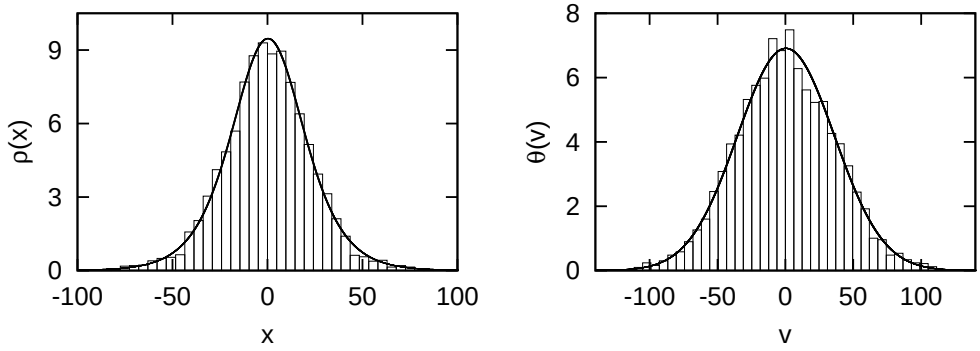

Figure 4.25: Density (left) and velocity (right) profiles obtained at $t = 100$ from counter-streamed initial condition with $N = 100$, with an ensemble average over 250 realizations. Solid lines are the corresponding thermal equilibrium profiles.

laxation: indeed we have just seen that the single measure of ϕ_{11} is sufficient to discard the interpretation of [154] of their results. This is simply because they are physically very appropriate indicators, for the reasons we have explained in introducing them: the property they probe — of entanglement of the phase space distribution — is one which must evolve significantly during relaxation, because the phase distribution must become separable. While ϕ_{11} and ϕ_{22} being zero does not *imply* thermalization, of course, we have not found a single QSS, despite exploring a broad range of initial conditions (considerably more extended that those reported here) in which they are *both* zero (within the uncertainty of fluctuations), i.e., the only states we have found in which they are both zero are states which we have concluded, using a range of other measures, are indistinguishable from the equilibrium state of Rybicki. It is not difficult, on the other hand, to find initial conditions which lead to a QSS in which $\phi_{11} \approx 0$ *or* $\phi_{22} \approx 0$.

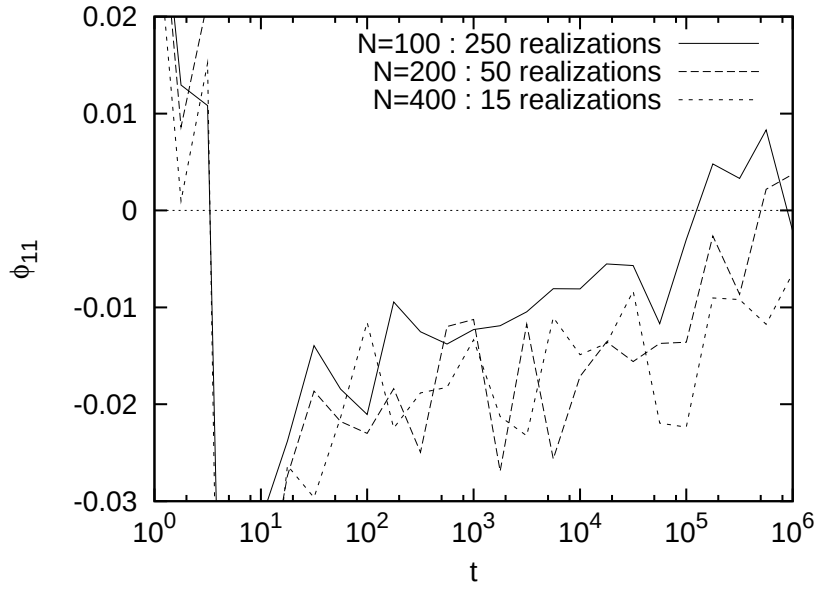

Figure 4.26: Temporal evolution of ϕ_{11} from a counterstreamed waterbag initial condition with different N.

Indeed for the waterbag initial conditions we have studied both ϕ_{11} and ϕ_{22} actually change sign as R_0 varies over the range we have considered, and one can thus find by trial and error the appropriate R_0 which make them zero individually.

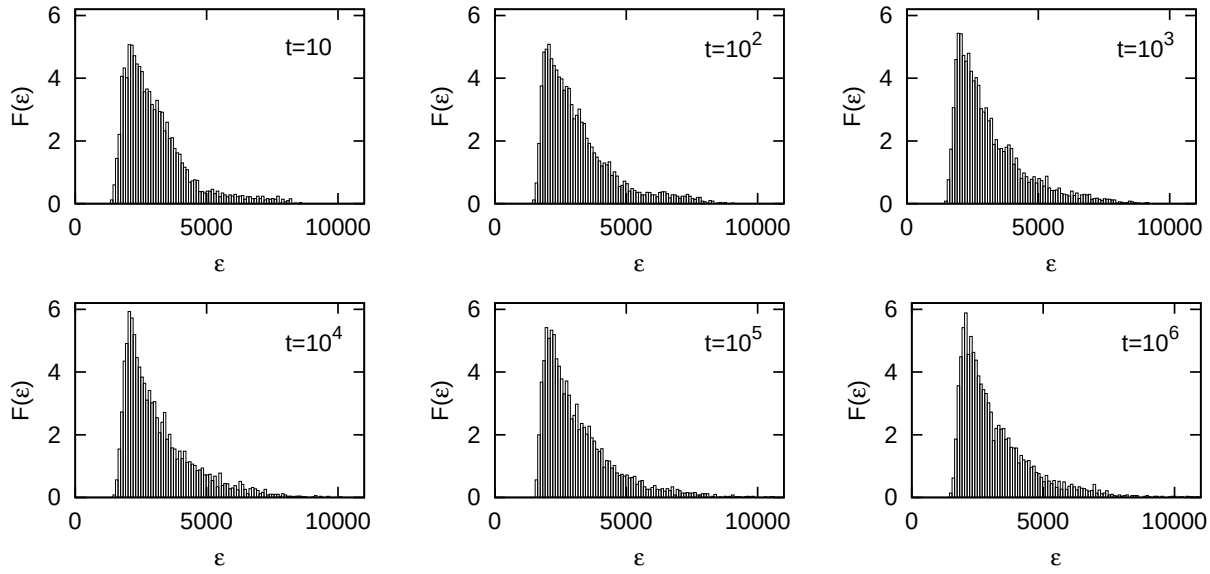

Figure 4.27: Energy distribution $F(\varepsilon)$ for counter-streamed initial conditions with $N = 100$, at the six times indicated on top-right of each panel. The curves are averages over 250 realizations. The thermal equilibrium $F(\varepsilon)$ is indistinguishable from the measured one at the final time shown.

Another evident quantity to measure, which we have in fact considered systematically but have not reported in detail, is the distribution $F(\varepsilon)$ of the individual particle energy ε. This is in fact generally a better discriminant of relaxation than either $\rho(x)$ and $\theta(v)$, i.e., we have found that in quite a lot of cases $\rho(x)$ and $\theta(v)$ are not easy to distinguish from the equilibrium profiles, but that $F(\varepsilon)$ allows one to see more clearly that one is indeed not in the equilibrium state. An example is the counter-streamed case just considered above. In Figs. 4.27 are shown, for $N = 100$, the evolution of the ensemble averaged $F(\varepsilon)$ at a few different times. We have not plotted the equilibrium curve, as it is indistinguishable from the measured curve at the final time shown. One can see clearly that, despite the good agreement of $\rho(x)$ and $\theta(v)$ shown in Fig. 4.25, the system is not in equilibrium at the early times: $F(\varepsilon)$ has a clearly visible excess of particles at high energies compared to that at the much later times at which the evolution of ϕ_{11} indicated relaxation (and $F(\varepsilon)$ indeed approaches very accurately its predicted equilibrium form). While such a measure of $F(\varepsilon)$, averaged over a large ensemble of realizations, can, in all the cases for which we have studied it, clearly discriminate relaxation, the use of just ϕ_{11} (and possibly ϕ_{22}) is an extremely efficient short-cut to "diagnose" relaxation.

Subsequent to [88], another group carried out, in the nineties, larger and more importantly, longer, simulations in order to clarify the issue. A first paper [87] reported the evolution of a rectangular waterbag initial condition corresponding to our case $R_0 = 1$, and reported a detection of relaxation to thermal equilibrium. These authors make a distinction between two time scales of relaxation: one of "microscopic relaxation", the other for "macroscopic relaxation". These are identified, and both found to be proportional to N, by considering the evolution of the mean standard deviation of the particle energies averaged over a time window T from their equipartition value. The former is estimated from the slope at short time of this function, and the latter from the position of "peaks" which are observed to occur at much longer times. While the latter is interpreted in terms of of macroscopic relaxation in the sense we have used here, the former is interpreted as a time scale on which particles sample the energy distribution but on which there is *no* macroscopic evolution. The justification for these interpretations are not clear, and no direct comparison with the equilibrium distribution derived by Rybicki, equation (2.162), has been reported which might show their correctness. Indeed both a subsequent article by the same authors [149] and a study in [161] place in doubt the correctness of the interpretation in terms of relaxation.

Nevertheless, in light of the results we have given here, it would be reasonable to infer that the results given in [87] are indeed correct, at least for what concerns the N dependence of the relaxation. Further comparison could of course clarify the relation of the behavior of their measured quantities and the macroscopic relaxation as we have probed it here (and should be much easier for the shorter lived, smaller R_0, initial conditions rather than the case $R_0 = 1$ studied by these authors). We do not believe, however, that there is any clear basis for either an operational or *physical* distinction between "microscopic" and "macroscopic" relaxation as described by these authors: as we have discussed there is an arbitrariness in the definition of the relaxation time because of the very slow nature of this relaxation. As we have noted, we could easily, for example, have obtained here estimates of the relaxation time differing by several of orders in magnitude in their prefactor, just like the two different time scales determined in [87], by using slightly different definitions, or choosing to use a different order parameter. This point can be illustrated by considering the evolution of $F(\varepsilon)$ for one of the cases we have considered: shown in Figs. 4.28 is this quantity for the case $R = 0.1$ and $N = 400$, averaged over 60 realizations. While we have associated (see Table 4.1 above) the time scale 7×10^5 to the relaxation in our analysis, one can discern by inspection of these figures significant evolution (in

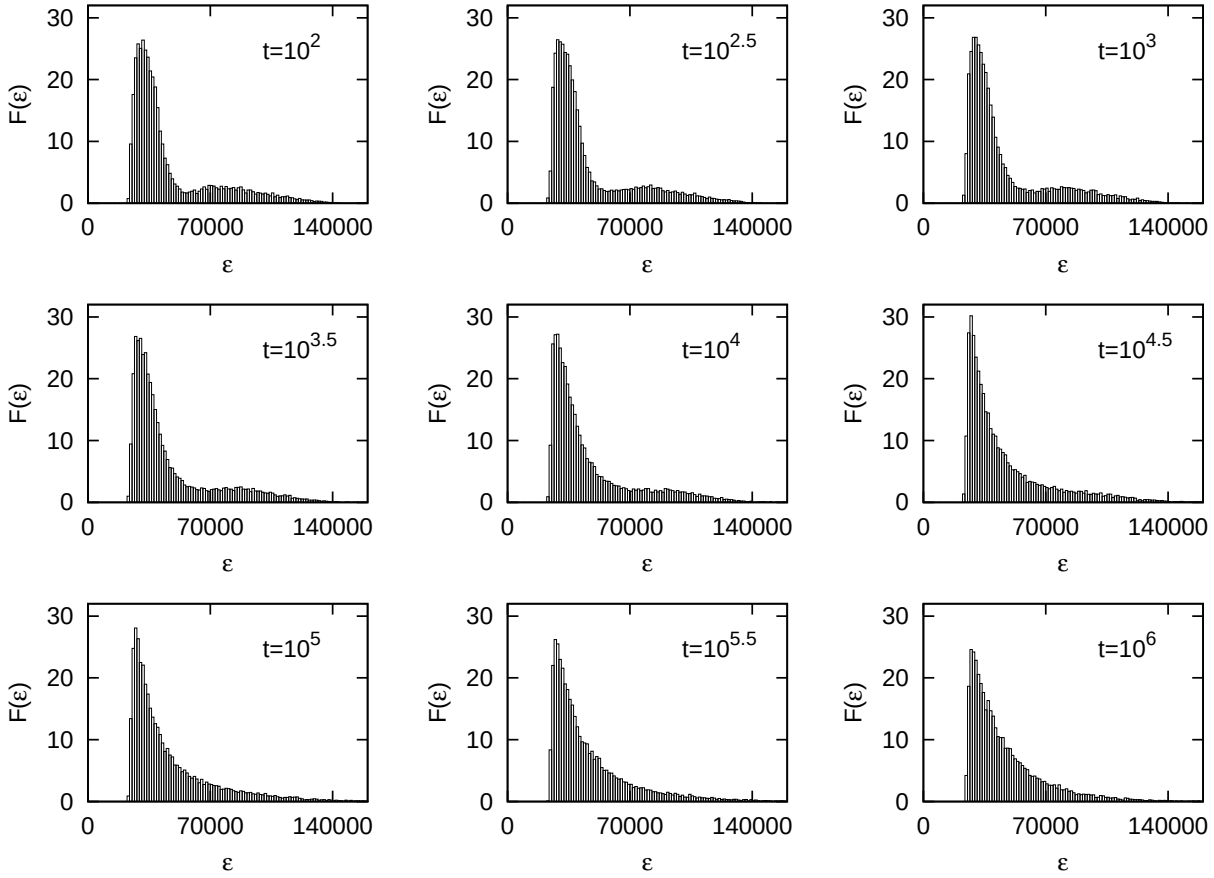

Figure 4.28: Energy distribution $F(\varepsilon)$ obtained from initial conditions with $N = 400$ and $R_0 = 0.1$, at the time indicated on the top-right of each panel. The distribution is obtained by averaging over 60 realizations.

particular of the initially clear "core-halo" structure) in $F(\varepsilon)$ already by $t = 10^{3.5}$, i.e., there *is* evolution of the energy distribution on the time scale of "microscopic" relaxation (of order Nt_{dyn}) identified in [87]. While it is possible that there are different time scales associated to different physical processes, it seems a more reasonable interpretation to us to suppose that there is single physical relaxation process leading, albeit very slowly, to macroscopic relaxation of the system, and to characterize this relaxation by a function and the scaling of its parameters with N. In this respect it is interesting to note that the specific stretched exponential form we fitted to the temporal behavior has the known property [165] that it can be written as a weighted integral over simple exponentials (i.e. it can be interpreted as arising from the superposition of an infinite number of relaxation processes each with a single characteristic time).

In [149] the same authors have also described chaotic "itinerant" behavior of these systems, starting from the same ($R_0 = 1$) initial conditions i.e., in which the system shows apparently stochastic *macroscopic* behavior. In our analysis this would correspond to such behavior for the parameters ϕ_{11} or ϕ_{22}. While we have seen that there are indeed very significant fluctuations in these parameters, which correspond to very significant differences in the "macroscopic" evolution of these systems, we have studied carefully their dependence on N and found them to decay

monotonically. The results of [149] were obtained for $N = 64$, a range in which we still see fluctuations of ϕ_{11} which are order unity. Only when we reach N of order several hundred do we see these fluctuations diminish significantly so that the macroscopic trajectory of the system becomes quite localized. We thus believe that as N increases these effects will becomes negligible, even on the time scales on which relaxation occurs, and an effectively deterministic macroscopic evolution will occur.

It is interesting to compare our results also to those of Yawn and Miller [89], who have analyzed in detail relaxation in a version of the sheet model in which there are sheets of different masses. In this case the relaxation toward thermal equilibrium may be clearly distinguished by testing for equipartition of the kinetic energy, and the associated spatial segregation of the mass populations. In simulations starting from waterbag type initial conditions with a virial ratio of two, for a range of different mass ratios and up to $N = 128$ particles, clear evidence was found in [89] for such relaxation using appropriately defined indicators. Like the order parameters we have employed here, these show characteristic behavior corresponding to the principal phases of the dynamical evolution (violent relaxation, QSS phase, relaxation toward thermal equilibrium). Although we cannot compare our results directly, we note that the time scales observed for relaxation of systems with $N \sim 10^2$ particles are quite consistent with those we have observed for the equal mass system with initial virial ratio $R_0 = 1$. Yawn and Miller [89] also measure temporal correlation properties and find weak but persisting correlations characterized by a power-law decay (in time), which they interpret as evidence for the incompleteness of relaxation. In the present study we have found, in contrast, that our principal observables decay in time with a functional form which allows the identification of characteristic time scales. Further all deviations of these observables from their equilibrium values decrease clearly as N increases, and thus we have interpreted the associated "incompleteness" of relaxation simply in terms of finite N effects. It would be interesting certainly to perform a more direct comparison of the results in the two models, and in particular to extend the study of Yawn and Miller to allow a determination of the N dependence of the parameters they study.

Let us finally mention some other issues of importance concerning aspects of the dynamics of this system which have been treated elsewhere but which we have not discussed here. As we have discussed, we interpret our results in line with those of many previous studies of this and other long-range systems: the evolution from an arbitrary out of equilibrium initial condition is characterized a first phase of relaxation to a QSS, interpreted as a finite particle sampling of a stationary solution of the Vlasov equation, on a time scale independent of N, followed by a slow relaxation to thermal equilibrium on an N-dependent time scale. Studies of the single mass sheet model for other specific initial conditions suggest that this simple scheme may be too limiting, for this model (and possibly, for all such models). On the one hand Reidl and Miller have reported numerical results [166] for specific "two cluster" initial conditions which show a dependence on N in the time scale for relaxation to a QSS. On the other hand, as mentioned in the beginning of this chapter, Rouet et al. [156, 157] have shown, using both particles simulations and simulations of the Vlasov equation, for yet other initial conditions that "holes" which rotate in phase space may be present after violent relaxation and persist on very long time scales. Although it is not evident that there is necessarily a relation between either finding and the mechanism of relaxation to thermal equilibrium, a study incorporating such initial conditions would certainly be more complete than that reported here. Extension of the study reported here to larger N still would likewise be desirable, despite the extremely rapidly growing numerical cost of such simulations with N.

Chapter 5

Quasi-stationary states and Lynden-Bell theory in 1D self-gravitating systems

As discussed in our introduction, the statistical mechanics of long-range interacting systems has been a subject of active study in recent years (for a recent reviews see e.g. [57, 58, 59, 60]). As for self-gravitating systems, such systems have been understood to give rise generically to non-equilibrium QSS which evolve only on time-scales which diverge with the number of particles. The degree to which such states can be understood, and their properties predicted, by a statistical approach is a question which is inevitably posed. In this context the theory of Lynden-Bell in the astrophysical context in the sixties [19], and which has been applied also in the study of two dimensional vortices [81], has seen revived interest in recent years. Study notably of the HMF Model which describes particles on a ring interacting by a cosine potential, showed that this theory can predict sometimes very accurately the properties of these states (see, e.g., [72, 77] and references therein), and more generally manages to capture the qualitative dependence of the QSS on initial conditions. While it is clear that the LB theory is not entirely adequate in general, these studies suggest that the basic physical principle behind it — maximization of an entropy subjected to the constraints appropriate to Vlasov dynamics — is, at the very least, a reference point for understanding the out of equilibrium dynamics of these systems. This contrasts strongly with the view of this theory in the (original) context of the astrophysical literature, where it has simply been discarded as a completely inadequate, and basically irrelevant, theory [21, 144]. One recent study [37] of 3D self-gravitating systems concludes, however, that LB theory may indeed be relevant also to this case. This study shows that in a certain limited range of initial conditions the LB theory predicts well the density profiles of QSS, and proposes an alternative theory to explain their properties in the regime where LB no longer works well. The same authors have shown that the same statements apply both to plasma systems [94] and 2D self-gravitating system [93], and, in a very recent article [167], have used the alternative theory to account for QSS in the HMF model.

In this chapter we study these issues in the self gravitating sheet model of particles in one dimension. Our main goal is to characterize more precisely than has been done previously the degree of validity of the LB theory in this model and to determine whether the properties of the QSS can be characterized in a simple manner and perhaps understood when the LB theory does not apply. That this theory does not provide an adequate theory of QSS in the sheet model

is clear from the earliest studies of this issue [128, 129, 168] which indeed used this model to probe the possible validity of LB theory for 3D gravitating systems. More recently a study of these questions in the 1D model has been reported by Yamaguchi [95], who finds reasonable agreement with LB in a certain range of initial conditions, and, like in the work of Levin et al. mentioned above, proposes a modification of it to account for the QSS observed in other cases. We will compare in detail our results to these previous works.

Studies of the 1D self-gravitating model in the astrophysical context go back at least as far as that of [90], and there have been numerous studies of it also in the statistical mechanics literature in the decades since. Many of these studies focussed on the question of relaxation to the thermal equilibrium of the model, for which the exact expression was first derived by Rybicki [92]. That this relaxation, like in other long-range systems, takes place very slowly, on a timescale which diverges with the number of particles, has been clear since the earliest works, but the precise time scale and parametric dependences thereof have been the subject of considerable study and even some controversy (see e.g. [96, 89] and references therein). In the previous chapter, we have established clearly that the relaxation time from a range of initial conditions depends *linearly* on the number of particles N, while also showing a strong dependence on the intermediate QSS state (or states). Besides the early and more recent studies cited above which consider the QSS attained on the shorter mean-field time scales (i.e. through violent relaxation) and LB theory, there are also studies [156, 157] which argue that the assumption that QSS always result from mean-field dynamics may not be always correct: starting from certain initial conditions the initial phase of relaxation is observed to lead to phase space densities which have large holes which rotate in phase space, which persist on the time scales of the simulations. In our analysis below we will examine this question carefully, as it is clearly of central importance to understand whether the formation of a QSS is indeed a good description of the outcome of violent relaxation if one is comparing with a theory which, by construction, assumes such a outcome.

The chapter is organized as follows. First we will start in section 5.1 in which we describe the specific class of initial conditions which we investigate. In section 5.2 we report our numerical results, comparing them to the theoretical LB predictions (see section 3.4). In the following section we confront our results with two proposals which have been made in the recent literature to explain the properties of QSS when the LB is clearly inadequate. In our conclusions we summarize our findings and conclusions, and suggest some directions for further investigation in both 1D and 3D self-gravitating systems.

5.1 Initial conditions

In our numerical study we consider particles distributed initially by randomly sampling different classes of waterbag initial conditions, i.e., in which the phase space density takes the same value f_0 everywhere it is non-zero. Specifically we consider, in order:

- **Single rectangular waterbags (SRW)**, in which the support of the initial phase space density is a rectangle centered on the origin, i.e.,

$$f(x,v) = f_0\Theta(x_0 - x)\Theta(x_0 + x)\Theta(v_0 - v)\Theta(v_0 + v) \tag{5.1}$$

  where Θ is the Heaviside function. As, in the continuum limit, the only parameters in the problem are then four — f_0, x_0, v_0 and the coupling g — there is in fact only one relevant parameter characterizing the system once units are chosen. A natural physical choice of

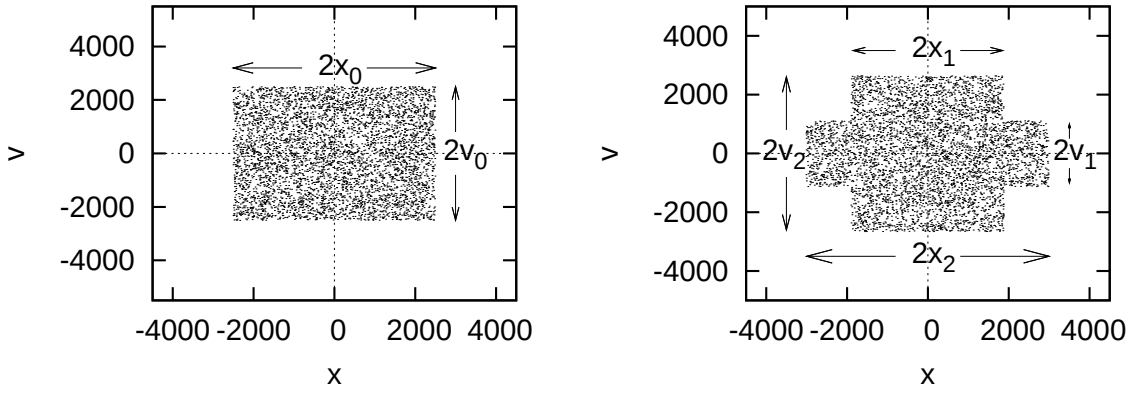

Figure 5.1: Realizations with $N = 5000$ particles of an SRW initial condition (left panel) and DRW initial condition (right panel). The two configurations have the same value of ξ_D (up to finite N corrections). The units used here are specified at the beginning of section 5.2 below.

this parameter is the initial virial ratio R_0, which a simple calculation shows is given by

$$R_0 \equiv \frac{2T_0}{U_0} = \frac{v_0^2}{gMx_0} \tag{5.2}$$

where T_0 and U_0 are the initial kinetic and potential energies given by

$$T_0 = \frac{1}{6}Mv_0^2 \quad , \quad U_0 = \frac{1}{3}gM^2x_0. \tag{5.3}$$

An example of such a configuration with $R_0 = 0.5$ is given in the left panel of Fig. 5.1.

As discussed in section 3.4 the LB prediction also depends on only one parameter, which we can take to be ξ_D, the ratio of the energy above the degenerate energy of the configuration to that of the degenerate limit of LB (i.e. the minimum allowed energy of the given mass at phase space density f_0). The energy and mass in the limit of a degenerate system are given as functions of μ by (3.74) and (3.73). Eliminating μ we obtain

$$E_D = \frac{B(\frac{3}{2},\frac{2}{3})}{12^{\frac{1}{3}}} g x_0 M^2 R_0^{\frac{1}{3}}\,, \tag{5.4}$$

and thus

$$\xi_D = \frac{E - E_D}{E_D} = \frac{12^{\frac{1}{3}}}{3B(\frac{3}{2},\frac{2}{3})}\left(\frac{1}{R_0^{\frac{1}{3}}} + \frac{R_0^{\frac{2}{3}}}{2}\right) - 1 = 0.688\left(\frac{1}{R_0^{\frac{1}{3}}} + \frac{R_0^{\frac{2}{3}}}{2}\right) - 1 \tag{5.5}$$

where $B(\frac{3}{2},\frac{2}{3})$ is a beta function. This expression is is plotted in Fig. 5.2. The SRW with $R_0 = 1$ is thus the lowest energy configuration, and there are otherwise two values of R_0 for each value of ξ_D.

- **Double rectangular waterbag (DRW)**, in which the support of the initial continuum phase space density is like that shown in the right panel of Fig. 5.1:

$$\begin{aligned} f(x,v) &= f_0\Theta(x+x_1)\Theta(x_1-x)\Theta(v+v_1)\Theta(v_1-v) \\ &+ f_0\Theta(x+x_2)\Theta(-x_1-x)\Theta(v+v_2)\Theta(v_2-v) \\ &+ f_0\Theta(x-x_2)\Theta(x_1-x)\Theta(v+v_2)\Theta(v_2-v)\,. \end{aligned}$$

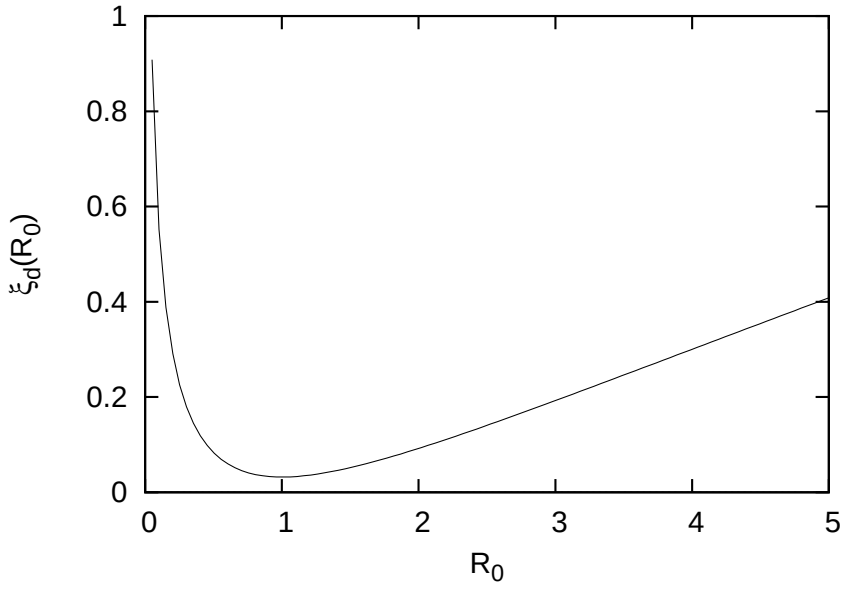

Figure 5.2: ξ_D as a function of R_0 for a SRW initial condition.

As this has two additional parameters compared to the SRW, it is effectively a *three* parameter family of initial conditions, which coincides with the SRW when $v_1 = v_2$, $x_1 = 0$ or $x_1 = x_2$. When they differ from the SRW, they are spatially inhomogeneous, with a ratio of densities $\delta = \frac{v_1}{v_2}$ in the two different regions. We will choose to characterize them by this parameter, together with ξ_D and the initial virial ratio R_0. LB theory thus predicts that the final state should be independent of R_0 and δ at given ξ_D. The relevant expressions for the kinetic and potential energies of the DRW configuration are given in appendix C.

- **Disjoint waterbags (DW)**, in which the initial phase space density is made of two disjoint regions with simple shapes, either rectangular or elliptical. We will use such configurations to further explore some of the conclusions draw from the study of the SRW and DRW configurations.

5.2 Numerical results

The numerical simulations are performed using heap-based algorithm (see appendix A) and most of them are run using the machines of the "Centre de Calcul" at the "Institut National de Physique Nucléaire et de Physique des Particules (IN2P3)".

5.2.1 Choice of units

We put $g = 1, M = N$ while L_0 (the initial size of the system) is not identical in all three types of waterbags. In SRW and DW initial conditions, L_0 is chosen to give the initial density $\rho_0 \equiv M/L_0$ equal to 1, i.e. $L = N$. In DRW initial condition we adjust L_0 so that f_0 is fixed in any ξ_D. ρ_0 for all DRW initial condition are of order unity. The characteristic time unit is

defined as

$$t_c = \sqrt{\frac{1}{g\rho_0}}. \tag{5.6}$$

In the cases $R_0 \to 0$ and $N \to \infty$ of the SRW initial conditions, it corresponds to the time at which all mass falls to the origin.

5.2.2 Attainment of QSS and their characterization: generalities

That the sheet model with a large number of particles — just as such 3D self-gravitating and other long range interacting systems which have been studied in the literature — give rise typically to QSS starting from initial conditions such as those above has been discussed elsewhere in many studies (see references given in the introduction). The attainment of a QSS should be tested, in theory, by considering the full phase space density coarse-grained at some chosen scale. One would then verify whether its evolution after some initial period (of violent relaxation) tends to

$$\bar{f}(x,v,t) = \bar{f}_{QSS}(x,v) + \delta\bar{f}(x,v,t) \tag{5.7}$$

where the amplitude of the fluctuations $|\delta\bar{f}(x,v,t)|$ decreases as N increases. For our study here, in which we consider how the properties of these QSS depend on the initial conditions, what is of importance is that we evolve the corresponding system to a time at which the approximation (5.7) indeed holds well, for N sufficiently large so that the fluctuations $\delta\bar{f}(x,v,t)$ introduce a negligible uncertainty into the quantities used to characterize the QSS.

In practice numerical limitations on N make a direct analysis extremely difficult, and one typically considers the behavior of single macroscopic parameters, such as the virial ratio, or the magnetization in models (e.g. the HMF model) where it is defined. This is then complemented by a visual inspection of the system represented in phase space. To describe the properties of the QSS one then considers typically the density profiles, velocity and/or energy distribution. We have shown in [96] (or see section 4), where we studied the very long time behavior of QSS resulting from SRW initial conditions, that the parameters ϕ_{11} and ϕ_{22} defined above are very useful macroscopic "order parameters", which can be used to diagnose both the attainment of a QSS and to characterize this state. We will use them here for the same purpose, supplementing their calculation where necessary or interesting by a fuller analysis of the distribution functions.

To determine whether a QSS is reached, and on what time scale, we thus study firstly the evolution of the virial ratio, and of ϕ_{11} and ϕ_{22}. While the characteristic time for the mean-field dynamics is of order t_c defined above, the completion of relaxation to QSS (in the sense defined above) takes typically of order several tens to hundred t_c for SRW initial conditions (as seen in the plots of ϕ_{11} and ϕ_{22} evolutions in chapter 4). Further this time depends, unsurprisingly, on the nature of the initial condition, with very cold initial conditions — further from virial equilibrium initially — taking significantly longer to relax. Shown in Figs. 5.3 are the evolution of the virial ratio (left panel) and ϕ_{11} and ϕ_{22} (right panel), and in Fig. 5.4 the full phase space plots, for an SRW initial condition with $R_0 = 1$ and $N = 10^4$. The former indicates that the system appears to "settle down" to a stationary state at a time $t \sim 200$, an interpretation which is very consistent with what is observed in the full phase space plots.

For DRW and DW initial conditions we observe even greater variation in the time for full relaxation to a QSS than for SRW, with, in some cases, significant persistent fluctuations in the macroscopic parameters. An example of such a case is shown in Fig. 5.5, in which the left panel shows the evolution of the virial ratio and the right panel that of the parameters ϕ_{11} and ϕ_{22}, for a DW initial condition sampled with $N = 10^4$ particles. The full phase space plot

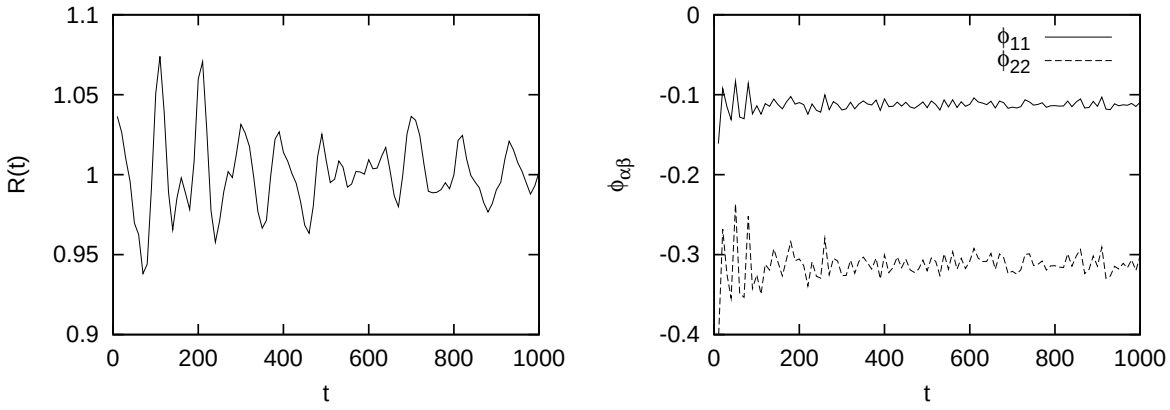

Figure 5.3: Temporal evolution of virial ratio (left) and order parameters (right) for SWR initial condition with $R_0 = 1$ $N = 10000$ (shown in first panel of Fig. 5.4)

.

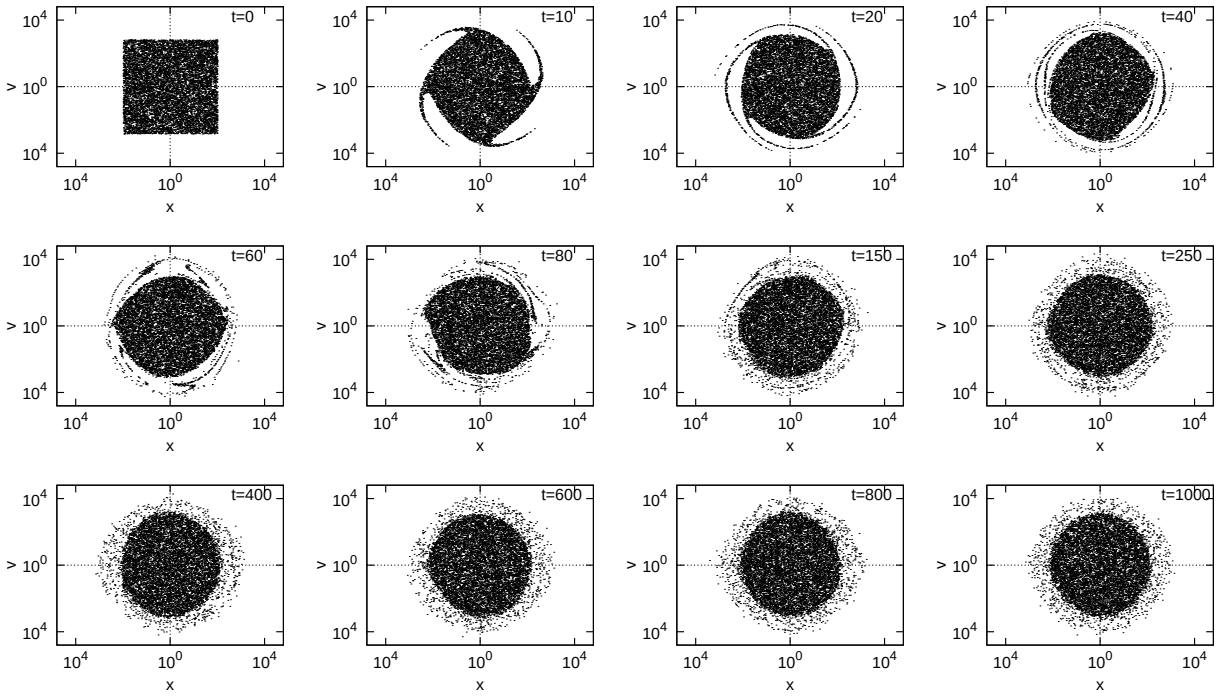

Figure 5.4: Phase space plots of particle obtained from a SRW initial condition (first panel) with $R_0 = 1$ and 10^4 particles, at the times indicated in top-right of each panel.

is shown in Fig. 5.6. This reveals that it is a persistent "rotating hole" feature in the phase space which gives rise to the (small but clearly visible) coherent fluctuations in the averaged parameters in Fig. 5.5. This is precisely the kind of effect which has been documented in the two studies [156, 157] mentioned in the introduction, and which has been argued in this context to show that LB theory is incorrect (as it predicts, by construction, the attainment of a time

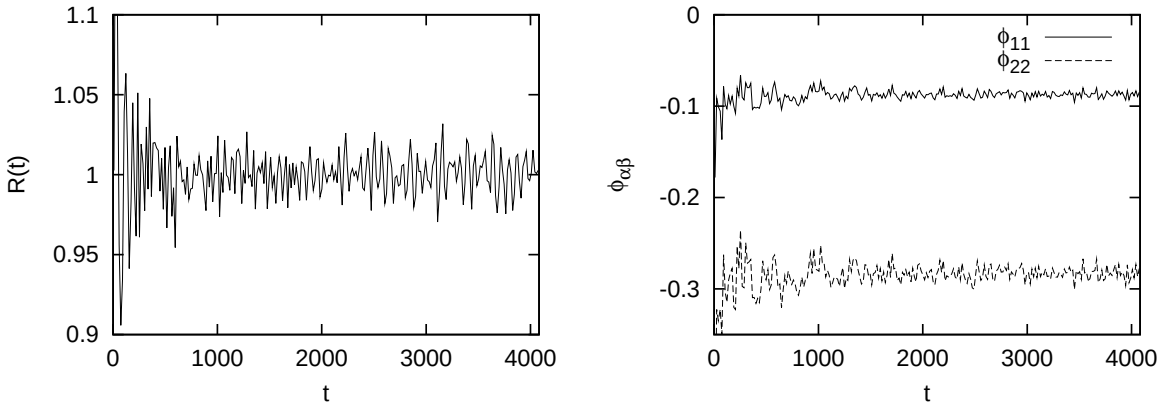

Figure 5.5: Temporal evolution of virial ratio (left), and ϕ_{11} and ϕ_{22} (right) starting from a realization with $N = 10^4$ particles of a DW initial condition (shown in first panel of Fig. 5.6).

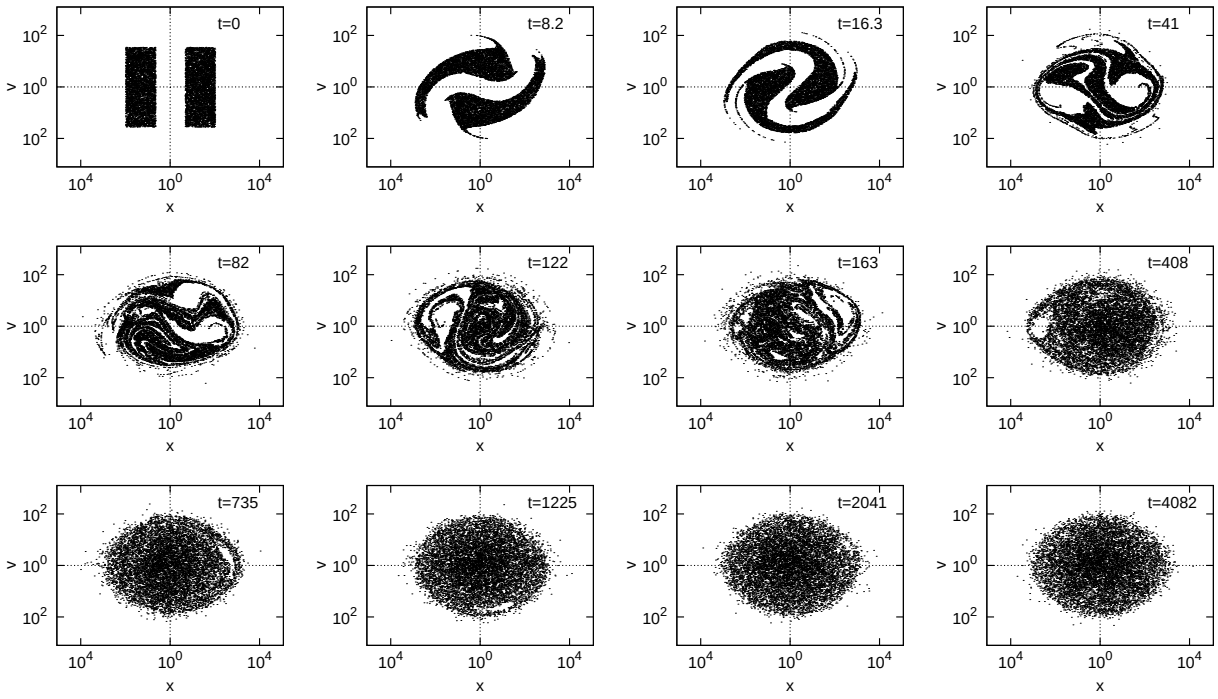

Figure 5.6: Phase space plot of particle trajectories evolved from the DW initial condition shown in the first panel (with $N = 10^4$ particles). The time units are those indicated in the previous figure.

independent phase space density). While the hole we observe is clearly visible at $t = 500$ and indeed rotates in phase space, the subsequent two panels show that it slowly disappears on a time scale of order a few thousand dynamical times. Thus it appears that the relaxation of these holes simply represents a prolongation of the *collisionless* relaxation to a well defined QSS, as no tendency of the system to evolve toward thermal equilibrium (corresponding to ϕ_{11} and

ϕ_{22} equal to zero) is evidenced on this time scale. Further study, however, would be required to establish this conclusion more definitively for a broader range of initial conditions, and to exclude notably that collisional relaxation may play some role.

5.2.3 SRW initial conditions

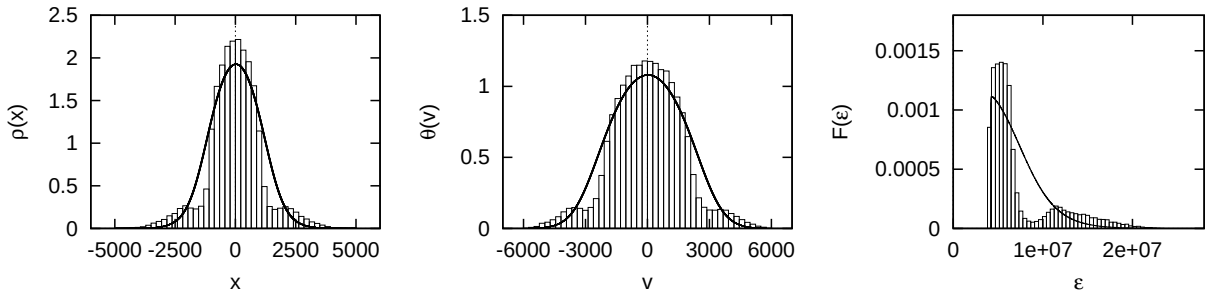

Figure 5.7: The density profile (left), velocity distribution (middle) and energy distribution (right) for the QSS obtained starting from SRW with $R_0 = 0.1$. The solid lines are the corresponding LB predictions.

The density profiles, velocity distributions and energy distributions in the QSS obtained starting from SRW configurations with $R_0 = 0.1, 0.5, 1$ are shown in Figs. 5.7, 5.8 and 5.9. These correspond to averages over 30 realizations of each initial condition sampled with $N = 5000$ particles, taken at $t = 200t_c$, by which time the QSS is well established. In each case the LB predictions given in section 3.4 are shown also, corresponding to $\xi_D = 0.56, 0.08, 0.03$ respectively. As observed already in early studies [129, 168] the qualitatively most striking deviation from the prediction of LB theory is marked by the appearance of a "core-halo" structure, most clearly evident in the energy distribution obtained from the $R_0 = 0.1$ initial condition. On the other hand, as underlined in the more recent study of [95] for these same initial conditions, the agreement of the LB theory with the observed QSS is in fact quite good for the case $R_0 = 1$, while the discrepancy progressively increases as R_0 deviates from unity and a core-halo type structure appears.

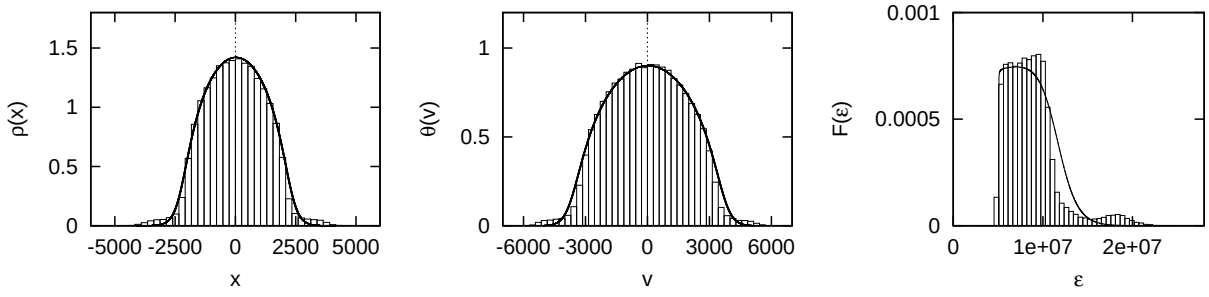

Figure 5.8: The density profile(left), velocity distribution (middle) and energy distribution (right) for the QSS obtained starting from SRW with $R_0 = 0.5$. The solid lines are the corresponding LB predictions.

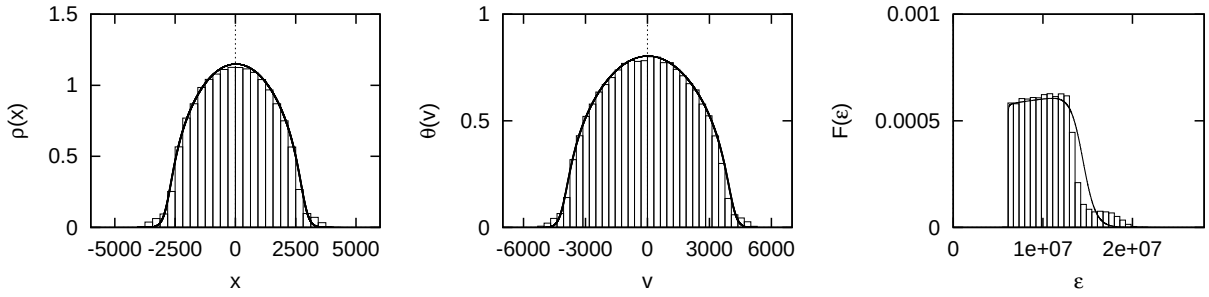

Figure 5.9: The density profile(left), velocity distribution (middle) and energy distribution (right) for the QSS obtained starting from SRW with $R_0 = 1$. The solid lines are the corresponding LB predictions.

Shown in Fig. 5.10 are the values of the parameters ϕ_{11} and ϕ_{22} in the QSS, and the values predicted by LB theory. This plot summarizes in a simple manner the conclusions above: the theory works quite well quantitatively at the lowest energy state corresponding to $R_0 = 1$, but deviates greatly as we go toward the less degenerate initial states. Further the plot shows that the theory gives very qualitatively the correct behavior of the parameters — they increase monotonically with the initial ξ_D. At low degeneracy the sign of these parameters is a result of the formation of a core which is colder than predicted: there is in this case an excess of low velocity particles at small x.

We note that these single parameters, ϕ_{11} and ϕ_{22}, actually allow a better diagnosis of the closeness to LB theory than the examination of the full density or velocity distribution functions. Indeed comparing just these two latter functions with the LB predictions, we might conclude that the agreement is almost perfect. The energy distribution, on the other hand, allows one to see clearly the discrepancies, which are then reflected well in ϕ_{11} and ϕ_{22} * When considering a larger space of initial conditions, as we do now, it is very convenient to use these parameters as diagnostics of the validity of LB.

5.2.4 DRW initial conditions

As described above the DRW initial conditions allow us to test further a basic prediction of LB theory: the same QSS should result starting from any initial configuration in the range of accessible "microstates" at given mass and energy. For 1D gravity and waterbag initial conditions, this means the QSS obtained should be the same at a given ξ_D independently of the shape of the waterbag. As discussed the DRW gives us a two dimensional space of such configurations, which we choose to parametrize by the initial virial ratio R_0 and density contrast δ.

For each of the three values of ξ_D corresponding to the SRW initial conditions above, we have simulated twenty different initial conditions chosen to explore the available (R_0, δ) space. In each of Figs. 5.11, 5.12 and 5.13 are shown two plots: one shows the initial conditions in the (R_0, δ) plane at the given value of ξ_D, the other the QSS obtained from them as represented

*This "efficiency" of these parameters as diagnostic tools was noted in chapter 4, where it was shown, notably, that they could identify clearly stationary states arising from certain initial conditions as QSS rather than the thermal equilibrium states which previous studies [154] had mistakenly inferred them to be based on an analysis using $\rho(x)$ and $\theta(v)$.

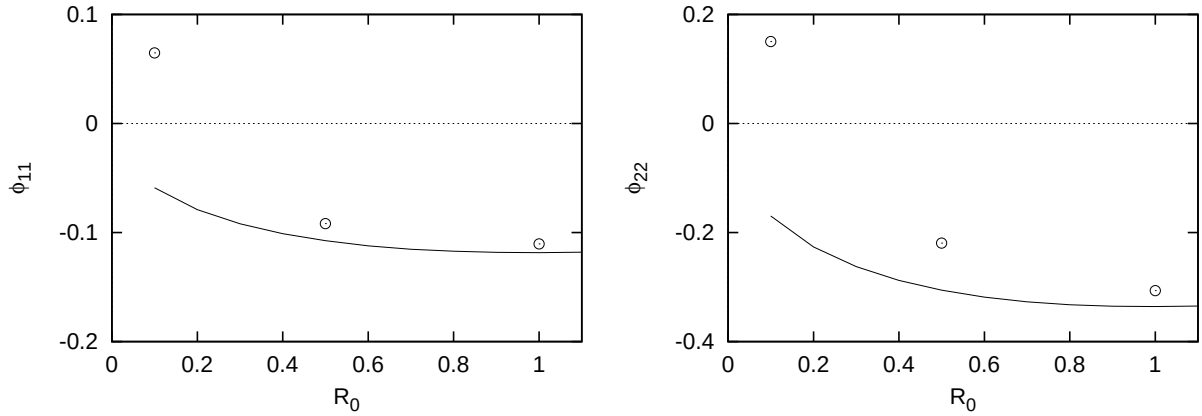

Figure 5.10: ϕ_{11} (left) and ϕ_{22} (right) in QSS as the function of R_0. The line indicates $\phi_{\alpha\beta}$ calculated by LB stationary state and the circle is the value obtained by numerical simulation.

in the plane (ϕ_{11}, ϕ_{22}). The results are, as for the SRW above, averages over 30 realizations of each initial condition sampled with $N = 5000$ particles, taken at $t \approx 200t_c$. The fact that the spread in values of (R_0, δ) is much smaller at smaller ξ_D is simply a reflection of the fact that as one goes toward the degenerate limit $\xi_D = 0$ the constraints limit the possible deformations more and more.

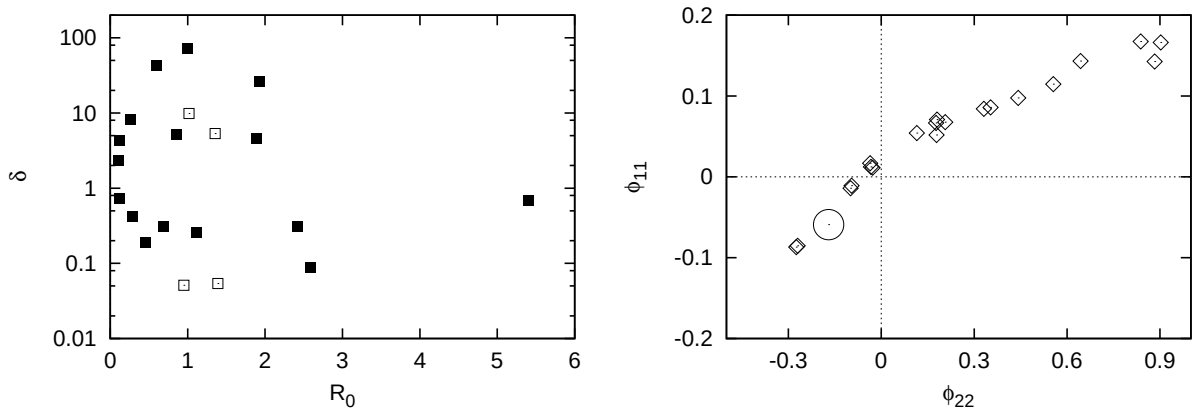

Figure 5.11: The plot on the left represents the twenty different DRW initial conditions with $\xi_D = 0.56$ (i.e. equal to that of SRW with $R_0 = 0.1$) according to their values of R_0 and δ. The plot on the right represents the values of (ϕ_{22}, ϕ_{11}) measured in the resulting QSS. The LB prediction lies at the center of the small circle. The unfilled points in the upper plot correspond to the four initial conditions which give QSS closest to the LB prediction.

In continuity with what we observed for the SRW, the results show that LB theory works reasonably well at the two lower values of ξ_D — the QSS varies only very little over the range of different initial conditions — it is grossly violated as we go toward the non-degenerate limit. Indeed the order parameters for QSS obtained starting from the same ξ_D can differ in sign. Direct

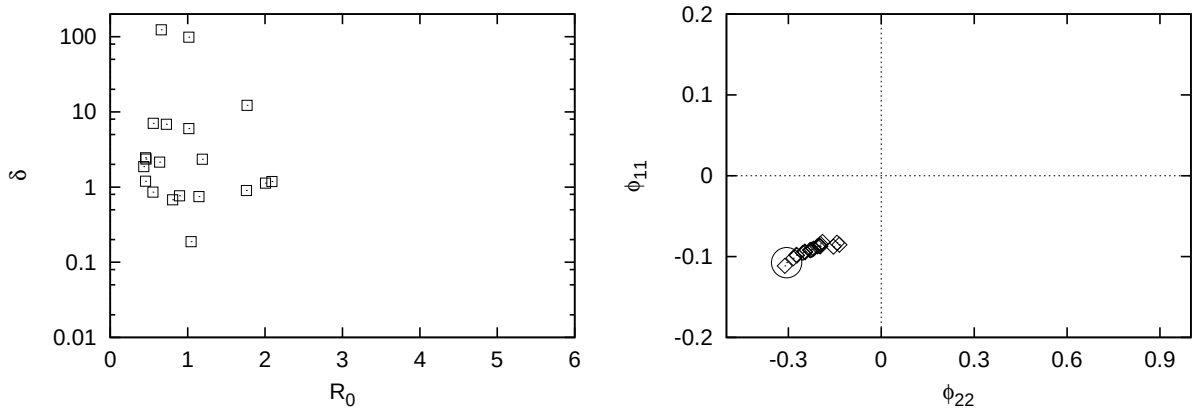

Figure 5.12: Same as in Fig. 5.11, but for DRW initial conditions with $\xi_D = 0.08$, i.e., equal to that of SRW with $R_0 = 0.5$. We keep the scale as in the previous figure for easier comparison.

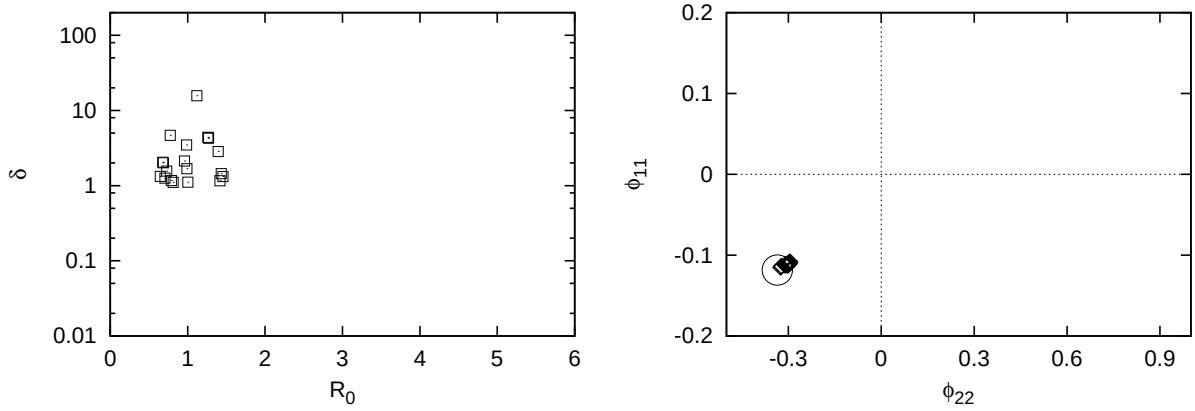

Figure 5.13: Same as in Fig. 5.12, but for DRW initial conditions with $\xi_D = 0.03$, i.e., equal to that of SRW with $R_0 = 1$. Same scale as in Fig. 5.11 for ease of comparison.

analysis of the distribution functions confirms that this corresponds to QSS which are completely different. On the other hand, certain initial conditions at $\xi_D = 0.56$ — those corresponding to the unfilled points in the upper plot of Fig. 5.11 — do appear to give QSS close to the LB prediction. To assess whether this is really the case the density profiles, velocity and energy distribution functions for two of these are shown in Figs. 5.14 and 5.15. While the agreement with the theoretical curves is not perfect, it is comparable than that obtained for the initial conditions with $\xi_D = 0.03$ — indeed the discrepancy between the LB prediction and the observed distributions is no more than observed above for the SRW initial conditions with $\xi_D = 0.03$.

The strong deviations from the LB prediction, just as in the SRW, manifest themselves in the shift toward positive values of ϕ_{11} and ϕ_{22}. Direct inspection of the distribution function of energy shows that this reflects again in all cases the appearance of a pronounced core-halo type structure. Inspection of the plot of the initial conditions in the (R_0, δ) space for $\xi_D = 0.56$

shows that all the cases which approach LB (unfilled points) are characterized by an initial virial ratio near unity, while the density contrast parameter δ appears to be irrelevant. On the other hand $R_0 \approx 1$ is clearly not a sufficient condition to guarantee agreement with LB.

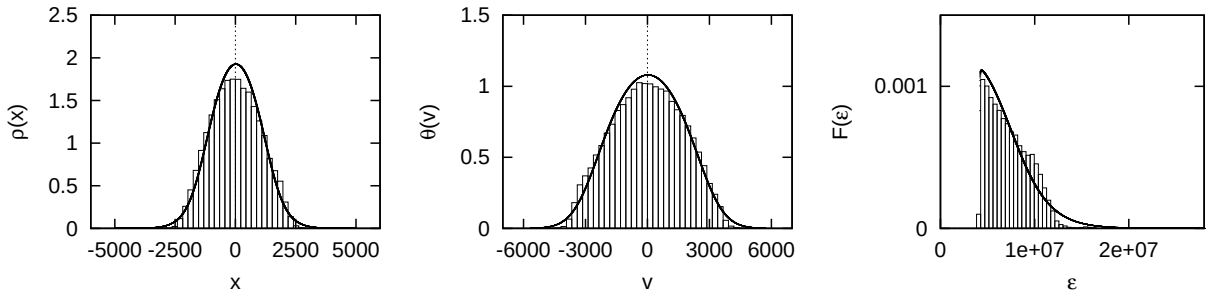

Figure 5.14: Density profile(left), velocity (middle) and energy distribution (right) for DRW initial conditions with $\xi_D = 0.56$ (i.e. the same energy as the SRW with $R_0 = 0.1$), $R_0 = 1.39$ and $\delta = 0.054$.

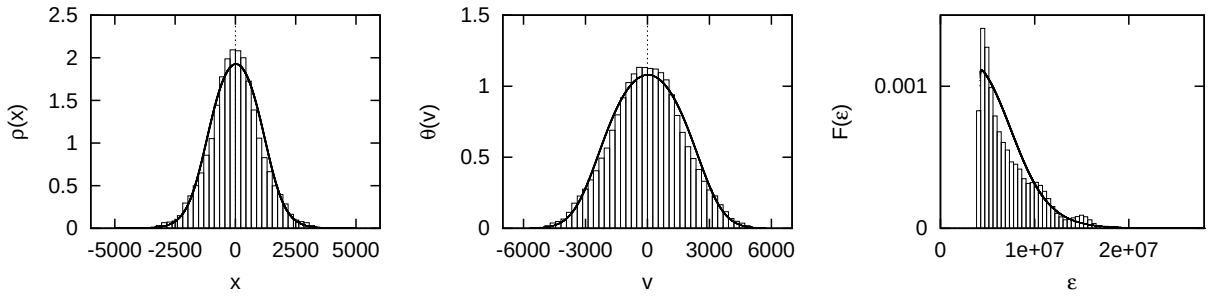

Figure 5.15: Density profile(left), velocity (middle) and energy distribution (right) for DRW initial conditions with $\xi_D = 0.56$ (i.e. the same energy as the SRW with $R_0 = 0.1$), $R_0 = 1.017$ and $\delta = 9.861$.

These results suggest therefore that LB theory works reasonably well always near the degenerate limit, and also for much higher energies for very specific initial conditions. In these cases, which seem to correlate strongly with an initial virial ratio near unity, the formation of a core-halo structure, not predicted by LB theory, is avoided.

To see the variation of the QSS from DRW initial conditions for $\xi_D = 0.56$ with different (R_0, δ), the density profiles of three chosen cases (a subset of those shown above) are plotted in Fig. 5.16. While the central part of the profile is almost indistinguishable, the outer region shows clearly significant differences. The energy distributions for these three cases are plotted in Fig. 5.17. The difference in the QSS may be seen clearly in energy space, especially in the high ε tail of the distribution.

5.2.5 DW initial conditions

To further explore these findings, and in particular to investigate the relevance of the initial virial ratio as a parameter, we consider finally a few other "disjoint" waterbag initial conditions

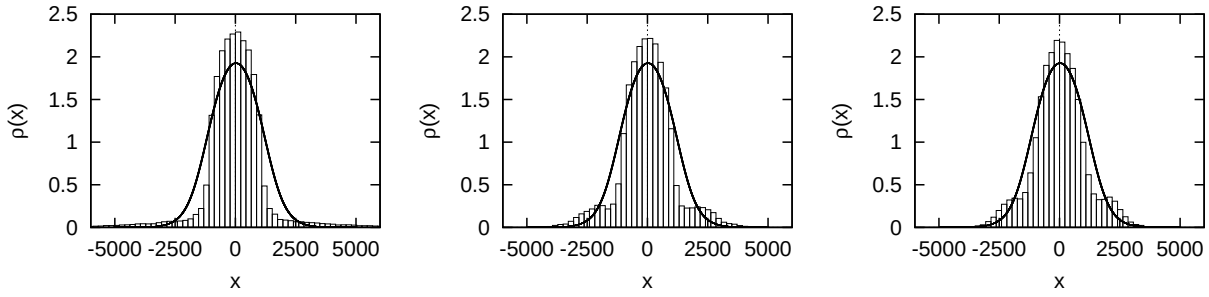

Figure 5.16: Ensemble-averaged density profiles for three chosen cases of DRW initial conditions with $\xi_D = 0.56$, where QSS deviate very much from the LB prediction (in solid line).

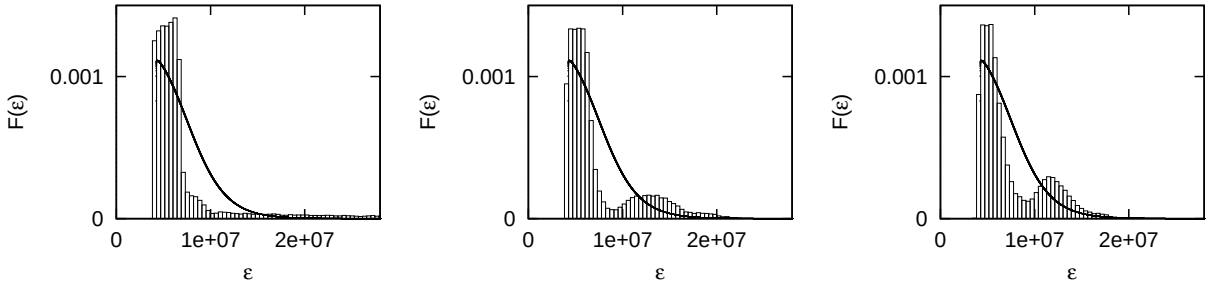

Figure 5.17: Ensemble-averaged energy distributions for the three cases shown in Fig. 5.16, with $\xi_D = 0.56$. The LB predictions are the solid line.

as described above. We report results for the four cases shown in Fig. 5.18. Each of the initial conditions has been adjusted to have $R_0 = 1$, and the values of the normalized energy are $\xi_D = 1.59, 0.58, 0.49$ and 0.23 for DW1 to DW4 respectively. We take in each case a single realization with $N = 10^4$ particles, and calculate a time average by sampling on 100 equally spaced time slices in the time window $[4000, 5000]$ (in the time units of our simulation, which differ in each case from units with $t_c = 1$ by a numerical factor of order unity). Shown in Fig. 5.19 are the QSS obtained as represented in the (ϕ_{11}, ϕ_{22}) plane. In each case the filled symbol represents the corresponding LB predictions. Comparing to the results for SRW and DRW initial conditions, the QSS appear in all cases much closer to the LB predictions. This is confirmed by inspection of the distribution functions, which are shown for DW2 in Fig. 5.20 and for DR1 in Fig. 5.21. For the former case the results are as close to the LB predictions as for the SRW and DRW cases which gave best agreement with LB, with the small deviation being visible again in the energy distribution but very difficult to discern in $\rho(x)$ or $\theta(v)$. The results for the cases DR3 and DR4 are similar. For DR1, on the other hand, the deviation from LB is much more marked, and we see in the energy space that this deviation is associated to the formation of a (in this case very small) core. Very much in line with the results for SRW and DRW initial conditions, the agreement with LB thus deteriorates as one goes away from the degenerate limit.

In summary these results confirm the conclusion drawn from the analysis of the SRW and DRW waterbags: the LB predictions are always reasonably good — and excellent for the spatial

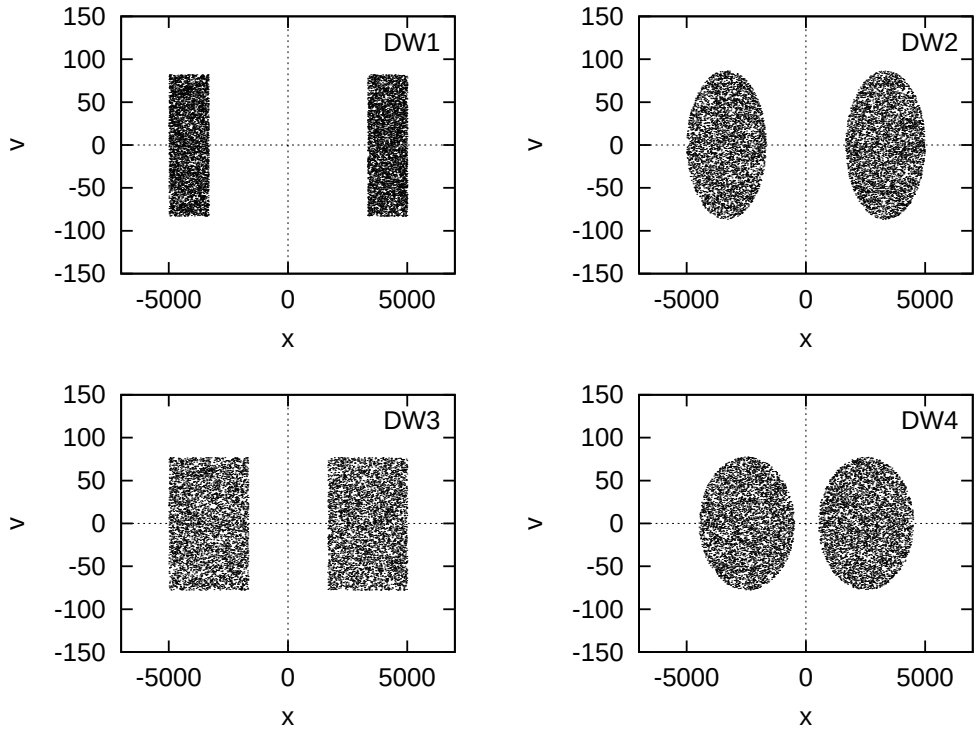

Figure 5.18: Four disjoint waterbag initial conditions with the number of case indicated in the panel. The corresponding ξ_D are equal to $1.59, 0.58, 0.49$ and 0.23 for case 1 to 4 respectively.

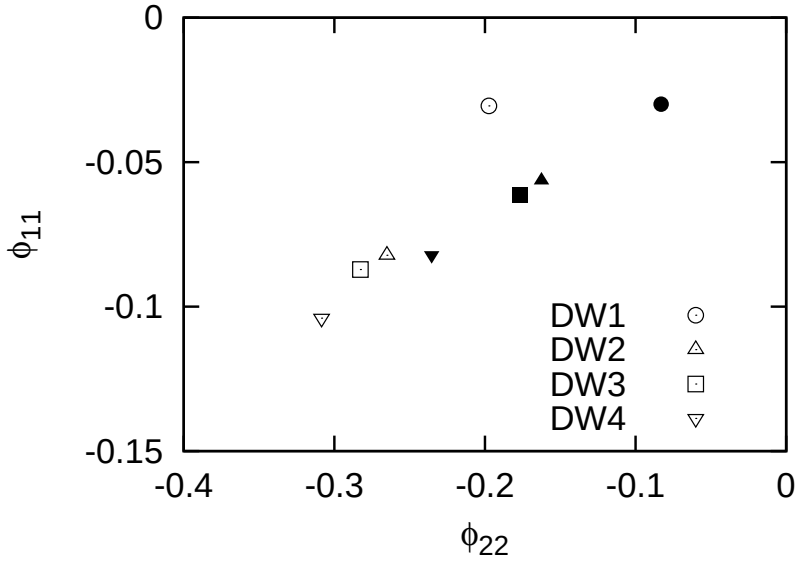

Figure 5.19: ϕ_{22} and ϕ_{11} of the QSS obtained from the initial conditions in the previous figure. The unfilled symbols corresponds to the values obtained from numerical simulations, while the filled symbols are the LB predictions.

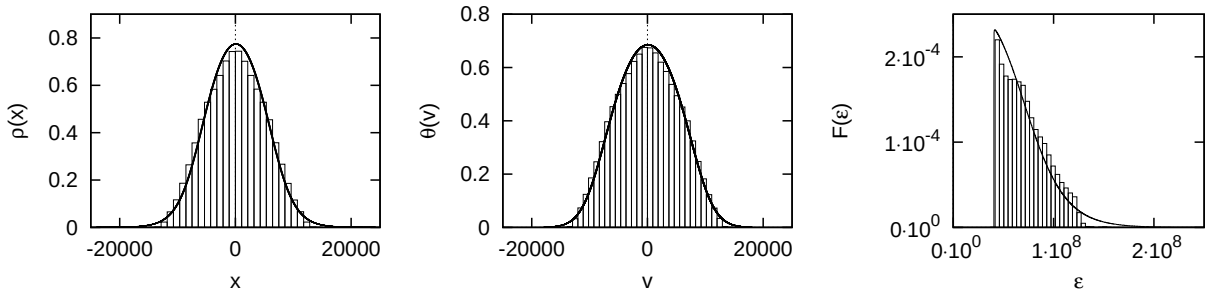

Figure 5.20: The density profile (left), velocity distribution (middle) and energy distribution (right) for the QSS obtained starting from the DW2 initial conditions ($\xi_D = 0.58$). The solid curves lines are the LB predictions.

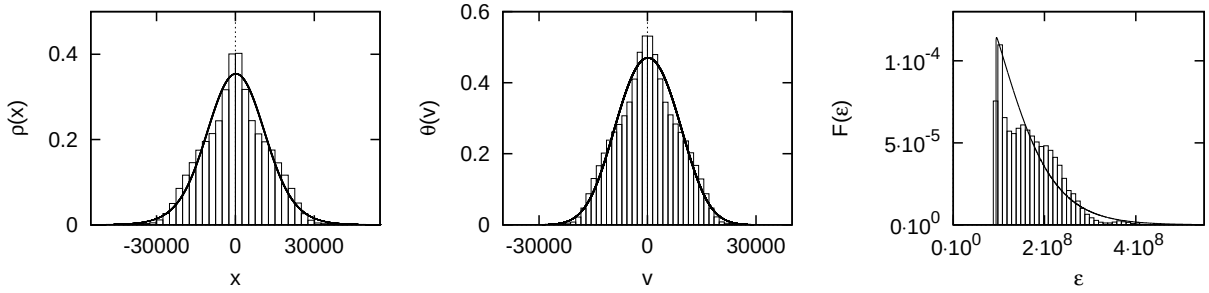

Figure 5.21: The density profile (left), velocity distribution (middle) and energy distribution (right) for the QSS obtained starting from the DW1 initial conditions ($\xi_D = 1.59$). The solid curves lines are the LB predictions.

and velocity distributions – for (waterbag) initial conditions with low ξ_D, but even at higher values good agreement can be obtained in cases characterized by an initial virial ratio of order unity. Further deviation from LB is always characterized by the appearance of a core-halo type structure.

5.2.6 Comparison with theoretical proposals beyond LB: direct analysis of phase space density

Let us consider how well two recent proposals in the literature can account for the properties of the QSS we observe:

- Yamaguchi [95] studies the SGS model for SRW initial conditions, and notes (as was remarked also in early studies [129, 168]) that the breakdown of LB theory is associated with the appearance of a core-halo structure. He proposes a phenomenological adaptation of LB theory which he uses to fit the resultant core, in which the LB theory is applied only to the mass and energy associated to the core. In practice this means that one parameter is measured *a posteriori* from the observed QSS.

- Levin et al. in a series of works on other models — plasmas [94], 3D gravity [37], 2D

gravity [93] and, most recently, the HMF model [167] — have proposed that, when LB theory breaks down, QSS correspond to the phase space density:

$$f(x,v) = f_0[\Theta(e_F - e) + \chi\,\Theta(e - e_F)\Theta(e_h - e)]\,. \tag{5.8}$$

As in the case of [95], this involves the addition of one parameter compared to LB theory. However, a physical explanation is proposed for the core-halo form of (5.8), and a prediction for this additional parameter is derived from the initial conditions: An analysis of particle dynamics in the coherent oscillating field associated with the relaxation shows that there are dynamical resonances which allow particles to gain energy, with e_h corresponding to the maximal energy which can be attained in this way. Assuming that resonance effect is "shut off" only by the upper bound on the phase space density imposed by the collisionless dynamics, the ansatz (5.8) is the simplest one possible for the QSS which will result.

To evaluate the validity of these approaches in this model, we consider directly the measured phase space density as a function of particle energy, $\bar{f}(\epsilon)$. To do so we measure the (averaged) values of the potential $\phi(x)$ and $a(\varphi)$ in the QSS, and then use (3.86) to calculate the phase space density $D(\epsilon)$. Shown in Fig. 5.22 are the results for nine chosen cases from the DRW initial conditions with $\xi_D = 0.56$ considered in section 5.2.4 above. In Fig. 5.23 a plot of exactly the same data is given, but now displaying the logarithm of the absolute value of $\bar{f}/(f_0 - \bar{f})$ as a function of ϵ (which in LB theory gives a straight line with slope β). Our choice is representative of the whole batch of initial conditions, in that 1) most QSS have a clear core-halo structure, and 2) those that do not agree reasonably well with the LB prediction. Indeed the two (left and middle) of three configurations in the uppermost panels of Fig. 5.22 are the same two cases for which the full distribution functions were shown in Figs. 5.14 and 5.15.

In Fig. 5.22 a vertical line indicates the initial phase phase density f_0, so that it is clear that whenever a core appears it is indeed *degenerate*. While the measured phase space distributions are clearly more structured than (5.8), in most cases this simple ansatz gives a reasonably good fit (i.e. about as close to the phase space density as the LB profile is to the observed one in the cases where it has been considered to work well above). In this respect we note that Levin et al. have not tested their ansatz directly against the phase space density, but have used it to derive predictions for $\rho(x)$ and $\theta(v)$ which have been compared with those observed. As we have seen in comparing numerical results with LB predictions above, these quantities typically wash out structure in energy space and make it difficult to see discrepancies which are localized in this space. We note further that our finding that it is initial conditions with $R_0 \approx 1$ which suppress the core-halo formation — and lead to QSS in reasonable agreement with LB — appears completely coherent with the mechanism described by Levin et al.: when the system starts close to virial equilibrium, the relaxation is typically indeed much "gentler" , simply because the system does not undergo the large contractions and expansions which result necessarily if there is a large imbalance between the initial potential and kinetic energy. It is precisely such macroscopic oscillations of the system which drive the resonances analyzed by Levin et al..

We consider finally comparison of our results with an analytical treatment of collisionless relaxation developed in [169] (see also further references therein). This work develops, under certain approximations and hypotheses, a kinetic equation for collisionless relaxation — similar to the Lenard-Balescu equation for collisional relaxation — with a term describing relaxation towards the LB equilibrium. One feature of this term is that it involves an effective space and time dependent diffusion coefficient, which is proportional to the product $\bar{f}(f_0 - \bar{f})$. Thus the

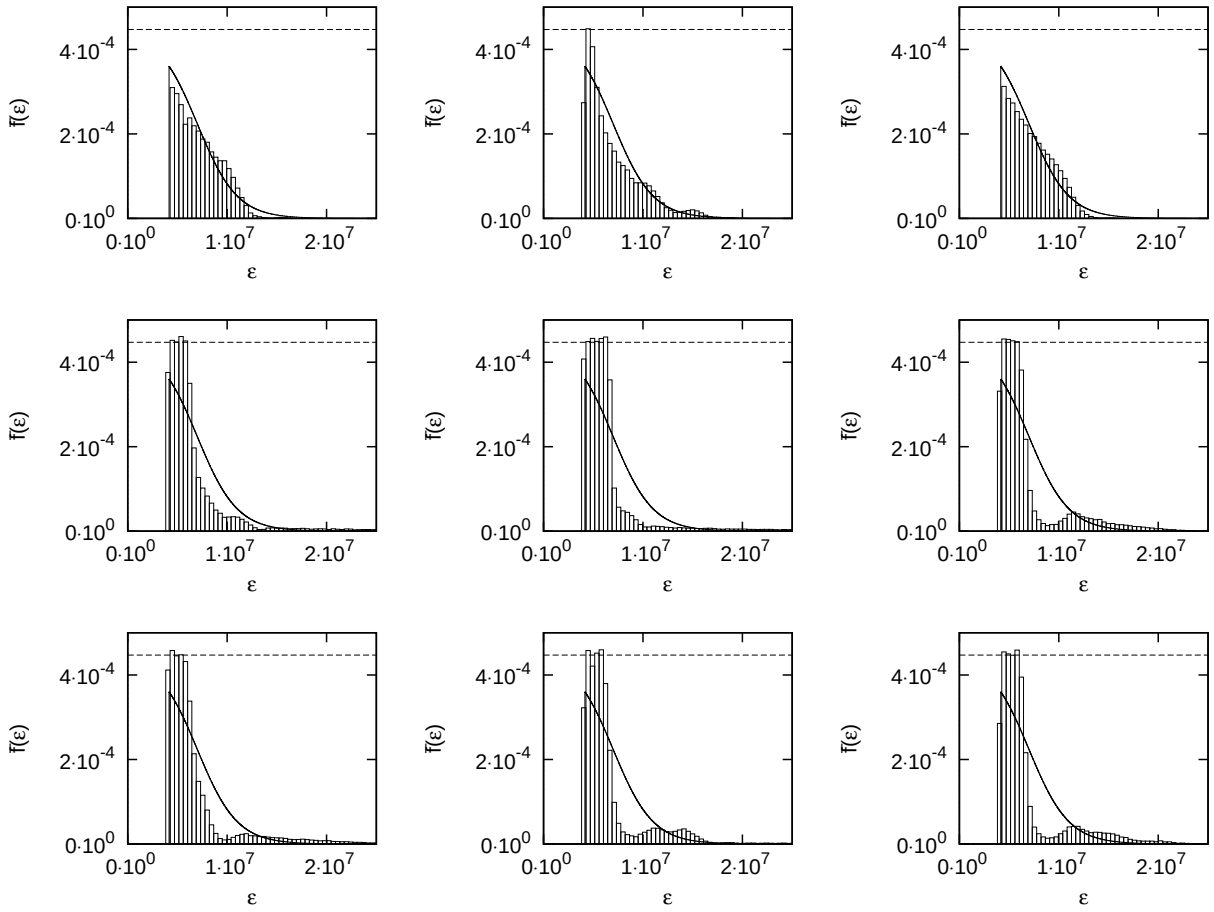

Figure 5.22: Phase space density as a function of energy $\bar{f}(\epsilon)$ for nine representative cases of DRW initial conditions with $\xi_D = 0.56$ (corresponding to $R_0 = 0.1$ for SRW). The two of three upper panels correspond to the two cases for which the distribution functions are shown in Figs. 5.14 and 5.15 where the QSS is close to LB. The dashed horizontal line indicates the initial phase space density, f_0, while the continuous lines correspond to the LB prediction.

theory suggests that relaxation should be expected to be most inefficient when $\bar{f}$ is close to degenerate ($\bar{f} \simeq f_0$) or very small ($\bar{f} \simeq 0$). In regions of energy where relaxation is more complete, the distribution is expected to approach the LB form, but with values of the parameters β and μ different from those in the global LB equilbrium. Our results in Figs. 5.22 and 5.23 do appear to be quite consistent with these qualitative predictions: indeed this theory would appear to account for why it is core-halo type states, whose dynamical origin is explained by Levin et al., which do not relax to the (global) LB equilibrium. In all cases the results in Fig. 5.23 show a region where the halo distribution is very consistent with a Maxwell-Boltzmann form with an inverse temperature lower than that of the global LB prediction (dashed line). This can be interpreted, following [169], as a "mixing region" where the (in this case, non-degenerate) LB distribution applies locally, while the deviation from the (local) LB form at higher and lower energies is considered as due to incompleteness of relaxation in these regions. Further the fact that the observed distributions are, compared to the extrapolated straight line ("local" LB) fit

in the"mixing region", sensibly higher at lower energies and lower at the highest energies is also in apparent agreement with the kinetic theory described in [169].

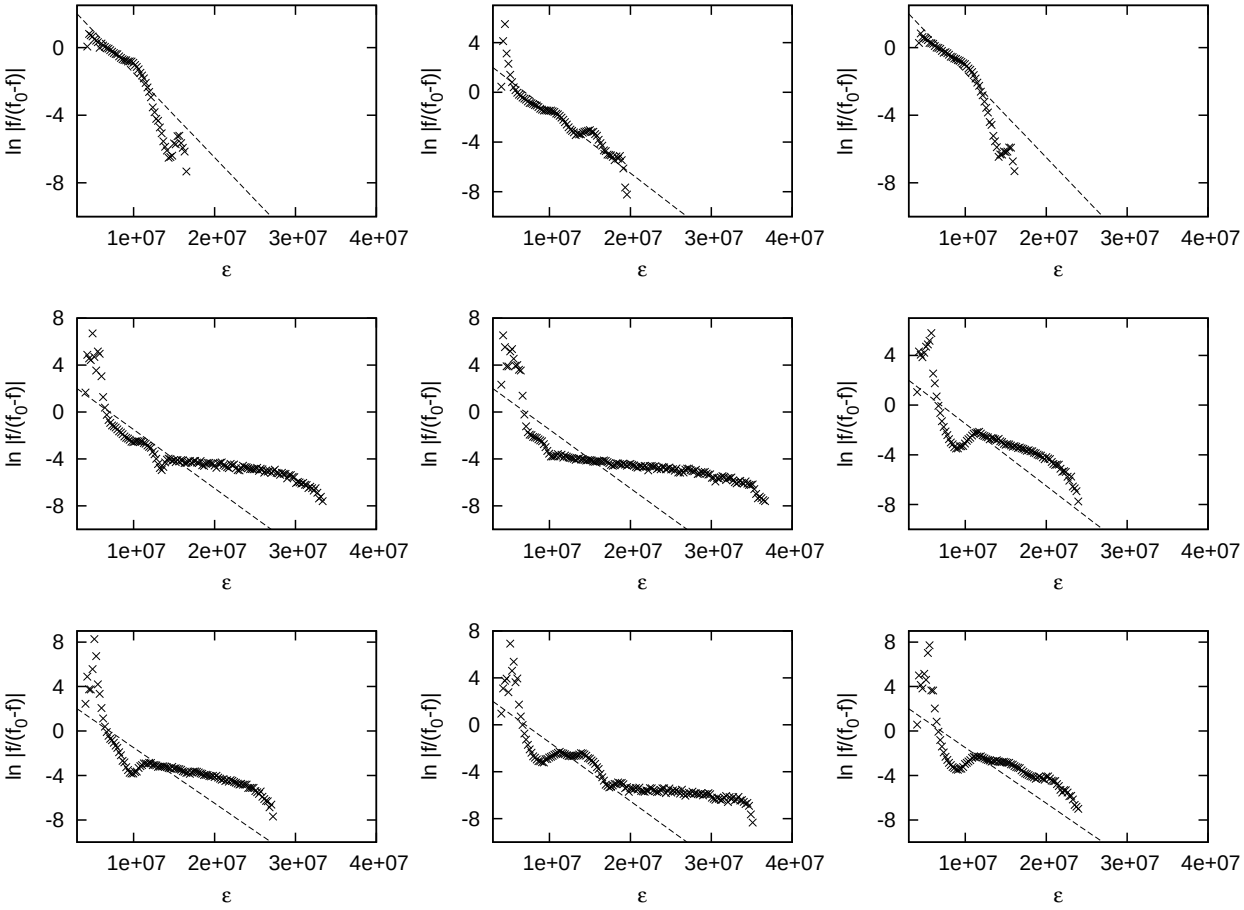

Figure 5.23: Exactly the same data as in the previous figure, but now with the logarithm of the absolute value of $\bar{f}/(f_0 - \bar{f})$ plotted as a function of particle energy ϵ. The dashed lines represent the predictions of LB theory (which become straight lines of slope β in this representation).

5.3 Conclusions and discussions

We summarize now our principal conclusions:

- **Attainment of QSS in the SGS model:** In all cases we have considered QSS do appear to be attained, but the time-scales for relaxation to them can vary very considerably. In some cases rotating "holes" formed in the phase space density during the initial phase of violent relaxation ($\sim 10^2 t_c$) survive for quite a long time, disappearing only on times scales of order ($\sim 10^3 t_c$). As on these latter time scales the system shows no apparent tendency to relax toward its thermodynamic equilibrium, we conclude that this is simply a manifestation of slow collisional relaxation, and does not imply that QSS are not attained as

argued by [156, 157]. A fuller study of the possible N dependence of such relaxation would be useful to establish this conclusion more firmly (but would be numerically challenging).

- **LB theory in the SGS model:** As was clear already from early studies [129, 168], and confirmed by more recent ones such as [95], LB theory is not an adequate theory for understanding fully, or even approximately, the properties of QSS arising from violent relaxation in the SGS model *for arbitrary initial conditions*. However, it is by no means an irrelevant theory to understanding these QSS. Our study of a quite broad range of initial conditions shows that the space of QSS in this model divides quite neatly into two: those for which LB works to quite a good approximation, and those for which the phase space density is characterized by a degenerate core, taking a form generally quite close to the simple ansatz (5.8) proposed by Levin et al. The initial conditions in the former class are either close to the degenerate limit, or in other cases characterized by initial virial ratio of order unity. These conditions are precisely those, in line with what has been described by Levin et al., which suppress resonances which otherwise act very efficiently to produce the degenerate core-halo structure.

- **Accuracy of predictions of QSS in the SGS model:** While, as just described, the QSS which result from violent relaxation divide into those which are close to the LB theory, on the one hand, or to the ansatz of Levin et al., on the other, the accuracy of the associated predictions is at best approximate: *in no case* do we see a perfect agreement with either LB theory or the ansatz (5.8). We underline that in this respect the spatial distribution of mass $\rho(x)$ and velocity distribution $\theta(v)$ are rather poor tools for diagnosing the agreement between observations and theory, as they wash out deviations which are most pronounced in energy space. We have also noted the apparent coherence of our results with the qualitative predictions of the kinetic theory approach described in [169].

Numerous results in the literature on various other models (see references in introduction) for specific ranges of initial conditions suggest that these latter two conclusions, and probably the first also, might apply much more generally to long-range systems. Further detailed investigation of such models, and in particular of broader classes of waterbag initial conditions like those considered here, or, for example, "multi-level" waterbag initial conditions would be required to establish if this is the case.

For the SGS it would be interesting to apply the analysis described by Levin et al. to determine a prediction of the form (5.8) for different initial conditions, and see how well it does in approaching the observed QSS. In this respect it is interesting perhaps to note that, at given value of ξ_D this is a one parameter family of solutions, so that it predicts QSS lying on a curve in the (ϕ_{11}, ϕ_{22}) plane. In Fig. 5.11, we see that the QSS obtained from the two parameter family of initial conditions at a fixed $\xi_D = 0.56$ do approximately collapse onto a curve. We would expect the degree to which the simple ansatz (5.8) can fit the QSS to be well characterized by determining the prediction it gives in this plane.

Of particular interest is of course the original context of 3D self-gravitating systems, to which the initial study of [37] for SRW suggests these conclusions may indeed apply. As mentioned, however, the results reported have been based, in this case, on examination of the density profile $\rho(x)$ alone, while the energy distribution is probably a finer diagnostic tool as we have seen here. In forthcoming work we will study this case, and discuss the possible relevance of our findings in the astrophysical context. In this respect we note one of the reasons why LB theory has not played — at least for what concerns it detailed predictions — a role in astrophysics

is that these predictions depend on unobservable initial phase space densities. In contrast the prediction of a degenerate core in many cases would give a simple link between observations and initial conditions, which may be of practical relevance notably in constraining the parameters in theories of structure formation in the universe.

Chapter 6

Quasi-stationary states and Lynden-Bell theory in 3D self-gravitating systems

In this chapter we report results of a numerical study in three dimensions, analogous to that given in the previous chapter for the 1D case. We thus address principally the same question: how well can the theory of LB account for the properties of QSS observed in numerical simulations. As in the 1D case we restrict ourselves to "waterbag" initial conditions, for which we have derived the detailed predictions of the LB theory in chapter 3.

We recall that these predictions depend, for this case, essentially on two parameters (instead of just a single one in the 1D case), which in chapter 3 we chose as

$$\tilde{\xi} = \frac{E - \tilde{E}_0}{|\tilde{E}_0|} \quad \text{and} \quad \tilde{R}_c = \frac{R_c}{\tilde{L}_0}$$

where

$$\tilde{E}_0 = -\frac{3}{10}(\frac{4}{3}\pi)^{\frac{4}{3}} G^2 M^{\frac{7}{3}} f_0^{\frac{2}{3}} \quad \text{and} \quad \tilde{L}_0 = \frac{1}{GM^{\frac{1}{3}} f_0^{\frac{2}{3}}}$$

where R_c is the radius of the confining box (required only in three dimensions). Thus, strictly speaking, to compare LB theory in this case with self-gravitating systems we need to consider such systems confined in a box. However, as discussed in chapter 3, there is a range in parameter space — sufficiently small value of $\tilde{\xi}$ corresponding to the regime which is sufficiently close to the degenerate limit — where the predictions of LB are only weakly sensitive to $\tilde{R}_c$. Given that this is the case we can ask (the potentially more relevant to astrophysics) question of whether LB theory can explain (partially) the results of violent relaxation of open self-gravitating systems. It is this question we address here.

The motivations for this "revisiting" of this theory have been given in the introduction: in the context of the study of long-range interactions in statistical mechanics interest has been revived in LB theory, suggesting that it has been discarded too quickly in astrophysics. Indeed in this context no full study of LB theory has in fact been performed — at most partial studies have been given showing that LB theory is a strictly not correct theory (e.g. [21]), which has been clear both observationally and in comparison with numerical simulations. Further, and more specifically, our motivation comes from recent study by Levin et al. [37] of the 3D case, which found that LB theory apparently can predict QSS in specific cases. Compared to [37] our

study uses full 3D simulations (rather than 1D simulations assuming spherical symmetry) with a wider range of initial conditions (both spherically and non-spherically symmetric).

6.1 Numerical simulations and choice of units

To simulate numerically 3D self-gravitating system we use the widely employed public code "GADGET-2" [170] (available at *http://www.mpa-garching.mpg.de/gadget/*). This code allows one to simulate, in particular, the case of an open system of N particles attracted by Newtonian self-gravity. It uses a hierarchical tree algorithm to calculate the gravitational force (optionally in combination with particle-mesh (PM) or smoothed particle hydrodynamics (SPH), if involving the gas dynamics). The effect of expansion of universe, or of the periodic boundary condition, can be alternatively added for cosmological simulations. The exact gravitational pair potential below an (adjustable) smoothing length ϵ is regularized by a splined interpolation to an every where attractive force which vanishes at zero separation (see [171] for exact smoothing function). In our simulations we choose ϵ sufficiently small so that this regularization plays no role in the dynamics on the short time scales. In practice we set $\epsilon \sim 1/10$ of the initial interparticle distance in all simulations. Or in other words, given a system with N particles, the interparticle distance is of order $\sim 1/N^{1/3}$ and we set $\epsilon = 0.1/N^{1/3}$. This is sufficient to ensure that this scale is much smaller than the minimal characteristic size of the system attained during it evolution (see e.g. [160, 172]).

The code requires, in addition, two other essential parameters: the opening angle (controlling precision on the force calculation) and the time step. For those we follow the guidelines given by [160]. The essential control on accuracy is given in practice by the energy. In all our simulations it is conserved over the length of the run up to 0.2%.

Our results will be given in units in which the gravitational constant $G = 1$, total mass $M = 1$ and initial density $\rho_0 = 1$*, except for plots of temporal evolution which employ the unit

$$t_{dyn} = \sqrt{\frac{1}{4\pi G\rho_0}} \tag{6.1}$$

which is of order the free-fall time, t_{ff}, (cf. section 3.1)

$$t_{ff} = \sqrt{\frac{3}{32\pi G\rho_0}} = \sqrt{\frac{3}{8}}\, t_{dyn}.$$

6.2 Initial condition

We consider here three classes of waterbag initial conditions, analogous to those treated in one dimension in the previous chapter. The initial phase space density is thus uniform in a finite region, and the different cases are the following:

1) Single sphere waterbag (SSW) initial condition

In this case we take, in coordinate space, a sphere of radius r_0 and randomly sample particles inside with constant mass density. The initial potential energy is thus

$$U_0 = -\frac{3GM^2}{5r_0}. \tag{6.2}$$

*The default unit employed in GADGET-2 is the cgs system.

and in our choice of units, $r_0 = 0.62$. We also suppose spherical symmetry in v-space, and generate the initial velocity distribution by randomly sampling (v_x, v_y, v_z) with uniform probability in a sphere of radius v_0. The center of mass is set to stay at the origin (i.e. sum of all particle velocity is zero). The total initial kinetic energy is therefore

$$T_0 = \frac{3Mv_0^2}{10}. \tag{6.3}$$

As in one dimension we choose to characterize the initial condition by the initial virial ratio

$$R_0 = \frac{2T_0}{|U_0|} = \frac{r_0 v_0^2}{GM}. \tag{6.4}$$

The phase space density f_0 is thus

$$f_0 = \frac{M}{(\frac{4}{3}\pi r_0^3)(\frac{4}{3}\pi v_0^3)}. \tag{6.5}$$

The total energy can be therefore expressed as a function of M, f_0 and R_0 as

$$E = \frac{3}{10}(\frac{4}{3}\pi)^{\frac{4}{3}} G^2 M^{\frac{7}{3}} f_0^{\frac{2}{3}} (R_0^2 - 2R_0) \tag{6.6}$$

which has a minimum at $R_0 = 1$. Recalling $\tilde{E}_0$ and $\tilde{\xi}$ from chapter 3

$$\tilde{E}_0 = -\frac{3}{10}(\frac{4}{3}\pi)^{\frac{4}{3}} G^2 M^{\frac{7}{3}} f_0^{\frac{2}{3}} \quad \text{and} \quad \tilde{\xi} \equiv \frac{E - \tilde{E}_0}{|\tilde{E}_0|},$$

we can thus express $\tilde{\xi}$ as function of R_0 by

$$\tilde{\xi} = 1 - 2R_0 + R_0^2. \tag{6.7}$$

The characteristic energy $\tilde{E}_0$ thus corresponds to that of an SSW initial condition with $R_0 = 1$. The summary of the parameters characterizing SSW initial conditions is shown in Tab. 6.1.

Table 6.1: Parameters of SSW initial conditions with different R_0 (or equivalently $\tilde{\xi}$). We give also the value of R_0 and v_0 in chosen units ($G = 1, M = 1, \rho_0 = 1$).

R_0	0.1	0.2	0.3	0.4	0.5	0.6	0.7	0.8	0.9	1
$\tilde{\xi}$	0.81	0.64	0.49	0.36	0.25	0.16	0.09	0.04	0.01	0
v_0	0.40	0.58	0.70	0.80	0.90	0.98	1.06	1.14	1.20	1.27

2) Double sphere waterbag (DSW) initial condition

In this case we consider, in configuration space, two concentric spheres with radius r_1 and r_2 where $r_1 < r_2$. The densities of inner region ($r < r_1$) and outer region (at $r_1 < r < r_2$) are ρ_1 and ρ_2, respectively, with $\rho_1 > \rho_2$. The initial density ρ_0 is taken as the averaged density of mass enclosed in the radius r_2. For the initial velocity, the particles in the inner and outer regions are independently distributed in the same manner as in SSW initial condition but the

regions with ρ_1 and ρ_2 are associated to the cut-off velocity v_1 and v_2 respectively, chosen so that initial phase space density in both regions is equal, and given by

$$f_0 = \frac{\rho_1}{\frac{4}{3}\pi v_1^3} = \frac{\rho_2}{\frac{4}{3}\pi v_2^3}. \tag{6.8}$$

The total mass is thus

$$M = \frac{4}{3}\pi r_1^3 \rho_1 + \frac{4}{3}\pi(r_2^3 - r_1^3)\rho_2 = f_0(\frac{4}{3}\pi)^2 r_1^3 v_1^3 + f_0(\frac{4}{3}\pi)^2(r_2^3 - r_1^3)v_2^3. \tag{6.9}$$

The initial kinetic energy is

$$T_0 = \frac{8\pi^2}{15} f_0 r_1^3 v_1^5 + \frac{8\pi^2}{15} f_0 (r_2^3 - r_1^3) v_2^5 \tag{6.10}$$

and the initial potential energy is

$$U_0 = -\frac{G(4\pi)^4}{135} f_0^2 v_1^6 r_1^5 - \frac{G(4\pi)^4}{54} f_0^2 v_1^3 v_2^3 r_1^3 (r_2^2 - r_1^2) - \frac{G(4\pi)^4}{135} f_0^2 v_2^6 (r_2^5 - r_1^5) + \frac{G(4\pi)^4}{54} f_0^2 v_2^6 r_1^3 (r_2^2 - r_1^2) \tag{6.11}$$

from which we calculate the initial virial ratio $R_0 = 2T_0/|U_0|$. Like our DRW initial condition in chapter 5, these initial conditions are a three parameter family, which we choose to be R_0, δ, r_1 where $\delta = \frac{\rho_1}{\rho_2} > 1$. If $\delta = 1, r_1 = 0$ or $r_1 = r_2$ DSW reduces to SSW. The details of the specific DSW initial conditions we have considered here are summarized in Tab. 6.2. As in one dimension, we choose DSW initial conditions with the same $\tilde{\xi}$ as in SSW initial conditions so that the LB theory predicts the same QSS for each pair. Note that by definition $r_2 = 0.62$.

Table 6.2: Parameters of DSW initial conditions and the corresponding values of $\tilde{\xi}$ (see choice of units in text).

$\tilde{\xi}$	0.81	0.64	0.49	0.36	0.25	0.16	0.09	0.04	0.01	0
δ	1.10	1.45	1.25	1.20	1.26	2.27	1.14	1.12	1.41	1.06
R_0	1.90	1.80	1.71	1.61	1.52	1.47	1.32	1.24	1.21	1.08
r_1	0.58	0.59	0.54	0.51	0.57	0.50	0.58	0.38	0.34	0.34

3) Cylindrical waterbag (CW) initial condition

Like in one dimension we finally consider some other shapes for the initial waterbag. In this case we exploit the specificity of three dimensions by taking initial condition which are not spherically symmetric in coordinate space. We consider an initial distribution which is a cylinder in this space. We restrict ourselves (as in one dimension) to the case of initial virial ratio unity. The initial condition is characterized then by the surface radius, r_{cy}, and height of the cylinder, h_{cy}. The axis of cylinder is aligned parallel to the z-axis. For initial velocity of particles, we use the same procedure as in SSW initial condition (i.e. spherically symmetrically distributed) with velocity cut-off v_0 chosen so that the initial virial ratio $R_0 = 1$. The detail of specific CW initial conditions we have studied are shown in Tab. 6.3 with the case number ordered by the degree of triaxiality (see below). The potential and kinetic energy has been determined numerically.

Table 6.3: Parameters of 3 cylindrical initial conditions, all of which have $\rho_0 = 1$ and $R_0 = 1$.

Case	$\tilde{\xi}$	r_{cy}	h_{cy}	v_0
CW1	0.16	0.78	0.52	0.81
CW2	0.07	0.68	0.68	0.78
CW3	0.04	0.60	0.89	0.69

6.3 Virialization to QSS

Before turning to our comparison with LB theory we examine first the qualitative behaviors observed in our simulations. The temporal evolution of the virial ratio $R(t) = \frac{2T}{|U|}$ for SSW initial conditions, sampled with $N = 5000$ particles, and the indicated R_0 is shown in Fig. 6.1. For $R_0 < 0.5$ (left panel), $R(t)$ does not converge to unity, while it does for $R_0 \geq 0.5$ (right panel). Note that for $R_0 \to 0$ the time at which $R(t)$ reaches the maximum (i.e. when the kinetic energy is maximum) approaches closely the free-fall time t_{ff}. Fig. 6.2 shows instead the virial ratio when all particles with $\varepsilon > 0$ are removed. Convergence to a virial ratio of unity *is* observed in all cases. The number of bound particles (i.e. $\varepsilon < 0$) is indicated in each case. These behaviors are thus explained by the fact that, in the case with smaller R_0, a significant fraction of the mass ends up being ejected completely from the (open) system, carrying away with it a non-negligible amount of energy. The limit case $R_0 = 0$ ("cold collapse") has been extensively studied in [160] with a focus precisely on this ejection of mass and energy. We observe here that the mass ejection persists up to $R_0 \simeq 0.5$, decreasing monotonically from the cold case (in which about $\sim 30\%$ of mass is ejected). The virialization time in all cases is of order a few dynamical times, in accordance with the violent relaxation time scale estimated in section 3.1.

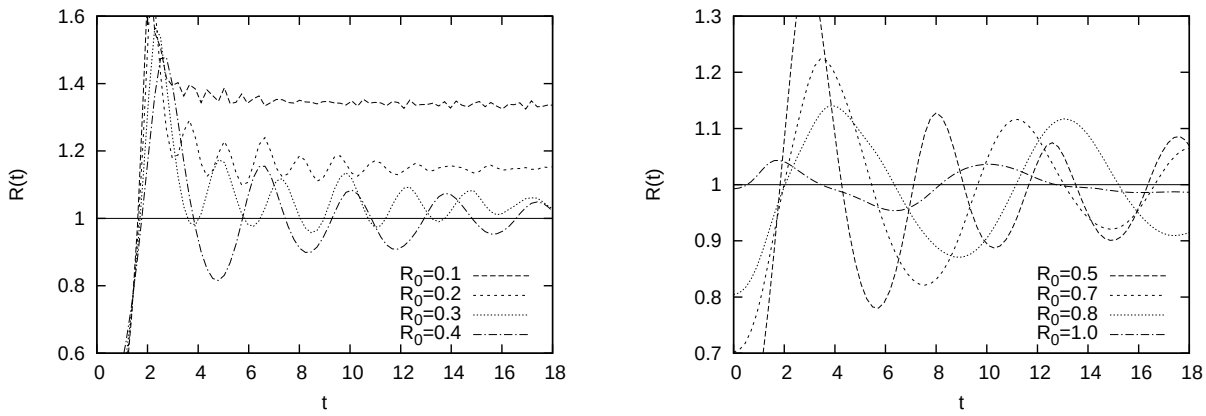

Figure 6.1: Temporal evolution of the virial ratio $R(t)$ of SSW initial conditions with $N = 5000$. Left panel is for the cases $R_0 < 0.5$ and right panel is for the cases $R_0 \geq 0.5$.

In Fig. 6.3 are shown the distribution of particles (projected on a plane) obtained at the end of a simulation (i.e. at $t = 18\ t_{dyn}$) starting from a realization of an SSW initial condition with $R_0 = 0.2$ ($\tilde{\xi} = 0.64$), as well as the corresponding radial density profile[†]. We see that the system

[†]The origin (i.e. $r = 0$) corresponds to the center of mass, which is fixed at rest at the origin.

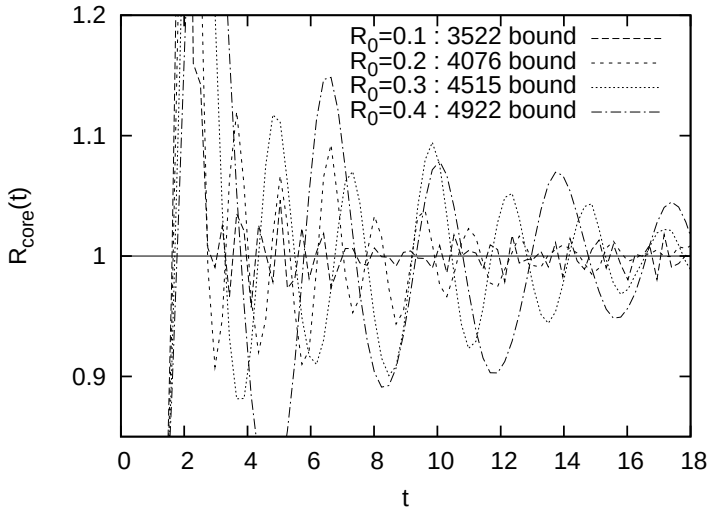

Figure 6.2: Temporal evolution of $R(t)$ for the cases in Fig. 6.1 (left panel) considering now only bound particles (whose number is indicated). The horizontal line indicates $R = 1$.

appears to consist of two components: a central region with a central "core" with density about one hundred times the initial (uniform) density ($\rho_0 = 1$, plotted in dashed line), which then falls off approximately as a power law surrounded by a very diffuse cloud of particles with a roughly constant density about six orders of magnitude smaller to that in the center. The outermost part in fact corresponds essentially to particles which are unbound and moving outward, and which will therefore escape from the system leaving behind just the central core and a few diffuse surrounding (but bound) particles. Shown in Fig. 6.4 are the same plots showing now only the bound particles. Also shown in the the same figure are the lines corresponding the an isothermal sphere behavior $\rho(r) \propto r^{-2}$ and $\propto r^{-4}$. We see that the stationary structure falls off considerably faster than r^{-2} and indeed (at intermediate r) fits better with r^{-4} line. The whole profile (excluding the very outermost part) is well fitted by

$$\rho(r) = \frac{\rho_c}{1 + (\frac{r}{r_c})^4}.$$

These results are in good agreement with results found in the literatures for similar (but not identical) initial conditions [22, 23, 29].

The velocity distribution averaged over the last five dynamical times of the simulations (i.e. from $t = 13$ to $t = 18$ t_{dyn} with twenty equally spaced time slices) is shown in Fig. 6.5, along with a Gaussian best-fit (solid line) given by

$$\theta(v) = Ae^{-\frac{v^2}{\sigma^2}} \tag{6.12}$$

with A and σ to be the fitting parameters. We use the least-square method to obtain the best fit. The distribution at high v is evidently not Gaussian. Non-Gaussianity of velocity distribution has been found in [173] for cold collapse of uniform spheres.

The same plots are shown in Figs. 6.6 and 6.7 for SSW initial condition with $R_0 = 0.6$ ($\tilde{\xi} = 0.16$). At this time ($t = 18$ t_{dyn}) the system is visibly well relaxed and has stopped

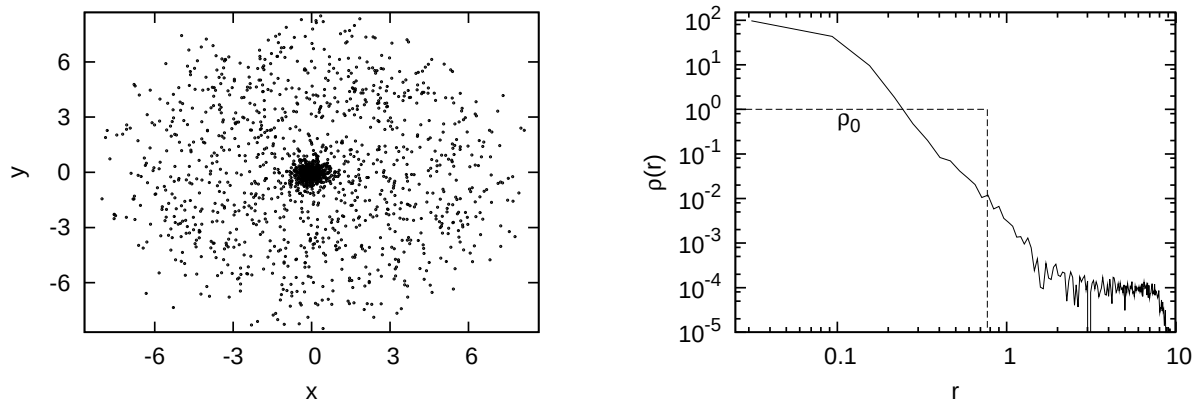

Figure 6.3: (Left panel) A snapshot at the end of simulation of an SSW initial condition with $R_0 = 0.2$ represented in a 2D spatial projection. (Right panel) The density profile as a function of radius for this snapshot. The dashed line corresponds to the initial density distribution ($\rho_0 = 1$).

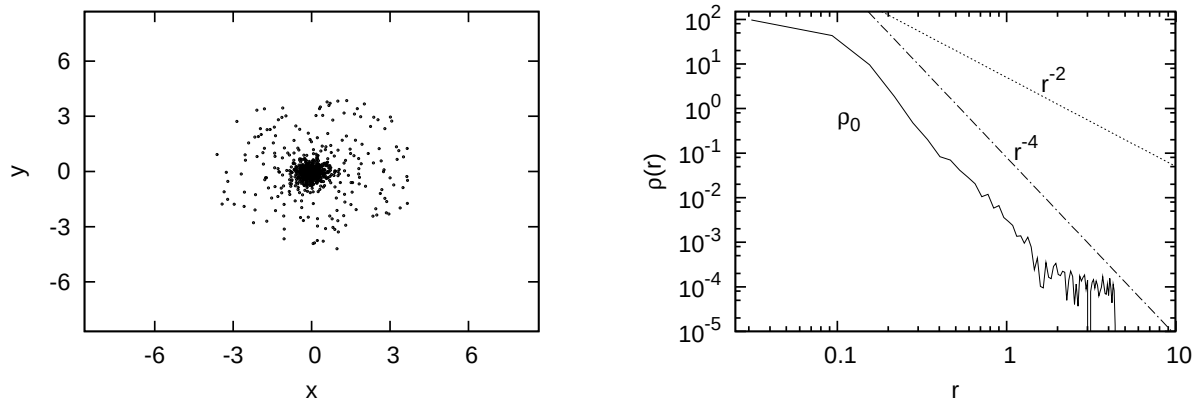

Figure 6.4: Same plots as in Fig. 6.3 with unbound particles ($\varepsilon > 0$) removed. In right panel two straight lines correspond to $\rho(r) \propto r^{-2}$ (isothermal sphere) and r^{-4}.

evolving both in size and shape. We observe similar qualitative behavior to the case $R_0 = 0.2$. The central density attained is considerably lower ($\sim 10\rho_0$) but it is close to constant over a large radius before dropping off even more rapidly than in the previous case, roughly decaying as r^{-5} (see straight line on the side, along with isothermal sphere line). The mass is thus considerably less concentrated in the "core". On the other hand there is no longer the "cloud" observed in the previous case and no ejected mass. The time averaged velocity distribution in Fig. 6.7 shows a somewhat similar qualitative behavior to the previous case, which is again not described by a Gaussian form.

Now let us consider the SSW initial condition with $R_0 = 0.9$ ($\tilde{\xi} = 0.01$). The snapshot and density profile at $t = 18\ t_{dyn}$ are shown in Fig. 6.8. In this case the final profile is very close to the starting one, with an almost exactly constant density cutting off extremely sharply, with

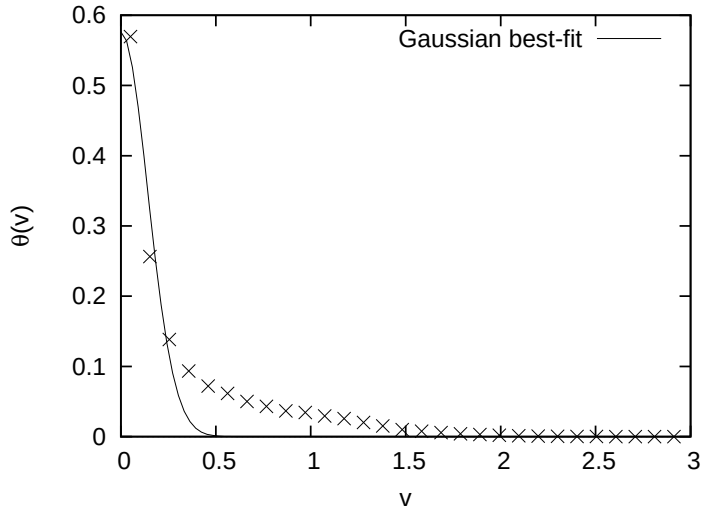

Figure 6.5: Time-averaged velocity distribution $\theta(v)$ obtained from SSW initial condition with $R_0 = 0.2$. The solid line stands for Gaussian best-fit (6.12).

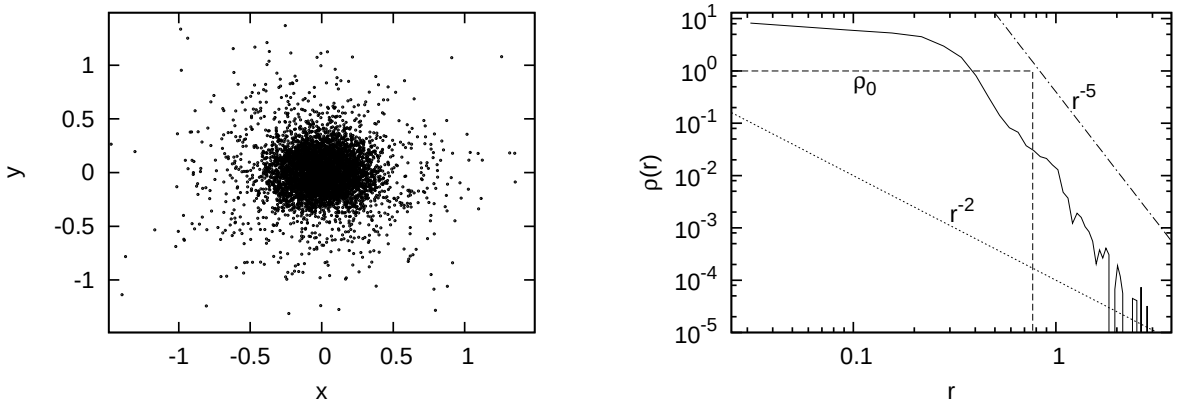

Figure 6.6: (Left panel) A snapshot at the end of simulation of an SSW initial condition with $R_0 = 0.6$ represented in a 2D spatial projection. (Right panel) The density profile as a function of radius for this snapshot. The dashed line corresponds to the initial density distribution ($\rho_0 = 1$). Two straight lines are for $\rho(r) \propto r^{-2}$ (or isothermal sphere) and $\propto r^{-5}$.

the absence of a "cloud" in the projected 2D spatial configuration. The velocity distribution (not shown) exhibits the same behavior as found in the case $R_0 = 0.6$.

The qualitative behaviors of the virialization and relaxed states observed starting from DSW initial condition are similar. In the case of CW initial condition an important qualitative difference arises due to the breaking of spherical symmetry. Shown if Figs. 6.9 are the 2D projections in y-z plane (note that cylinder axis is initially aligned parallel to the z-axis) of the snapshots at the beginning and the end ($t = 46\ t_{dyn}$) for the three cases (e.g. CW1, CW2 and CW3). We can see by visual inspection that the final distributions depart also from spherical symmetry (albeit

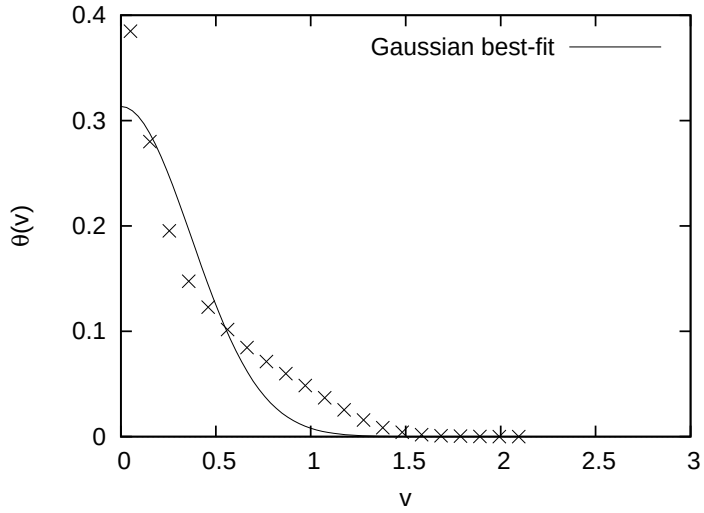

Figure 6.7: Time-averaged velocity distribution $\theta(v)$ obtained from SSW initial condition with $R_0 = 0.6$. The solid line stands for Gaussian best-fit (6.12).

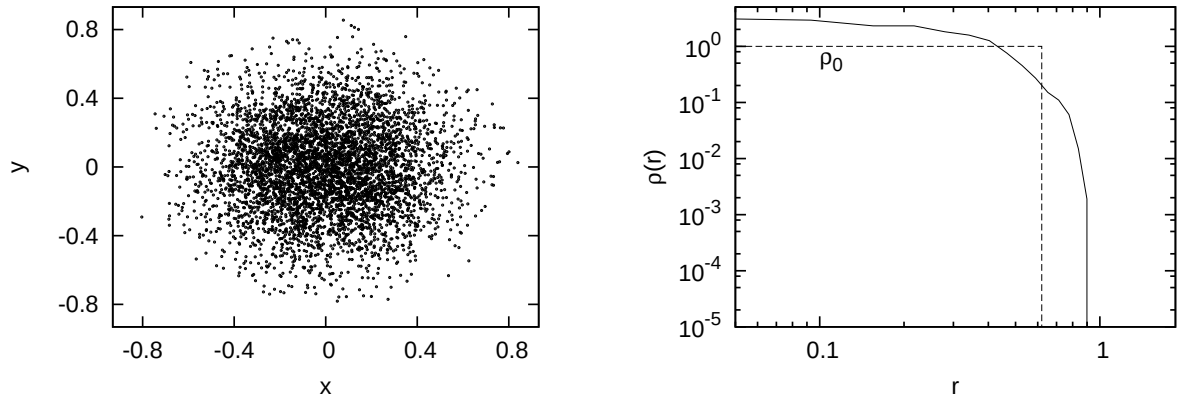

Figure 6.8: (Left panel) A snapshot at the end of simulation of an SSW initial condition with $R_0 = 0.9$ represented in a 2D spatial projection. (Right panel) The density profile as a function of radius for this snapshot. The dashed line corresponds to the initial density distribution ($\rho_0 = 1$).

less than the initial conditions).

In Fig. 6.10 are shown the plots of the evolution in time of the virial ratio (top-left panel) for three CW initial conditions, and then, for two cases, the evolution of the normalized diagonal elements of the moment of inertia tensor (two bottom panels), i.e.

$$i_{xx} \equiv \frac{I_{xx}}{I_{xx}+I_{yy}+I_{zz}}\,,\; i_{yy} \equiv \frac{I_{yy}}{I_{xx}+I_{yy}+I_{zz}}\,,\; i_{zz} \equiv \frac{I_{zz}}{I_{xx}+I_{yy}+I_{zz}},$$

where I_{xx}, I_{yy} and I_{zz} are the diagonal elements of moment of inertia tensor with respect to x, y

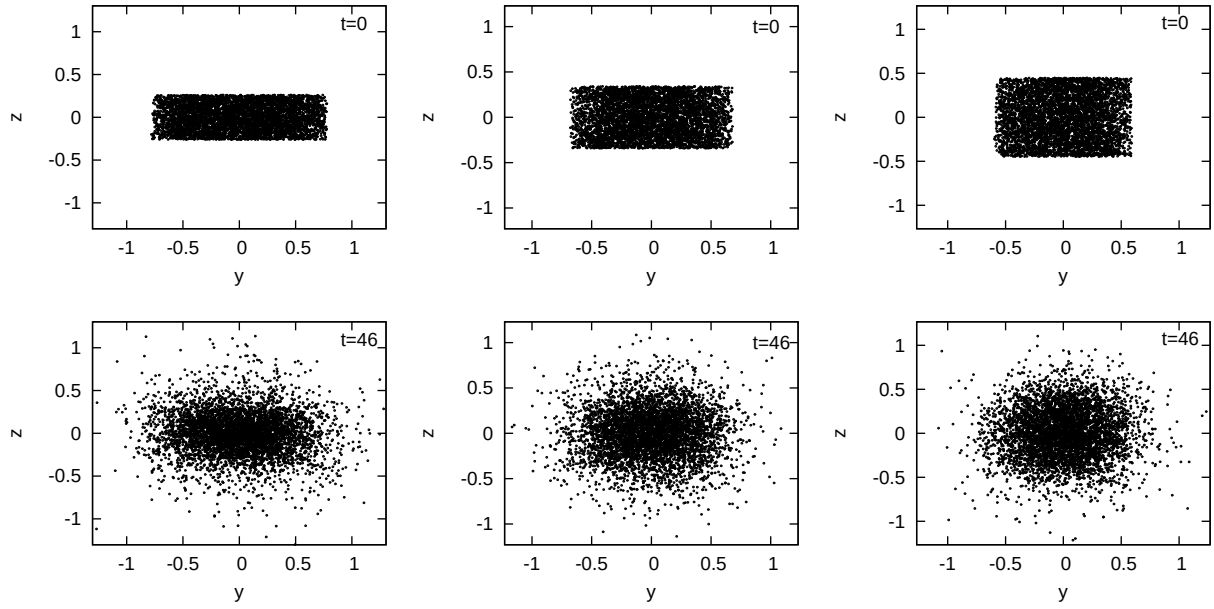

Figure 6.9: The snapshots at the beginning (top panels) and the end (bottom panels) of simulation of CW1-CW3 initial conditions (from left to right) projected in y-z plane.

and z axes. The parameter $\mathcal{T}$ defined by

$$\mathcal{T} = \frac{3i_{zz}}{i_{xx} + i_{yy} + i_{zz}} - 1,$$

which measures the degree of triaxiality, is also plotted, for three cases, in the top-right panel. These plots show, in line with what is seen from visual inspection of the initial and final configurations, that while the triaxiality decreases in all cases during the violent relaxation it does not disappear completely. In the case of CW1, $\mathcal{T}$ decreases from $\simeq 0.4$ to a final value of 0.2, while in CW3 on the other hand, which starts from less triaxial with $\mathcal{T} = 0.1$ ends up with $\mathcal{T} = 0.02$. The symmetry about z-axis is preserved, at least in two cases. The triaxial QSS found here are in line with results of numerical investigations in the literatures of similar (but not identical) initial conditions [174].

6.4 Comparison with LB theory

In this section we compare the results of our numerical simulations with the predictions of LB theory, detailed in section 3.5. All simulations are for 5000 particles.

6.4.1 QSS of SSW initial conditions with different R_0

Consider first the SSW initial conditions with $R_0 = 1$ and $R_0 = 0.9$ (see Tab. 6.1 for $\tilde{\xi}$). The density profile $\rho(r)$ and mass distribution $M_\rho(r)$ are shown in Fig. 6.11 ($R_0 = 1$) and 6.12 ($R_0 = 0.9$), averaged from $t = 13$ to $18\, t_{dyn}$ in twenty equally spaced time slices. The end of the r-axis corresponds to the cut-off radius i.e. $R_c = 3r_0$ (or $\tilde{R}_c = 0.44$ and 0.49 for $R_0 = 1$ and

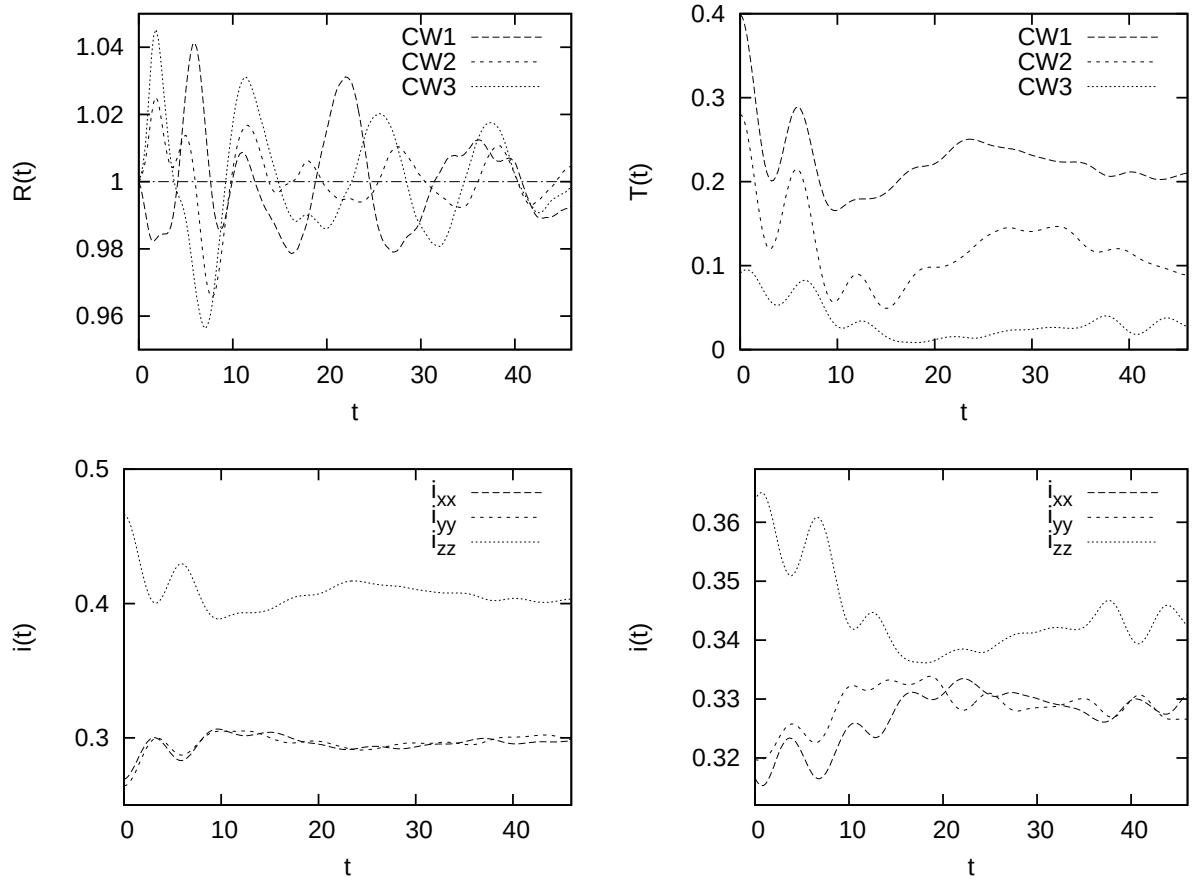

Figure 6.10: Temporal evolution of the virial ratio (top-left panel) and the triaxial parameter $\mathcal{T}$ (top-right panel) for three CW initial conditions. Two bottom panels are the temporal evolution of diagonal elements of the moment of inertia tensor for CW1 (bottom-left panel) and CW3 (bottom-right panel).

0.9, respectively) used in the calculation of LB predictions, shown as solid lines. For $\rho(r)$ the agreement is quite good at smaller r, fitting the decay of the density until $\rho \sim 10^{-2}$, but then deviates in the very outer part. For $M_\rho(r)$ this deviation at large radius has less effect because the contribution from this density tail is not significant. The deviation in this quantity is most pronounced at intermediate r. As discussed in chapter 3, as the LB prediction decays rapidly and $M_\rho(r)$ at R_c is very low (more precisely $M_\rho(R_c) \sim 0.003$ of the peak value), this prediction is not significantly sensitive to the box size.

Shown in Fig. 6.13 and 6.14 are $\theta(v)$ and $N_\theta(v)$ for the same cases (with time average performed as described above), with the LB predictions as solid lines. $\theta(v)$ shows a very significant deviation from theory at low v where the theory largely overestimates the velocity distribution, predicting almost twice the value observed in the simulation. For higher v there is better (but still not perfect) agreement. The deviations are less evident in $N_\theta(v)$ in which there is a visible (but modest) discrepancy at intermediate v. At high v the simulation data is slightly below the LB prediction.

The time-averaged energy distributions $F(\varepsilon)$ together with the LB predictions for the same

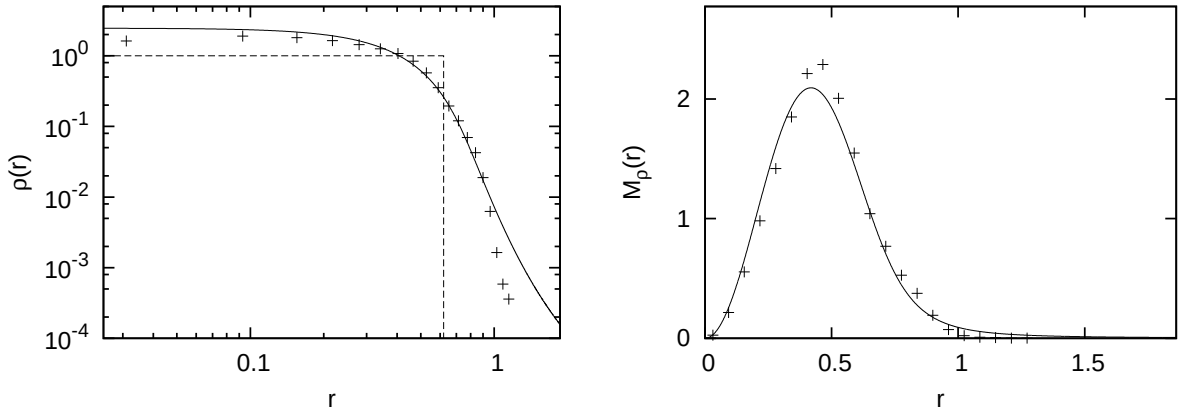

Figure 6.11: Time-averaged $\rho(r)$ (left panel), in log-log scale, and $M_\rho(r)$ (right panel) of SSW initial condition with $R_0 = 1$ ($\xi_D = 0$). The solid lines are the LB predictions. The end of the r-axis in both panels corresponds to the cut-off radius $R_c = 3r_0$ (or $\tilde{R}_c = 0.44$) used to calculate the LB prediction.

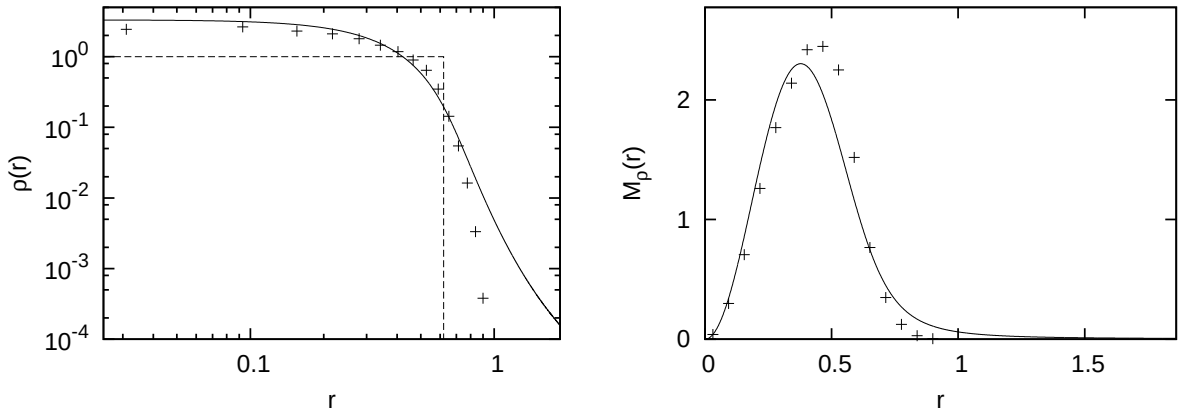

Figure 6.12: Time-averaged $\rho(r)$ (left panel), in log-log scale, and $M_\rho(r)$ (right panel) of SSW initial condition with $R_0 = 0.9$ ($\xi_D = 0.01$). The solid lines are the LB predictions. The end of the r-axis in both panels corresponds to the cut-off radius $R_c = 3r_0$ (or $\tilde{R}_c = 0.49$) used to calculate the LB prediction.

initial conditions are shown in Fig. 6.15. The agreement is very good at low ε in both cases, while at higher ε the simulation shows significant deviation from theory. We note that in both cases the LB predictions extend up to close to $\varepsilon = 0$ (and indeed are non-zero beyond, decaying exponentially), while the plots from simulations are cut off well below $\varepsilon = 0$. As discussed in section 3.5.4 we can calculate for the LB prediction the fraction of unbound mass M^+/M. For $R_0 = 1$ and 0.9 they are 0.00014 and 0.00022 respectively (for the given box size), i.e. ~ 1 particle from a system of 5000 particles. We note that our result here for $M_\rho(r)$ with $R_0 = 1$ agrees well with that reported by Levin et al. [37] (obtained using a 1D simulation assuming

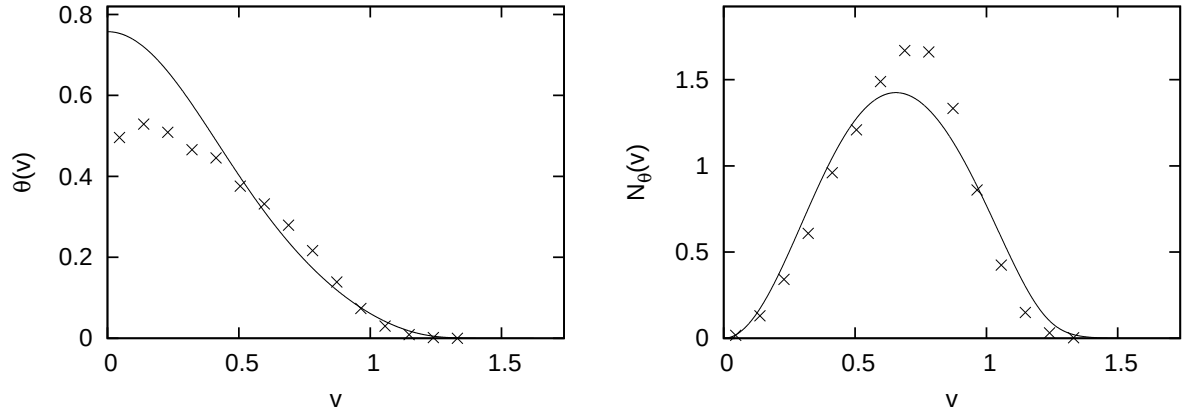

Figure 6.13: Time-averaged $\theta(v)$ (left panel) and $N_\theta(v)$ (right panel) of SSW initial condition with $R_0 = 1$. The solid lines are the LB predictions.

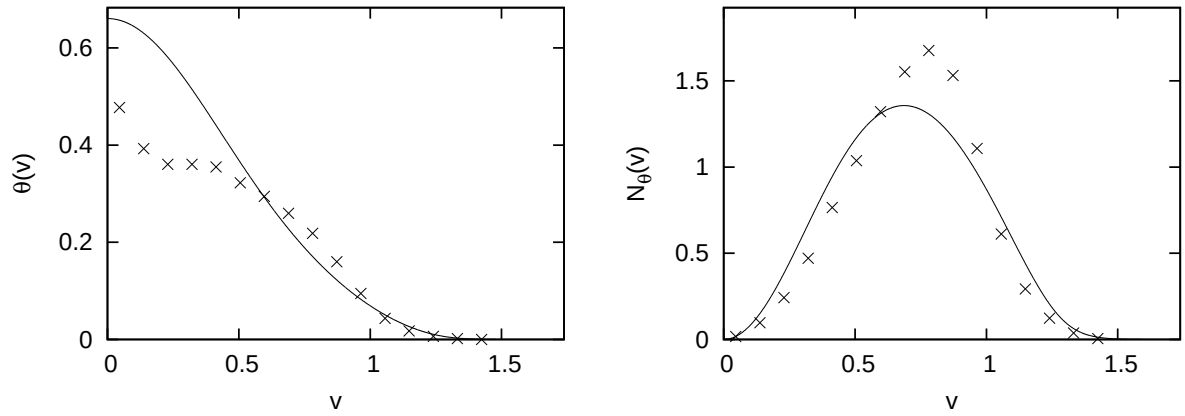

Figure 6.14: Time-averaged $\theta(v)$ (left panel) and $N_\theta(v)$ (right panel) of SSW initial condition with $R_0 = 0.9$. The solid lines are the LB predictions.

spherical symmetry).

We next consider the SSW initial conditions with $R_0 = 0.6$ and 0.5. $\rho(r)$ (log-log plot) and $M_\rho(r)$ (linear plot) are shown in Fig. 6.16 and 6.17 for $R_0 = 0.6$ and 0.5 respectively, time-averaged in the same way as detailed above. The LB predictions are again given as solid lines for $R_c = 3r_0$ (or $\tilde{R}_c = 0.74$ and 0.89 for $R_0 = 0.6$ and 0.5, respectively). For $\rho(r)$, the simulation gives excellent agreement with LB prediction at small r while at larger r there is some visible deviations (albeit less marked than in the previous cases). For $M_\rho(r)$ the simulations match quite well with LB predictions with only small deviation. The dependence on the size of the box is still very weak because (as seen in the plots of $M_\rho(r)$) most of the mass is confined to a region of characteristic size considerably smaller than the box. The ratio of $M_\rho(R_c)$ to the peak value is ~ 0.01. Shown in Fig. 6.18 and 6.19 are the time-averaged $\theta(v)$ and $N_\theta(v)$ for the same cases along with the LB predictions. As in previous cases the discrepancy is large

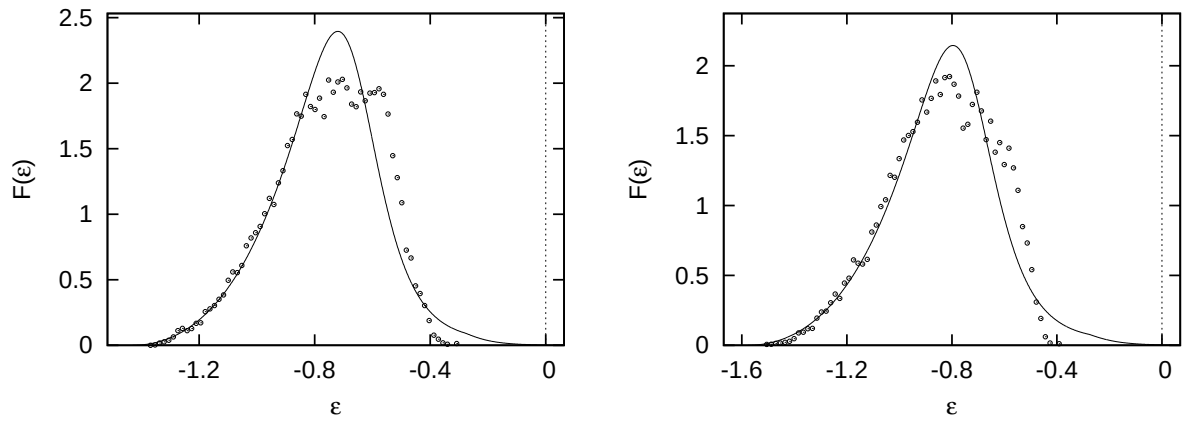

Figure 6.15: Time-averaged $F(\varepsilon)$ of SSW initial conditions with $R_0 = 1$ (left panel) and $R_0 = 0.9$ (right panel). The solid lines are the LB energy distributions.

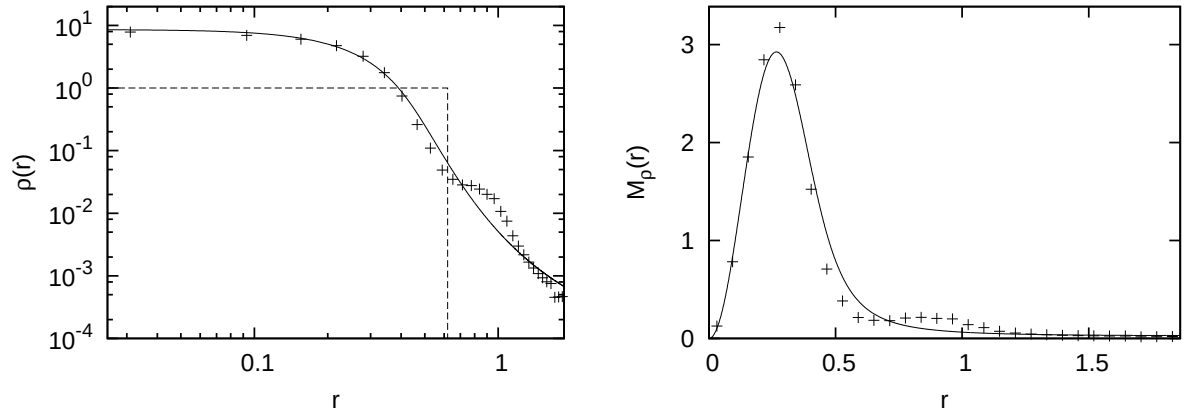

Figure 6.16: Time-averaged $\rho(r)$ (left panel), in log-log scale, and $M_\rho(r)$ (right panel) of SSW initial condition with $R_0 = 0.6$. The solid lines are the LB predictions. The end of the r-axis in both panels corresponds to the cut-off radius $R_c = 3r_0$ (or $\tilde{R}_c = 0.74$) used to calculate the LB prediction.

at low v (indeed greater than in previous cases) while good agreement is observed at larger v. Comparing with Fig. 6.7 (right), we see that LB theory gives better agreement than a Gaussian (except at low v). In plots of $N_\theta(v)$ the discrepancy is not evident for $R_0 = 0.6$, but it is more visible for $R_0 = 0.5$ where deviation is evident at low and intermediate v.

The time-averaged energy distribution of those two cases are shown in Fig. 6.20 along with the LB predictions. Again, like in the cases $R_0 = 1$ and 0.9, the agreement is good at low ε while at large ε a very clear deviation between the numerical data and LB theory is seen. Compared to the previous case ($R_0 = 1$ and 0.9) the difference between the two is more marked and characterized by the appearance of a second local maximum in $F(\varepsilon)$. The LB theory predicts (for $R_c = 3r_0$) $M^+/M = 0.004$ and 0.01 for $R_0 = 0.6$ and 0.5, respectively, but there is no particle

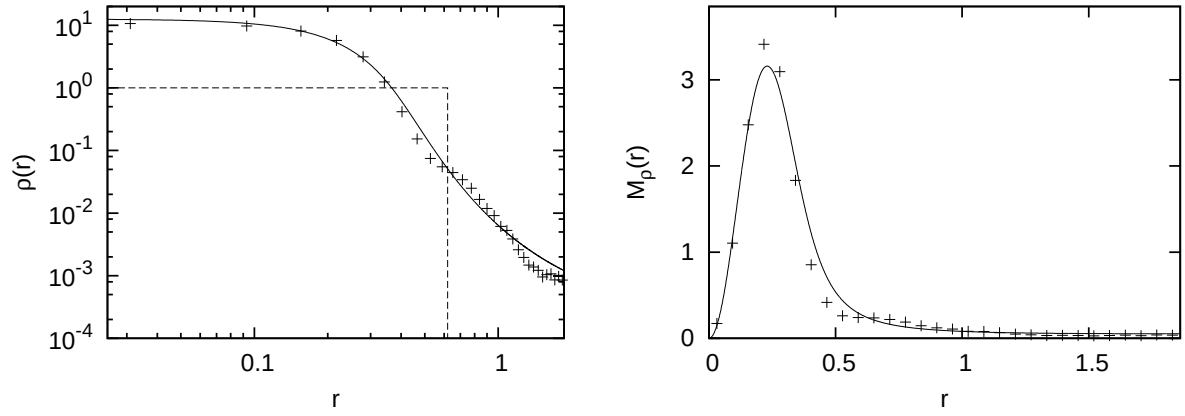

Figure 6.17: Time-averaged $\rho(r)$ (left panel), in log-log scale, and $M_\rho(r)$ (right panel) of SSW initial condition with $R_0 = 0.5$. The solid lines are the LB predictions. The end of the r-axis in both panels corresponds to the cut-off radius $R_c = 3r_0$ (or $\tilde{R}_c = 0.89$) used to calculate the LB prediction.

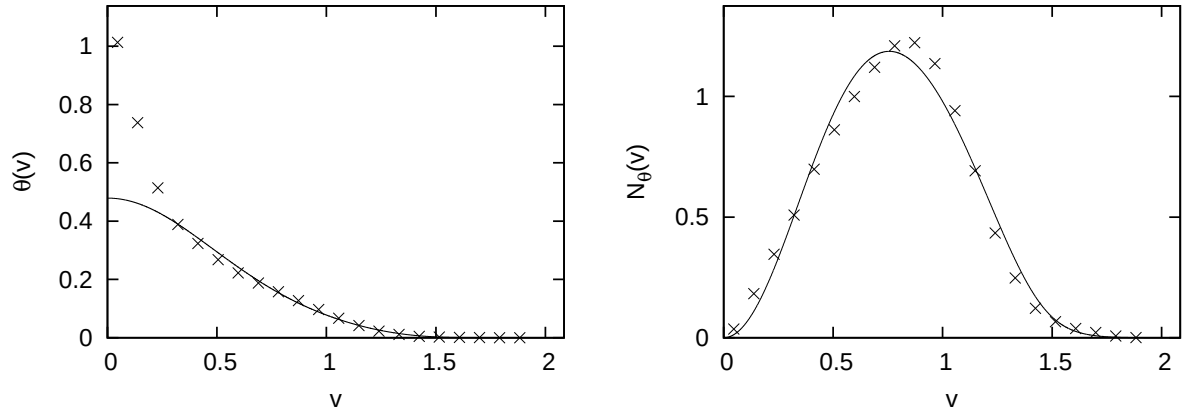

Figure 6.18: Time-averaged $\theta(v)$ (left panel) and $N_\theta(v)$ (right panel) of SSW initial condition with $R_0 = 0.6$. The solid lines are the LB predictions.

ejection observed. The "core-halo" structures, like those in one dimension, appears in the energy distribution which show (at least) two peaks: the large one at lower energy corresponding to the tightly bound particles (the "core") and a small peak (or perhaps group of smaller peaks) at higher ε (the "halo"). It is interesting to note that although the LB prediction does not fit the simulated data well at large ε, it does show, like the data, a second peak — albeit of much lower amplitude — in the same energy range. We will discuss this further below.

Next we consider the SSW initial condition with $R_0 = 0.3$. The time-averaged $\rho(r)$ and $M_\rho(r)$ are plotted in Fig. 6.21 along with the LB predictions. The cut-off radius (i.e. $R_c = 3r_0$ or equivalently $\tilde{R}_c = 1.48$) is now indicated by a dotted vertical line. The measured density profile and mass distribution in the simulations deviate very greatly from the LB predictions,

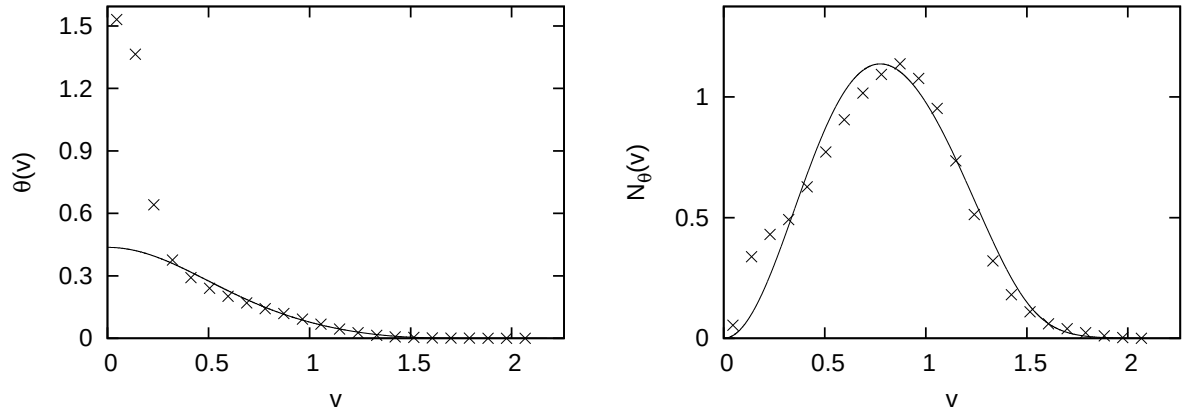

Figure 6.19: Time-averaged $\theta(v)$ (left panel) and $N_\theta(v)$ (right panel) of SSW initial condition with $R_0 = 0.5$. The solid lines are the LB predictions.

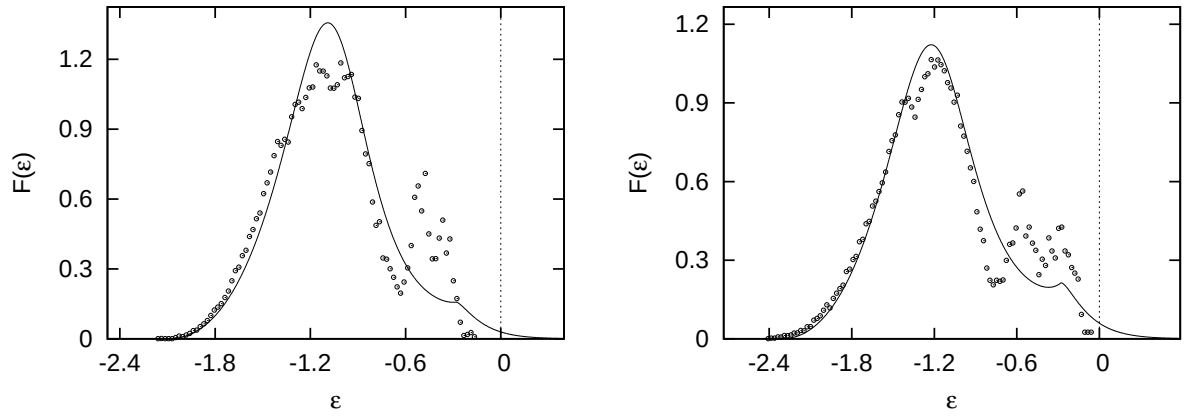

Figure 6.20: Time-averaged $F(\varepsilon)$ of SSW initial conditions with $R_0 = 0.6$ (left panel) and $R_0 = 0.5$ (right panel). The solid lines are the LB energy distributions.

showing at best approximate agreement in a small range of inner radii. In this simulation 485 of the 5000 particles are ejected completely from the system and thus the remaining bound mass is less than the mass of the LB prediction (which is, by construction, equal to the initial mass). In these plots it is manifest that we are now in the regime (of sufficiently non-degenerate energy) where the dependence of the LB prediction on the chosen box size becomes significant. This implies in turn that a priori the comparison of our data (for an open system) does not make sense. Indeed because the mass per unit radius $M_\rho(r)$ is now no longer so small at $r = R_c$ it is clear, as discussed in chapter 3, that varying the box size even modestly (e.g. by a factor of 2) will change the prediction very significantly. We will discuss this part further below in our conclusions.

Shown in Fig. 6.22 are the time-averaged $\theta(v)$ and $N_\theta(v)$ for the same case. $\theta(v)$ shows now an even greater over-estimation compared to the LB prediction at small v than in the previous

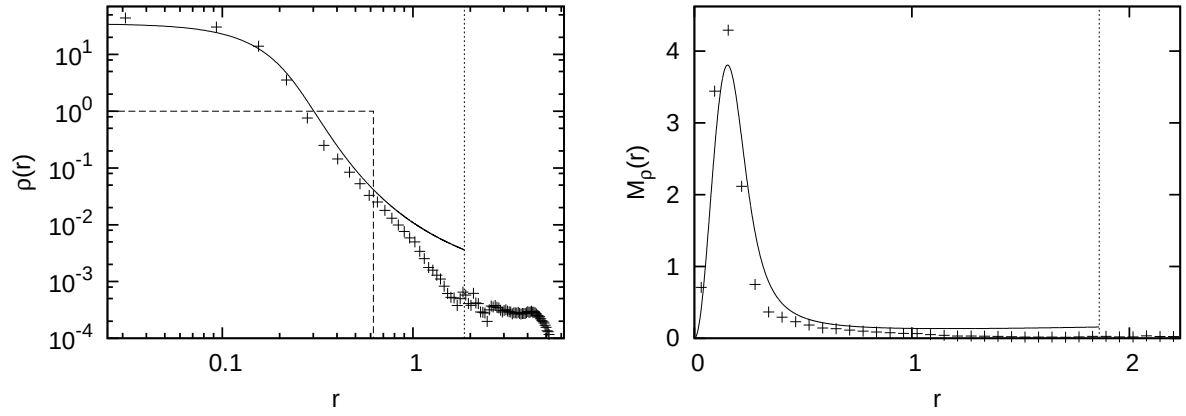

Figure 6.21: Time-averaged $\rho(r)$ (left panel) and $M_\rho(r)$ (right panel) of SSW initial condition with $R_0 = 0.3$. The solid lines are the LB predictions and the dotted vertical lines indicate the cut-off radius $R_c = 3r_0$ (or equivalently $\tilde{R}_c = 1.48$).

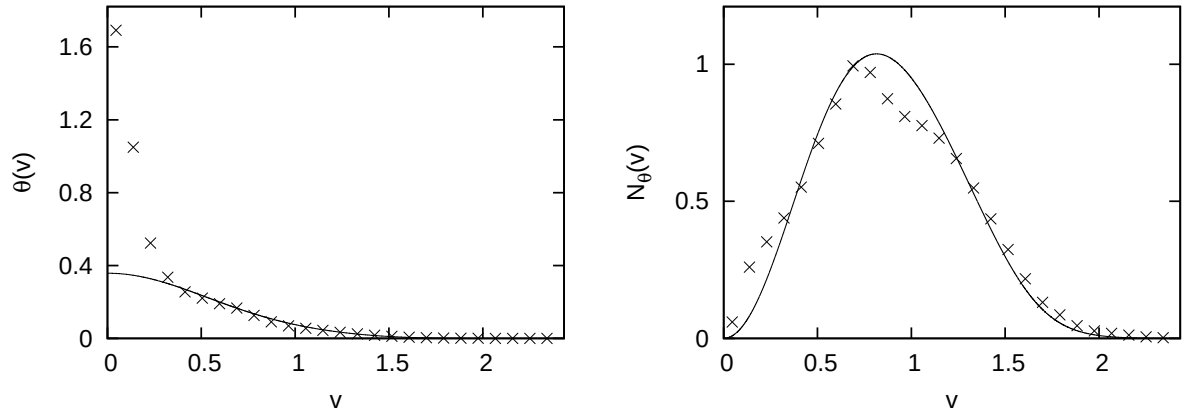

Figure 6.22: Time-averaged $\theta(v)$ (left panel) and $N_\theta(v)$ (right panel) of SSW initial condition with $R_0 = 0.3$. The solid lines are the LB predictions.

cases. These differences are now clearly observed in the $N_\theta(v)$ plot. At high v the agreement improves (but this concerns a very modest fraction of the mass).

Shown in Fig. 6.23 is the time-averaged $F(\varepsilon)$ for the same case. Again the numerical result is much further from the LB prediction than in the previous cases. Interestingly the theoretical prediction does produce now a clear double-peak configuration in ε-space but its structure and position do not agree well with the simulated result. The energy distribution crosses, in both simulation and theory, clearly to $\varepsilon > 0$. We note that (at the chosen box size) the LB theory predicts $M^+/M = 0.046$ (i.e. $\sim 5\%$) while we observe that 485 particles (i.e. $\sim 10\%$) are ejected. As we will discuss further below this suggests that if a comparison with LB theory can be appropriate, we need to choose a large box size.

In summary our results for SWB initial conditions give a picture quite similar to the anal-

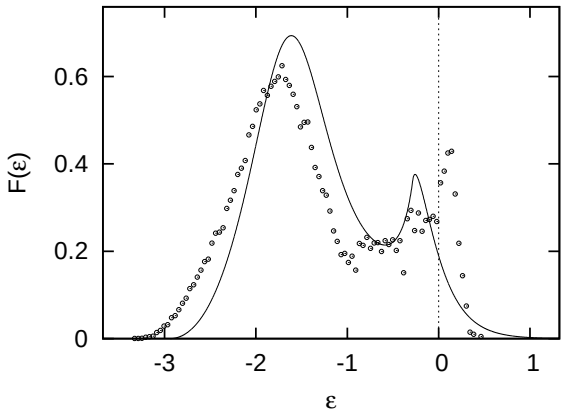

Figure 6.23: Time-averaged energy distribution of SSW initial conditions with $R_0 = 0.3$. The solid lines are the LB energy distribution.

ogous 1D case, modulo the additional difficulty of the dependence on box size: at lower energy the LB predictions work qualitatively quite well. As in one dimension we find that the discrepancies between LB theory and simulations can be identified much more clearly — close to the degenerate limit — in the energy distribution. Just as in one dimension it is at the high energy end — corresponding to particles which spend more time in the outer parts of the structure — that discrepancies show up. As we consider the initial conditions at higher energies these discrepancies increase greater, and the breakdown of LB theory can apparently be clearly associated with the appearance of a "core-halo" structure, i.e. a bimodal distribution in energy space of high and low energy particles.

6.4.2 DSW initial conditions: dependence on initial waterbag shape

Let us now use our DSW class of initial conditions to explore further the specific predictions of LB theory that the QSS does not depend on the shape of the waterbag, is correct.

Shown in Fig. 6.24 are the $M_\rho(r), N_\theta(v)$ and $F(\varepsilon)$ for DSW initial condition with $\tilde{\xi} = 0$ (equivalent to SSW with $R_0 = 1$), $\delta = 1.058$ and $R_0 = 1.08$, averaged from $t = 16$ to 21 t_{dyn} over twenty equally spaced time slices[‡]. The LB predictions are plotted as solid lines (calculated, as in Fig. 6.11, with $\tilde{R}_c = 0.44$ which corresponds here to $R_c = 3.25 r_2$). The distributions of $M_\rho(r)$ and $N_\theta(v)$ are very close to the plots from SSW with $R_0 = 1$ (see Figs. 6.11 and 6.13 for comparison). The plot of $F(\varepsilon)$ differs a little from the one for SSW (see Fig. 6.15). The agreement with LB is in fact slightly better than for the SSW case. As in one dimension, we cannot choose DSW with arbitrary δ because of the closeness to the degenerate limit.

Shown in Figs. 6.25 are $M_\rho(r), N_\theta(v)$ and $F(\varepsilon)$ for DSW initial condition with $\tilde{\xi} = 0.16$ (equivalent to SSW with $R_0 = 0.6$), $\delta = 2.27$ and $R_0 = 1.47$, averaged from $t = 55$ to $72\, t_{dyn}$ over twenty equally spaced time slices. The LB predictions are solid lines (calculated with $\tilde{R}_c = 0.44$, or $R_c = 3.25 r_2$, which corresponds to those in Fig. 6.16). Both this QSS and the QSS of SSW with $R_0 = 0.6$ are quite close to the LB predictions. Comparing with Figs. 6.16,

[‡]The different duration of the dynamical time in the simulations arises from the fact that all simulations were run for the same time in the units used by the GADGET-2 code.

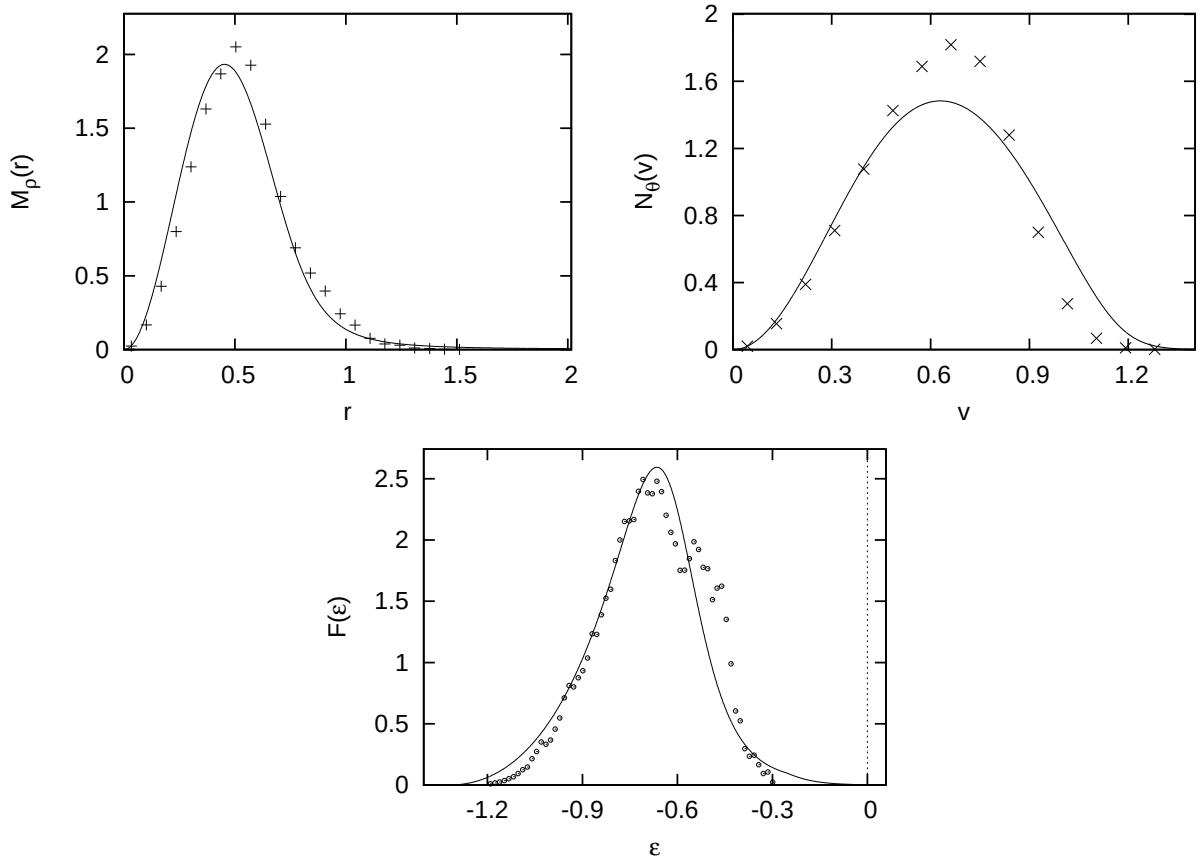

Figure 6.24: Time-averaged $M_\rho(r)$ (top-left panel), $N_\theta(v)$ (top-right panel) and $F(\varepsilon)$ (bottom panel) for DSW initial condition with $\tilde{\xi} = 0$ (equivalent to SSW with $R_0 = 1$), $\delta = 1.06$ and $R_0 = 1.08$. The solid lines are the LB predictions with $R_c = 3.25 r_2$ (or $\tilde{R}_c = 0.44$). See Figs. 6.11, 6.13 and 6.15 for comparison.

6.18 and 6.20, we see that the difference between the QSS in each case, although not so large, is greater than in the case $\tilde{\xi} = 0$. The core-halo structure appears in $F(\varepsilon)$ as in the QSS of the corresponding SSW.

Shown in Figs. 6.26 are the same plots now for DSW initial condition with $\tilde{\xi} = 0.49$ (equivalent to SSW with $R_0 = 0.3$), $\delta = 1.25$ and $R_0 = 1.71$, averaged from $t = 189$ to $252\, t_{dyn}$ over twenty equally spaced time slices. The LB predictions as solid lines (calculated using $\tilde{R}_c = 17.3 r_2$, or $\tilde{R}_c = 1.48$, corresponding to those in Fig. 6.21). The vertical dotted line in $M_\rho(r)$ plot indicates R_c. Comparing with Figs. 6.21, 6.22 and 6.23, the QSS resulting from DSW initial condition is significantly different from the one from the corresponding SSW initial condition, especially in the energy distribution where the core and halo are of equal size. The number of ejected particles in this case is 91, compared to 485 for the SSW case.

In summary, very much like in our 1D study in the previous chapter, we find that the QSS obtained from initial conditions which differ only in the shape of the waterbag show increasing differences as the energy increases. Thus the conclusion that the divergence from LB theory becomes increasingly significant as energy increases is confirmed by these tests.

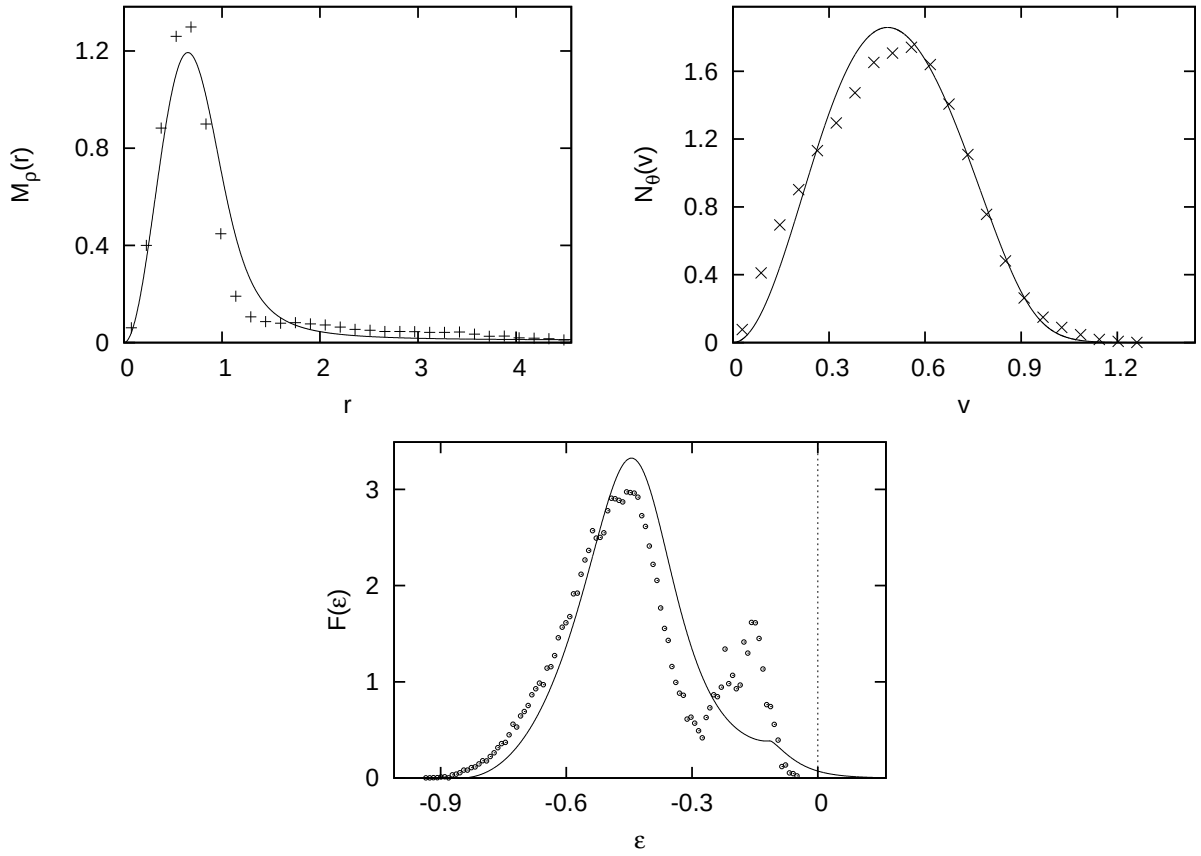

Figure 6.25: Time-averaged $M_\rho(r)$ (top-left panel), $N_\theta(v)$ (top-right panel) and $F(\varepsilon)$ (bottom panel) for DSW initial condition with $\tilde{\xi} = 0.16$ (equivalent to SSW with $R_0 = 0.6$), $\delta = 2.27$ and $R_0 = 1.47$. The solid lines are the LB predictions with $R_c = 7.34 r_2$ (or $\tilde{R}_c = 0.74$). See Figs. 6.16, 6.18 and 6.20 for comparison.

6.4.3 CW conditions and spherical symmetry breaking

As described above in section 6.3, the triaxial waterbag initial conditions relax to states which are still triaxial, although the degree of triaxiality is reduced, in some cases to a very small residual level. We have been comparing here with the predictions of LB theory when this is regulated by a spherical box, and in this case LB theory necessarily predicts spherical symmetric QSS. While one could of course in principle obtain triaxial QSS using a non-spherical box, this is not of interest here: we wish to consider the predictions of LB theory in which dependence on the regularization is (practically) negligible. Thus the geometry of the regularizing box should be of no importance and the predictions of LB thus should be spherical symmetric. The persistence of triaxiality therefore represents a deviation from LB theory. Given the weak triaxiality (in particular for CW3) it is, however, interesting to compare the spherical averaged quantities with the (spherical symmetric) predictions of LB theory.

The $\rho(r)$ (in log-log scale) and $M_\rho(r)$ are shown in Fig. 6.27 for CW3 (least triaxial QSS)

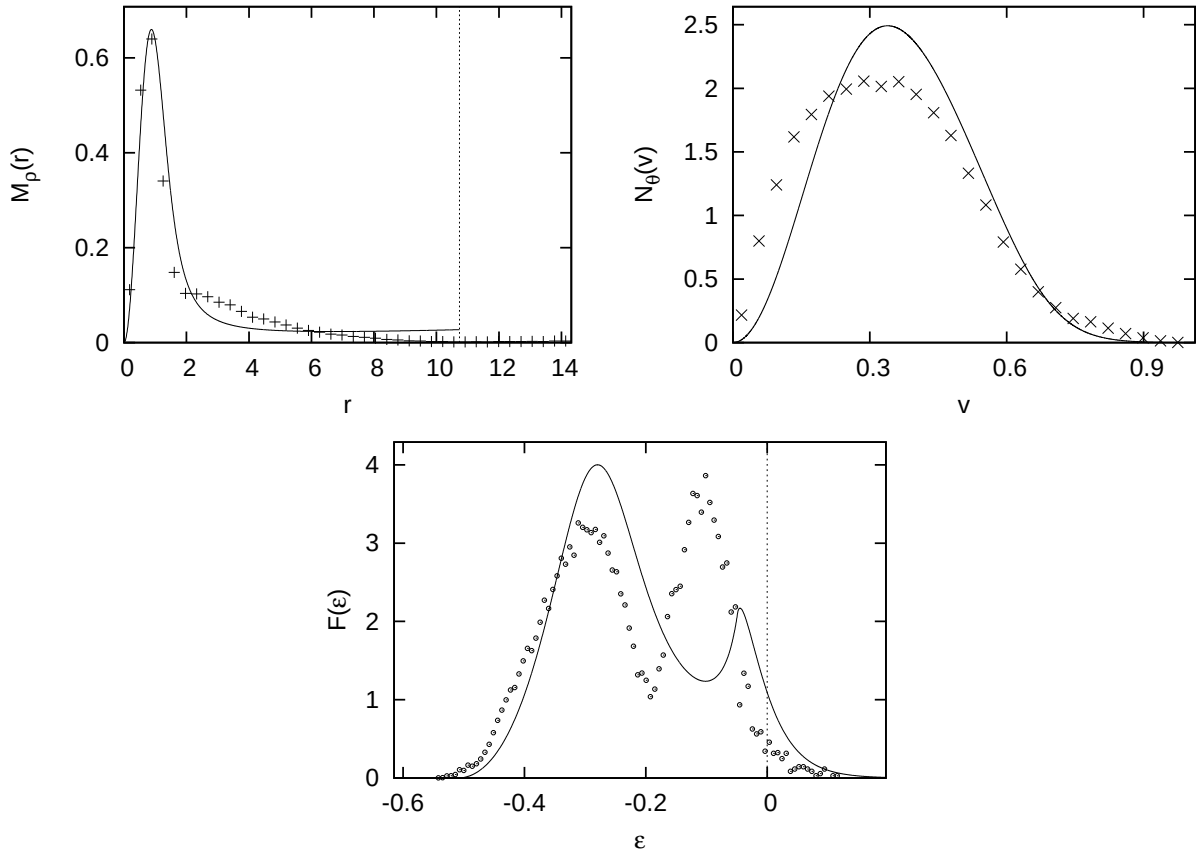

Figure 6.26: Time-averaged $M_\rho(r)$ with R_c in vertical line (top-left panel), $N_\theta(v)$ (top-right panel) and $F(\varepsilon)$ (bottom panel) for DSW initial condition with $\tilde{\xi} = 0.49$ (equivalent to SSW with $R_0 = 0.3$), $\delta = 1.25$ and $R_0 = 1.71$. The solid lines are the LB predictions with $R_c = 17.3r_2$ (or $\tilde{R}_c = 1.48$). See Figs. 6.21, 6.22 and 6.23 for comparison.

and 6.28 for CW1 (most triaxial QSS)[§], averaged from $t = 41$ to $46\,t_{dyn}$ over twenty equally spaced time slices. The solid lines correspond to the spherically symmetric LB predictions, using $R_c = 3.75r_{cy}$ and $2.5r_{cy}$ (or $\tilde{R}_c = 0.54$ and 0.51) for CW3 and CW1 respectively. The agreement for CW3, both in $\rho(r)$ and $M_\rho(r)$, is very good, even better than the best cases of SSW and DSW. Deviation in $\rho(r)$ at large r is observed but it so small that it is almost unobservable in $M_\rho(r)$. For the case CW1, the agreement with the LB prediction is less good, but still comparable to the best cases for SSW and DSW.

Shown in Fig. 6.29 and 6.30 are corresponding $\theta(v)$ and $N_\theta(v)$, averaged in the same time window. Interestingly for these quantities CW1 gives very good agreement, considerably better than for CW3. This is probably because the initial velocity distribution is spherically symmetric and, apparently, does not correlate to the spatial asymmetry of the initial state.

The time-averaged $F(\varepsilon)$ for the same cases are shown in Fig. 6.31. Again for CW3 the agreement is quite good, comparable to the best of SSW and DSW. For CW1, on the other hand, the overall shapes of the curves agree approximately but the simulated data is shifted

[§]see initial parameters in Tab. 6.3.

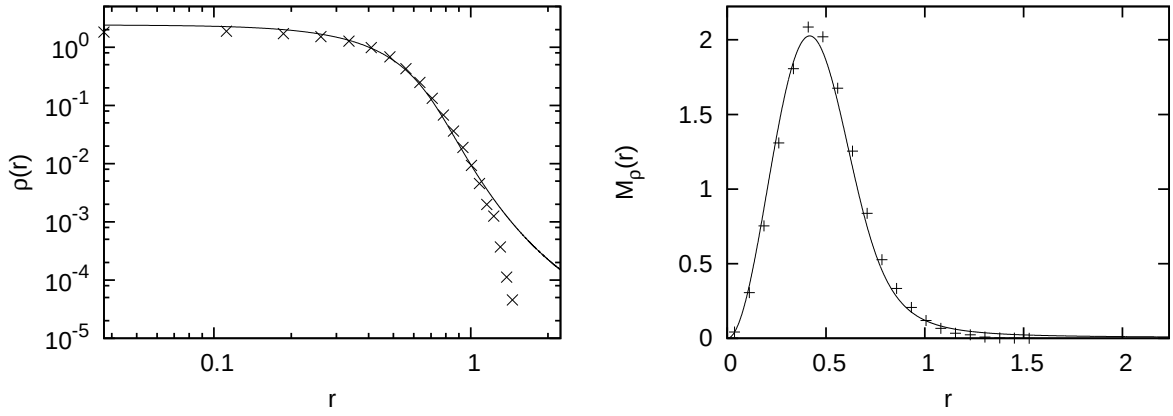

Figure 6.27: Time-averaged $\rho(r)$ in log-log scale (left panel) and $M_\rho(r)$ (right panel) of CW3. The solid lines are the spherically symmetric LB predictions calculated using $R_c = 3.75 r_{cy}$ (or $\tilde{R}_c = 0.54$). The end of r-axis corresponds to R_c.

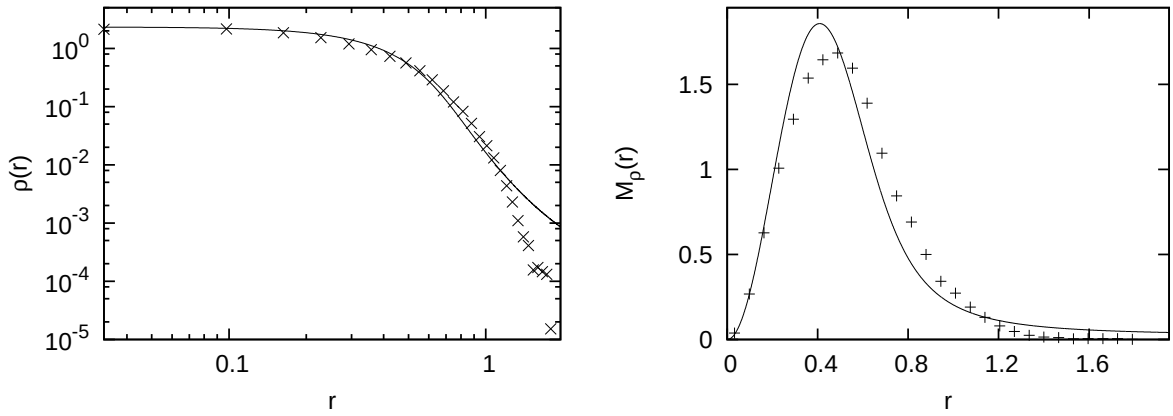

Figure 6.28: Time-averaged $\rho(r)$ in log-log scale (left panel) and $M_\rho(r)$ (right panel) of CW1. The solid lines are the spherically symmetric LB predictions calculated using $R_c = 2.5 r_{cy}$ (or $\tilde{R}_c = 0.51$). The end of r-axis corresponds to R_c.

strongly to the right. This is a result of the triaxiality, which corresponds to a less condensed configuration than that predicted by LB (leading to a higher value of Φ_0).

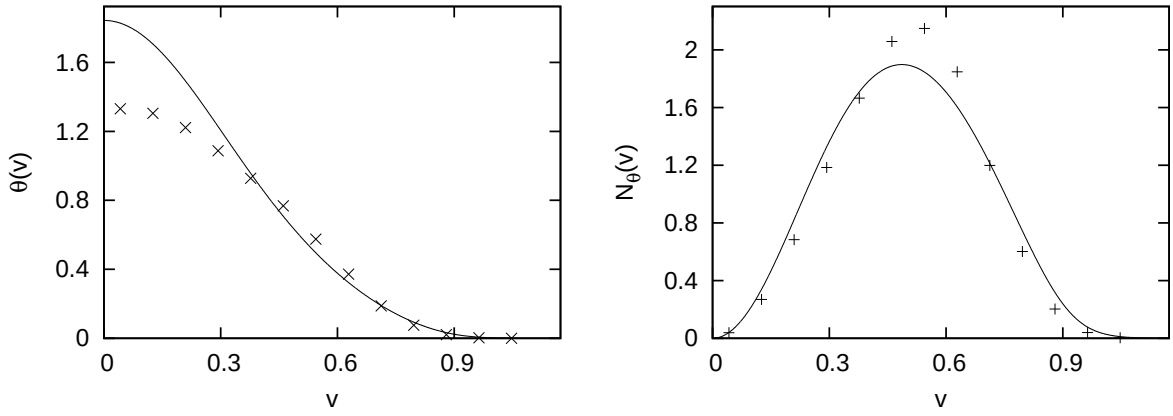

Figure 6.29: Time-averaged $\theta(v)$ (left panel) and $N_\theta(v)$ (right panel) of CW3. The solid lines are the corresponding LB predictions.

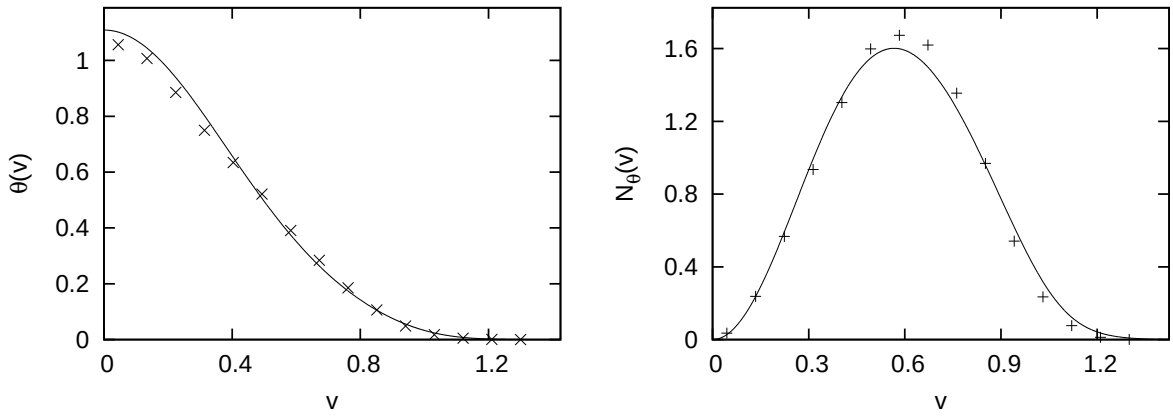

Figure 6.30: Time-averaged $\theta(v)$ (left panel) and $N_\theta(v)$ (right panel) of CW1. The solid lines are the corresponding LB predictions.

6.5 Conclusions and discussions

Our central conclusion is that, for the families of waterbag initial condition explored, detailed comparison with LB theory shows that this theory works quite well to explain the properties of QSS obtained for a open system in a range of energy of order comparable to (but significantly above) the degenerate energy. Further the range where reasonable agreement is found coincides approximately with the range in which LB produces predictions which do not depend strongly on the size of the regularizing box (for a box with size greater than, but of order of, the system size). In other words LB theory works reasonably well in the range where it produces appropriate predictions. There is, however, no case where the agreement between LB theory and the observed QSS is perfect: in all cases deviations may be observed. In particular we see modest disagreement at low velocities in the velocity PDF (which correspond to disagreement in real space at larger radii, and in energy space at higher energies). It is in general the energy PDF which appears

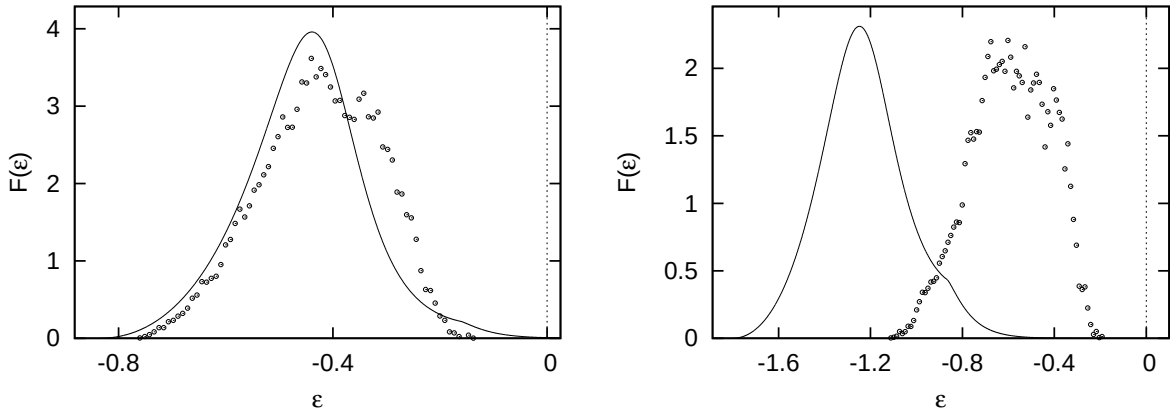

Figure 6.31: Time-averaged $F(\varepsilon)$ for CW3 (left panel) and CW1 (right panel). The solid lines are the LB predictions.

to be the best diagnostic of such deviation (and indeed in some cases the integrated mass and velocity distributions "mask" deviations). These overall results agree strikingly well with those found in one dimension (where, however, a regularizing box was not required).

For higher energy (i.e. $\tilde{\xi} \gtrsim 0.36$) we see also, as in one dimension, the appearance of a "core-halo" structure in energy space. We have not yet sufficient statistics to perform (as we have done in one dimension) the necessary determination of the phase space density function to determine whether the core is, in these cases, degenerate. If it is it would support a priori the physical explanation of this deviations given by Levin et al. [37] in term of dynamical resonances.

In our 3D simulations we have also tested one aspect which has no analogy in one dimension: how the breaking of spherical symmetry in the initial condition affects the QSS. We have found, in cases with "cylindrical waterbags" and initial virial ratio equal to unity, that the degree of accord varies. The LB theory still predicts reasonably well the property of QSS, but there is in some case the residual of spherical symmetry breaking. In this case the deviations from LB reflect that the system stays closer to its initial condition than predicted by LB. Such deviation clearly cannot be ascribed to dynamical resonances which develop during violent relaxation. One interesting issue is to explore further in the range of initial conditions where the LB solution is significantly sensitive to box size whether we can obtain a reasonably good fit for LB prediction for an appropriate box size. In this case one could interpret this box as the "effective size" of the system during violent relaxation. Specifically it would be interesting to see if this can lead to a qualitative (or even quantitative) understanding of why mass and energy are ejected for a certain range of initial conditions. It is also interesting to see if there is any physical relevance to the appearance of the core-halo type structure in the LB predictions at higher $\tilde{\xi}$. This is related to the question of the degeneracy of the core (claimed by Levin et al.) which we have not yet resolved here.

Appendix

Appendix A

Heap-based algorithm

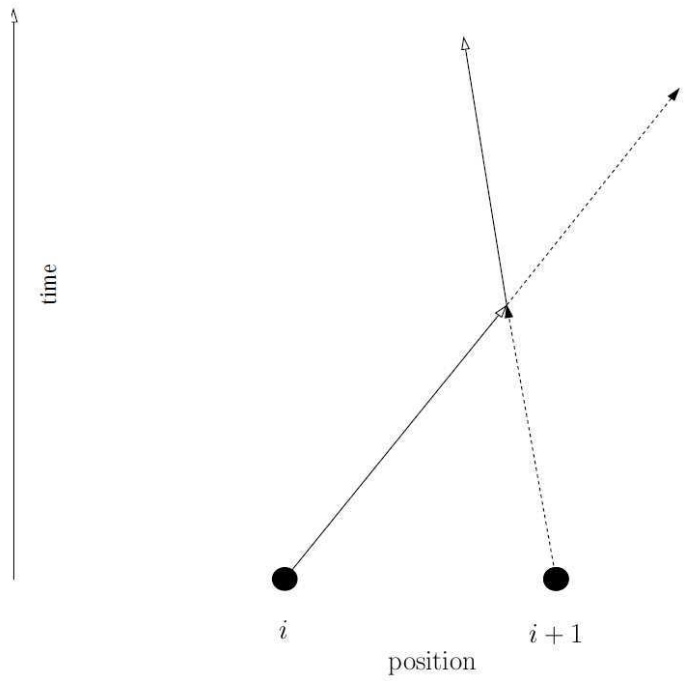

Figure A.1: The bouncing of two particles evolving in time.

In continuity from chapter 1.2 we explain the dynamical integration of the 1D self-gravitating system. Let us label particles by $i = 1 - N$ (from left to right), and take them to "bounce" rather than "cross" (i.e. velocities are switched, see Fig. A.1 for example). The force acting on the particle i is then always constant and given by

$$F_i = N - 2i + 1, \tag{A.1}$$

in units in which $g = 1$ and $m = 1$. Defining t_i to be the crossing time (i.e. the time when particles are bouncing) of particles i and $i + 1$, it follows (from Newton's equation) that

$$t_i = \frac{(v_{i+1} - v_i) + \sqrt{(x_{i+1} - x_i)^2 + 4(x_{i+1} - x_i)}}{2} \tag{A.2}$$

where x_i and v_i are spatial position and velocity of particle i, respectively. Note that there are $N-1$ crossing times to be calculated for a system of N particles.

Starting from an initial configuration, the principle of dynamical integration is to determine the shortest t_i (we call the "integration time step", Δt, from now on) and evolve the system by Δt, at which particles i and $i+1$ bounce. After exchanging their velocities we update t_i of the bouncing particles (in general we update t_{i-1}, t_i and t_{i+1} for $i \neq 1$ and $i \neq N-1$) and determine the next integral time step. An example of the evolution of a system of six particles until the first crossing is shown in Fig. A.2. Thus the simulation time depends on how fast we can determine the integration time step. The direct comparison of t_i (i.e. one by one) requires $N-1$ steps, while there is an algorithm where the determination of integration time step is done using the binary heap, which reduces the number of steps to $\sim \log N$. This algorithm is the so-called "heap-based algorighm" (see [159]).

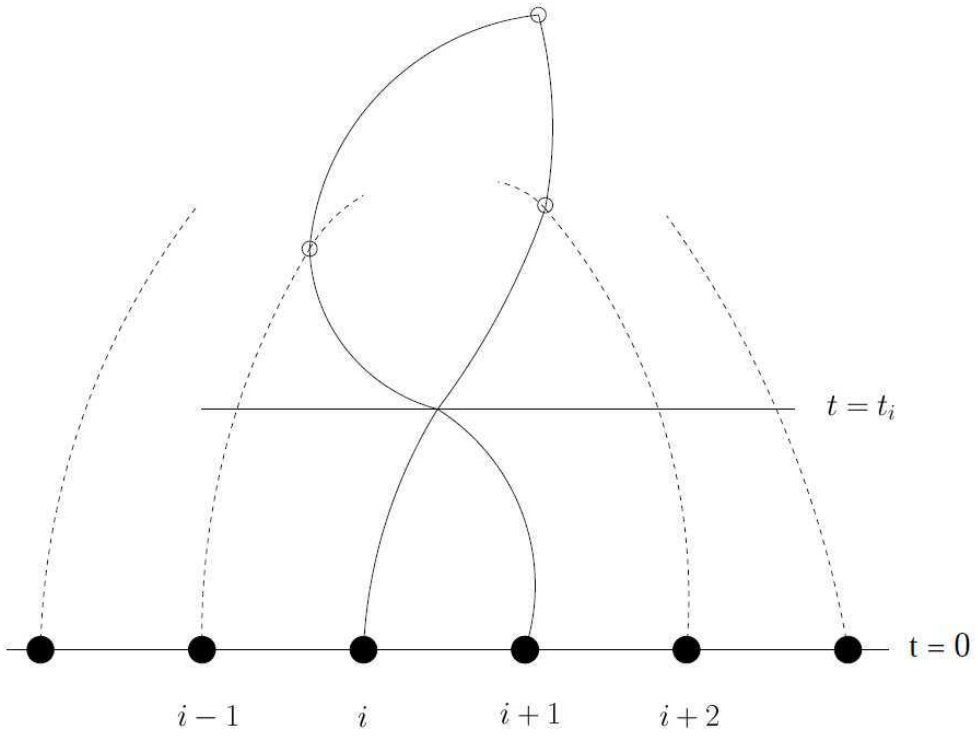

Figure A.2: Evolution from an initial condition to the first crossing (between particles i and $i+1$) with integration time step equal to t_i.

To build a binary heap, we use the concept of a tree that the "nodes" contating t_i are arranged in levels, denoted h where $h \geq 1$. At level h there are 2^{h-1} nodes at most. The nodes are connected to each other by the "links". An example of a binary heap is shown in Fig. A.3. The node at level h has a unique "parent" at level $h-1$, except the node at $h=1$ called the "root". And the node at level h has two "children" at most at level $h+1$. We label each node with a number, denoted j. Starting from root with $j=1$, we number the nodes level by level (in order starting from $h=1$) and in each level the nodes are numbered from left to right (see Fig. A.3 for example of numbering). By construction $j=1$ corresponds to the root. For the node j at level h (where $h>1$), its parent is $\lfloor j/2 \rfloor$. Similarly the children of node j are thus $2j$

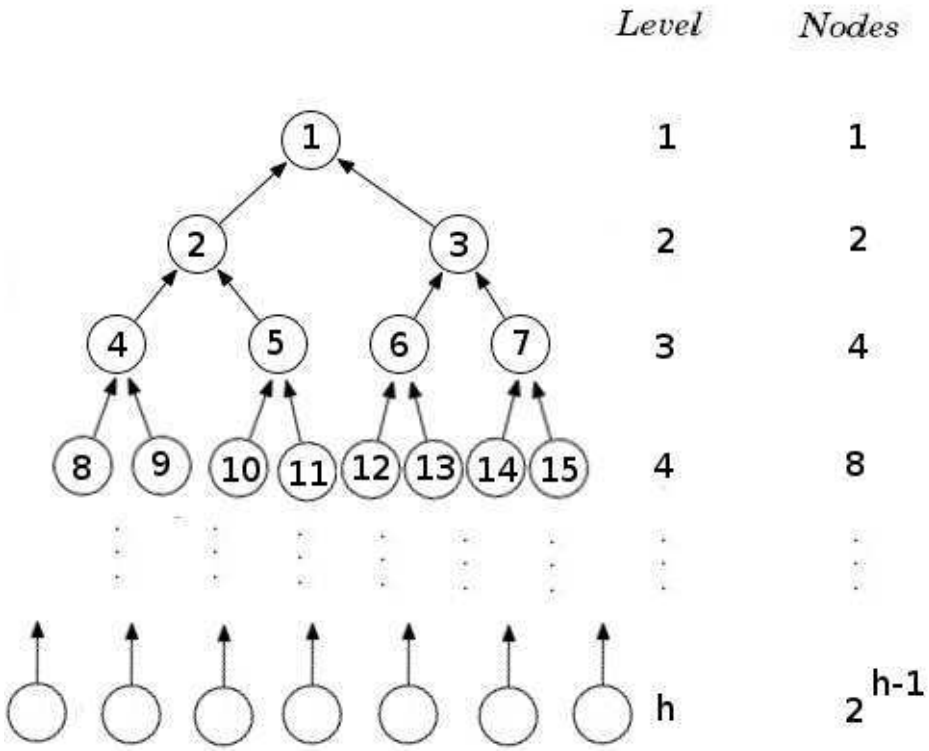

Figure A.3: A binary heap with the number of nodes (j) labelled inside the nodes. The links (i.e. the arrows) point from child to parent.

and $2j + 1$. A node that has no children is called a "leaf" and is usually placed at the bottom.

We impose the "heap condition" in which the values of children must be greater or equal to those of their parents. The heap where this condition is satisfied is called the "ordered heap". Consider a set of $N - 1$ crossing times t_i (i.e. $t_1, ..., t_{N-1}$), we arrange them in a heap by the following strategies: first we put t_1 in the root. Next we fill the next crossing times in order. At each filling the comparison with its parent is made. If the heap condition is satisfied, we leave it and continue filling the next one. But if the heap condition is not satisfied, we switch it with its parent (or "sift-up") until the heap condition is satisfied. This implies that we cannot fill the next t_i unless the heap condition is satisfied. This first filling of all $N - 1$ crossing time takes of order $\mathcal{O}(NlogN)$ steps at most.

Once the filling is finished, the integral time step is definitely at the root, which we use to evolve the dynamics. After the particles bounce and we update the crossing time, the heap condition is usually violated. Thus we need to rearrange the heap by either sift-up or sift-down until the heap condition is satisfied again, from which the next integral time step is on the root. The process continues until the time limit of simulation is reached. Consider the number of operation, determining integral time step using binary heap takes at most $\mathcal{O}(\log N)$ steps, compared to $\mathcal{O}(N)$ for the exact (or one-by-one) determination. Thus the integral time

of implementing this algorithm increases as $N^2 \log N$, instead of N^3.

Appendix B

Calculation of energy fluctuation in rectangular waterbag initial condition

Consider a cold initial condition obtained by throwing N particles randomly in the interval $[0, L]$ (where L is the initial size of system). The N-particle probability density reads

$$P_N(x_1, x_2, \ldots, x_N) = \frac{1}{L^N}. \tag{B.1}$$

The potential energy is thus

$$U = g\frac{m^2}{2} \sum_{j \neq i} \sum_{i=1}^{N} |x_i - x_j| \,, \tag{B.2}$$

and the mean potential energy is then

$$< U >= \frac{\int_0^L \ldots \int_0^L g\frac{m^2}{2} \sum_{j \neq i} \sum_{i=1}^{N} |x_i - x_j| \, P_N(x_1, x_2, \ldots, x_N) dx_1 \ldots dx_N}{\int_0^L \ldots \int_0^L P_N(x_1, x_2, \ldots, x_N) dx_1 \ldots dx_N}. \tag{B.3}$$

Integrating over coordinate spaces, (B.3) reduces to

$$\begin{aligned} < U > &= \frac{gm^2}{2L^N}\Big[(N^2 - N)L^{N-2} \int_0^L \int_0^L |x_i - x_j| \, dx_i dx_j\Big] \\ &= \frac{gm^2(N^2 - N)}{2L^2}\Big[\int_0^L \big(\int_{x_j}^L (x_i - x_j) dx_i + \int_0^{x_j} (x_j - x_i) dx_i\big) dx_j\Big] \\ &= \frac{gm^2(N^2 - N)}{2L^2}\Big[\int_0^L \big(\frac{L^2}{2} - x_j L + x_j^2\big) dx_j\Big] = \frac{gm^2(N^2 - N)L}{6}. \end{aligned} \tag{B.4}$$

For $N \gg 1$, $< U >$ converges to $gm^2N^2L/6$, which corresponds to the potential energy of the spatially homogeneous initial condition of the initial size L in $N \to \infty$ limit. Defining the

normalized variance of U as

$$\sigma_U^2 = \frac{< (U - < U >)^2 >}{< U >^2}, \tag{B.5}$$

it follows that

$$\begin{aligned}
\sigma_U^2 &\equiv \frac{1}{< U >^2 L^N} \int_0^L \dots \int_0^L (\frac{gm^2}{2} \sum_{j \neq i} \sum_{i=1}^N |x_i - x_j| - \frac{gm^2(N^2-N)L}{6})^2 dx_1 \dots dx_N \\
&= \frac{1}{< U >^2 L^N} \Bigg[\int_0^L \dots \int_0^L \frac{g^2 m^4 (N^2-N)^2 L^2}{36} dx_1 \dots dx_N \\
&\quad - \frac{g^2 m^4 (N^2-N)L}{6} \int_0^L \dots \int_0^L \sum_{j \neq i} \sum_{i=1}^N |x_i - x_j| \, dx_1 \dots dx_N \\
&\quad + \frac{g^2 m^4}{4} \int_0^L \dots \int_0^L (\sum_{j \neq i} \sum_{i=1}^N |x_i - x_j|)^2 dx_1 \dots dx_N \Bigg].
\end{aligned} \tag{B.6}$$

The integration of first and second terms is straightforward using B.4. For the third term, we expand it and then integrate as following:

$$\begin{aligned}
\sigma_U^2 &= \frac{1}{< U >^2 L^N} \Bigg[\frac{g^2 m^4 (N^2-N)^2 L^{N+2}}{36} - \frac{gm^2(N^2-N)L^{N+1}}{3} \cdot \frac{gm^2(N^2-N)L}{6} \\
&\quad + \frac{g^2 m^4}{4} \int_0^L \int_0^L (x_i - x_j)^2 2(N(N-1)) L^{N-2} dx_i dx_j \\
&\quad + \frac{g^2 m^4}{4} \int_0^L \int_0^L \int_0^L |x_i - x_j| \cdot |x_j - x_k| \, 4N(N-1)(N-2) L^{N-3} dx_i dx_j dx_k \\
&\quad + \frac{g^2 m^4}{4} \int_0^L \int_0^L \int_0^L \int_0^L |x_i - x_j| \cdot |x_k - x_l| \, N(N-1)(N-2)(N-3) L^{N-4} dx_i dx_j dx_k dx_l \Bigg].
\end{aligned}$$

Substituting $< U >^2$, we have

$$\begin{aligned}
\sigma_U^2 &= \frac{9}{(N^2-N)^2 L^2} \Bigg[- \frac{(N^2-N)^2 L^2}{9} + \frac{(N^2-N)L^2}{3} \\
&\quad + \frac{4N^3 - 12N^2 + 8N}{L^3} \int_0^L \int_0^L |x_j - x_k| \, (\frac{L^2}{2} - x_j L + x_j^2) dx_k dx_j \\
&\quad + \frac{N^4 - 6N^3 + 11N^2 - 6N}{L^4} \int_0^L \int_0^L |x_i - x_j| \, dx_i dx_j \int_0^L \int_0^L |x_k - x_l| \, dx_k dx_l \Bigg] \\
&= \frac{1}{5N} \Bigg[\frac{N^2 + 2N - 3}{N^2 - 2N + 1} \Bigg].
\end{aligned} \tag{B.7}$$

The variance of potential energy is clearly scaled with $1/N$ in large N (or $1/\sqrt{N}$ for the standard deviation). For SRW initial conditions the total energy can in particular be expressed as a function of initial virial ratio R_0 as

$$E = U(1 + \frac{R_0}{2}).$$

Therefore the variance of total energy, σ_E^2, is given by

$$\sigma_E^2 \equiv \frac{< (E - < E >)^2 >}{< E >^2} = \frac{< (U - < U >)^2 >}{< U >^2} = \frac{1}{5N}\left[\frac{N^2 + 2N - 3}{N^2 - 2N + 1}\right]. \tag{B.8}$$

An example of σ_E^2 plot comparing the variance of E over realizations and theoretical prediction (B.8) is shown in Fig. B.1 for $R_0 = 0$ SRW initial conditions with $N = 100, 200, 400$ and 800 determined over $1000, 400, 120$ and 20 realizations (i.e. corresponding to the study in chapter 4), respectively. Good agreement is observed and should be even better with more statistics.

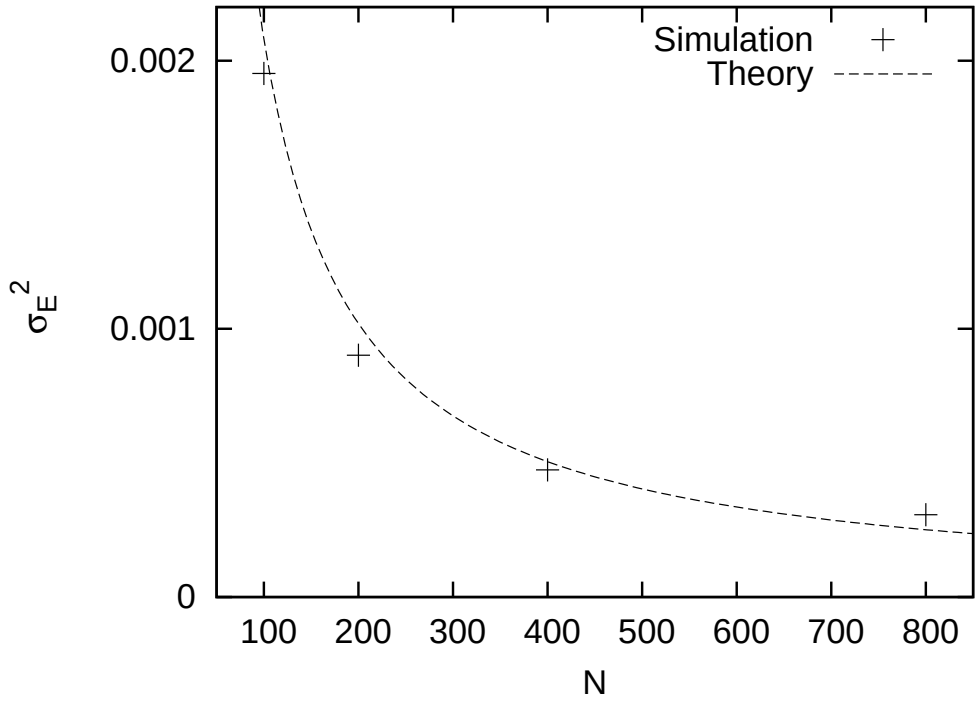

Figure B.1: Comparison of σ_E^2 between simulation (point) and theory (dashed line) for SRW initial condition with $R_0 = 0$.

Appendix C

Generation of DRW initial condition

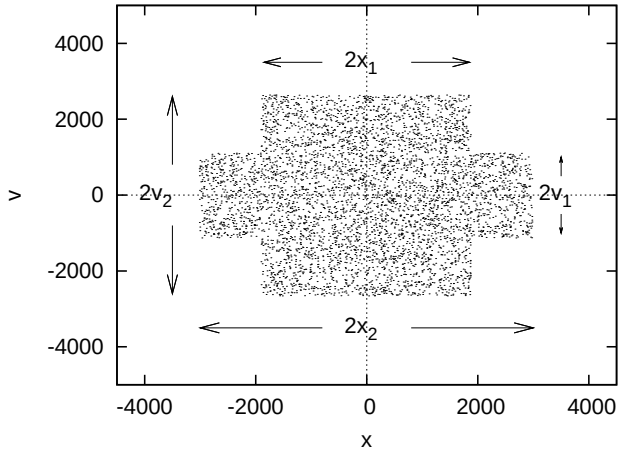

Figure C.1: An example of DRW initial condition, with parameters x_1, x_2, v_1 and v_2.

This appendix explains how to generate the DRW initial condition. An example of a DRW initial condition is shown in Fig. C.1, along with the characteristic parameters x_1, x_2, v_1 and v_2. Given the phase space density of DRW initial conditions in section 5.1, the initial kinetic energy is

$$T_0 = f_0[\frac{2(x_2 - x_1)v_2^3}{3} + \frac{2x_1v_1^3}{3}],$$

and the initial potential energy is

$$U_0 = 4f_0^2v_2^2g[\frac{4x_2^3}{3} + \frac{2x_1^3}{3} - 2x_2^2x_1] + 8f_0^2v_1v_2g[x_1(x_2^2 - x_1^2)] + \frac{16}{3}f_0^2v_1^2gx_1^3$$

where the total energy (as function of x_1, x_2, v_1 and v_2) is

$$E(x_1, x_2, v_1, v_2) = T_0 + U_0.$$

The total mass, M, is then given by

$$M(x_1, x_2, v_1, v_2) = f_0(4x_1v_1 + 4x_2v_2 - 4x_1v_2).$$

These expressions reduce to those of SRW initial conditions if we set $x_1 = 0$, $x_1 = x_2$ or $v_1 = v_2$.

To generate an initial condition for any given E and M (let us call then E_0 and M_0) with chosen f_0, we first randomly sample x_1, x_2, v_1 and v_2 uniformly in an interval of width a few times x_0 or v_0 (corresponding to SRW with same energy and mass). We keep the points that giving values of $E(x_1, x_2, v_1, v_2)$ and $M(x_1, x_2, v_1, v_2)$ close to E_0 and M_0. We then perform a linear interpolation using the points closest to the target values, to obtain a solution with mass and energy

$$E(x_1, x_2, v_1, v_2) = E_0 \quad \text{and} \quad M(x_1, x_2, v_1, v_2) = M_0.$$

within 1% of these values.

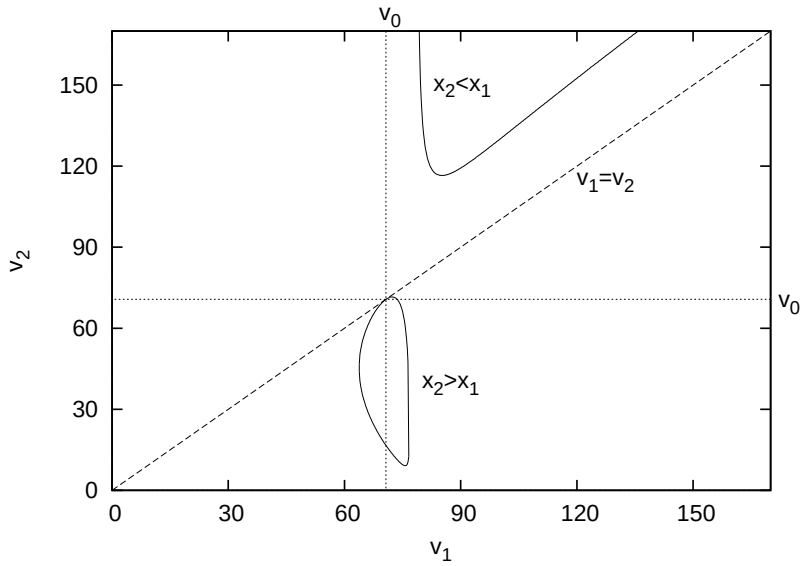

Figure C.2: The solid lines show the solutions for DRW initial conditions at a given $x_1 (< x_0), M, E$ and f_0 in the (v_1, v_2) plane (obtained using the method described). The solutions on the upper curve are unphysical ($x_2 < x_1$) while those on the lower curve are physical, and intersect the axis at the corresponding SRW solution.

Unphysical solutions with $x_1 < 0, x_2 < 0$ or $x_2 < x_1$ can of course arise. An example of a family of solution at fixed x_1 ($< x_0$), M, E and f_0 plotted in (v_1, v_2) plane is shown in Fig. C.2. The solutions we obtain are plotted as solid lines: the upper curve corresponds to unphysical cases where $x_2 < x_1$ and the lower curve corresponds to physical solutions. The dashed line corresponds to $v_1 = v_2$ and the horizontal and vertical dotted lines indicate v_0 (i.e. width of SRW initial condition for the same ξ_D). At the intersection of the three straight lines the DRW reduces to an SRW initial condition.

Bibliography

[1] V.A. Antonov. [English translation in: Dynamics of Globular Clusters, IAU Symp. 113]. *Vestn. Leningrad Gos. Univ.*, 7:135, 1962.

[2] T. Padmanabhan. Statistical mechanics of gravitating systems. *Phys. Rep.*, 188:285, 1990.

[3] P.H. Chavanis. Gravitational instability of finite isothermal spheres. *Astron. Astrophys.*, 381:340, 2002.

[4] V.C. Rubin, W.K. Ford, and N. Thonnard. Extended rotation curves of high-luminosity spiral galaxies, IV Systematic dynamical properties, Sa to Sc. *Astrophys. J.*, 225:107, 1978.

[5] C.J. Peterson, V.C. Rubin, W.K. Ford, and M.S. Roberts. Extended rotation curves of high-luminosity spiral galaxies, III the spiral galaxy NGC 7217. *Astrophys. J.*, 226:770, 1978.

[6] G. de Vaucouleurs. Recherches sur les nebuleuses extragalactiques. *Ann. Astroph.*, 11:247, 1948.

[7] F. Schweizer. Effects of seeing on the light distribution in the cores of elliptical galaxies. *Astrophys. J.*, 233:23, 1979.

[8] J.M. Schombert. The structure of brightest cluster members. I - Surface photometry. *Astrophys. J. Suppl. Ser.*, 60:603, 1986.

[9] S. Chandrasekhar. Stochastic problems in physics and astronomy. *Rev. Mod. Phys.*, 1:1, 1943.

[10] S. Chandrasekhar. Brownian motion, dynamical friction, and stellar dynamics. *Rev. Mod. Phys.*, 21:383, 1949.

[11] S.S. Larsen, J.P. Brodie, B.G. Elmegreen, Y.N. Efremov, P.W. Hodge, and T. Richtler. Structure and mass of a young globular cluster in NGC 6946. *Astrophys. J.*, 556:801, 2002.

[12] R.W. Michie. On the distribution of high energy stars in spherical stellar systems. *Mon. Not. R. Astr. Soc.*, 125:127, 1963.

[13] I.R. King. The structure of star clusters. III. Some simple dynamical models. *Astro. J.*, 71:64, 1966.

[14] P.W. Hodge. The structure and content of NGC 205. *Astrophys. J.*, 182:671, 1973.

[15] C. Pryor, R.D. McClure, J.M. Fletcher, F.D.A. Hartwick, and J. Kormendy. Dynamics of the globular cluster M2 (NGC 7089). *Astro. J.*, 91:546, 1986.

[16] P. Côté, D.L. Welch, P. Fischer, and K. Gebhardt. Dynamics of the galactic globular cluster NGC 3201. *Astrophys. J.*, 454:788, 1995.

[17] J. Binney and S. Tremaine. *Galactic Dynamics*. Princeton University Press, 1994.

[18] M. Hénon. Vlasov equation. *Astron. Astrophys.*, 114:211, 1982.

[19] D. Lynden-Bell. Statistical mechanics of violent relaxation in stellar systems. *Mon. Not. R. Astr. Soc.*, 136:101, 1967.

[20] I. Arad and P.H. Johansson. A numerical comparison of theories of violent relaxation. *Mon. Not. R. Astr. Soc.*, 362:252, 2005.

[21] I. Arad and D. Lynden-Bell. Inconsistency in theories of violent relaxation. *Mon. Not. R. Astr. Soc.*, 361:385, 2005.

[22] M. Hénon. L'évolution initiale d'un amas sphérique. *Ann. Astroph.*, 27:83, 1964.

[23] J.R. Gott. Dynamics of rotating stellar systems: Collapse and violent relaxation. *Astrophys. J.*, 186:481, 1973.

[24] J.R. Gott. On the formation of elliptical galaxies. *Astrophys. J.*, 201:296, 1975.

[25] T.A. McGlynn. Dissipationless collapse of galaxies and initial conditions. *Astrophys. J.*, 281:13, 1984.

[26] J.V. Villumsen. Violent relaxation and dissipationless collapse. *Astrophys. J.*, 284:75, 1984.

[27] J.E. Gunn. Massive galactic halos. I - Formation and evolution. *Astrophys. J.*, 218:592, 1977.

[28] C. Pryor and M. Lecar. Can secondary infall produce flat rotation curves? *Astrophys. J.*, 269:513, 1983.

[29] T.S. van Albada. Dissipationless galaxy formation and the $r^{\frac{1}{4}}$ law. *Mon. Not. R. Astr. Soc.*, 201:939, 1982.

[30] P. Londrillo, A. Messina, and M. Stiavelli. Dissipationless galaxy formation revisited. *Mon. Not. R. Astr. Soc.*, 250:54, 1991.

[31] C.C. Dantas, H.V. Capelato, R.R. de Carvalho, and A.L.B. Ribeiro. Dissipationless collapse of spherical protogalaxies and the fundamental plane. *Astron. Astrophys.*, 384:772, 2002.

[32] Ch. Theis and R. Spurzem. On the evolution of shape in N-body simulations. *Astron. Astrophys.*, 341:361, 1999.

[33] K.W. Min and C.S. Choi. Cold collapse of a spherical stellar system. *Mon. Not. R. Astr. Soc.*, 238:253, 1989.

[34] C.M. Boily and E.Athanassoula. On the equilibrium morphology of systems drawn from spherical collapse experiments. *Mon. Not. R. Astr. Soc.*, 369:608, 2006.

[35] J.F. Navarro, C.S. Frenk, and S.D.M. White. The structure of cold dark matter halos. *Astrophys. J.*, 462:563, 1996.

[36] J.F. Navarro, C.S. Frenk, and S.D.M. White. A universal density profile from hierarchical clustering. *Astrophys. J.*, 490:493, 1997.

[37] Y. Levin, R. Pakter, and F.B. Rizzato. Collisionless relaxation in gravitational systems: From violent relaxation to gravothermal collapse. *Phys. Rev. E*, 78:021130, 2008.

[38] J. Diemand, B. Moore, J. Stadel, and S. Kazantzidis. Two-body relaxation in cold dark matter simulations. *Mon. Not. R. Astr. Soc.*, 348:977, 2004.

[39] J. Binney and A. Knebe. Two-body relaxation in cosmological simulations. *Mon. Not. R. Astr. Soc.*, 325:845, 2001.

[40] A. El Zant. Two-body relaxation in simulated cosmological haloes. *Mon. Not. R. Astr. Soc.*, 370:1247, 2006.

[41] F. Zwicky. Die Rotverschiebung von extragalaktischen Nebeln. *Helv. Phys. Acta*, 6:110, 1933.

[42] F. Zwicky. On the masses of nebulae and of clusters of nebulae. *Astrophys. J.*, 86:217, 1937.

[43] W.J. de Blok, S.S. McGaugh, A. Bosma, and V.C. Rubin. Mass density profiles of low surface brightness galaxies. *Astrophys. J.*, 552:L23, 2001.

[44] S.M. Faber and J.S. Gallagher. Masses and mass-to-light ratios of galaxies. *ARA & A*, 17:135, 1979.

[45] L.V.E. Koopmans and T. Treu. The structure and dynamics of luminous and dark matter in the early-type lens galaxy of 0047-281 at $z = 0.485$. *Astrophys. J.*, 583:606, 2003.

[46] X.P. Wu, T. Chiueh, L.Z. Fang, and Y.J. Xue. A comparison of different cluster mass estimates: consistency or discrepancy? *Mon. Not. R. Astr. Soc.*, 301:861, 1998.

[47] G. Bertone, D. Hooper, and J. Silk. Particle dark matter: evidence, candidates and constraints. *Phys. Rep.*, 405:279, 2005.

[48] D.C. Brydges and P.A. Martin. Coulomb systems at low density: A review. *J. Stat. Phys.*, 96:1163, 1999.

[49] D.H. Dubin and T.M. O'neil. Trapped nonneutral plasmas, liquids, and crystals (the thermal equilibrium states). *Rev. Mod. Phys.*, 71:87, 1999.

[50] P.H. Chavanis and J. Sommeria. Classification of robust isolated vortices in two-dimensional hydrodynamics. *J. Fluid. Mech.*, 356:259, 1998.

[51] R. Robert and J. Sommeria. Relaxation towards a statistical equilibrium state in two-dimensional perfect fluid dynamics. *Phys. Rev. Lett.*, 19:2776, 1992.

[52] P. Barge and J. Sommeria. Did planet formation begin inside persistent gaseous vortices? *Astron. Astrophys.*, 295:1, 1995.

[53] P.H. Chavanis. Statistical mechanics of geophysical turbulence: application to jovian flows and jupiter's great red spot. *Physica D*, 200:257, 2005.

[54] B. Turkington, A. Majda, K. Haven, and M. Dibattista. Statistical equilibrium predictions of jets and spots on jupiter. *Proc. Natl. Acad. Sci*, 98:12346, 2001.

[55] A. Antoniazzi, Y. Elskens, D. Fanelli, and S. Ruffo. Statistical mechanics and Vlasov equation allow for a simplified Hamiltonian description of single-pass free electron laser saturated dynamics. *Eur. Phys. J. B*, 50:603, 2006.

[56] J. Barré, T. Dauxois, G. de Ninno, D. Fanelli, and S. Ruffo. Statistical theory of high-gain free-electron laser saturation. *Phys. Rev. E*, 69:045501, 2004.

[57] A. Campa, A. Giansanti, G. Morigi, and F. Sylos Labini. Thermodynamics and dynamics of systems with long-range interactions: Theory and experiments. *AIP Conference Proceeding*, 2008.

[58] A. Campa, T. Dauxois, and S. Ruffo. Statistical mechanics and dynamics of solvable models with long-range interactions. *Phys. Rep.*, 480:57, 2009.

[59] E. Arimondo, T. Dauxois, S. Ruffo, and M. Wilkens. *Dynamics and Thermodynamics of Systems with Long Range Interactions*. Springer, Berlin, 2002.

[60] T. Dauxois, S. Ruffo, and L. Cugliandolo. *Long-Range Interacting Systems*. Oxford University Press, 2008.

[61] R. Balescu. *Equilibrium and nonequilibrium statistical mechanics*. New York: Wiley, 1975.

[62] A.A. Vlasov. The vibration properties of an electron gas. *Sov. Phys. Usp.*, 10:721, 1968.

[63] Y.Y. Yamaguchi, J. Barré, F. Bouchet, T. Dauxois, and S. Ruffo. Stability criteria of the Vlasov equation and quasi-stationary states of the HMF model. *Physica A*, 337:36, 2004.

[64] M. Antoni and S. Ruffo. Clustering and relaxation in Hamiltonian long-range dynamics. *Phys. Rev. E*, 52:2361, 1995.

[65] J. Barré, F. Bouchet, T. Dauxois, S. Ruffo, and Y.Y. Yamaguchi. The Vlasov equation and the Hamiltonian mean-field model. *Physica A*, 365:177, 2006.

[66] Y.Y. Yamaguchi. Relaxation and diffusion in a globally coupled Hamiltonian system. *Phys. Rev. E*, 68:066210, 2003.

[67] P.H. Chavanis, J. Vatteville, and F. Bouchet. Dynamics and thermodynamics of a simple model similar to self-gravitating system: the HMF model. *Eur. Phys. J. B*, 46:61, 2005.

[68] A. Pluchino, V. Latora, and A. Rapisarda. Dynamics and thermodynamics of a model with long-range interactions. *Continuum Mechanics and Thermodynamics*, 16:245, 2004.

[69] P.H. Chavanis, G. De Ninno, D. Fanelli, and S. Ruffo. Out-of-equilibrium phase transitions in mean-field hamiltonian dynamics. *ARXIV*, 07/12, 2007.

[70] F. Staniscia, P.H. Chavanis, G. De Ninno, and D. Fanelli. Out-of-equilibrium phase re-entrance(s) in long-range interacting systems. *Phys. Rev. E*, 80:021138, 2009.

[71] F. Staniscia, P.H. Chavanis, G. De Ninno, and D. Fanelli. Out-of-equilibrium phase re-entrance(s) in long-range interacting systems: a closer look. *Phys. Rev. E*, 83:051111, 2011.

[72] A. Antoniazzi, D. Fanelli, J. Barré, P.H. Chavanis, T. Dauxois, and S. Ruffo. A maximum entropy principle explains quisi-stationary states in systems with long-range interactions: the example of the Hamiltonian mean field model. *Phys. Rev. E*, 75:011112, 2007.

[73] A. Antoniazzi, D. Fanelli, S. Ruffo, and Y.Y. Yamaguchi. Nonequilibrium tricritical point in a system with long-range interactions. *Phys. Rev. Lett.*, 99:040601, 2007.

[74] A. Antoniazzi, F. Califano, D. Fanelli, and S. Ruffo. Exploring the thermodynamic limit of Hamiltonian models: Convergence to the Vlasov equation. *Phys. Rev. Lett.*, 98:150602, 2007.

[75] C. Tsallis. Possible generalization of Boltzmann-Gibbs statistics. *J. Stat. Phys*, 52:479, 1988.

[76] A. Campa, P.H. Chavanis, A. Giansanti, and G. Morelli. Dynamical phase transitions in long-range hamiltonian systems and Tsallis distributions with a time-dependent index. *Phys. Rev. E*, 78:040102, 2008.

[77] P.H. Chavanis and A. Campa. Inhomogeneous Tsallis distributions in the HMF model. *Eur. Phys. J. B*, 76:581, 2010.

[78] J. Miller. Statistical mechanics of Euler equations in two dimensions. *Phys. Rev. Lett.*, 65:213, 1990.

[79] R. Robert and J. Sommeria. Statistical equilibrium states for two-dimensional flows. *J. Fluid. Mech.*, 229:291, 1991.

[80] S.D. Meyers, J. Sommeria, and H.L. Swinney. Laboratory study of the dynamics of Jovian-type vortices. *Physica D*, 37:515, 1989.

[81] P.H. Chavanis, J. Sommeria, and R. Robert. Statistical mechanics of two-dimensional vortices and collisionless stellar systems. *Astrophys. J.*, 471:385, 1996.

[82] P.H. Chavanis. Statistical mechanics of two-dimensional vortices and stellar systems. *Dynamics and thermodynamics of systems with long range interactions, edited by T. Dauxois, S. Ruffo, E. Arimondo, M. Wilkens, Lecture Notes in Physics*, 602, 2002.

[83] B.N. Miller and P. Youngkins. Phase transition in a model gravitating system. *Phys. Rev. Lett.*, 81:4794, 1998.

[84] J. Binney. Discreteness effects in cosmological N-body simulations. *Mon. Not. R. Astr. Soc.*, 350:939, 2004.

[85] P. Valageas. Thermodynamics and dynamics of a 1-D gravitational system. *Astron. Astrophys.*, 450:445, 2006.

[86] A. Gabrielli, M. Joyce, and F. Sicard. One-dimensional gravity in infinite point distributions. *Phys. Rev. E*, 80:041108, 2010.

[87] T. Tsuchiya, N. Gouda, and T. Konishi. Relaxation processes in one-dimensional self-gravitating many-body systems. *Phys. Rev. E*, 53:2210, 1996.

[88] C.J. Reidl and B.N. Miller. Gravity in one dimension: Selective relaxation? *Astrophys. J.*, 318:248, 1987.

[89] K.R. Yawn and B.N. Miller. Incomplete relaxation in a two-mass one-dimensional self-gravitating system. *Phys. Rev. E*, 68:056120, 2003.

[90] G.L. Camm. Self-gravitating star systems. *Mon. Not. R. Astr. Soc.*, 110:305, 1950.

[91] J.H. Oort. The force exerted by the stellar system in the direction perpendicular to the galactic plane and some related problems. *Bull. Astron. Inst. Neth.*, 6:249, 1932.

[92] G.B. Rybicki. Exact statistical mechanics of a one-dimensional self-gravitating system. *Astrophys. Space Sci.*, 14:56, 1971.

[93] T.N. Teles, Y. Levin, R. Pakter, and F.B. Rizzato. Statistical mechanics of unbound two dimensional self-gravitating systems. *J. Stat. Mech.*, 05:05007, 2010.

[94] Y. Levin, R. Pakter, and T.N. Teles. Collisionless relaxation in non-neutral plasma. *Phys. Rev. Lett.*, 100:040604, 2008.

[95] Y.Y. Yamaguchi. One-dimensional self-gravitating sheet model and Lynden-Bell statistics. *Phys. Rev. E*, 78:1114, 2008.

[96] M. Joyce and T. Worrakitpoonpon. Relaxation to thermal equilibrium in the self-gravitating sheet model. *J. Stat. Mech.*, 10:10012, 2010.

[97] M. Joyce and T. Worrakitpoonpon. Quasi-stationary states in the self-gravitating sheet model. *ARXIV*, 1012.5042, 2010.

[98] P.H. Chavanis. Hamiltonian and Brownian systems with long-range interactions: II Kinetic equations and stability analysis. *Physica A*, 361:88, 2006.

[99] P.H. Chavanis. Hamiltonian and Brownian systems with long-range interactions: III The BBGKY hierarchy for spatially inhomogeneous systems. *Physica A*, 387:787, 2008.

[100] W. Braun and K. Hepp. The Vlasov dynamics and its fluctuations in the $1/n$ limit of interacting classical particles. *Commun. Math. Phys.*, 56:101, 1977.

[101] W. Saslaw. *Gravitational Physics of Stellar and Galactic Systems.* Cambridge University Press, 1987.

[102] P.H. Chavanis. Kinetic equations for systems with long-range interactions: a unified description. *J. Stat. Mech.*, 5:19, 2010.

[103] F. Bouchet, S. Gupta, and D. Mukamel. Thermodynamics and dynamics of systems with long-range interactions. *Physica A*, 20:4389, 2010.

[104] J. Binney. On the rotation of elliptical galaxies. *Mon. Not. R. Astr. Soc.*, 183:501, 1978.

[105] V.D. Shafranov. Virial theorem for a system of charged particles. *Sov. Phys. Uspekhi.*, 22:368, 1979.

[106] S. Chandrasekhar and E. Fermi. Problems of gravitational stability in the presence of a magnetic field. *Astrophys. J.*, 118:116, 1953.

[107] N.R. Lebovitz. The virial tensor and its application to self-gravitating fluids. *Astrophys. J.*, 134:500, 1961.

[108] J.H. Lane. On the theoretical temperature of the sun. *Am. J. Sci.*, 50:57, 1870.

[109] J.C. Emden. *Gaskugeln: Anwendungen der mechanischen Wrmetheorie auf kosmologische und meteorologische Probleme*. Leipzig und Berlin Druck und Verlag von B.G. Teubner, 1907.

[110] G.P. Horedt. Seven-digit tables of Lane-Emden functions. *Astrophys. Space Sci.*, 126:357, 1986.

[111] P.H. Chavanis and C. Sire. Anomalous diffusion and collapse of self-gravitating Langevin particles in D dimensions. *Phys. Rev. E*, 69:016116, 2004.

[112] A.S. Eddington. The distribution of stars in globular clusters. *Mon. Not. R. Astr. Soc.*, 76:572, 1916.

[113] E. Aurell, D. Fanelli, and P. Muratore-Ginanneschi. On the dynamics of a self-gravitating medium with random and non-random initial conditions. *Physica D*, 148:272, 2001.

[114] G. Janin. Numerical experiments with a one-dimensional gravitational system by a Euler-type method. *Astron. Astrophys.*, 11:188, 1971.

[115] C. Alard and S. Colombi. A cloudy Vlasov solution. *Mon. Not. R. Astr. Soc.*, 359:123, 2005.

[116] P.H. Chavanis. Newtonian gravity in d dimensions. *C. R. Physique*, 7:331, 2006.

[117] P.H. Chavanis. Nonlinear mean field Fokker-Planck equations. Application to the chemotaxis of biological populations. *Eur. Phys. J. B*, 62:179, 2008.

[118] T. Padmanabhan. Antonov instability and gravothermal catastrophe - revisited. *Astrophys. J. Supp.*, 71:651, 1989.

[119] I. Ispolatov and E.G.D. Cohen. Phase transitions in systems with $1/r^{\alpha}$ attractive interactions. *Phys. Rev. E*, 64:056103, 2001.

[120] S. Chandrasekhar. *An Introduction to The Study of Stellar Structure*. The University of Chicago Press, 1939.

[121] D. Lynden-Bell and R. Wood. The gravo-thermal catastrophe in isothermal spheres and the onset of red-giant structure for stellar systems. *Mon. Not. R. Astr. Soc.*, 138:495, 1968.

[122] P.H. Chavanis. Gravitational instability of isothermal and polytropic spheres. *Astron. Astrophys.*, 401:15, 2003.

[123] C. Sire and P.H. Chavanis. Thermodynamics and collapse of self-gravitating Brownian particles in D dimensions. *Phys. Rev. E*, 66:046133, 2002.

[124] S. Inagaki. The gravothermal catastrophe of stellar systems. *PASJ*, 32:213, 1980.

[125] M.N. Rosenbluth, W.M. MacDonald, and D.L. Judd. Fokker-Planck equation for an inverse-square force. *Phys. Rev.*, 107:1, 1957.

[126] Jr.L. Spitzer. The dynamics of the interstellar medium. III. Galactic distribution. *Astrophys. J.*, 95:329, 1942.

[127] B.N. Miller. Source of relaxation in the one-dimensional gravitating system. *Phys. Rev. E*, 53:4279, 1996.

[128] F. Hohl and J.W. Campbell. Statistical mechanics of a collisionless self-gravitating system. *Astron. J.*, 73:611, 1968.

[129] M. Lecar and L. Cohen. Numerical experiments on Lynden-Bell's statistics. *Astrophys. Space Sci.*, 13:397, 1971.

[130] M. David and T. Theuns. Numerical experiments on radial virial oscillations in N-body systems. *Mon. Not. R. Astr. Soc.*, 240:957, 1989.

[131] P.H. Chavanis. Coarse-grained distributions and superstatistics. *Physica A*, 359:177, 2006.

[132] P.H. Chavanis and J. Sommeria. Degenerate equilibrium states of collisionless stellar systems. *Mon. Not. R. Astr. Soc.*, 296:569, 1998.

[133] P.H. Chavanis. Phase transitions in self-gravitating systems: Self-gravitating fermions and hard-sphere models. *Phys. Rev. E*, 65:056123, 2002.

[134] P.H. Chavanis. Phase transitions in self-gravitating systems. *Int. J. Mod. Phys. B*, 20:3113, 2006.

[135] P.H. Chavanis. Statistical mechanics and thermodynamic limit of self-gravitating fermions in D dimensions. *Phys. Rev. E*, 69:066126, 2004.

[136] P.H. Chavanis and M. Rieutord. Statistical mechanics and phase diagrams of rotating self-gravitating fermions. *Astron. Astrophys.*, 412:1, 2003.

[137] H.J. Ziegler and H. Wiechen. Relaxation of collisionless self-gravitating matter - The final state. *Mon. Not. R. Astr. Soc.*, 238:1261, 1989.

[138] J. Madsen. On the applicability of the statistical mechanical theories of violent relaxation. *Astrophys. J.*, 316:497, 1987.

[139] J. Hjorth and J. Madsen. Violent relaxation and the R exp 1/4 law. *Mon. Not. R. Astr. Soc.*, 253:703, 1991.

[140] P.H. Chavanis. On the 'coarse-grained' evolution of collisionless stellar systems. *Mon. Not. R. Astron. Soc.*, 300:981, 1998.

[141] F.H. Shu. On the statistical mechanics of violent relaxation. *Astrophys. J.*, 225:83, 1978.

[142] F.H. Shu. On statistical mechanical theories of violent relaxation. *Astrophys. J.*, 316:502, 1987.

[143] T.K. Nakamura. Statistical mechanics of a collisionless system based on the maximum entropy principle. *Astrophys. J.*, 531:739, 2000.

[144] S. Tremaine, M. Hénon, and D. Lynden-Bell. H-functions and mixing in violent relaxation. *Mon. Not. R. Astr. Soc.*, 219:285, 1986.

[145] R.W. Michie. Structure and evolution of globular clusters. *Astrophys. J.*, 133:781, 1961.

[146] R.W. Michie and P.H. Bodenheimer. The dynamics of spherical stellar systems, II. *Mon. Not. R. Astr. Soc.*, 126:269, 1963.

[147] I.R. King. The structure of star clusters. II. Steady-state velocity distributions. *Astro. J.*, 70:376, 1965.

[148] Lj. Milanovič, H.A. Posch, and W. Thirring. Statistical mechanics and computer simulation of systems with attractive positive power-law potentials. *Phys. Rev. E*, 57:2763, 1998.

[149] T. Tsuchiya, N. Gouda, and T. Konishi. Chaotic itinerancy and thermalization in one-dimensional self-gravitating systems. *Astrophys. Space Sci.*, 257:319, 1997.

[150] K.R. Yawn and B.N. Miller. Ergodic properties and equilibrium of one-dimensional self-gravitating systems. *Phys. Rev. E*, 56:2429, 1997.

[151] K.R. Yawn and B.N. Miller. Equipartition and mass segregation in a one-dimensional self-gravitating system. *Phys. Rev. Lett.*, 79:3561, 1997.

[152] P. Valageas. Relaxation of a one-dimensional gravitational system. *Phys. Rev. E*, 74:016606, 2006.

[153] F. Bouchet, S. Gupta, and D. Mukamel. Thermodynamics and dynamics of systems with long-range interactions. *Physica A*, 389:4389, 2010.

[154] M. Luwel, G. Severne, and P.J. Rousseeuw. Numerical study of the relaxation of one-dimensional gravitational systems. *Astrophys. Space Sci.*, 100:261, 1984.

[155] C.J. Reild and B.N. Miller. Gravity in one dimension: A correction for ensemble averaging. *Astrophys. J.*, 371:260, 1991.

[156] J.L. Rouet and M.R. Feix. Persistence of collective fluctuation in N-body metaequilibrium gravitating and plasma systems. *Phys. Rev. E*, 59:73, 1999.

[157] P. Mineau, M.R. Feix, and J.L. Rouet. Numerical simulations of violent relaxation and formation of phase space holes in gravitational systems. *Astron. Astrophys.*, 228:344, 1990.

[158] T. Tsuchiya and N. Gouda. Relaxation and Lyapunov time scale in a one-dimensional gravitating sheet system. *Phys. Rev. E*, 61:948, 2000.

[159] A. Noullez, D. Fanelli, and E. Aurell. A heap-based algorithm for the study of one-dimensional particle systems. *IAU Symposium*, 208, 2003.

[160] M. Joyce, B. Marcos, and F. Sylos Labini. Energy ejection in the collapse of a cold spherical self-gravitating cloud. *Mon. Not. R. Astr. Soc.*, 397:775, 2009.

[161] K.R. Yawn and B.N. Miller. Ergodic properties and equilibrium of one-dimensional self-gravitating systems. *Phys. Rev. E*, 56:2429, 1997.

[162] R.M.C. Del Almeida, N. Lemke, P. Jund, R. Julien, I.A. Campbell, and D. Bertrand. Dynamics of complex systems above the glass temperature. *J. Non-Cryst. Sol.*, 287:201, 2001.

[163] F. Hohl and D. Tilghman Broaddus. Thermalization effects in one-dimensional self-gravitating system. *Phys. Lett.*, 25:713, 1967.

[164] H.L. Wright, B.N. Miller, and W.E. Stein. The relaxation time of a one-dimensional self-gravitating system. *Astrophys. Space Sci.*, 84:421, 1982.

[165] E. Montroll and D. Bendler. On Levy (or stable) distributions and the Williams-Watts model of dielectric relaxation. *J. Stat. Phys.*, 34:129, 1984.

[166] C. Reidl and B.N. Miller. Population dependence of early relaxation. *Phys. Rev. E*, 51:884, 1995.

[167] R. Pakter and Y. Levin. Universality of collisionless relaxation: Core-halo distribution in the Hamiltonian mean-field model. *Phys. Rev. Lett.*, 106, 2011.

[168] S. Goldstein, S. Cuperman, and M. Lecar. Numerical experimental check of Lynden-Bell statistics for a collisionless one-dimensional stellar system. *Mon. Not. R. Astr. Soc.*, 143:209, 1969.

[169] P.H. Chavanis. Hamiltonian and Brownian systems with long-range interactions: IV General kinetic equations from the quasilinear theory. *Physica A*, 387:1504, 2008.

[170] V. Springel, N. Yoshida, and S.D.M. White. GADGET: a code for collisionless and gas dynamical cosmological simulations. *New Astron.*, 6:79, 2001.

[171] V. Springel. The cosmological simulation code GADGET-2. *Mon. Not. R. Astr. Soc.*, 364:1105, 2005.

[172] C.M. Boily, E. Athanassoula, and P. Kroupa. Scaling up tides in numerical models of galaxy and halo formation. *Mon. Not. R. Astr. Soc.*, 332:971, 2002.

[173] O. Iguchi, Y. Sota, T. Tatekawa, A. Nakimichi, and M. Morikawa. Universal non-Gaussian velocity distribution in violent gravitational processes. *Phys. Rev. E*, 71:016102, 2005.

[174] L.A. Aguilar and D. Merritt. The structure and dynamics of galaxies fromed by cold dissipationless collapse. *Astrophys. J.*, 354:33, 1990.